



University
of Antwerp

Faculty of Medicine and Health Sciences

Department of Medical Genetics (MEDGEN)

Genomics and innovative induced pluripotent stem cell (iPSC) modeling to improve understanding of pathomechanisms underlying Brugada syndrome (BrS)

Genomische en innovatieve modelering van geïnduceerde pluripotente stamcellen (iPSC) om een beter inzicht te krijgen in de pathomechanismen van Brugada syndroom (BrS)

Thesis submitted for the degree of doctor of Medical Sciences at the University of Antwerp to be defended by **Aleksandra Nijak-Paeske**

Supervisors:

Prof. Bart L. Loeys

Prof. Maaïke Alaerts

Prof. Alain J. Labro

Disclaimer

The author allows to consult and copy parts of this work for personal use. Further reproduction or transmission in any form or by any means, without the prior permission of the author is strictly forbidden.

*"I never dreamed about success,
I worked for it."
Estée Lauder*

Members of the jury

Prof. Dr Bart Loeys, *promotor*

Center of Medical Genetics, University of Antwerp and Antwerp University Hospital, Antwerp, Belgium

Prof. Maaïke Alaerts, *promotor*

Center of Medical Genetics, University of Antwerp and Antwerp University Hospital, Antwerp, Belgium

Prof. Alain J. Labro, *promotor*

Laboratory of Molecular Biophysics, Cellular and Network Excitability, Department of Biomedical Sciences, University of Antwerp, Antwerp, Belgium; Department of Basic and Applied Medical Sciences, Faculty of Medicine and Health Sciences, Ghent University, Ghent, Belgium

Dr Wim Wuyts, *chairman*

Center of Medical Genetics, University of Antwerp and Antwerp University Hospital, Antwerp, Belgium

Prof. Dr Johan Saenen

Department of Cardiology, University of Antwerp & Antwerp University Hospital, Antwerp, Belgium

Prof. Dr Connie Bezzina

Department of Clinical and Experimental Cardiology, Amsterdam Cardiovascular Sciences, Amsterdam UMC, University of Amsterdam, Heart Center, Amsterdam, The Netherlands; European Reference Network for Rare and Low Prevalence Complex Diseases of the Heart (ERN GUARD-Heart), Brussels, Belgium

Prof. Dr Antoine Bondue

Department of Cardiology, Université Libre de Bruxelles, Belgium

Summary

Rapid development in the next-generation sequencing methods during the past ten years led to its' smooth implementation in clinical practice. Inherited cardiac arrhythmias, including Brugada syndrome (BrS), affecting young adults are an important health problem in the Western world. Genetic testing of patients with the use of whole exome sequencing (WES) or targeted gene panels has become a standard procedure. Nevertheless, looking at the contemporary knowledge about BrS pathophysiology, it is striking that although multiple genes have been linked with Brugada disease development, about 70% of BrS cases remain genetically unresolved. In the Cardiogenetics clinic at the Antwerp University Hospital, over the past decade extensive phenotypic information was collected on Brugada families in which genetic screening with an in-house developed cardiac arrhythmia gene panel (primary electrical disorder PED panel) did not yield any result. Three of those families became the basis for this project, in which a combined linkage analysis and whole genome sequencing (WGS) approach was used to look for potential disease causing variants.

With the growing amount of novel genetic candidate variants of uncertain significance (VUS) detected in diagnostic screening, appropriate *in vitro* modeling methods are required to perform functional validation of the variants and assess their involvement in disease etiology. For that purpose, heterologous expression models, or more recently - induced pluripotent stem cell (iPSC) derived models are applied. Although heterologous expression models are the gold standard in electrophysiological modeling of arrhythmia-related genetic variants, their main drawback is expression of a single specific channel, which limits the possibilities of investigation of the interactions of the mutant channel protein with other proteins involved in cardiac action potential (AP) generation. Here, iPSC derived cardiomyocytes come as a tool, providing the opportunity to obtain tissue- as well as patient-specific cells, where the entire repertoire of ionic channels are expressed, which undergo tissue specific post translational modifications. This novel approach has already been successfully applied in studies of long-/short-QT syndrome, catecholaminergic polymorphic ventricular tachycardia, arrhythmogenic (right ventricular) cardiomyopathy as well as BrS.

In this project functional characterization of a VUS c.4711T>C p.(Phe1571Leu) in the SCN5A gene, identified in a severe case presenting with sodium channelopathy and BrS was performed (**Chapter 3**). The variant was identified using the in-house developed PED panel, where inheritance of the novel VUS p.(Phe1571Leu) was confirmed in trans with a Belgian SCN5A founder mutation – c.4813+3_4813+6dupGGGT. This pathogenic variant was previously shown to lead to a loss-of-function of Na_v1.5 protein. Electrophysiological characterization of the novel VUS in transiently transfected HEK293 cells alone or co-expressed with the β1-subunit showed a hyperpolarizing shift in the voltage dependence of inactivation (loss-of-function of Na_v1.5), while the activation parameters were unaffected. We were able to show that application of the sodium channel activator toxin nemertide α-1 indeed restored the variant effect on the channel function due to a toxin-dependent reduction of channel inactivation. The observed properties of the analysed mutant channel led to variant classification as a likely pathogenic. The presence of p.(Phe1571Leu) together with a 'second hit' compound heterozygous Belgian SCN5A founder mutation explained the observed severe phenotype in the characterized case.

As one aim of this project was to perform phenotyping of the BrS patient derived iPSC-cardiomyocytes (iPSC-CMs), the author performed comparison of two published monolayer-based differentiation protocols, using sequential addition of small molecules modulating the canonical Wnt signalling pathway (**Chapter 4**). Their performance was investigated based on the molecular and electrophysiological phenotyping of the obtained iPSC-CMs, using i.e. patch clamping and calcium imaging techniques. Based on this comprehensive morpho-functional analysis, a conclusion that both tested protocols result in a high percentage of contracting CMs, presenting with typical iPSC-CM AP and calcium transient (CT) characteristics and showing acceptable survival and cell quality after dissociation was made. One protocol involving sequential addition of CHIR99021 and Wnt-C59 rendered iPSC-CMs that were more accessible for patch-clamp and CT experiments and showed an expression pattern of cardiac-specific markers more

similar to this observed in human heart left ventricle samples. Based on these results, this protocol was chosen to be used as the standard differentiation protocol in our lab. It was further optimized during functional modeling of the Belgian *SCN5A* founder mutation in iPSC-CMs.

Based on heterologous expression experiments in CHO cells, the Belgian BrS *SCN5A* founder mutation (c.4813+3_4813+6dupGGGT) has shown to cause a loss-of-function of the sodium current (I_{Na}) due to activation of an alternative splice site in exon 27 of the *SCN5A* gene, which results in a deletion of 32 amino acids in the $Na_v1.5$ protein. As such, parts of segment 2 and 3 of domain IV of $Na_v1.5$ are spliced out, which leads to a translation of a non-functional channel protein. We established iPSC-CM models for this unique founder mutation, identified in more than 25 families. Dermal fibroblasts from skin biopsies of selected patients with different severity of the phenotype and two unrelated healthy individuals were reprogrammed to iPSCs (**Chapter 5**). iPSC-CMs for functional characterization of the Belgian *SCN5A* founder mutation were obtained using the selected monolayer-based protocol as described above. Triiodothyronine (T3) hormone addition to improve cell maturity, and lactate treatment to obtain purified iPSC-CM cultures were tested. Several differentiation rounds of the selected cell lines were performed. Investigation of the expression patterns of cardiac-specific markers on RNA with qPCR and protein with immunofluorescence staining, as well as electrophysiological characterization of AP, sodium currents (I_{Na}) and CT was carried out. All of the generated iPSC-CMs expressed the tested cardiac markers. We did not observe significant differences in the obtained data between the differentiation batches, however, we noted significant variability between iPSC clones generated from one donor. Addition of T3 improved expression of the tested cardiac markers and organization of the sarcomeres, as well as diminished the observed interclonal variability of the results. The combination of T3 and lactate treatments also improved electrophysiological characteristics of the recorded cells. In Brugada patient iPSC-CMs obtained with basic differentiation protocol we observed reduction of I_{Na} density, together with shortening of AP and CT duration in comparison with the control iPSC-CMs. Meanwhile in T3 treated iPSC-CMs only part of the tested patient cell lines showed a loss-of-function of the sodium channel characteristics, based on reduced I_{Na} density or affected $V_{1/2}$ of inactivation of the $Na_v1.5$ channel. As in iPSC-CMs the whole repertoire of ion channels involved in cardiac conduction are expressed, it is possible to observe different functional effects of the analysed mutant channel (less or more pronounced), than this observed in heterologous expression experiments. It would be interesting to investigate the localization and quantity of the produced mutant $Na_v1.5$ channel in more detail to properly evaluate if the observed electrophysiological changes in obtained iPSC-CMs were the true functional effect of the tested *SCN5A* founder mutation. Furthermore, we prove that T3 addition improves the maturity of the cells, however with no impact on the variability of the obtained results.

In the three mentioned genetically unresolved families (based on prior PED panel analysis) we performed whole genome sequencing on 10 selected BrS patients. We recruited 35 extra affected and unaffected relatives from the selected families to perform SNP-based linkage analysis, and obtained total of 11 linked loci with suggestive LOD score ($\sim 1.3-1.8$), and 1 linked locus with a significant LOD score (3.162). Combining the linkage and sequencing data, we identified several deep intronic candidate VUS, which were predicted to alter normal splicing (**Chapter 6**). In order to evaluate a causal effect of selected variants, we performed splicing analysis of 4 variants using RNA samples obtained from patient-derived iPSC-CMs. However, this analysis could not demonstrate altered splicing and led to disqualification of the selected variants as potential candidates. In one of the tested families (BrS family 2), for which we obtained the highest LOD score of 3.162, we identified one potential candidate variant - a missense variant located within the linked locus in the *DCLRE1A* gene (predicted to reduce the acceptor site activity), that segregated with the disease phenotype in the family. The effect of this variant on the normal splicing of the affected protein is currently under investigation. A follow up study, involving re-analysis of WGS data combined with the new information obtained from RNA sequencing of iPSC-CMs from proband and family members will be performed after completion of this PhD project. The obtained results support the hypothesis that the sum of several genetic mutations may be explaining the occurrence of the symptoms in BrS cases where no mutation in BrS-related genes was identified.

iPSC-CM modeling of BrS has already been applied successfully in investigation of the functional phenotype of BrS (described in detail in **Chapter 1**). Although this technique helped in advancement of contemporary knowledge about disease aetiology, literature data suggest that iPSC-CM modeling of genotype-negative BrS patients does not yield significant findings. In this PhD project, we continued pursuing the correlation between the genetic and functional phenotype in one of the analysed but genetically unresolved BrS families, BrS family 2. We performed molecular and electrophysiological characterization of the phenotype in iPSC-CMs obtained from two affected (BrS1 and BrS2) and one unaffected (Famctrl) family members, in comparison to an unrelated healthy control (Ctrl) as well as an unrelated positive control - *SCN5A* Belgian founder mutation carrier donor (BrSfounder) (**Chapter 7**). We observed reduction in I_{Na} density, positive shift in voltage dependence of activation and negative shift in voltage dependence of inactivation in one of the probands (BrS1), while the second patient (BrS2) showed I_{Na} properties similar to the tested controls. Furthermore, BrS1 iPSC-CMs showed reduced AP amplitude (APA) in comparison to all the tested cell lines, and upstroke velocity (dV/dT_{max}) reduction in comparison to BrS2. We observed prolongation of action potential duration (APD) and calcium transient duration (CTD) in BrSfounder in comparison to the other tested cell lines. Significant CTD and rise time changes in BrSfounder and BrS2 iPSC-CMS were observed in comparison with the familial and unrelated control. Moreover, we noted enhanced arrhythmic events in iPSC-CMs of both familial BrS patients, where arrhythmia-like events were identified in 5% and 33% of all traces obtained from BrS1 and BrS2 iPSC-CMs respectively (no arrhythmia-like events were obtained in BrSfounder or negative controls). As ajmaline can unmask the BrS phenotype, we performed AP recordings with different concentrations (0.3 – 10 μ M) of this channel blocker. However, we did not observe the blocking effect of the ajmaline in our control lines, thus we were not able to determine the effect of the channel blocker in the tested BrS iPSC-CMs. Our results suggest impairment of the cardiac sodium channel in BrS1 iPSC-CMs (reduced I_{Na} density, affected voltage dependence of activation and inactivation and reduced APA and dV/dT_{max} , consistent with previously reported sodium loss-of-function BrS phenotypes), while in BrS2 iPSC-CMs Ca^{2+} flux abnormalities were observed. Both mechanisms led to higher susceptibility of the obtained cells to arrhythmia-like events. As the obtained results show impairment of sodium and/or calcium handling in patient iPSC-CMs, further molecular investigation using RNA sequencing to identify signalling pathways that are affected in this BrS family will be performed in follow-up studies.

In summary, while BrS used to be considered as a monogenic disorder, nowadays the disease is thought to have a more complex inheritance model. While heterologous expression models remain a gold standard in studies of single causal mutations (as shown in **Chapter 3**), iPSC models provide the solution for studies of complex cases, where a sum of multiple factors is at play for the expression of the phenotype. While literature data showed that iPSC-CM modeling of genotype-negative BrS patients did not yield significant findings, in this PhD project we did find interesting results. Although our combined linkage analysis and WGS approach in the three unresolved BrS families did not yield any strong genetic candidate variant (**Chapter 6**), iPSC-CMs of two of the patients displayed a BrS phenotype observed in either I_{Na} reduction and/or calcium handling abnormalities (**Chapter 7**). The obtained results suggested different underlying disease mechanisms within one family, which underscores the complex nature of Brugada syndrome.

Samenvatting

De snelle ontwikkeling van *next-generation sequencing*-methoden in de afgelopen tien jaar heeft geleid tot een soepele implementatie in de klinische praktijk. Erfelijke hartritmestoornissen die jonge volwassenen treffen, waaronder het Brugada-syndroom (BrS), vormen een belangrijk gezondheidsprobleem in de Westerse wereld. Genetisch testen van patiënten met behulp van *whole exome sequencing* (WES) of gerichte genpanels is een standaardprocedure geworden. Maar hoewel meerdere genen in verband zijn gebracht met de ontwikkeling van de ziekte van Brugada, kan voor ongeveer 70% van de BrS-patiënten geen genetische diagnose gesteld worden. In de Cardiogenetica kliniek van het Universitair Ziekenhuis Antwerpen werd het afgelopen decennium uitgebreide fenotypische informatie verzameld van Brugada families waarin genetische screening met een in-house ontwikkeld hartritme-genenpanel (*primary electrical disorder*, PED-panel) geen resultaat opleverde. Drie van die families werden de basis voor dit project, waarin een gecombineerde methode van koppelingsanalyse en *whole genome sequencing* (WGS) werd gebruikt om te zoeken naar mogelijke ziekteverwekkende varianten.

Met de groeiende hoeveelheid nieuwe genetische kandidaat-varianten van ongekende betekenis (*variant of uncertain significance*, VUS) die worden gedetecteerd in diagnostische screening, zijn geschikte *in vitro* modelleringsmethoden vereist om de functie van deze varianten te bestuderen en hun betrokkenheid bij de etiologie van de ziekte te beoordelen. Hiertoe worden heterologe expressiemodellen, of meer recentelijk geïnduceerde pluripotente stamcel (iPSC)-afgeleide modellen gebruikt. Hoewel heterologe expressiemodellen de gouden standaard zijn in elektrofysiologische modellering van aritmie-gerelateerde genetische varianten, is hun belangrijkste nadeel dat ze slechts een enkel specifiek kanaal tot expressie brengen. Dit beperkt de mogelijkheden om de interacties van het mutante kanaaleiwit met andere eiwitten die betrokken zijn bij het opwekken en geleiden van de cardiale actiepotentiaal (AP) te onderzoeken. Hier komen iPSC-afgeleide cardiomyocyten als een hulpmiddel, omdat ze de mogelijkheid bieden om zowel weefsel- als patiëntspecifieke cellen te verkrijgen, waarin het volledige repertoire aan ionkanalen tot expressie wordt gebracht, met weefsel-specifieke post-translationele modificaties. Deze nieuwe benadering is al met succes toegepast in onderzoek naar hartritmestoornissen zoals het lange-/korte-QT-syndroom, catecholaminerge polymorfe ventriculaire tachycardie, aritmogene rechterventrikelcardiomyopathie en BrS.

In dit project werd de functionele karakterisering van een VUS c.4711T>C p.(Phe1571Leu) in het *SCN5A*-gen uitgevoerd, geïdentificeerd in een ernstig aangetaste patiënt met BrS, (**Hoofdstuk 3**). De variant werd geïdentificeerd met behulp van het PED-panel, waarmee werd bevestigd dat de nieuwe VUS p.(Phe1571Leu) in trans ligt met een Belgische *SCN5A*-foundermutatie - c.4813+3_4813+6dupGGGT. Eerder werd aangetoond dat deze laatste pathogene variant leidt tot functieverlies van het Na_v1.5-eiwit. Elektrofysiologische karakterisering van de nieuwe VUS in getransfecteerde HEK293-cellen, alleen of co-geëxprimeerd met de β_1 -subeenheid, toonde een hyperpolariserende verschuiving in de spanningsafhankelijkheid van inactivatie (verlies van functie van Na_v1.5), terwijl de activeringsparameters onveranderd waren. We konden aantonen dat toediening van het toxine nemertide α -1 dat het natriumkanal activeert, inderdaad de kanaalfunctie herstelde vanwege een toxine-afhankelijke vermindering van kanaalinactivatie. Deze resultaten stelden ons in staat de nieuwe variant te classificeren als waarschijnlijk pathogeen. Het heterozygoot voorkomen van p.(Phe1571Leu) samen met de Belgische *SCN5A*-foundermutatie als 'tweede hit' verklaarde het waargenomen ernstige fenotype in deze patiënt.

Omdat een van de doelstellingen van dit project was om BrS-patiënt afgeleide iPSC-cardiomyocyten (iPSC-CMs) te fenotyperen, werd een vergelijking uitgevoerd van twee gepubliceerde monolaag-gebaseerde differentiatieprotocollen. Beide bewerkstelligen de differentiatie aan de hand van kleine moleculen die de canonieke Wnt-signaleringsmoduleren en opeenvolgend worden toegevoegd (**Hoofdstuk 4**). De protocols werden geëvalueerd op basis van moleculaire en elektrofysiologische kenmerken van de verkregen iPSC-CMs, o.a. bestudeerd met behulp van patch-clamp en calciumbeeldvormingstechnieken. Op basis van deze uitgebreide morfo-functionele analyse werd geconcludeerd dat beide geteste

protocollen resulteren in een hoog percentage contraherende CMs, met typische iPSC-CM AP- en calcium transiënt (CT)-kenmerken en acceptabele overleving en celkwaliteit na dissociatie. Eén protocol met opeenvolgende toevoeging van CHIR99021 en Wnt-C59 maakte iPSC-CMs die beter toepasbaar waren voor patch-clamp- en CT-experimenten. Deze iPSC-CMs vertoonden ook een expressiepatroon van hartspecifieke merkers dat meer lijkt op het patroon waargenomen in weefselstalen van het linkerventrikel van het menselijke hart. Op basis van deze resultaten werd dit protocol gekozen om te worden gebruikt als het standaard differentiatieprotocol in ons laboratorium. Het werd verder geoptimaliseerd tijdens functionele modellering van de Belgische *SCN5A*-founderermutatie in iPSC-CMs.

Heterologe expressie-experimenten in CHO-cellen toonden aan dat bij de Belgische BrS *SCN5A*-founderermutatie (c.4813+3_4813+6dupGGGT) het functieverlies van de natriumstroom (I_{Na}) veroorzaakt wordt door activering van een alternatieve splice site in exon 27 van het *SCN5A*-gen, die resulteert in een deletie van 32 aminozuren in het $Na_v1.5$ -eiwit. Als zodanig gaan delen van segment 2 en 3 van het domein IV van $Na_v1.5$ verloren, wat leidt tot een niet-functioneel kanaaleiwit. We hebben iPSC-CM-modellen aangemaakt voor deze unieke founderermutatie, geïdentificeerd in meer dan 25 families. Dermale fibroblasten uit huidbiopten van geselecteerde patiënten met verschillende fenotypische ernst en twee niet-verwante gezonde individuen werden 'geherprogrammeerd' tot iPSCs (**Hoofdstuk 5**). iPSC-CMs voor functionele karakterisering van de Belgische *SCN5A*-founderermutatie werden verkregen met behulp van het geselecteerde monolaag-gebaseerde protocol zoals hierboven beschreven. De toevoeging van triiodothyronine (T3) hormoon om de maturatie van de cellen te verbeteren, en lactaatbehandeling om zuivere iPSC-CM-culturen te verkrijgen, werden getest. Er werden verschillende differentiatierondes van de geselecteerde cellijnen uitgevoerd. De expressiepatronen van hartspecifieke merkers werden onderzocht op RNA-niveau met qPCR en op eiwitniveau met immunofluorescentiekleuring. Ook elektrofysiologische karakterisering van AP, natriumstromen (I_{Na}) en CT werd uitgevoerd. Alle geteste merkers kwamen tot expressie in de gegenereerde iPSC-CMs. We namen geen significante verschillen waar tussen de verschillende differentiatiebatches van één iPSC cellijn, maar merkten wel een significante variabiliteit op tussen iPSC cellijnen afkomstig van eenzelfde donor. Toevoeging van T3 verbeterde de expressie van de geteste hartmerkers en de organisatie van de sarcomeren in de iPSC-CM, en verminderde de waargenomen inter-klonale variabiliteit van de resultaten. De combinatie van T3- en lactaatbehandelingen verbeterde ook de elektrofysiologische kenmerken van de cellen.

In iPSC-CMs van Brugada-patiënten verkregen met het basisdifferentiatieprotocol observeerden we een vermindering van de I_{Na} -densiteit en een verkorting van de AP- en CT-duur in vergelijking met de controles. In T3 behandelde iPSC-CMs daarentegen vertoonde slechts een deel van de geteste patiënt cellijnen een functieverlies van het natriumkanal, zichtbaar in een verminderde I_{Na} -densiteit of verlaagde $V_{1/2}$ van inactivatie van het $Na_v1.5$ -kanaal. Omdat in iPSC-CMs alle ionenkanalen die betrokken zijn bij hartgeleiding tot expressie worden gebracht, is het mogelijk om een ander functioneel effect van de geanalyseerde mutant (minder of meer uitgesproken) waar te nemen dan dit waargenomen in heterologe expressie experimenten. Het zou interessant zijn om de lokalisatie en hoeveelheid van het geproduceerde mutante $Na_v1.5$ -kanaal meer in detail te onderzoeken om goed te kunnen inschatten of de waargenomen elektrofysiologische veranderingen in de iPSC-CMs het echte functionele effect waren van de geteste *SCN5A*-founderermutatie. Verder bewijzen we dat T3-toevoeging de maturatie van de cellen verbetert, echter zonder invloed op de variabiliteit van de verkregen resultaten.

In de drie reeds vermelde genetisch onopgeloste families (gebaseerd op eerdere PED-panel analyse) voerden we sequencering van het hele genoom uit op 10 geselecteerde BrS-patiënten. We rekruteerden 35 extra aangetaste en niet-aangetaste familieleden uit de geselecteerde families om SNP-gebaseerde koppelinganalyse uit te voeren. Deze analyse resulteerde in 11 gekoppelde *loci* met suggestieve LOD-score ($\sim 1.3-1.8$), en één gekoppelde locus met een significante LOD-score (3.162). Door de resultaten van de koppelings- en sequentie analyse te combineren, identificeerden we verschillende diep-intronische kandidaat-VUSsen, waarvan werd voorspeld dat ze de normale splicing zouden aantasten (**Hoofdstuk 6**). Om een causaal effect van deze varianten te evalueren, hebben we een splicing-analyse van vier geselecteerde varianten uitgevoerd met behulp van RNA-stalen uit de patiënt afgeleide iPSC-

CMs. Deze analyse kon echter geen veranderde splicing aantonen en leidde tot diskwalificatie van deze geselecteerde varianten als potentiële kandidaten. In één van de geteste families (BrS-familie 2), waarvoor we de hoogste LOD-score van 3.162 behaalden, identificeerden we één potentiële kandidaat variant die segregeerde met het ziektefenotype in de familie: een missense variant die zich in de gekoppelde locus in het *DCLRE1A*-gen bevindt en waarvan voorspeld wordt dat deze de activiteit van de splice acceptorsite vermindert. Het effect van deze variant op de normale splicing van het aangetaste eiwit wordt momenteel onderzocht. Na afronding van dit doctoraatsproject zal een vervolgstudie worden uitgevoerd, waarbij de WGS-gegevens opnieuw worden geanalyseerd in combinatie met de nieuwe informatie die is verkregen uit RNA-sequencing van gegenereerde iPSC-CM's van proband en familieleden. De verkregen resultaten, ondersteunen de hypothese dat de som van verschillende genetische mutaties het ontstaan van de symptomen verklaart in BrS patiënten waarbij geen mutatie in BrS-gerelateerde genen werd geïdentificeerd.

iPSC-CMs werden al met succes gebruikt in onderzoek naar het functionele fenotype van BrS (in detail beschreven in **Hoofdstuk 1**). Hoewel dit model heeft geholpen onze hedendaagse kennis over de etiologie van de ziekte te vergroten, suggereren literatuurgegevens dat iPSC-CM-modellering van genotype-negatieve BrS-patiënten geen significante bevindingen oplevert. In dit doctoraatsproject gingen we verder met het bestuderen van de genotype-fenotype correlatie in een van de genetisch onopgeloste BrS-families, BrS-familie 2. We voerden moleculaire en elektrofysiologische karakterisering uit van iPSC-CMs gegenereerd van twee aangetaste (BrS1 en BrS2) en één niet-aangetast (Famctrl) familielid, in vergelijking met een niet-verwante gezonde controle (Ctrl) en een niet-verwante positieve controle – drager van de Belgische *SCN5A* foundermutatie (BrSfounder) (**Hoofdstuk 7**). We observeerden een afname in I_{Na} -densiteit, positieve verschuiving in spanningsafhankelijkheid van activatie en negatieve verschuiving in spanningsafhankelijkheid van inactivatie in een van de probands (BrS1), terwijl de tweede patiënt (BrS2) I_{Na} -eigenschappen vertoonde die vergelijkbaar waren met de geteste controles. Bovendien vertoonden BrS1 iPSC-CMs een verminderde AP-amplitude (APA) in vergelijking met alle geteste cellijnen, en een verlaging van de snelheid van depolarisatie (dV/dT_{max}) in vergelijking met BrS2. We observeerden een verlenging van de duur van de actiepotentiaal (APD) en de duur van de calciumtransiënt (CTD) in BrSfounder in vergelijking met de andere geteste cellijnen. Significante CT-veranderingen werden waargenomen in BrSfounder en BrS2 iPSC-CMs in vergelijking met de familiale en niet-verwante controle. Bovendien konden we aritmische activiteit detecteren in iPSC-CMs van beide familiale BrS patiënten in respectievelijk 5% en 33% van alle opnames van BrS1- en BrS2-iPSC-CMs en geen in BrSfounder of negatieve controles. Omdat ajmaline het BrS-fenotype kan ontmaskeren, hebben we AP-opnames uitgevoerd met verschillende concentraties (0,3 – 10 μ M) van deze natriumkanalblokker. We konden echter het blokkerende effect van de ajmaline niet waarnemen in onze controlelijnen, dus we waren niet in staat om het effect van de kanaalblokker in de geteste BrS iPSC-CMs te bepalen. Onze resultaten suggereren een aantasting van het natriumkanal in BrS1 iPSC-CMs, geobserveerd als verminderde I_{Na} -densiteit, veranderde spanningsafhankelijkheid van activatie en inactivatie, verminderde APA en dV/dT_{max} , consistent met eerder gepubliceerde resultaten. In BrS2 iPSC-CM's werden daarentegen Ca^{2+} -fluxafwijkingen waargenomen. Beide leidden tot een hogere gevoeligheid van de verkregen cellen voor aritmieën. Aangezien deze resultaten een verstoring van natrium- en/of calcium in iPSC-CMs van patiënten aantoonden, zal verder moleculair onderzoek worden uitgevoerd met behulp van RNA-sequencing om eiwitten en pathways te identificeren die in deze BrS-familie zijn aangetast.

In conclusie, hoewel BrS oorspronkelijk als een monogene aandoening beschouwd werd, wordt tegenwoordig aangenomen dat de ziekte een complexer overervingsmodel heeft. Terwijl heterologe expressiemodellen een gouden standaard blijven in studies van enkelvoudige causale mutaties (zoals getoond in **Hoofdstuk 3**), bieden iPSC-modellen een oplossing voor de studie van complexe situaties, waarbij meerdere factoren een rol spelen bij de expressie van het fenotype. Hoewel in vorige studies iPSC-CM-modellering van genotype-negatieve BrS-patiënten geen significante bevindingen opleverde, werden in dit PhD-project wel interessante resultaten bekomen. Onze strategie van gecombineerde koppelingsanalyse en WGS leverde geen sterke kandidaat genetische variant op in de drie onopgeloste

BrS-families (**Hoofdstuk 6**), maar iPSC-CMs van twee van de patiënten vertoonden een BrS-fenotype, waargenomen in I_{Na} -reductie en/of afwijkingen in calcium metabolisme (**Hoofdstuk 7**). Deze resultaten suggereerden de aanwezigheid van verschillende onderliggende ziektemechanismen binnen één familie, wat de complexe aard van het Brugada syndroom onderstreept.

Abbreviations

ACM Arrhythmogenic Cardiomyopathy

ANK2 Ankyrin 2

ANK3 Ankyrin 3

ANOVA Analysis of Variance

AP Action Potential

APA Action Potential Amplitude

APD Action Potential Duration

APD30/50/90 Action Potential Duration at 30/50/90 % of depolarization

ARVC Arrhythmogenic Ventricular Cardiomyopathy

BMP4 Bone Morphogenic Protein 4

BPM Beats Per Minute

BrS Brugada syndrome

BSA Bovine Serum Albumin

Ca²⁺ Calcium ions

CACNA1C Calcium Voltage-Gated Channel Subunit Alpha1 C

cACT Cardiac α -Actinin

CADD Combined Annotation Dependent Depletion

Ca_v1.2 Calcium voltage-dependent channel

cDNA complementary DNA

CHO Chinese Hamster Ovary cells

Chr Chromosome

CMOS Complementary Metal-Oxide-Semiconductor

CMs cardiomyocytes

CNV copy number variation

Cnx43 Connexin 43

CRISPR/Cas

CT Calcium Transient

CTD Calcium Transient Duration

CTD50/70 Calcium Transient Duration at 50/70% depolarization

CTNNA3 Catenin Alpha 3

cTNNI Cardiac Troponin I

D0 Day 0

DAD Delayed AfterDepolarizations

DAPI 4',6-diamidino-2-phenylindole

dbSNP database for Single Nucleotide Polymorphisms

DCLRE1A DNA Cross-Link Repair 1A

Del deletion

Dex Dexametazone

DMEM Dulbecco's Modified Eagle Medium

DMSO Dimethyl sulfoxide

DNA DeoxyriboNucleic Acid

DPP6 Dipeptidyl Peptidase Like 6

dV/dT_{max} Upstroke Velocity

E8 flex Essential 8 flex medium

EAD Early AfterDepolarization

EB Embryoid Bodies

ECG ElectroCardioGram

ECHS1 Enoyl-CoA Hydrase Short Chain 1

ECS ExtraCellular Solution

EDTA Ethylenediaminetetraacetic acid

ENCODE Encyclopedia of DNA Elements

EP ElectroPhysiological

ExAC Exome Aggregation Consortium

FB FibroBlasts

FBS Fetal Bovine Serum

FGF2 Fibroblast Growth Factor 2

FOXP1 Forkhead Box P1

FPD Field Potential Duration

GAPDH Glyceraldehyde 3-Phosphate Dehydrogenase

GECI Genetically Encoded Calcium Indicator

GEVI Genetically Encoded Voltage Indicator

GJA1 Gap Junction Protein Alpha 1 (Connexin 43)

GLI2 GLI Family Zinc Finger 2

G_{max} Maximal conductance

GnomAD Genome Aggregation Database

GTEx Genotype-Tissue Expression Portal

G-V Conductance-Voltage

GWAS Genome Wide Association Study

HCN4 Hyperpolarization Activated Cyclic Nucleotide Gated Potassium Channel 4

HEK293 Human Embryonic Kidney

hESCs human Embryonic Stem Cells

hERG human Ether-a-go-go Related Gene

HEY2 Hes Related Family BHLH Transcription Factor With YRPW Motif 2

I_{CaL} Late Calcium Current

ICC ImmunoCytoChemistry

ICD Implantable Cardioverter Defibrillator

ICS IntraCellular Solution

I_f Funny current

IGV Integrative Genomics Viewer

I_{K1} Inward Rectifier Current

I_{Ks} Slow Delayed Rectifier Potassium Current

I_{Kr} Delayed Rectifier Potassium Current

I_{Na} Sodium Current

I_{NaL} Late Sodium Current

I_{to} Cardiac Transient Outward Potassium Current

iPSC induced Pluripotent Stem Cells

iPSC-CMs induced Pluripotent Stem Cell-derived CardioMyocytes

K⁺ Potassium ions

KAVIAR Known VARIants Genomic Variant Database

kb kilo bases

KCND3 Potassium Voltage-Gated Channel Subfamily D Member 3

KCNE1 Potassium Voltage-Gated Channel Subfamily E Regulatory Subunit 1

KCNH2 Potassium Voltage-Gated Channel Subfamily H Member 2

KCNJ2 Potassium Inwardly Rectifying Channel Subfamily J Member 2

KCNJ8 Potassium Inwardly Rectifying Channel Subfamily J Member 6

KCNQ1 Potassium Voltage-Gated Channel Subfamily Q Member 1

LOD Logarithm of ODds

LQTS Long QT-Syndrome

LSM Lymphocyte Separation Media

LV Left Ventricle

MAF Minor Allele Frequency

Mb Mega bases

MEA Multiple Electrode Array

miRNA micro RNA

mRNA Messenger RNA

MLC2 α Myosin Regulatory Light Chain 2a

MLC2 ν Myosin Regulatory Light Chain 2v

MNCs Mononuclear cells

mV miliVolt

MYH6 Myosin Heavy chain 6

MYH7 Myosin Heavy Chain 7

Na⁺ Sodium ions

Nkx2.5 NK2 Homeobox 5

Na_v1.5 Voltage-Gated Cardiac Sodium Channel α -subunit

Na_v1.8 Voltage-Gated Sodium Channel

NMD Nonsense Mediated Decay

Oct 3/4 Octamer-Binding Transcription Factor 3/4

OMIM Online Mendelian Inheritance in Man

P10 Passage 10

PBS Phosphate-Buffered Saline

PCR Polymerase Chain Reaction

PBMCs Peripheral Blood Mononuclear Cells

PED Primary Electrical Disorder

PKP2 Plakophilin 2

PolyPhen Polymorphism Phenotyping tool

qPCR quantitative PCR

RAD GTP-binding protein RAD

RC Rate of Constant decay

Rcf Relative centrifugal field

Ref. seq. Reference Sequence

RMP Resting Membrane Potential

RNA RyboNucleic Acid

ROBO1 Roundabout Homolog 1

ROH Region of Homozygosity

RPL13A Ribosomal Protein L13a

RRAD Ras Related Glycolysis Inhibitor And Calcium Channel Regulator

RT Room Temperature

RUNX2 Run-related Transcription Factor 2

RVOT Right Ventricular Outflow Tract

RYR2 Ryanodine Receptor 2

SCD Sudden Cardiac Death

SCN10A Sodium Voltage-Gated Channel Alpha Subunit 10

SCN1B Sodium Voltage-Gated Channel Beta Subunit 1

SCN3B Sodium Voltage-Gated Channel Beta Subunit 3

SCN5A Sodium Voltage-Gated Channel Alpha Subunit 5

SD Standard Deviation

SEM Standard Error of Mean

SIFT Sorting Intolerant From Tolerant algorithm

siRNA small interfering RNA

SNAP29 Synaptosomal-associated protein 29

SNP single nucleotide polymorphism

SNV single nucleotide variant

SR Sarcoplasmic Reticulum

SSS Sick Sinus Syndrome

TAAD Thoracic Aortic Aneurysm and Dissection

T3 Triiodothyronine

TH Thyroid Hormone

TNNI3 Troponin I3, Cardiac Type

TNNT2 Troponin T2, Cardiac Type

TOPMED Trans-Omics for Precision Medicine dataset
tSA Mouse Mammary Adenocarcinoma Cell Line
UniProt The Universal Protein Knowledgebase
UTR Untranslated Region
V_{1/2} Mid-point of Voltage-Dependence
VEGF Vascular Endothelial Growth Factor
VF Ventricular Fibrillation
VMCs Ventricular Cardiomyocytes
V/s Volt/second
VT Ventricular Tachycardia
VUS Variant of Unknown Significance
WES Whole Exome Sequencing
WGS Whole Genome Sequencing
WT wild type

Contents

Chapter 1. General introduction.....	7
1.1 Abstract	9
1.2 Introduction.....	9
1.3 Methods for Derivation of iPSC-CM Models	10
1.3.1 Fibroblast Reprogramming Protocols	10
1.3.2 Cardiomyocyte Differentiation	11
1.4 Phenotyping Methods of iPSC-CMs.....	11
1.4.1 Patch-Clamping.....	13
1.4.2 Calcium and Voltage Fluorescence Imaging	16
1.4.3 Micro-Electrode Array (MEA)	16
1.5 Findings from Published BrS iPSC-CM Models	16
1.5.1 Sodium Channel Genes.....	17
1.6 iPSC-CM Models of Variants in Other Arrhythmia-Related Genes.....	21
1.6.1 Calcium Channel Related Proteins.....	21
1.6.2 Desmosomal Proteins.....	21
1.7 Unknown Genetic Contribution.....	22
1.8 Conclusions and Future Perspective	23
1.9 References.....	27
1.10 Supplementary material.....	35
Chapter 2. Aim of the thesis	53
Chapter 3. Compound Heterozygous <i>SCN5A</i> Mutations in a Severe Sodium Channelopathy With Brugada Syndrome: A Case Report	55
3.1 Abstract	57
3.2 Introduction.....	58
3.3 Materials and Methods	58
3.3.1 Mutation analysis of <i>SCN5A</i>	58
3.3.2 Site-directed mutagenesis and transfection of HEK293 cells.....	58
3.3.3 Electrophysiological recordings	59
3.3.4 Data analysis	59
3.4 Case description and diagnostic assessment	60
3.4.1 Clinical presentation of index patient and available family members	60
3.4.2 Molecular genetics.....	61
3.5 Electrophysiological characteristics	62

3.6	Discussion.....	64
3.7	References.....	65
Chapter 4. Morpho-functional Comparison of Differentiation Protocols to Create iPSC-derived Cardiomyocytes 67		
4.1	Abstract.....	69
4.2	Introduction	70
4.3	Results.....	72
4.3.1	Reprogrammed iPSC clones express pluripotency markers and show appropriate iPSC morphology.....	72
4.3.2	Protocol comparison: iPSC-CMs obtained with protocol B show higher similarity in transcript expression in comparison to ventricular tissue, and show less 3D clumps morphology.....	72
4.3.3	Protocol validation: iPSC-CMs generated with protocol B are suitable for patch-clamping and intracellular Ca ²⁺ imaging	78
4.4	Discussion.....	80
4.5	Materials and methods	82
4.5.1	Fibroblast reprogramming to iPSCs and validation.....	82
4.5.2	Immunofluorescence staining.....	83
4.5.3	Sendai vectors presence test.....	83
4.5.4	Genomic integrity test using SNP array.....	83
4.5.5	Cardiomyocyte differentiation	84
4.5.6	Electrophysiological experiments.....	84
4.5.7	qPCR.....	85
4.5.8	Imaging data analysis	85
4.6	References.....	87
4.7	Supplementary material.....	91
4.8	References.....	104
Chapter 5. Electrophysiological Characterization of a Brugada Syndrome <i>SCN5A</i> Belgian Founder Mutation Modeled in Induced Pluripotent Stem Cell Derived Cardiomyocytes105		
5.1	Abstract.....	107
5.2	Introduction	108
5.3	Aims and objectives	109
5.4	Materials and methods	109
5.4.1	Patients, control individuals and cell lines	109
5.4.2	iPSC culture and differentiation to iPSC-CMs.....	110
5.4.3	Molecular characterization	110
5.4.4	Electrophysiological recordings.....	110
5.4.5	Data analysis.....	111

5.5	Results	111
5.5.1	Comparison of T3 versus T3+lactate treatment	111
5.5.2	Obtained iPSC-CMs show low intra-clonal (batch-to-batch) differentiation variability.....	114
5.5.3	Inter-clonal variability of a single donor	116
5.5.4	Overall comparison of basic versus T3 protocol.....	120
5.5.5	Patient-control differences are dependent on the used differentiation protocol.....	132
5.6	Discussion	139
5.7	References.....	147
Chapter 6.	A Wild-geese Chase – in Search of Novel Brugada Syndrome Candidate Variants.....	151
6.1	Abstract	153
6.2	Introduction.....	154
6.3	Materials and methods	155
6.3.1	Genetic screening	155
6.3.2	Cell culture and derivation.....	157
6.4	Results	158
6.4.1	BrS family 1	158
6.4.2	BrS family 2	162
6.4.3	BrS family 3	169
6.5	Discussion	173
6.6	References.....	177
Chapter 7.	Functional Phenotyping of iPSC-CMs Obtained From Genetically Unresolved BrS Family Members in Search for Pathophysiological Mechanisms	181
7.1	Abstract	183
7.2	Introduction.....	184
7.3	Materials and methods	185
7.3.1	PBMC, iPSC and iPSC-CM derivation and culture	185
7.3.2	Molecular characterization of obtained cell types	185
7.3.3	Imaging data analysis.....	187
7.3.4	Patch-clamping and calcium imaging	187
7.3.5	Statistical analysis.....	188
7.4	Results	188
7.4.1	Obtained iPSC-CMs show similar differentiation efficiency, transcript levels and protein organisation of the tested cardiac markers.....	188
7.4.2	Sodium current analysis revealed differences in channel function between the tested affected family members.....	193

7.4.3	iPSC-CMs of one of the affected donors reveal dV/dT_{max} and APA reduction, while ajmaline testing in the obtained iPSC-CMs yielded inconclusive results.....	198
7.4.4	CT analysis revealed arrhythmia-like events in both BrS patient iPSC-CMs.....	205
7.5	Discussion.....	208
7.6	References.....	212
Chapter 8.	General discussion	215
8.1	Brugada syndrome development – the status of current knowledge.....	216
8.2	Looking for a candidate in a haystack of genetic information.....	217
8.3	iPSC-CMs in Brugada syndrome modeling – a challenge of maturity.....	217
8.4	It’s always the small pieces that make the big picture	220
8.5	References.....	222

Chapter 1. General introduction

This chapter is partially modified from

iPSC-Cardiomyocyte Models of Brugada Syndrome-Achievements, Challenges and Future Perspectives

Aleksandra Nijak ¹, Johan Saenen ², Alain J Labro ^{3,4}, Dorien Schepers ^{1,3}, Bart L Loeys ^{1,5}, Maaïke Alaerts ¹

International Journal of Molecular Sciences, 2021; 22(6):2825. doi: 10.3390/jims22062825

¹Centre of Medical Genetics, faculty of Medicine and Health Sciences, University of Antwerp & Antwerp University Hospital, Antwerp, Belgium

²Department of Cardiology, University of Antwerp & Antwerp University Hospital, Antwerp, Belgium

³Laboratory of Molecular Biophysics, Cellular and Network Excitability, Department of Biomedical Sciences, University of Antwerp, Antwerp, Belgium

⁴Department of Basic and Applied Medical Sciences, Faculty of Medicine and Health Sciences, Ghent University, Ghent, Belgium

⁵Department of Human Genetics, Radboud University Medical Centre, Nijmegen, The Netherlands

1.1 Abstract

Brugada syndrome (BrS) is an inherited cardiac arrhythmia that predisposes to ventricular fibrillation and sudden cardiac death. It originates from oligogenic alterations that affect cardiac ion channels or their accessory proteins. The main hurdle for the study of the functional effects of those variants is the need for a specific model that mimics the complex environment of human cardiomyocytes. Traditionally, animal models or transient heterologous expression systems are applied for electrophysiological investigations, each of these models having their limitations. The ability to create induced pluripotent stem cell-derived cardiomyocytes (iPSC-CMs), providing a source of human patient-specific cells, offers new opportunities in the field of cardiac disease modeling. Contemporary iPSC-CMs constitute the best possible *in vitro* model to study complex cardiac arrhythmia syndromes such as BrS. To date, thirteen reports on iPSC-CM models for BrS have been published and with this review we provide an overview of the current findings, with a focus on the electrophysiological parameters. We also discuss the methods that are used for cell derivation and data acquisition. In the end, we critically evaluate the knowledge gained by the use of these iPSC-CM models and discuss challenges and future perspectives for iPSC-CMs in the study of BrS and other arrhythmias.

1.2 Introduction

Brugada syndrome (BrS) is an inherited cardiac arrhythmia characterized by a typical pattern of ST-segment elevation on the electrocardiogram (ECG) and an increased risk of ventricular fibrillation and sudden cardiac death (SCD). It accounts for 20% of SCD in individuals without structural heart disease. [1]. In 20–25% of BrS patients, loss-of-function mutations are identified in the *SCN5A* gene, which encodes the α subunit of the cardiac sodium channel $Na_v1.5$ [2]. To date, more than 20 other genes have been associated with this oligogenic disease with variants impairing specific ion channels or their accessory proteins involved in the cardiac action potential (AP) (reviewed in [2,3]). Still, three quarters of the diagnosed BrS patients remain without an implicated genetic variant [4]. Importantly, no comprehensive clinical and cellular studies have confirmed most of the candidate gene associations. A recent burden analysis and re-evaluation of reported genes only classified the *SCN5A* gene as demonstrating definitive evidence as a cause for BrS [5,6].

Concerning pathophysiology, currently three major hypotheses aim to explain the electric abnormality in BrS, namely the repolarization, depolarization and neural crest models [7–13]. In short, the characteristic ECG changes are respectively explained by (1) transmural dispersion of repolarization in the right ventricle between the endocardium and epicardium; (2) delayed depolarization due to conduction slowing and presence of subtle structural abnormalities in the right ventricular outflow tract (RVOT) and (3) abnormal cardiac neural crest cell migration, cell–cell communication and the development of the RVOT. Despite their differences, these models agree that the major region of pathology is the anterior RV and RVOT and that micro tissue architectural changes or cellular uncoupling effects play a role. Moreover, they are not mutually exclusive and could act in combination. Further studies are required to deepen our understanding of these mechanisms, how they lead to sustained ventricular arrhythmias and link them with the molecular changes underlying BrS.

BrS is well-known to display reduced penetrance and variable expressivity, characterized by a wide range of severity from a lifetime asymptomatic status to syncopes and SCD at a young age, even in patients with the identical familial mutation [1]. This clearly hampers patient risk stratification and management. Both environmental and genetic disease modifiers play a role in this variability [14] and over the past years, BrS has been recognized as a more complex disease, with the involvement of multiple common and rare genetic variants acting in concert in its etiology [15–19]. Current application of gene panels, whole exome sequencing (WES) and whole genome sequencing (WGS) in (familial) patients will continue to identify variants potentially involved in BrS, though most of these remain “variants of uncertain significance” (VUS) and without functional studies, a gap remains to translate potential genotype–phenotype correlation into clinical practice.

To further elucidate the oligogenic architecture and pathogenic mechanisms of BrS, understand the functional effects of candidate pathogenic variants at the cell and tissue level and interpret the causality of VUS, representative functional disease models are highly needed. If successful, these models can be applied to test therapeutic approaches. Since currently no proper pharmacological treatment for BrS is available, the implantation of a cardioverter defibrillator (ICD) is the only effective preventative treatment for symptomatic patients. Recently, radio frequency ablation of the arrhythmogenic substrate, mostly in the epicardial surface of the RV(OT), is emerging as a potential alternative [20–23].

The challenge for functional modeling of cardiac arrhythmias, including BrS, is obtaining tissue specific material. Cardiac biopsies are considered too invasive and the obtained cardiomyocytes (CMs) have a short lifespan *in vitro*, making them not readily available at sufficient quantities, though some studies on native human CMs have been performed [24–28]. This issue has been addressed by the study of murine, canine, zebrafish or pig cardiomyocytes and cardiac tissue, which offered interesting insights in BrS pathophysiology (extensively reviewed in [29]). The major drawback of those systems are the species-specific differences in physiology, which impacts the translation of the results into the human clinical setting. As another alternative, non-cardiac cellular models have been employed (mostly human embryonic kidney (HEK)293, Chinese hamster ovary (CHO) cells or *Xenopus laevis* oocytes) to transiently overexpress human cardiac proteins, which enables one to study the function of individual channel complexes and specific mutations (extensively reviewed in [29]). The main shortcoming of these transient expression systems is their disability to mirror the complex CM physiology, as they lack the structural morphology and multi-ion channel environment of native CMs. In addition, results also tend to differ according to the cell-type used. The discovery of induced pluripotent stem cell (iPSC) reprogramming by Takahashi and Yamanaka in 2006 [30], and their subsequent differentiation to functional induced pluripotent stem cell (iPSC)-derived cardiomyocytes (iPSC-CMs) provided an interesting new alternative to the field of cardiac disease modeling. iPSC-CMs provide the (near) complete repertoire of ion channels and accessory proteins expressed in native human CMs, and currently represent the closest resemblance to these cells [31,32]. Since iPSC-CMs can be obtained directly from the patient, they carry the patient's exact genetic background, including potential modifiers influencing the phenotype.

To date, multiple studies on cardiac arrhythmias using iPSC-CMs have been reported, proving the beneficial impact of this model in the field. A Pubmed literature review, performed in December 2020, identified thirteen articles reporting findings from iPSC-CM models for BrS. In this review, we will provide a comprehensive synthesis of these reports, with a focus on the electrophysiological findings and advances in the field of BrS pathogenesis. We will first discuss the methods used for the derivation of the cell models as well as the techniques used for phenotypic investigations.

1.3 Methods for Derivation of iPSC-CM Models

1.3.1 Fibroblast Reprogramming Protocols

The first step in the generation of patient-specific iPSC-CMs is the generation of iPSC lines from a donor sample such as a skin biopsy, or the more easily accessible blood or urine samples [30,33,34]. In all of the reviewed articles, the traditional approach with iPSC reprogramming from skin fibroblasts was applied (**Supplementary Table 1**). Several delivery methods to introduce the Yamanaka transcription factors can be used. Lenti- or retro-viral vectors are very efficient but have the major drawback of viral genome integration into the host genome [35]. To overcome that issue, non-integrating episomal vectors or Sendai virus vectors are increasingly used [36,37]. In the generation of the published iPSC-CM BrS models, we observed an equal distribution of the delivery methods, with 9/17 (53%) of the cell lines generated using integrating vectors and 8/17 (47%) using a non-integrating approach (**Supplementary Table 1**), but with the non-integrating methods indeed overrepresented in the more recent articles.

1.3.2 Cardiomyocyte Differentiation

Over the past 10 years, a constant progress in cardiomyocyte differentiation protocols has been made. From initial protocols employing 3D aggregate embryoid body (EB) differentiation with BMP4 and activin A, disease modeling moved to monolayer-based approaches with Wnt pathway modulation using the timed addition of small molecules [38–42]. In the latter, to start the differentiation process the Wnt pathway is indirectly activated through the inhibition of glycogen synthase kinase 3β (e.g., the addition of CHIR99021). Subsequently, after culturing for two or three days, a Wnt pathway inhibitor is added to the culture medium (e.g., Wnt-C59 or IWR1). By day seven or eight, the cultured cells start beating spontaneously, which is one of the first signs of differentiation towards CMs [43].

Though both EB and monolayer-based methods provide decent efficiency in the derivation of functional iPSC-CMs, the monolayer approach provides the most optimal conditions for the diffusion of the differentiating factors and highest differentiation efficiency. This is also reflected in the literature, as the majority of iPSC-CMs were derived through monolayer-based protocols (9/15) (**Supplementary Table 1**). These protocols were shown to produce mainly ventricular cardiomyocytes, with few atrial and nodal cells present, which is favourable in view of the ventricular origin of BrS pathology.

Nonetheless, the major and well-known disadvantages of iPSC-CM models are the immaturity of the cells, as well as heterogeneity of the cell culture obtained during the differentiation procedure [21,32,44,45]. Maturation can be improved through long-term culture, mechanical stretching or electrical stimulation, via the application of maturing agents such as triiodothyronine hormone (T3) and glucocorticoid hormone, 3D-culture, specific miRNAs or co-culture with human mesenchymal cells [46–54]. In most of the published iPSC-CM BrS models, no specific maturation strategies were used, just a slightly longer culture of at least 30 days before functional testing was performed (except for [55] with at least 19 days). Only de la Roche and colleagues used the cultivation of the iPSC-CMs on a stiff matrix to improve maturation [56]. Further purification of the cell culture with the selection of properly differentiated cardiomyocytes can be obtained with metabolic enrichment approaches, including simple glucose starvation, or substitution of glucose in culture media with lactic acid or fatty acids, to force the switch to a non-oxidative metabolism in the cell culture [57–59]. In 6/13 reports, culture heterogeneity was not addressed, and in the other 7/13 glucose starvation or puromycin or lactate treatment was implemented (**Supplementary Table 1**).

1.4 Phenotyping Methods of iPSC-CMs

Since BrS is associated with ventricular pathology [60], analysis of the electrical activity of ventricular cardiomyocytes is the main focus in BrS iPSC-CM modeling and it is important to understand its basis.

As indicated in **Figure 1-1**, the ventricular action potential (AP) reflects a sequential activation and inactivation of ion channels, conducting inward depolarizing Na^+ and Ca^{2+} , and outward repolarizing K^+ currents [61,62]. The shape of the AP waveform is a reflection of the electrical function of the expressed ion channels (including their auxiliary subunits), and subtle changes in their well-regulated ion conductance (i.e., their time and/or voltage dependence) can have a substantial effect on AP morphology.

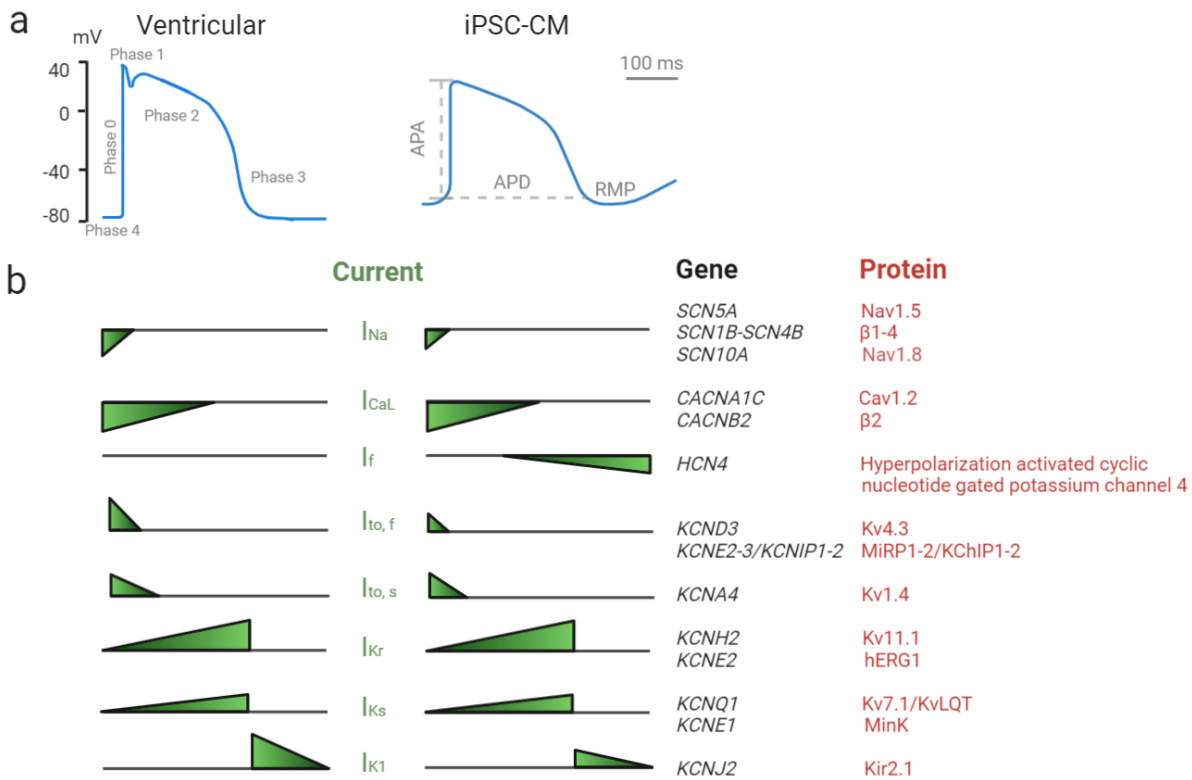


Figure 1-1 Ventricular action potential and underlying ionic currents (adapted from [32,61,63]). Schematic representation of human ventricular and human induced pluripotent stem cell-derived cardiomyocyte (iPSC-CM) action potential waveforms (a) with indicated in grey: action potential (AP) phases (on ventricular AP waveform) as well as action potential amplitude (APA), action potential duration (APD) and resting membrane potential (RMP) (on iPSC-CM AP waveform). Bottom panel represents the relative magnitude of the underlying ionic currents (b) together with the list of genes (in black) encoding alpha and auxiliary (beta) ion channel protein subunits (in red) which cooperate in generation of the represented ion currents (created with biorender.com December 2020).

Phase 0 of the ventricular AP, a rapid depolarizing upstroke, reflects the function of voltage-gated sodium channels ($Na_v1.5$ with possible contribution of $Na_v1.8$) generating the inward sodium current (I_{Na}). It is followed by a transient repolarization of the cell membrane, phase 1, with inactivation of I_{Na} and activation of a transient outward voltage-gated K^+ current (I_{to} ; consisting of a fast $I_{to,f}$ and slower $I_{to,s}$ component). This activity contributes to development of a characteristic prominent “notch” in the ventricular AP waveform. During the plateau phase, phase 2, the depolarization of the cell membrane activates voltage-gated Ca^{2+} channels, triggering the influx of Ca^{2+} (I_{CaL}). While the Ca_v channels inactivate, the outward K^+ currents dominate (I_{Kr} and I_{Ks}) and drive further re-polarization of the cell membrane in phase 3. Inwardly rectifying K^+ channels (mediating I_{K1}) contribute to late phase three repolarization and to the maintenance of the resting membrane potential (RMP) in phase four [61, 62, 64].

Unlike adult ventricular CMs, iPSC-derived CMs beat spontaneously due to a more positive RMP caused by reduced I_{K1} and presence of a pacemaker current (I_f , generated by $HCN4$ channels). The depolarized state of the iPSC-CMs results in the inactivation of the majority of $Na_v1.5$ channels, leaving very little I_{Na} available during phase 0 and reducing upstroke velocity, and leads to I_{to} inactivation, which reduces phase one repolarization. In addition, in iPSC-CMs $I_{to,s}$ seems to be dominant compared to $I_{to,f}$, while in adult CMs this is the other way round [61]. These are important characteristics to take into account when studying the electrophysiological phenotype of this model.

In the next paragraphs, we will briefly discuss different techniques employed in the investigations of BrS iPSC-CM electrophysiological parameters, including patch-clamping, calcium and voltage imaging, and micro electrode arrays (MEA).

1.4.1 Patch-Clamping

Considered the gold standard procedure in electrophysiological characterization, patch-clamping is a technique which allows for the measurement of ionic currents to study the behaviour of the channels, or measurement of voltage changes across the cell membrane suited for AP characterization [63,65]. This technique allows for both the actual measurement of the membrane potential, enabling precise characterization of the AP, as well as the analysis of single ionic currents and ion channel activity. As this is an advantage when studying iPSC-CM disease models in detail, in all the discussed reports the patch-clamp technique has been applied (**Table 1-1**). Patch-clamping also offers the opportunity to resolve the more depolarized RMP of the iPSC-CMs and achieve a proper upstroke velocity and phase 1 repolarization by using dynamic clamp or injecting a sustained current to reach an RMP of $-80 - -90$ mV. The disadvantages of the method remain its low throughput and its invasive and terminal nature, allowing only short-term recordings. Moreover, the need to record from single cells excludes the possibility to measure AP propagation between iPSC-CMs, though this clearly is a characteristic affected and worth studying in arrhythmias.

Table 1-1 Summary of the findings from published BrS iPSC-CM models. Table represents an overview of the identified gene variants, patient diagnosis, electrophysiological characterization methods used and obtained results. Data shown indicate the most important findings from investigated BrS iPSC-CMs models in comparison to control iPSC-CMs for action potential (AP) (APA—AP amplitude; APD—AP duration, dV/dT—upstroke velocity), sodium current (I_{Na}) (current density, voltage dependence of activation/inactivation, recovery from inactivation), late sodium current (I_{NaL}) (current density), calcium current (I_{CaL}) (current density, activation/inactivation, recovery), potassium currents: I_{to} , I_{Ks} and I_{Kr} (current density), calcium transients (CT) (CTD—CT duration, amplitude, rise rate, decay, presence of early afterdepolarization (EAD)/ delayed afterdepolarization (DAD)/arrhythmias) and field potential duration (FPD) characteristics. Legend: + performed analysis; - not performed analysis; \uparrow significant increase/positive shift in voltage dependence; \downarrow significant decrease/negative shift in voltage dependence; = no difference in comparison to control iPSC-CMs. BrS—Brugada syndrome; LQTS3/BrS—mixed Brugada syndrome and long-QT syndrome type 3 phenotype; Amp. - amplitude.

Reference	Gene	Variant	Diagnosis	EP characterization		Electrophysiological findings											FPD								
				methods			AP				I_{Na}			I_{NaL}	I_{CaL}			I_{to}	I_{Ks}	I_{Kr}	CT				
				Patch-clamping	Ca ²⁺ imaging	MEA	APA	APD	dV/dT	Current density	Voltage dependence of activation	Voltage dependence of inactivation	Time of recovery from inactivation	Current density	Current density	Activation		Inactivation	Recovery	Current density	Current density	Current density	CTD	Amp.	Rise rate
Kosmidis et al. 2016 [89]	SCN5A	c.4912C>T (p.R1638X)	BrS	+	-	-	=	=	\downarrow	\downarrow	=	=													
		c.468G>A (p.W156X)	BrS				=	=	\downarrow	\downarrow	=	=													
Liang et al. 2016 [68]	SCN5A	c.2053G>A (p.R620H) and c.2626G>A (p.R811H)	BrS	+	+	-	=	=	\downarrow	\downarrow											\uparrow	\downarrow	\downarrow	\uparrow	
		c.4190delA (p.K1397Gfs*5)	BrS				=	=	\downarrow	\downarrow													=	\downarrow	\downarrow
Ma et al. 2018 [90]	SCN5A	c.677C>T (p.A226V) and c.4885C>T (p.R1629X)	BrS	+	-	-	\downarrow	\uparrow	\downarrow	\downarrow	\downarrow	\downarrow	\uparrow				=								
		c.4859C>T (p.T1620M)	BrS				=	=	\uparrow	=															
Selga et al. 2018 [91]	SCN5A	c.1100G>A (p.R367H)	BrS	+	-	-				\downarrow	\uparrow	\downarrow	\downarrow												
de la Roche et	SCN5A	c.2204C>T (p.A735V)	BrS	+	-	-	\downarrow	=	\downarrow	\downarrow	\uparrow	\downarrow	=				\downarrow								

al. 2019 [56]																										
Davis et al. 2012 [88]	SCN5A	c.5537insTG A (p.1795insD)	LQTS3/BrS	+	-	-	=	↑	↓	↓																
Okata et al. 2016 [86]	SCN5A	c.5349G>A (p.E1784K)	LQTS3/BrS	+	-	+	=	↑	↓	=	=	↓							↑							
El-Batrawy et al. 2019 [69]	SCN10A	c.3749G>A (p.R1250Q) and c.3808G>A (p.R1268Q)	BrS	+	+	-	↓	=	↓	↓	=	=	↓	↓	↓	↑	↓	=	↓	=	↑					
El-Batrawy et al. 2019 [70]	SCN1B	c.629T>C (p.L210P) and c.637C>A (p.P213T)	BrS	+	+	-	↓	=	↓	↓	↑	↓	↑	↓	=	=	=	↑	=	↓	↓	=	=	=	↑	
Belbachir et al. 2019 [71]	RRAD	(p.R211H)	BrS	+	+	-	=	↑	↓	↓	=	=	↓	↑	↓					↑				↓	↑	
Cerrone et al. 2014 [92]	PKP2	c.1904G>A (p.R635Q)	BrS	+	-	-				↓																
Miller et al. 2017 [87]	Undefined	Undefined	BrS	-	-	+																			=	
	Undefined	Undefined	BrS																							=
	PKP2	c.302G>A (p.R101H)	BrS	+	-	+	=	↓	=																	=
Veerman et al. 2016 [55]	Undefined	Undefined	BrS				=	=	=	=	=	=	=													
	Undefined	Undefined	BrS	+	-	-	=	=	=	=	=	=	=	=	=											
	CACNA1C	int19 position -7 (benign)	BrS				=	=	=	=	=	=	=													

1.4.2 Calcium and Voltage Fluorescence Imaging

The use of calcium- or voltage- sensitive dyes in combination with fluorescence microscopy provides a non-invasive and high-throughput method for measuring intracellular Ca^{2+} fluctuations and membrane voltage changes in iPSC-CMs (single cells or growing in clusters or monolayers) [66,67]. With calcium imaging not only Ca^{2+} flux across the cell membrane but also intracellular Ca^{2+} oscillations defining the excitation–contraction coupling are captured, allowing more in-depth investigation of the intracellular Ca^{2+} balance. It should be noted though that iPSC-CMs show structural immaturity with a lack of T-tubules and reduced sarcomere organization, resulting in more immature calcium handling and excitation–contraction coupling. In four of the discussed reports [68–71] calcium imaging was used in addition to patch-clamping (**Table 1-1**). Nevertheless, the use of dyes prohibits long term recordings due to their phototoxicity and the signals have a high noise ratio [63,72].

To overcome these challenges, genetically encoded calcium and voltage indicators (GECI and GEVI) have recently been introduced [73]. The cells are then transfected with genes encoding fluorescent indicators, which consist of a Ca^{2+} or voltage sensing element coupled to one or two fluorophores that alter their fluorescent intensity based on conformational changes in the sensing element. An advantage of iPSC-CMs compared to native CMs in this case is that iPSC-lines with stable GEVI/GECI expression can be created, stored and repeatedly differentiated to cardiomyocytes. Several GECIs (GCaMP5G, R-GECO1) and one GEVI (ArcLight) have been used in control and patient-derived iPSC-CMs and shown to consistently represent the calcium transients [73–77] and the transmembrane APs [75–79]. Although these reporters offer significant advantages over the traditional dyes, a major drawback is that the transgenes integrate randomly into the genome, raising serious concerns about potential gene disruption and alteration of local and global gene expression that could adversely affect normal cellular functions. Thus far, these genetically encoded indicators have not been used in BrS disease modeling yet.

1.4.3 Micro-Electrode Array (MEA)

MEA platforms offer the possibility of high-throughput, non-invasive, label-free and long-term measurement of extracellular field potentials (FPs) from clusters and monolayers of iPSC-CMs [63, 80–83, 84]. It requires the iPSC-CMs to be seeded on MEA plates, with multiple microelectrodes embedded in 2D grids in the cell culture surface. MEAs have the advantage that AP conduction velocity over a layer of iPSC-CMs can be measured. Conventional arrays have a limited spatial resolution (typically 100 μm) due to the limited number of electrodes in the grid. A new class of MEAs that is based on complementary metal–oxide semiconductor (CMOS) technology has been developed as a solution to this limitation [82,85]. In CMOS-MEAs, thousands of microelectrodes are arranged at high spatial resolution on a chip, tremendously increasing the amount of information that can be gathered from a single iPSC-CM culture. In only two of the discussed articles MEA was used to study BrS iPSC-CMs [86,87] (**Table 1-1**), in one to confirm field potential duration (FPD) prolongation correlating to the long QT syndrome (LQTS) part of a mixed phenotype [86] and in the other to perform drug challenges on the cells [87].

1.5 Findings from Published BrS iPSC-CM Models

Most of the published functional reports from iPSC-CM models, focused on sodium channel genes such as *SCN5A* [56,68,86,88–91], *SCN10A* [69] or *SCN1B* [70]. In addition, pathogenic variants in other BrS-related genes, such as *RRAD* [71] or *PKP2* [87,92] were modelled. Finally, as BrS is a complex disease with a large proportion of cases being genetically unresolved, characterization of iPSC-CM models from patients with undefined genetic cause has also been performed [55,87]. In this review, we will summarize the findings from these thirteen reports, with a focus on the electrophysiological results. An overview of the studied genes, exact investigated genetic variants and electrophysiological results obtained is given in **Table 1-1** and extra information is available in the **Supplement** (used reprogramming and differentiation approach with additional patient information are summarized in **Supplementary Table 1-1**; reported electrophysiological parameters for AP, CT, FPD and tested ion channels are summarized in **Supplementary Tables 1-2 and 1-9**).

1.5.1 Sodium Channel Genes

1.5.1.1 Sodium Channel α -Subunits—*SCN5A*

BrS is mainly associated with loss-of-function mutations in *SCN5A*, leading to reduced I_{Na} due to lower expression levels or the production of defective $Na_v1.5$ protein, while gain-of-function mutations in *SCN5A* contribute to LQT syndrome 3 (LQTS3) [93,94]. In some cases, an overlap of the symptoms of both arrhythmias can be observed in patients carrying specific *SCN5A* mutations [95–97]. Until now, ten iPSC-CM models of BrS-related *SCN5A* variants have been published. Eight of them were generated from patients with a pure BrS phenotype [56,68,89–91] and two from patients with a mixed LQTS/BrS phenotype [86,88] and will be discussed as such in the following paragraphs.

1.5.1.1.1 Pure BrS Phenotype

Kosmidis et al. [89] generated two iPSC-CM models with nonsense *SCN5A* variants, for which they recruited one BrS patient with a more severe phenotype carrying a p.(Arg1638*) variant and one with a relatively mild phenotype related to a p.(Trp156*) variant (Table S1). Both variants caused a reduction in I_{Na} density and slowed down the upstroke velocity of the AP in the iPSC-CMs (**Supplementary Tables 1-2 and 1-3**) compared to iPSC-CMs from two unrelated control individuals. There were no significant differences in the activation or inactivation process of the I_{Na} between patient iPSC-CMs and controls. As both modelled variants were predicted to generate a premature stop codon, the presence of nonsense mediated decay (NMD) was investigated in cloning experiments. 61% of patient iPSC-CMs expressed the p.(Arg1638*) variant, confirming that its location in the last exon caused NMD escape, while only 19% of patient iPSC-CMs expressed the p.(Trp156*) variant, confirming the occurrence of NMD. The authors tested two nonsense readthrough-promoting drugs, gentamycin and PTC124, on patient iPSC-CMs to investigate their therapeutic potential on the nonsense variants. Unfortunately, they did not observe any significant increase in I_{Na} in treated iPSC-CMs in comparison to baseline conditions, leading to their conclusion that these drugs are unlikely to represent an effective treatment for patients carrying the studied mutations.

Liang et al. performed the characterization of two BrS cases: one (BrS1) with double missense *SCN5A* mutation: p.(Arg620His) and p.(Arg811His), and a second one (BrS2) with a c.4190delA; p.(Lys1397Glyfs*5) frameshift *SCN5A* mutation [68]. For comparison, iPSC-CMs were also created of two healthy unrelated control individuals. Both patient iPSC-CMs showed AP profiles of a closely coupled single triggered beat (in 39.6% and 34.5% of recordings in BrS1 and BrS2, respectively), and of sustained triggered activity (5.6% and 6.8% in BrS1 and BrS2, respectively), increased peak-to-peak interval variability and slower upstroke velocity (**Supplementary Table 1-2**). Sodium current analysis in both patient iPSC-CMs showed visible I_{Na} reduction (**Supplementary Table 1-3**), which correlated with a lower protein expression of $Na_v1.5$ in comparison to controls. Calcium imaging experiments showed about 60% reduction in Ca^{2+} transient amplitude, 50–80% decreased rise rate and increased variation in beating intervals in both patient iPSC-CMs (**Supplementary Table 1-5**). RNA-seq revealed a closer homology in overall gene expression profile between the two BrS iPSC-CMs compared to the two control lines, suggesting disease-specific gene expression changes. RT-qPCR analysis confirmed a reduced expression of *SCN5A*, *KCND3* and *KCNJ2* in patients compared to control iPSC-CMs, suggesting reduced I_{to} and reduced I_{K1} could also be involved in the arrhythmic phenotype. Finally, they used the CRISPR/Cas9 technique to correct the c.4190delA variant in BrS2 patient iPSCs. Genome edited iPSC-CMs (BrSp2-GE) showed a marked reduction in arrhythmic activity, improved upstroke velocity (**Supplementary Table 1-2**) normalized calcium transient (CT) parameters (**Supplementary Table 1-5**), increased $Na_v1.5$ membrane expression and a partial rescue of the I_{Na} density (**Supplementary Table 1-3**). As such, the authors were able to prove that the frameshift variant was solely responsible for the observed cellular phenotype.

Ma and colleagues reported an iPSC-CM model from a compound heterozygous *SCN5A* mutation carrier, carrying p.(Ala226Val) and p.(Arg1629*) (BrS1) and a healthy sibling control (CON1, his unaffected brother) [90]. They also created iPSC-CMs with a milder p.(Thr1620Met) mutation through genome

editing (BrS2) and used an extra control iPSC-CM line of commercial iCell® Cardiomyocytes (Fujifilm Cellular Dynamics, Inc., Madison WI) (CON2). BrS1 iPSC-CMs showed 50% reduced *SCN5A* mRNA expression in comparison to CON1 iPSC-CMs, suggesting the occurrence of NMD and corresponding with an observed 75% reduction in I_{Na} (**Supplementary Table 1-3**). At first, the AP recordings of patient iPSC-CMs did not show significant differences in comparison to controls, which may be explained by the more positive RMP of these cells (about -45 mV) at which most of the I_{Na} is not available and I_{to} is inactivated (**Supplementary Tables 1-2 and 1-3**). The application of an in silico I_{K1} injection revealed a $>75\%$ reduction in upstroke velocity and a reduction in AP amplitude in BrS1 iPSC-CMs (**Supplementary Table 1-2**) and appearance of phase 1 repolarization, only in CON1 iPSC-CMs. Moderate changes in the rate of steady-state activation and inactivation and a more significant change in the rate of recovery from the inactivation of the sodium channels was observed in BrS1 compared to CON1. BrS2 iPSC-CM characterization revealed normal I_{Na} and normal APs, with upstroke velocity (dV/dT) max even higher than in both controls (**Supplementary Table 2**). Since BrS pathology is linked with slow heart rates, AP recordings at different lower pacing frequencies were performed. In 25% of BrS1 patient cells, at 0.1 Hz an average 66% action potential duration (APD)₉₀ reduction was observed, while APD prolongation or moderate shortening was observed in the rest of the patient iPSC-CMs and the control cells. (**Supplementary Table 1-2**). The observed marked reduction in APD, represented an increased phase 1 repolarization and loss of phase 2 AP pattern, highly resembling the proarrhythmic loss-of-dome in epicardial ventricular CMs, fitting with the repolarization disorder hypothesis. I_{to} measurements in patient and control iPSC-CMs showed similar current density with an increase in the low pacing rate. To investigate I_{to} influence on the observed phenotype in BrS1 iPSC-CMs, the cells were treated with 4-aminopyridine (4-AP, blocker of $I_{to,f}$ and $I_{to,s}$) and APs were measured at 0.1 Hz. The authors noticed that 0.5 mM 4-AP completely reversed the increased phase one repolarization and loss of phase two dome (Table S2). They concluded that I_{Na} and I_{to} could play a coordinated role in BrS causation, where loss of I_{Na} together with heterogeneous elevated I_{to} in a fraction of iPSC-CMs (at lower heart rates) make the ventricular CMs undergo proarrhythmic changes. Such an observation would not have been possible in a heterologous expression system and supports the value of iPSC-CMs to reveal interplay between different currents in CMs.

Selga et al. performed a comparison of I_{Na} properties in iPSC-CMs from a BrS patient carrying a p.(Arg367His) *SCN5A* variant and an unrelated healthy control individual (two clones each), obtained using two differentiation protocols: an EB-based spontaneous differentiation and monolayer-based differentiation (**Supplementary Table 1-1**) [91]. The authors reported similar observations from both differentiation protocols: a similar reduction in peak I_{Na} , a positive shift in the voltage dependence of channel activation (i.e., channel opening) concomitantly with a negative shift in voltage dependence of inactivation (a process that makes the channels non-conductive upon opening), reflecting a clear loss-of-function (**Supplementary Table 3**). They also reported accelerated recovery from inactivation in patient iPSC-CMs in comparison to the control in both tested groups. Interestingly, experiments in tSA cells revealed only the I_{Na} reduction of about 48% for the mutant protein, while the steady-state activation/inactivation properties were not changed in comparison to the wild type (WT). This again shows an added value of the iPSC-CM model, revealing pro-arrhythmic channel function changes that were not detected in a conventional heterologous expression system, probably due to the absence of auxiliary subunits.

In 2019, de la Roche and colleagues used CRISPR/Cas9 technology to introduce a homozygous p.(Ala735Val) *SCN5A* variant in a healthy control iPSC line and obtained two independently derived mutant clones (MUT1 and MUT2) [56]. They state that they used both isogenic and non-genetically related iPSC-CM controls (“wild type” WT) for the electrophysiological characterization. Long-term cultivation (27–42 days) of the iPSC-CMs on a stiff matrix was applied to promote the maturation of the cells. AP recordings carried out with a hyperpolarizing current (I_{K1}) injection showed similar APD₅₀ values in WT and A735V iPSC-CMs, but significantly reduced action potential amplitude (APA), 74% reduction in upstroke velocity and A735V cells not displaying a sharp AP peak with phase one repolarization notch

(**Supplementary Table 1-2**). These recordings strongly indicated altered activation or inactivation characteristics of the mutant $\text{Na}_v1.5$ channel. They measured I_{CaL} contribution to the I_{Na} current and showed the same I_{CaL} density in both groups (**Supplementary Table 1-4**). A735V iPSC-CMs showed a +30 mV depolarizing shift in the voltage dependence of channel activation and a negative shift in the voltage dependence of inactivation, resulting in the reduced availability of the channels for AP generation at physiological membrane potentials (60% of inactivated channels in mutant and 40% in WT at -80mV) (**Supplementary Table 1-2**). In simultaneous experiments in HEK cells, the reduction in I_{Na} as well as the shift in channel activation were observed, however, no differences in the voltage dependence of the inactivation of the mutant channel were noted. This again confirms that different cellular composition can lead to different channel characteristics and emphasizes the importance of the iPSC-CM model. De la Roche et al. investigated differences between two mutant and two WT clones and between five independent differentiation experiments in both groups. As they did not see significant differences in values between clones and differentiations, they were able to pool the data together for the comparisons (**Supplementary Tables 1-2 and 1-3**).

1.5.1.1.2 Mixed Phenotype (BrS/LQTS)

Davis et al. used iPSC-CMs to model an *SCN5A* p.(1795insAsp) mutation, identified in a large family where mutation carriers presented with variable phenotypes, including diagnosed cases of BrS as well as LQTS and cardiac conduction defects (**Supplementary Table 1-1**) [88]. This mutation was previously modelled in cardiomyocytes isolated from transgenic mice, where a prolongation of APD was observed together with a slowing of the upstroke velocity and reduced I_{Na} density but unchanged kinetic properties of this current [98,99]. However, experiments in expression systems (HEK 293) showed a disruption of the fast inactivation, causing a sustained Na^+ current (i.e., a late sodium current, I_{NaL}) throughout the action potential plateau and prolonging cardiac repolarization at slow heart rates (explaining LQTS phenotype), as well as an increase/augmentation in the slow inactivation component, delaying the recovery of the sodium channel availability between stimuli and reducing the I_{Na} at rapid heart rates (explaining BrS phenotype) [100]. In the present study, they first used mouse iPSC-CMs generated from heterozygous mutant and wild type mice and showed reduced upstroke velocity, prolonged APD and I_{Na} reduction in the mutant miPSC-CMs but no changes in the voltage dependence of the activation and inactivation parameters. In their human iPSC-CMs, Davis et al. observed a 54% reduction in I_{Na} density and an increase in I_{NaL} (**Supplementary Table 1-3**) compared to control iPSC-CMs from an independent healthy individual, but they did not characterize activation or inactivation kinetics. Action potential analysis revealed significantly reduced upstroke velocity and prolonged APD90, recapitulating both arrhythmia phenotypes (**Supplementary Table 1-2**).

Another paper reporting an iPSC-CM model of a p.(Glu1784Lys) *SCN5A* mutation, underlying/causing a mixed BrS/LQTS phenotype, was published by Okata et al. [86]. They used control iPSC-CMs from two unrelated healthy individuals and reported FPD (MEA) as well as APD90 (patch-clamp) prolongation in patient iPSC-CMs (**Supplementary Tables 1-2 and 1-6**). No differences in upstroke velocity as well as I_{Na} density were observed in patient iPSC-CMs, however, they observed an increase in I_{NaL} in patient iPSC-CMs (**Supplementary Tables 1-2 and 1-3**). As they observed a high expression of *SCN3B* in iPSC-CMs compared to adult CMs and in experiments with tsA-201 cells, they saw that *SCN3B* co-expression with the mutant E1784K-*SCN5A* protein increased peak I_{Na} and caused a positive shift in the voltage dependence of channel inactivation compared to WT. They performed *SCN3B* siRNA knockdown in patient iPSC-CMs to check if the expression of this embryonic type Na^+ channel β -subunit can mask the BrS phenotype. In iPSC-CMs with *SCN3B* knockdown, they reported a decrease in I_{Na} density and a negative shift in the voltage dependence of channel inactivation only in the patient iPSC-CMs, explaining the BrS phenotype related to the *SCN5A* mutation. To investigate if the *SCN5A* p.(Glu1784Lys) mutation is sufficient to produce the observed electrophysiological changes, they generated an isogenic control of the patient iPSCs, using an adenoviral vector. Corrected iPSC-CMs showed shortened APD90 (**Supplementary Table 1-2**), no significant difference in I_{Na} density but a significant decrease in I_{NaL} (**Supplementary Table 1-3**) compared to the patient iPSC-CMs. They did not discuss this, but it seems they

did not perform *SCN3B* knockdown in these experiments, which could explain these sodium current results. Those results confirmed that the p.(Glu1784Lys) *SCN5A* mutation contributes solely to the development of the mixed LQTS/BrS phenotype, and that the *SCN3B* expression in iPSC-CMs can mask the electrophysiological properties characteristic to BrS syndrome.

1.5.1.2 Sodium Channel α -Subunits—*SCN10A*

Genome-wide association study (GWAS) analysis of QRS interval duration led to the first identification of *SCN10A* as a candidate gene in cardiac ventricular conduction disorders [15]. In addition, a GWAS for BrS also detected an association with common variants in *SCN10A* (coding for the $\text{Na}_v1.8$ channel) [19]. These studies were followed by multiple reports of *SCN10A* variants involved in development of BrS, together with their functional analysis in expression systems, suggesting *SCN10A* is an important player in BrS etiology [101–105]. Recently, El-Battrawy et al. reported a successful attempt of the iPSC-CM modeling of a double *SCN10A* mutation (p.(Arg1250Gln) and p.(Arg1268Gln)) related to the BrS phenotype [69]. They used three clones of the patient iPSCs, as well as iPSC-CMs from three independent healthy control individuals. They observed reduced peak I_{Na_r} , reduced I_{Na_L} and accelerated recovery from inactivation in patient iPSC-CMs (**Supplementary Table 1-3**), contrasting with the increased expression of both *SCN5A* as well as *SCN10A* mRNA in patient iPSC-CMs in comparison to controls. El-Battrawy and colleagues also detected about a 50% reduction in *KCNJ2* expression in patient iPSC-CMs in comparison to controls, without changes in I_{K_1} . Regarding calcium and other potassium currents, they observed reduced peak density, a positive and negative shift of the voltage dependence of channel activation and inactivation, respectively, of I_{Ca_L} (**Supplementary Table 1-4**), together with a reduction in I_{K_S} (**Supplementary Table 1-9**). AP characterization showed reduced APA and upstroke velocity, but similar APD (**Supplementary Table 1-2**). An ajmaline addition revealed an increased susceptibility of patient iPSC-CMs to the sodium blocker, visible in reduction in APA as well as upstroke velocity already with a 3 μM ajmaline addition (**Supplementary Table 1-2**). They investigated the presence of arrhythmic events in patient iPSC-CMs using calcium imaging, which revealed an increased frequency of EAD-like events in patient iPSC-CMs (90%) in comparison to controls (50% and 45% in two control lines).

1.5.1.3 Sodium Channel β -Subunits—*SCN1B*

The proper function of the cardiac $\text{Na}_v1.5$ channel is known to be regulated by the β -subunits of the channel complex [106]. It was previously reported that variants in *SCN1B*, encoding the β_1 -subunit, associate with BrS, including successful investigation in expression systems [107]. El-Battrawy et al. performed electrophysiological investigations of compound variants in *SCN1B* (p.(Leu210Pro) and p.(Pro213Thr)) in patient iPSC-CMs compared with control iPSC-CMs of three independent healthy individuals [70]. They re-reported increased expression levels of *SCN5A* and decreased expression levels of *CACNA1C*, *KCNJ2*, *KCNH2*, *SCN1B* and *SCN3B* in the patient iPSC-CMs, while on the protein level, they observed reduced *SCN1B* and similar $\text{Na}_v1.5$ expression in comparison to controls. Electrophysiological investigation showed reduced peak I_{Na_a} and I_{Na_L} together with a positive shift in the voltage dependence of activation and negative shift of the inactivation process as well as decelerated recovery from inactivation of I_{Na_a} in the patient iPSC-CMs (**Supplementary Table 1-3**). When characterizing other ion channels, El-Battrawy et al. reported decelerated recovery from inactivation for I_{Ca_L} , as well as a reduction in I_{K_S} and I_{K_r} and no change in I_{to} in patient iPSC-CMs (**Supplementary Tables 1-4, 1-7, 1-8 and 1-9**). They postulated that these changes probably resulted from secondary changes induced by the *SCN1B* variants. AP analysis of patient iPSC-CMs revealed reduced APA and upstroke velocity, while APD did not change (**Supplementary Table 1-2**). They investigated the effect of ajmaline addition (30 μM) and observed a more pronounced change in APA as well as upstroke velocity in patient iPSC-CMs in comparison to controls, especially at higher beating frequencies, indicating a higher sensibility of BrS cells to ajmaline application. Using calcium imaging, they observed no differences in Ca^{2+} transients, but increased arrhythmia like events in patient compared to control iPSC-CMs (85% vs. 45% of cells). After treatment with 10 μM of carbachol, a parasympathetic stimulator, control cells showed a reduction in the beating

frequency, whereas the patient iPSC-CMs showed an increase in the beating frequency, an observation that they could not explain.

1.6 iPSC-CM Models of Variants in Other Arrhythmia-Related Genes

1.6.1 Calcium Channel Related Proteins

Whole exome sequencing analysis has been proven a powerful tool in genetic screening of BrS patients. WES analysis of five familial BrS patients performed by Belbachir et al. led to the identification of a p.(Arg211His) variant in the *RRAD* gene [71]. *RRAD* encodes RAD (Ras associated with diabetes) GTPase, known to play a role in $Ca_v1.2$ trafficking and associated with ventricular arrhythmia in mice. The variant identified by Belbachir and colleagues has a Combined Annotation Dependent Depletion (CADD) score of 33, occurs only once in GnomAD and co-segregated with disease phenotype in the patient family, indicating potential pathogenicity of the variant, and their studies in mouse CMs suggested a gain-of-function effect. Sanger sequencing of *RRAD* coding regions in 186 unrelated BrS patients led to the identification of three additional rare mutations, showing a trend for *RRAD* variant enrichment in BrS patients in comparison to 856 tested control individuals. The authors derived iPSC-CMs of two patients (BrS1 and BrS2) and two unaffected non-carrier siblings (Ctl1 and Ctl2) and investigated both I_{Na} and I_{CaL} properties, together with AP and CT analysis (**Table 1**). Electrophysiological tests on patient iPSC-CMs showed the presence of slower spontaneous rhythms, prolonged AP duration and reduced upstroke velocity in comparison to Ctl1 (**Supplementary Table 1-2**). BrS1 iPSC-CMs also showed a ~40% reduction in I_{Na} , with a slight acceleration of recovery from inactivation in comparison to Ctl1 (**Supplementary Table 1-3**). The authors correlated these changes with a lower expression of $Na_v1.5$ protein in patient compared to control iPSC-CMs, while on the transcript levels there was no detectable difference. They reported a larger persistent Na^+ current I_{NaL} and ~30% reduced I_{CaL} in BrS1 iPSC-CMs (**Supplementary Tables 1-3 and 1-4**). CT results showed the presence of early afterdepolarizations (EADs), slower calcium transient decay and calcium transient duration (CTD) prolongation in patient iPSC-CMs (**Supplementary Table 1-5**). To prove the pathogenicity of the *RRAD* variant, CRISPR/Cas9 was used to knock it in in an unrelated control iPSC line (Rad R211H ins in **Supplementary Tables 1-3 to 1-5**). Similar to patient iPSC-CMs, genome-edited cells showed slowed spontaneous rhythms, lower upstroke velocity, prolonged APD, reduced peak I_{Na} and increased persistent Na^+ current compared to the isogenic WT control (**Supplementary Tables 1-2 and 1-3**). No I_{CaL} differences were observed between the lines, suggesting no significant effect of the variant on $Ca_v2.1$ trafficking. However, calcium imaging showed an uneven beat rate, with EADs in 20% of recorded cells and slowed calcium reuptake in the genome-edited iPSC-CMs (**Supplementary Tables 1-3 to 1-5**). Using immunostaining and confocal microscopy, Belbachir et al. observed cytoskeleton defects with impaired F-actin organization and cortical distribution of troponin I in 70% of patient iPSC-CMs. This led to a decrease in cell contractility and focal adhesion formation and patient cells showed a preferential round shape, with increased thickness in comparison to flat control iPSC-CMs [71]. Genome edited knock-in iPSC-CMs confirmed the influence of *RRAD* p.(Arg211His) on the observed phenotype, as the cytoskeletal defects were now detected in ~40% of the tested cells. The authors concluded that due to preferred expression of RAD in the RVOT, the decreased cell-cell connection could lead to abnormal cardiac conduction in that region and cause BrS. All these results confirmed a causal role of the p.(Arg211His) *RRAD* variant in development of the BrS phenotype.

1.6.2 Desmosomal Proteins

Although desmosomal protein abnormalities are predominantly linked with arrhythmogenic (right ventricular) cardiomyopathy (ARVC or ACM) [108,109], several studies showing the association of variants in *PKP2* with the BrS phenotype have been reported [92,110]. Two BrS-related *PKP2* variants of unknown significance have so far been modelled in iPSC-CMs [87,92]. Although Cerrone et al. performed only a small part of their study in iPSC-CMs, they showed that the p.(Arg635Gln) variant in *PKP2* alone can contribute to a significant reduction in peak I_{Na} density [92]. As their experiments in HL1 cells showed that knockdown of the endogenous *PKP2* of the cells in combination with co-expression of the p.(Arg635Gln)

variant (as well as other BrS-related missense variants) with WT *PKP2* led to a reduction in peak I_{Na} , they performed a rescue experiment in the iPSC-CM line derived from an ARVC patient with a homozygous c.2484C > T *PKP2* frameshift loss-of-function variant [111] using lentiviral constructs containing WT-*PKP2* and *PKP2*-R635Q. At baseline, I_{Na} was significantly reduced in the patient iPSC-CMs compared to the control embryonic stem cell (ESC)-CMs obtained from H9 ESCs (**Supplementary Table 1-2**) and the rescue experiments showed that only WT-*PKP2* transduction led to a significant increase in I_{Na} density. These results confirmed that I_{Na} depends on the expression and structural integrity of *PKP2*.

A p.(Arg101His) variant in *PKP2* (classified as VUS or likely benign) was present in one of the patient iPSC-CMs investigated by Miller et al. in a study aiming to identify ajmaline's mode of action in iPSC-CMs and test whether differences in ajmaline response could be determined between BrS patients and controls on a MEA platform [87]. AP analysis revealed no differences in upstroke velocity, while APD90 was significantly reduced in patient iPSC-CMs in comparison to the control (**Supplementary Table 1-2**). Although a prolongation of the FPD in the p.(Arg101His) patient iPSC-CMs was visible in the presence of 100 nM of ajmaline (average 43.8 ms; 1.1-fold) in comparison to baseline conditions, while this was not observed in iPSC-CMs from an unrelated healthy control individual (iPSC-HS1M; **Supplementary Table 1-6**), the authors noted comparable FPD prolongation in the presence of 1, 10 and 100 μ M of ajmaline in patient and control iPSC-CMs (**Supplementary Table 1-6**). They concluded there was no significantly increased susceptibility to ajmaline in the patient cell lines (see also further below). The authors provided proof of ajmaline blocking both I_{Na} and I_{Kr} on control iPSC-CMs, however, in the scope of this study they did not include the characterization of any of the underlying currents of the patient iPSC-CMs, but did show reduced APD90 using patch-clamp [87].

1.7 Unknown Genetic Contribution

Attempts have been made in the iPSC-CM modeling of BrS phenotypes from patients with unknown genetic causes [55,87]. In the study by Veerman et al., iPSC-CMs were generated from three BrS patients with spontaneous BrS type-1 ECG pattern. Two did not carry variants in *SCN5A* and other BrS-related genes, while one patient carried a *CACNA1C* variant in intron 19 (position -7) that was predicted not to affect the splicing of the gene and was classified as benign. For the electrophysiological characterization, they used iPSC-CMs from two unrelated healthy control subjects (iCtrl1 and iCtrl2) as well as a positive iPSC-CM control (*SCN5A* p.(1795insAsp) carrier; iSCN5A **Supplementary Tables 1-3 and 1-4**). While in this positive control, Veerman and colleagues observed APD prolongation and the expected dV/dT_{max} reduction, in the analysed patient lines they did not see significant differences in all tested AP properties in comparison to the negative controls (**Supplementary Table 1-2**), although in one patient line APD was significantly shorter compared to one of the control lines (iCtrl2). Similarly, they did not detect any differences in I_{Na} density in patient iPSC-CMs in comparison to negative controls, while in the positive control, they saw a significant reduction in the peak current (**Supplementary Table 1-3**). Interestingly, the authors observed significant differences in $V_{1/2}$ voltage dependence of the inactivation of I_{Na} and I_{CaL} between iCtrl1 and iCtrl2 and the investigated patient iPSC-CMs were similar to one or the other control cell line (**Supplementary Tables 1-3 and 1-4**), showing variability in channel inactivation kinetics in iPSC-CMs. Nevertheless, in summary, the authors were not able to observe a BrS phenotype in their iPSC-CMs obtained from BrS patients with unknown genetic contributions.

In the study by Miller et al., investigating the effects of ajmaline, two out of three selected iPSC-CM lines were obtained from BrS patients with unknown genetic causes and spontaneous BrS type-1 ECG pattern. The authors observed consistent FPD prolongation in all of the tested patient clones (iBR1-P5M-L1, iBR1-P5M-L9 and iBR1-P6M-L1) with addition of increasing ajmaline concentrations (100 nM–100 μ M) with a maximum 1.46-fold increase at a 100 μ M ajmaline concentration (**Supplementary Table 1-6**). However, no significant differences in ajmaline susceptibility could be observed between patient and control iPSC-CMs [87]. This study did demonstrate that iPSC-CMs were suitable to test the blocking effect of ajmaline on both depolarization (I_{Na}) and repolarization (I_{Kr}).

1.8 Conclusions and Future Perspective

A decade of disease modeling using the novel iPSC-CM approach in the field of cardiac arrhythmias and Brugada syndrome has proven its feasibility in modeling patient-specific cellular phenotypes (**Figure 1-2**). In this review, we gathered information from thirteen currently available reports studying BrS-specific iPSC-CMs and discussed the resulting electrophysiological findings.

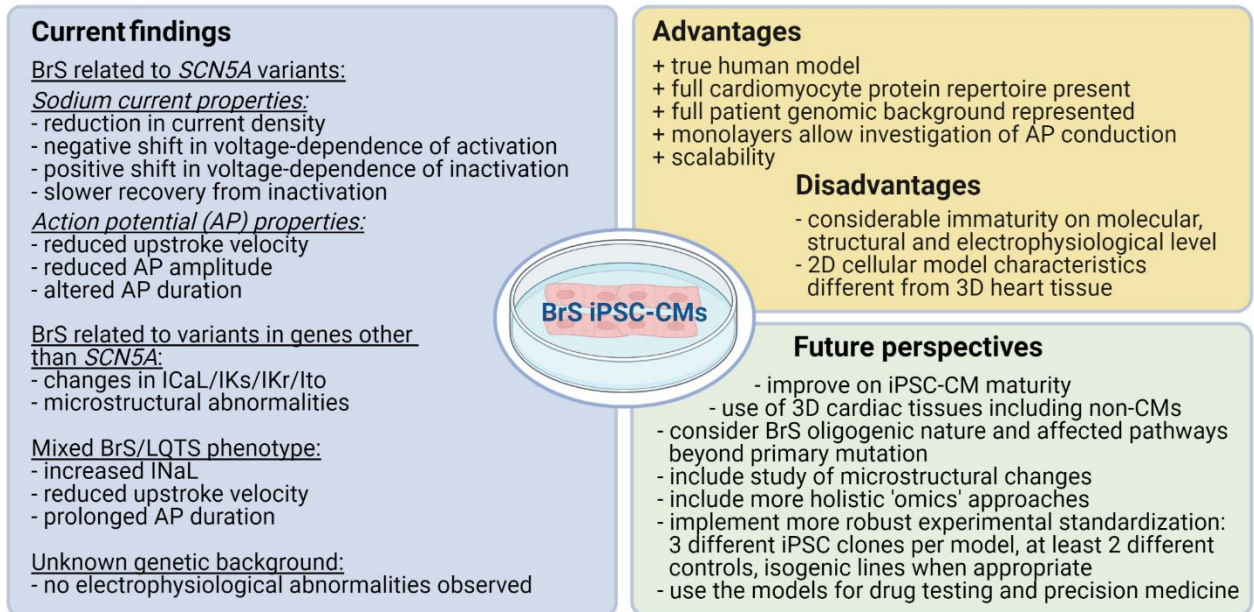


Figure 1-2 Summary of the main findings from the reviewed BrS iPSC-CM models, advantages and disadvantages of the model, as well as future perspectives for the use of iPSC-CMs in BrS research. (Generated with Biorender.com March 2021).

These findings confirmed that the main electrophysiological changes in BrS iPSC-CMs affect sodium channel activity, as previously observed in expression systems and murine models. In particular, a reduced peak I_{Na} density [56,68–71,88–92] was observed in all the described patient iPSC-CMs with an identified mutation, both in *SCN5A* or the other genes. So, all genetic variants led to the development of a phenotype with reduced I_{Na} (**Table 1-1 and Supplementary Table 1-3**). When sodium channel kinetics were studied, mostly a negative shift in the voltage dependence of channel inactivation (leading to a higher number of non-conductive inactivated channels) [56,70,86,90,91], a positive shift in the voltage dependence of channel activation (i.e., stronger membrane depolarization is required to open the channels) [56,70,91] and in two reports, an increased time of recovery from inactivation (leading to the prolonged inactivation of the channels) [70,90] was observed, all fitting with the reduced I_{Na} phenotype. In one report, a negative shift in the voltage dependence of channel activation [90] and in three reports, an accelerated recovery from inactivation [69,71,91] were observed, which were not explained with regard to the phenotype. Interestingly, in two papers [56,91], changes in channel kinetics were not detected in a conventional heterologous expression system, confirming the value of the iPSC-CM model expressing a more complete CM intracellular environment, including channel auxiliary subunits. In line with the sodium current defects, reduced upstroke velocity was observed in 11 out of 15 models, where AP properties were tested [56,68–71,86,88–90] and APA reduction was seen in four models [56,69,70,90] (**Table 1-1 and Supplementary Table 1-2**). When other currents apart from I_{Na} were investigated, mostly when modeling variants in other genes than *SCN5A*, also I_{CaL} [69–71] and/or in some instances I_{Ks} [69,70], I_{Kr} [70] as well as I_{to} [56] property changes were reported. Taking into account the oligogenic nature of BrS, it would be interesting to study several currents in BrS iPSC-CM models.

Interestingly, in two reports authors noticed microstructural changes in their disease models, which could contribute to the observed electrophysiological abnormalities [71,92]. Belbachir and colleagues observed that the *RRAD* p.(Arg211His) variant disturbed F-actin organization in patient iPSC-CMs, compromising

focal adhesion and potentially cell–cell communication and AP conductance, mainly in the RVOT where RAD is expressed [71]. Cerrone et al. reported a microtubule abnormality in adult CMs from a heterozygous *PKP2* p.R635Q mouse, they did not study this in their iPSC-CM model. As sodium channel proteins are transported via the microtubule network, their results show that *PKP2* deficiency can affect the ability of microtubules to reach intercalated discs and impair $\text{Na}_v1.5$ expression there [92]. It has already been suggested that disturbances in *PKP2*, and other desmosomal or junctional proteins at the CM intercalated discs (the “connexome”) can affect the trafficking or activity of sodium channels over there [84,112–114] explaining the link between structural abnormalities, electrophysiological changes and BrS. The interplay and dependency of all these intercalated disc proteins, integrating both mechanical and electrical functions of the CMs, have been beautifully illustrated in recent reviews [115–117]. In addition, in clinical studies, discrete structural abnormalities in the right ventricle of BrS patients have been observed [23,118,119]. Based on these insights, it would be interesting to look in more detail into structural changes in all BrS iPSC-CM models generated, since these could be part of the primary defect or play a modifying role in the disease phenotype.

iPSC-CMs from carriers of *SCN5A* variants presenting with a mixed BrS/LQTS pathology were shown to recapitulate both phenotypes: reduced upstroke velocity (i.e., $\text{dV}/\text{dT}_{\text{max}}$) or increased I_{NaI} as well as APD prolongation was noted [86,88] (**Table 1-1**). Interestingly, APD changes were also observed in iPSC-CMs from pure BrS patients, one carrying a compound heterozygous *SCN5A* mutation (p.(Ala226Val) and p.(Arg1629*)) and one a p.(Arg211His) *RRAD* variant, where APD prolongation was noted [71,90], and one with a *PKP2* p.(Arg210His) variant, where APD was reduced in comparison to control [87]. Similarly, in studies where Ca^{2+} imaging and MEA technology were used, calcium transient and FPD differences have been reported in patient iPSC-CMs in comparison to controls (in six out of seven tested BrS iPSC-CMs at baseline) (**Supplementary Tables 1-5 and 1-6**) [68,71,86].

An interesting advantage of iPSC-CM models is that they provide the opportunity to study cellular disease mechanisms in patients without an identified mutation, and two groups indeed investigated this. In one study [55], iPSC-CMs of three different patients showed no changes in sodium currents, nor other AP characteristics studied, even at different pacing frequencies. In the other study [87], only the effect of ajmaline on FPD was investigated and no increased susceptibility to ajmaline was observed in the two studied patients. Perhaps very subtle or non-studied electrophysiological changes were present in the models. Another explanation could be that the clinical phenotype was not caused by defects in ion currents but involved structural abnormalities at the cell and/or tissue level or disturbances of other unexpected pathways. This again supports the importance of in-depth study of the generated iPSC-CM BrS models, and the value of such models containing the full CM intracellular protein repertoire as well as the possibility to create and study more tissue-like structures. When the genetic cause is unknown or when modifiers underlying variable disease expressivity are sought, an approach including transcriptome and proteome analysis of iPSC-CMs could provide a more holistic picture and valuable indications on involved genes, proteins or pathways.

The fact that patient iPSC-CMs carry the patient’s full genetic background, including potential modifiers, can be a drawback of the model as well, when trying to establish the causal relationship between genotype and phenotype and to prove the pathogenic effect of a specific genetic variant. This is especially important when evaluating VUS or potential novel BrS candidate genes. In such cases, genetic engineering, such as CRISPR Cas genome editing, should be applied to correct the studied variant in the patient iPSCs (creating an isogenic control) or introduce it into one or more control iPSC-lines. The study of these models will reveal whether the investigated variant is necessary and sufficient to cause the phenotype or suggest the contribution of other genetic factors in the observed phenotype. In four of the discussed reports, genetic engineering was used to create isogenic controls [68,86] or introduce the variant of interest on a control background [56,71]. In each study, the modified iPSC-CMs showed rescue or development of the phenotype [56,68,71,86], confirming the causative status of novel variants and in one case, providing evidence for the involvement of *SCN3B* in subtle changes in the BrS/LQTS phenotype [86].

Over the years, it has been shown that iPSC-CMs display an immature phenotype with an expression pattern resembling that of fetal human cardiomyocytes [31,32,120,121]. They are spontaneously active (like fetal hCMs) due to a substantially reduced I_{K1} density and the presence of a pacemaker current. Though sodium channel expression is normal in iPSC-CMs, the more positive RMP results in the inactivation of the channels, leaving very limited I_{Na} available during the phase 0 depolarization and thereby potentially masking the impact of I_{Na} deficiency on the AP, more specifically the upstroke velocity. The depolarized state of iPSC-CMs could also lead to I_{to} inactivation and the absence of phase one repolarization in iPSC-CMs. This obviously poses a problem for BrS modeling, leading to the choice of several groups to impose I_{K1} onto their iPSC-CMs to achieve an RMP of -80 – -90 mV and a more mature electrophysiological phenotype. It should be noted that this is performed on isolated cells, deprived of cell–cell contacts that are also potentially important for current expression, such as I_{Na} . It is clear from **Supplementary Table 1-2** that in studies without I_{K1} injection and with depolarized RMP of the iPSC-CMs, the values of upstroke velocity were much lower than the normal range of native adult CMs and it is questionable whether they represent trustworthy values and true differences between patient and control models. Other interesting observations brought forward in the discussed articles, are the likely different expression profiles of $I_{to,f}$ and $I_{to,s}$ in hiPSC-CMs compared with that in adult epicardial ventricular CMs ($I_{to,s}$ dominant in the first and $I_{to,f}$ dominant in the latter) [61], and the expression of a fetal form of sodium channel β -subunit (*SCN3B*) that could be masking the BrS phenotype by compensating I_{Na} reduction [86]. In addition, iPSC-CMs show structural immaturity including a lack of T-tubules, and reduced sarcomere organization. This has been shown to affect calcium handling and excitation–contraction coupling in iPSC-CMs [32]. Additionally, in light of the previously mentioned potential microstructural abnormalities in BrS, this could affect readouts and should certainly be taken into consideration when interpreting results. Methods to mature iPSC-CMs, such as hormone treatments, mechanical and electrical stimulation, 3D cell culture etc., are hot topic of investigations and are anticipated to show their value in future studies. It should be noted as well that every model has its limits, but it is important to recognize them and take them into account when interpreting and extrapolating data.

Since the differentiation of iPSCs to CMs is not fully defined and the addition of Wnt signalling pathway influencing factors is certainly a minimization of all processes present during actual embryonic development, the current methodology results in a heterogeneous iPSC-CM culture (mixed with non-CMs) that can vary with every differentiation round. To create robust and comparable data between BrS disease modeling studies, iPSC-CM populations of comparable purity, subtype and maturity should be used. On top of that, genetic alterations induced during reprogramming and/or passaging of iPSCs in culture create additional variability in the model, calling for the replication of obtained phenotypic and functional results in several (clonal) cell lines. Here, the scalability of iPSC-CMs in combination with high-throughput phenotyping techniques clearly present an advantage. In all of the cited BrS iPSC-CM reports, data from several differentiation rounds were combined, which is good practice. De la Roche and colleagues even specifically showed that the results between differentiation experiments were not significantly different and could be indeed pooled together [56]. Additionally, in the report of Selga et al., differences between iPSC-CM differentiation methods were addressed, and the effect of the mutation was shown to be similar in magnitude in iPSC-CMs derived using an EB- as well as a monolayer-based approach [91]. Selga et al. reported no significant differences between two clones differentiated from the same cell line. In most of the articles, several clones of patient and/or control iPSC-CMs were tested, but often not all were used for all comparisons. In fact, best practice to obtain rigid data from the models would require at least three different iPSC clones to be used for each patient and control individual and should be compared for all characteristics. Additionally, the use of multiple patient and control iPSC-CM lines is recommended. This should account for variability between individuals with different genetic backgrounds and comorbidities. In about half of the discussed reports, a single control iPSC-CM line was used [71,86–88,91,92], while in five articles two [55,56,68,89,90] and in two articles three [69,70] controls were analysed. In some cases, authors observed differences in electrophysiological properties between their control cell lines [55,90] and then tended to compare their results to each control line separately. In other cases, where similar

discrepancies between the control lines were observed (e.g., APD50 or dV/dT_{max} values) [56,69,70], the authors compared their results from patient iPSC-CMs to the pooled range of values from all characterized control iPSC-CMs. It is clear that standardization, with the use of multiple clones and multiple individuals for all functional characterization studies, is needed in the field of iPSC-CM modeling.

Another important note is that the current iPSC-CM models only provide a cellular system demonstrating abnormal electrical behaviour or structural abnormalities in single cells or 2D sheets, and caution must be exercised in extrapolating findings to the whole heart. The current iPSC differentiation protocols predominantly generate ventricular-like iPSC-CMs [40,41] but protocols aimed at specifically generating atrial-like [122] and nodal-like [123] iPSC-CMs have also been described. The co-culture of a controlled mixture of these different cell-types, potentially including non-cardiomyocytes (such as cardiac fibroblasts) in 3D tissues with proper extracellular matrix is predicted to be relevant to the study of cardiac arrhythmias. Though it will be hard to get these tissues organized in layers of endocardium and epicardium and/or attribute left- or right sidedness, study of arrhythmic events such as re-entry, conductance problems, local AP and current heterogeneity and even tissue fibrosis and structural changes that could all be relevant to the BrS phenotype and disease pathomechanisms should be feasible. In addition, such culture systems are very likely to improve on the maturity of the iPSC-CMs. Although quite some effort has already been made to create engineered heart tissue (EHT), 3D cardiac microtissues, organoids or microfluidic human-body-on-a-chip systems [48,124–129], this field needs further development and application of these novel, more physiological iPSC-CM based models. The latter will certainly provide interesting improvements for BrS disease modeling, as well as for the application of these models for drug testing, precision medicine and cardiotoxicity screening [130–132].

In conclusion, the thirteen discussed studies have proven the capability of the iPSC-CM models to recapitulate the BrS patient phenotype (**Figure 1-2**). However, no particularly compelling novel disease insights for BrS have emerged yet and it is important to take the current limitations of iPSC-CMs into account when using them as a model in studying Brugada syndrome and other cardiac arrhythmias. Focus on technologies to improve iPSC-CM maturity and create proper engineered heart tissues in combination with standardization of the experimental setups and more in-depth (functional) studies of the generated iPSC-CM models will help bridge the gap between model and clinical practice (**Figure 1-2**). Taken together, this exciting approach clearly holds great promise for BrS and cardiac disease research.

1.9 References

- [1] Antzelevitch, C. Brugada syndrome. *Pacing Clin. Electrophysiol.* 2006, 29, 1130–1159.
- [2] Brugada, J.; Campuzano, O.; Arbelo, E.; Sarquella-Brugada, G.; Brugada, R. Present Status of Brugada Syndrome: JACC State-of-the-Art Review. *J. Am. Coll. Cardiol.* 2018, 72, 1046–1059.
- [3] Watanabe, H.; Minamino, T. Genetics of Brugada syndrome. *J. Hum. Genet.* 2016, 61, 57–60.
- [4] Kapplinger, J.D.; Tester, D.J.; Alders, M.; Benito, B.; Berthet, M.; Brugada, J.; Brugada, P.; Fressart, V.; Guerchicoff, A.; Harris-Kerr, C.; et al. An international compendium of mutations in the *SCN5A*-encoded cardiac sodium channel in patients referred for Brugada syndrome genetic testing. *Heart Rhythm* 2010, 7, 33–46.
- [5] Hosseini, S.M.; Kim, R.; Udupa, S.; Costain, G.; Jobling, R.; Liston, E.; Jamal, S.M.; Szybowska, M.; Morel, C.F.; Bodwin, S.; et al. Reappraisal of Reported Genes for Sudden Arrhythmic Death: Evidence-Based Evaluation of Gene Validity for Brugada Syndrome. *Circulation* 2018, 138, 1195–1205.
- [6] Le Scouarnec, S.; Karakachoff, M.; Gourraud, J.B.; Lindenbaum, P.; Bonnaud, S.; Portero, V.; Duboscq-Bidot, L.; Daumy, X.; Simonet, F.; Teusan, R.; et al. Testing the burden of rare variation in arrhythmia-susceptibility genes provides new insights into molecular diagnosis for Brugada syndrome. *Hum. Mol. Genet.* 2015, 24, 2757–2763.
- [7] Antzelevitch, C. The Brugada syndrome: Ionic basis and arrhythmia mechanisms. *J. Cardiovasc. Electrophysiol.* 2001, 12, 268–272.
- [8] Meregalli, P.G.; Wilde, A.A.; Tan, H.L. Pathophysiological mechanisms of Brugada syndrome: Depolarization disorder, repolarization disorder, or more? *Cardiovasc. Res.* 2005, 67, 367–378.
- [9] Elizari, M.V.; Levi, R.; Acunzo, R.S.; Chiale, P.A.; Civetta, M.M.; Ferreiro, M.; Sicouri, S. Abnormal expression of cardiac neural crest cells in heart development: A different hypothesis for the etiopathogenesis of Brugada syndrome. *Heart Rhythm* 2007, 4, 359–365.
- [10] Antzelevitch, C. Role of spatial dispersion of repolarization in inherited and acquired sudden cardiac death syndromes. *Am. J. Physiol. Heart Circ. Physiol.* 2007, 293, H2024–H2038.
- [11] Morita, H.; Zipes, D.P.; Fukushima-Kusano, K.; Nagase, S.; Nakamura, K.; Morita, S.T.; Ohe, T.; Wu, J. Repolarization heterogeneity in the right ventricular outflow tract: Correlation with ventricular arrhythmias in Brugada patients and in an in vitro canine Brugada model. *Heart Rhythm* 2008, 5, 725–733.
- [12] Lambiase, P.D.; Ahmed, A.K.; Ciaccio, E.J.; Brugada, R.; Lizotte, E.; Chaubey, S.; Ben-Simon, R.; Chow, A.W.; Lowe, M.D.; McKenna, W.J. High-density substrate mapping in Brugada syndrome: Combined role of conduction and repolarization heterogeneities in arrhythmogenesis. *Circulation* 2009, 120, 106–117, 1-4.
- [13] Wilde, A.A.; Postema, P.G.; Di Diego, J.M.; Viskin, S.; Morita, H.; Fish, J.M.; Antzelevitch, C. The pathophysiological mechanism underlying Brugada syndrome: Depolarization versus repolarization. *J. Mol. Cell. Cardiol.* 2010, 49, 543–553.
- [14] Verkerk, A.O.; Amin, A.S.; Remme, C.A. Disease Modifiers of Inherited *SCN5A* Channelopathy. *Front. Cardiovasc. Med.* 2018, 5, 137.
- [15] Sotoodehnia, N.; Isaacs, A.; de Bakker, P.I.; Dorr, M.; Newton-Cheh, C.; Nolte, I.M.; van der Harst, P.; Muller, M.; Eijgelsheim, M.; Alonso, A.; et al. Common variants in 22 loci are associated with QRS duration and cardiac ventricular conduction. *Nat. Genet.* 2010, 42, 1068–1076.
- [16] Schwartz, P.J.; Ackerman, M.J.; Antzelevitch, C.; Bezzina, C.R.; Borggrefe, M.; Cuneo, B.F.; Wilde, A.A.M. Inherited cardiac arrhythmias. *Nat. Rev. Dis. Primers* 2020, 6, 58.
- [17] Wilde, A.A.; Bezzina, C.R. Genetics of cardiac arrhythmias. *Heart* 2005, 91, 1352–1358.
- [18] Polovina, M.M.; Vukicevic, M.; Banko, B.; Lip, G.Y.H.; Potpara, T.S. Brugada syndrome: A general cardiologist's perspective. *Eur. J. Intern. Med.* 2017, 44, 19–27.

- [19] Bezzina, C.R.; Barc, J.; Mizusawa, Y.; Remme, C.A.; Gourraud, J.B.; Simonet, F.; Verkerk, A.O.; Schwartz, P.J.; Crotti, L.; Dagradi, F.; et al. Common variants at *SCN5A-SCN10A* and *HEY2* are associated with Brugada syndrome, a rare disease with high risk of sudden cardiac death. *Nat. Genet.* 2013, 45, 1044–1049.
- [20] Morita, H.; Zipes, D.P.; Morita, S.T.; Lopshire, J.C.; Wu, J. Epicardial ablation eliminates ventricular arrhythmias in an experimental model of Brugada syndrome. *Heart Rhythm* 2009, 6, 665–671.
- [21] Brugada, J.; Pappone, C.; Berruezo, A.; Vicedomini, G.; Manguso, F.; Ciconte, G.; Giannelli, L.; Santinelli, V. Brugada Syndrome Phenotype Elimination by Epicardial Substrate Ablation. *Circ. Arrhythm. Electrophysiol.* 2015, 8, 1373–1381.
- [22] Rudic, B.; Chaykovskaya, M.; Tsyganov, A.; Kalinin, V.; Tulumen, E.; Papavassiliu, T.; Dosch, C.; Liebe, V.; Kuschyk, J.; Roger, S.; et al. Simultaneous Non-Invasive Epicardial and Endocardial Mapping in Patients with Brugada Syndrome: New Insights into Arrhythmia Mechanisms. *J. Am. Heart Assoc.* 2016, 5, e004095.
- [23] Pappone, C.; Brugada, J.; Vicedomini, G.; Ciconte, G.; Manguso, F.; Saviano, M.; Vitale, R.; Cuko, A.; Giannelli, L.; Calovic, Z.; et al. Electrical Substrate Elimination in 135 Consecutive Patients with Brugada Syndrome. *Circ. Arrhythm. Electrophysiol.* 2017, 10, e005053.
- [24] Schmidt, C.; Wiedmann, F.; El-Battrawy, I.; Fritz, M.; Ratte, A.; Beller, C.J.; Lang, S.; Rudic, B.; Schimpf, R.; Akin, I.; et al. Reduced Na(+) Current in Native Cardiomyocytes of a Brugada Syndrome Patient Associated With beta-2-Syntrophin Mutation. *Circ. Genom. Precis. Med.* 2018, 11, e002263.
- [25] Johnson, W.B.; Katugampola, S.; Able, S.; Napier, C.; Harding, S.E. Profiling of cAMP and cGMP phosphodiesterases in isolated ventricular cardiomyocytes from human hearts: Comparison with rat and guinea pig. *Life Sci.* 2012, 90, 328–336.
- [26] Ajiro, Y.; Hagiwara, N.; Katsube, Y.; Sperelakis, N.; Kasanuki, H. Levosimendan increases L-type Ca(2+) current via phosphodiesterase-3 inhibition in human cardiac myocytes. *Eur. J. Pharmacol.* 2002, 435, 27–33.
- [27] Qu, Y.; Page, G.; Abi-Gerges, N.; Miller, P.E.; Ghetti, A.; Vargas, H.M. Action Potential Recording and Pro-arrhythmia Risk Analysis in Human Ventricular Trabeculae. *Front. Physiol.* 2017, 8, 1109.
- [28] Nguyen, N.; Nguyen, W.; Nguyenton, B.; Ratchada, P.; Page, G.; Miller, P.E.; Ghetti, A.; Abi-Gerges, N. Adult Human Primary Cardiomyocyte-Based Model for the Simultaneous Prediction of Drug-Induced Inotropic and Pro-arrhythmia Risk. *Front. Physiol.* 2017, 8, 1073.
- [29] Sendfeld, F.; Selga, E.; Scornik, F.S.; Perez, G.J.; Mills, N.L.; Brugada, R. Experimental Models of Brugada syndrome. *Int. J. Mol. Sci.* 2019, 20, 2123.
- [30] Takahashi, K.; Yamanaka, S. Induction of pluripotent stem cells from mouse embryonic and adult fibroblast cultures by defined factors. *Cell* 2006, 126, 663–676.
- [31] Kodama, M.; Furutani, K.; Kimura, R.; Ando, T.; Sakamoto, K.; Nagamori, S.; Ashihara, T.; Kurachi, Y.; Sekino, Y.; Frurukawa, T.; et al. Systematic expression analysis of genes related to generation of action potentials in human iPSC-derived cardiomyocytes. *J. Pharmacol. Sci.* 2019, 140, 325–330.
- [32] Karakikes, I.; Ameen, M.; Termglinchan, V.; Wu, J.C. Human induced pluripotent stem cell-derived cardiomyocytes: Insights into molecular, cellular, and functional phenotypes. *Circ. Res.* 2015, 117, 80–88.
- [33] Lee, Y.M.; Zampieri, B.L.; Scott-McKean, J.J.; Johnson, M.W.; Costa, A.C.S. Generation of Integration-Free Induced Pluripotent Stem Cells from Urine-Derived Cells Isolated from Individuals with Down Syndrome. *Stem Cells Transl. Med.* 2017, 6, 1465–1476.
- [34] Ye, L.; Muench, M.O.; Fusaki, N.; Beyer, A.I.; Wang, J.; Qi, Z.; Yu, J.; Kan, Y.W. Blood cell-derived induced pluripotent stem cells free of reprogramming factors generated by Sendai viral vectors. *Stem Cells Transl. Med.* 2013, 2, 558–566.
- [35] Vannucci, L.; Lai, M.; Chiuppesi, F.; Ceccherini-Nelli, L.; Pistello, M. Viral vectors: A look back and ahead on gene transfer technology. *New Microbiol.* 2013, 36, 1–22.

- [36] Fusaki, N.; Ban, H.; Nishiyama, A.; Saeki, K.; Hasegawa, M. Efficient induction of transgene-free human pluripotent stem cells using a vector based on Sendai virus, an RNA virus that does not integrate into the host genome. *Proc. Jpn. Acad. Ser. B Phys. Biol. Sci.* 2009, 85, 348–362.
- [37] Lufino, M.M.; Edser, P.A.; Wade-Martins, R. Advances in high-capacity extrachromosomal vector technology: Episomal maintenance, vector delivery, and transgene expression. *Mol. Ther.* 2008, 16, 1525–1538.
- [38] Weng, Z.; Kong, C.W.; Ren, L.; Karakikes, I.; Geng, L.; He, J.; Chow, M.Z.; Mok, C.F.; Chan, H.Y.S.; Webb, S.E.; et al. A simple, cost-effective but highly efficient system for deriving ventricular cardiomyocytes from human pluripotent stem cells. *Stem Cells Dev.* 2014, 23, 1704–1716.
- [39] Bhattacharya, S.; Burridge, P.W.; Kropp, E.M.; Chuppa, S.L.; Kwok, W.M.; Wu, J.C.; Boheler, K.R.; Gundry, R.L. High efficiency differentiation of human pluripotent stem cells to cardiomyocytes and characterization by flow cytometry. *J. Vis. Exp.* 2014, 52010, doi:10.3791/52010.
- [40] Lian, X.; Hsiao, C.; Wilson, G.; Zhu, K.; Hazeltine, L.B.; Azarin, S.M.; Raval, K.K.; Zhang, J.; Kamp, T.J.; Palecek, S.P. Robust cardiomyocyte differentiation from human pluripotent stem cells via temporal modulation of canonical Wnt signaling. *Proc. Natl. Acad. Sci. USA* 2012, 109, E1848–E1857.
- [41] Burridge, P.W.; Matsa, E.; Shukla, P.; Lin, Z.C.; Churko, J.M.; Ebert, A.D.; Lan, F.; Diecke, S.; Huber, B.; Mordwinkin, N.M.; et al. Chemically defined generation of human cardiomyocytes. *Nat. Methods* 2014, 11, 855–860.
- [42] Mummery, C.L.; Zhang, J.; Ng, E.S.; Elliott, D.A.; Elefanty, A.G.; Kamp, T.J. Differentiation of human embryonic stem cells and induced pluripotent stem cells to cardiomyocytes: A methods overview. *Circ. Res.* 2012, 111, 344–358.
- [43] Zhao, M.; Tang, Y.; Zhou, Y.; Zhang, J. Deciphering Role of Wnt Signalling in Cardiac Mesoderm and Cardiomyocyte Differentiation from Human iPSCs: Four-dimensional control of Wnt pathway for hiPSC-CMs differentiation. *Sci. Rep.* 2019, 9, 19389.
- [44] Dias, T.P.; Pinto, S.N.; Santos, J.I.; Fernandes, T.G.; Fernandes, F.; Diogo, M.M.; Prieto, M.; Cabral, J.M.S. Biophysical study of human induced Pluripotent Stem Cell-Derived cardiomyocyte structural maturation during long-term culture. *Biochem. Biophys. Res. Commun.* 2018, 499, 611–617.
- [45] Zhou, Y.; Wang, L.; Liu, Z.; Alimohamadi, S.; Yin, C.; Liu, J.; Qian, L. Comparative Gene Expression Analyses Reveal Distinct Molecular Signatures between Differentially Reprogrammed Cardiomyocytes. *Cell Rep.* 2017, 20, 3014–3024.
- [46] White, M.C.; Pang, L.; Yang, X. MicroRNA-mediated maturation of human pluripotent stem cell-derived cardiomyocytes: Towards a better model for cardiotoxicity? *Food Chem. Toxicol.* 2016, 98 Pt A, 17–24.
- [47] Yang, X.; Rodriguez, M.; Pabon, L.; Fischer, K.A.; Reinecke, H.; Regnier, M.; Sniadecki, N.J.; Ruohola-Baker, H.; Murry, C.E. Triiodo-L-thyronine promotes the maturation of human cardiomyocytes-derived from induced pluripotent stem cells. *J. Mol. Cell. Cardiol.* 2014, 72, 296–304.
- [48] Yoshida, S.; Miyagawa, S.; Fukushima, S.; Kawamura, T.; Kashiyama, N.; Ohashi, F.; Toyofuku, T.; Toda, K.; Sawa, Y. Maturation of Human Induced Pluripotent Stem Cell-Derived Cardiomyocytes by Soluble Factors from Human Mesenchymal Stem Cells. *Mol. Ther.* 2018, 26, 2681–2695.
- [49] Ulmer, B.M.; Stoehr, A.; Schulze, M.L.; Patel, S.; Gucek, M.; Mannhardt, I.; Funcke, S.; Murphy, E.; Eschenhagen, T.; Hansen, A. Contractile Work Contributes to Maturation of Energy Metabolism in hiPSC-Derived Cardiomyocytes. *Stem Cell Rep.* 2018, 10, 834–847.
- [50] Lewandowski, J.; Rozwadowska, N.; Kolanowski, T.J.; Malcher, A.; Zimna, A.; Rugowska, A.; Fiedorowicz, K.; Labeledz, W.; Kubaszewski, L.; Chojnacka, K.; et al. The impact of in vitro cell culture duration on the maturation of human cardiomyocytes derived from induced pluripotent stem cells of myogenic origin. *Cell Transplant.* 2018, 27, 1047–1067.
- [51] Nunes, S.S.; Miklas, J.W.; Liu, J.; Aschar-Sobbi, R.; Xiao, Y.; Zhang, B.; Jiang, J.; Masse, S.; Gagliardi, M.; Hsieh, A.; et al. Biowire: A platform for maturation of human pluripotent stem cell-derived cardiomyocytes. *Nat. Methods* 2013, 10, 781–787.

- [52] Parikh, S.S.; Blackwell, D.J.; Gomez-Hurtado, N.; Frisk, M.; Wang, L.; Kim, K.; Dahl, C.P.; Fiane, A.; Tonnessen, T.; Kryshtal, D.O.; et al. Thyroid and Glucocorticoid Hormones Promote Functional T-Tubule Development in Human-Induced Pluripotent Stem Cell-Derived Cardiomyocytes. *Circ. Res.* 2017, 121, 1323–1330.
- [53] Ruan, J.L.; Tulloch, N.L.; Razumova, M.V.; Saiget, M.; Muskheli, V.; Pabon, L.; Reinecke, H.; Regnier, M.; Murry, C.E. Mechanical Stress Conditioning and Electrical Stimulation Promote Contractility and Force Maturation of Induced Pluripotent Stem Cell-Derived Human Cardiac Tissue. *Circulation* 2016, 134, 1557–1567.
- [54] Huang, C.Y.; Peres Moreno Maia-Joca, R.; Ong, C.S.; Wilson, I.; DiSilvestre, D.; Tomaselli, G.F.; Reich, D.H. Enhancement of human iPSC-derived cardiomyocyte maturation by chemical conditioning in a 3D environment. *J. Mol. Cell. Cardiol.* 2020, 138, 1–11.
- [55] Veerman, C.C.; Mengarelli, I.; Guan, K.; Stauske, M.; Barc, J.; Tan, H.L.; Wilde, A.A.; Verkerk, A.O.; Bezzina, C.R. hiPSC-derived cardiomyocytes from Brugada Syndrome patients without identified mutations do not exhibit clear cellular electrophysiological abnormalities. *Sci. Rep.* 2016, 6, 30967.
- [56] de la Roche, J.; Angsutararux, P.; Kempf, H.; Janan, M.; Bolesani, E.; Thiemann, S.; Wojciechowski, D.; Coffee, M.; Franke, A.; Schwanke, K.; et al. Comparing human iPSC-cardiomyocytes versus HEK293T cells unveils disease-causing effects of Brugada mutation A735V of NaV1.5 sodium channels. *Sci. Rep.* 2019, 9, 11173.
- [57] Tohyama, S.; Hattori, F.; Sano, M.; Hishiki, T.; Nagahata, Y.; Matsuura, T.; Hashimoto, H.; Suzuki, T.; Yamashita, H.; Satoh, Y.; et al. Distinct metabolic flow enables large-scale purification of mouse and human pluripotent stem cell-derived cardio-myocytes. *Cell Stem Cell* 2013, 12, 127–137.
- [58] Sharma, A.; Li, G.; Rajarajan, K.; Hamaguchi, R.; Burrige, P.W.; Wu, S.M. Derivation of highly purified cardiomyocytes from human induced pluripotent stem cells using small molecule-modulated differentiation and subsequent glucose starvation. *J. Vis. Exp.* 2015, doi:10.3791/52628.
- [59] Ramachandra, C.J.A.; Mehta, A.; Wong, P.; Ja, K.; Fritsche-Danielson, R.; Bhat, R.V.; Hausenloy, D.J.; Kovalik, J.P.; Shim, W. Fatty acid metabolism driven mitochondrial bioenergetics promotes advanced developmental phenotypes in human induced pluripotent stem cell derived cardiomyocytes. *Int. J. Cardiol.* 2018, 272, 288–297.
- [60] Brugada, R.; Campuzano, O.; Sarquella-Brugada, G.; Brugada, J.; Brugada, P. Brugada syndrome. *Methodist Debakey Cardiovasc. J.* 2014, 10, 25–28.
- [61] Nerbonne, J.M.; Kass, R.S. Molecular physiology of cardiac repolarization. *Physiol. Rev.* 2005, 85, 1205–1253.
- [62] Shih, H.T. Anatomy of the action potential in the heart. *Tex. Heart Inst. J.* 1994, 21, 30–41.
- [63] Garg, P.; Garg, V.; Shrestha, R.; Sanguinetti, M.C.; Kamp, T.J.; Wu, J.C. Human Induced Pluripotent Stem Cell-Derived Cardiomyocytes as Models for Cardiac Channelopathies: A Primer for Non-Electrophysiologists. *Circ. Res.* 2018, 123, 224–243.
- [64] Amin, A.S.; Tan, H.L.; Wilde, A.A. Cardiac ion channels in health and disease. *Heart Rhythm* 2010, 7, 117–126.
- [65] Ince, C.; van Bavel, E.; van Duijn, B.; Donkersloot, K.; Coremans, A.; Ypey, D.L.; Verveen, A.A. Intracellular microelectrode measurements in small cells evaluated with the patch clamp technique. *Biophys. J.* 1986, 50, 1203–1209.
- [66] Bedut, S.; Seminatore-Nole, C.; Lamamy, V.; Caignard, S.; Boutin, J.A.; Nosjean, O.; Stephan, J.P.; Coge, F. High-throughput drug profiling with voltage- and calcium-sensitive fluorescent probes in human iPSC-derived cardiomyocytes. *Am. J. Physiol. Heart Circ. Physiol.* 2016, 311, H44–H53.
- [67] Broyles, C.N.; Robinson, P.; Daniels, M.J. Fluorescent, Bioluminescent, and Optogenetic Approaches to Study Excitable Physiology in the Single Cardiomyocyte. *Cells* 2018, 7, 51.
- [68] Liang, P.; Sallam, K.; Wu, H.; Li, Y.; Itzhaki, I.; Garg, P.; Zhang, Y.; Vermglinchan, V.; Lan, F.; Gu, M.; et al. Patient-Specific and Genome-Edited Induced Pluripotent Stem Cell-Derived Cardiomyocytes Elucidate Single-Cell Phenotype of Brugada Syndrome. *J. Am. Coll. Cardiol.* 2016, 68, 2086–2096.

- [69] El-Battrawy, I.; Albers, S.; Cyganek, L.; Zhao, Z.; Lan, H.; Li, X.; Xu, Q.; Kleinsorge, M.; Huang, M.; Liao, Z.; et al. A cellular model of Brugada syndrome with *SCN10A* variants using human-induced pluripotent stem cell-derived cardiomyocytes. *Europace* 2019, 21, 1410–1421.
- [70] El-Battrawy, I.; Muller, J.; Zhao, Z.; Cyganek, L.; Zhong, R.; Zhang, F.; Kleinsorge, M.; Lan, H.; Li, X.; Xu, Q.; et al. Studying Brugada Syndrome with an *SCN1B* Variants in Human-Induced Pluripotent Stem Cell-Derived Cardiomyocytes. *Front. Cell. Dev. Biol.* 2019, 7, 261.
- [71] Belbachir, N.; Portero, V.; Al Sayed, Z.R.; Gourraud, J.B.; Dilasser, F.; Jesel, L.; Guo, H.; Wu, H.; Gaborit, N.; Guilluy, C.; et al. *RRAD* mutation causes electrical and cytoskeletal defects in cardiomyocytes derived from a familial case of Brugada syndrome. *Eur. Heart J.* 2019, 40, 3081–3094.
- [72] Walter, A.; Saric, T.; Hescheler, J.; Papadopoulos, S. Calcium Imaging in Pluripotent Stem Cell-Derived Cardiac Myocytes. *Methods Mol. Biol.* 2016, 1353, 131–146.
- [73] Bassett, J.J.; Monteith, G.R. Genetically Encoded Calcium Indicators as Probes to Assess the Role of Calcium Channels in Disease and for High-Throughput Drug Discovery. *Adv. Pharmacol.* 2017, 79, 141–171.
- [74] Hou, J.H.; Kralj, J.M.; Douglass, A.D.; Engert, F.; Cohen, A.E. Simultaneous mapping of membrane voltage and calcium in zebrafish heart in vivo reveals chamber-specific developmental transitions in ionic currents. *Front. Physiol.* 2014, 5, 344.
- [75] Shaheen, N.; Shiti, A.; Huber, I.; Shinnawi, R.; Arbel, G.; Gepstein, A.; Setter, N.; Goldfracht, I.; Gruber, A.; Chorna, S.V.; et al. Human Induced Pluripotent Stem Cell-Derived Cardiac Cell Sheets Expressing Genetically Encoded Voltage Indicator for Pharmacological and Arrhythmia Studies. *Stem Cell Rep.* 2018, 10, 1879–1894.
- [76] Shinnawi, R.; Huber, I.; Maizels, L.; Shaheen, N.; Gepstein, A.; Arbel, G.; Tijssen, A.J.; Gepstein, L. Monitoring Human-Induced Pluripotent Stem Cell-Derived Cardiomyocytes with Genetically Encoded Calcium and Voltage Fluorescent Reporters. *Stem Cell Rep.* 2015, 5, 582–596.
- [77] Song, L.; Awari, D.W.; Han, E.Y.; Uche-Anyia, E.; Park, S.H.; Yabe, Y.A.; Chung, W.K.; Yazawa, M. Dual optical recordings for action potentials and calcium handling in induced pluripotent stem cell models of cardiac arrhythmias using genetically encoded fluorescent indicators. *Stem Cells Transl. Med.* 2015, 4, 468–475.
- [78] Leyton-Mange, J.S.; Mills, R.W.; Macri, V.S.; Jang, M.Y.; Butte, F.N.; Ellinor, P.T.; Milan, D.J. Rapid cellular phenotyping of human pluripotent stem cell-derived cardiomyocytes using a genetically encoded fluorescent voltage sensor. *Stem Cell Rep.* 2014, 2, 163–170.
- [79] Sun, Y.H.; Kao, H.K.J.; Chang, C.W.; Merleev, A.; Overton, J.L.; Pretto, D.; Yechikov, S.; Maverakis, E.; Chiamvimonvat, N.; Chan, J.W.; et al. Human induced pluripotent stem cell line with genetically encoded fluorescent voltage indicator generated via CRISPR for action potential assessment post-cardiogenesis. *Stem Cells* 2020, 38, 90–101.
- [80] Miccoli, B.; Lopez, C.M.; Goikoetxea, E.; Putzeys, J.; Sekeri, M.; Krylychkina, O.; Chang, S.W.; Firrincieli, A.; Andrei, A.; Reumers, V.; et al. High-Density Electrical Recording and Impedance Imaging with a Multi-Modal CMOS Multi-Electrode Array Chip. *Front. Neurosci.* 2019, 13, 641.
- [81] Zhu, H.; Scharnhorst, K.S.; Stieg, A.Z.; Gimzewski, J.K.; Minami, I.; Nakatsuji, N.; Nakano, H.; Nakano, A. Two dimensional electrophysiological characterization of human pluripotent stem cell-derived cardiomyocyte system. *Sci. Rep.* 2017, 7, 43210.
- [82] Jans, D.; Callewaert, G.; Krylychkina, O.; Hoffman, L.; Gullo, F.; Prodanov, D.; Braeken, D. Action potential-based MEA platform for in vitro screening of drug-induced cardiotoxicity using human iPSCs and rat neonatal myocytes. *J. Pharmacol. Toxicol. Methods* 2017, 87, 48–52.
- [83] Kussauer, S.; David, R.; Lemcke, H. hiPSCs Derived Cardiac Cells for Drug and Toxicity Screening and Disease Modeling: What Micro-Electrode-Array Analyses Can Tell Us. *Cells* 2019, 8, 1331.
- [84] Halbach, M.; Egert, U.; Hescheler, J.; Banach, K. Estimation of action potential changes from field potential recordings in multicellular mouse cardiac myocyte cultures. *Cell. Physiol. Biochem.* 2003, 13, 271–284.

- [85] Muller, J.; Ballini, M.; Livi, P.; Chen, Y.; Radivojevic, M.; Shadmani, A.; Viswam, V.; Jones, I.L.; Fiscella, M.; Diggelmann, R.; et al. High-resolution CMOS MEA platform to study neurons at subcellular, cellular, and network levels. *Lab. Chip.* 2015, 15, 2767–2780.
- [86] Okata, S.; Yuasa, S.; Suzuki, T.; Ito, S.; Makita, N.; Yoshida, T.; Li, M.; Kurokawa, J.; Seki, T.; Egashira, T.; et al. Embryonic type Na(+) channel beta-subunit, *SCN3B* masks the disease phenotype of Brugada syndrome. *Sci. Rep.* 2016, 6, 34198.
- [87] Miller, D.C.; Harmer, S.C.; Poliandri, A.; Nobles, M.; Edwards, E.C.; Ware, J.S.; Sharp, T.V.; McKay, T.R.; Dunkel, L.; Lambiase, P.D.; et al. Ajmaline blocks I_{Na} and I_{Kr} without eliciting differences between Brugada syndrome patient and control human pluripotent stem cell-derived cardiac clusters. *Stem Cell Res.* 2017, 25, 233–244.
- [88] Davis, R.P.; Casini, S.; van den Berg, C.W.; Hoekstra, M.; Remme, C.A.; Dambrot, C.; Salvatori, D.; Oostwaard, D.W.; Wilde, A.A.; Bezzina, C.R.; et al. Cardiomyocytes derived from pluripotent stem cells recapitulate electrophysiological characteristics of an overlap syndrome of cardiac sodium channel disease. *Circulation* 2012, 125, 3079–3091.
- [89] Kosmidis, G.; Veerman, C.C.; Casini, S.; Verkerk, A.O.; van de Pas, S.; Bellin, M.; Wilde, A.A.; Mummery, C.L.; Bezzina, C.R. Readthrough-Promoting Drugs Gentamicin and PTC124 Fail to Rescue $Na_v1.5$ Function of Human-Induced Pluripotent Stem Cell-Derived Cardiomyocytes Carrying Nonsense Mutations in the Sodium Channel Gene *SCN5A*. *Circ. Arrhythm. Electro-physiol.* 2016, 9, e004227.
- [90] Ma, D.; Liu, Z.; Loh, L.J.; Zhao, Y.; Li, G.; Liew, R.; Islam, O.; Wu, J.; Chung, Y.Y.; Teo, W.S.; et al. Identification of an I_{Na} -dependent and Ito-mediated proarrhythmic mechanism in cardiomyocytes derived from pluripotent stem cells of a Brugada syndrome patient. *Sci. Rep.* 2018, 8, 11246.
- [91] Selga, E.; Sendfeld, F.; Martinez-Moreno, R.; Medine, C.N.; Tura-Ceide, O.; Wilmut, S.I.; Perez, G.J.; Scornik, F.S.; Brugada, R.; Mills, N.L. Sodium channel current loss of function in induced pluripotent stem cell-derived cardiomyocytes from a Brugada syndrome patient. *J. Mol. Cell. Cardiol.* 2018, 114, 10–19.
- [92] Cerrone, M.; Lin, X.; Zhang, M.; Agullo-Pascual, E.; Pfenniger, A.; Chkourko Guskys, H.; Novelli, V.; Kim, C.; Tirasawadichai, T.; Judge, D.P.; et al. Missense mutations in plakophilin-2 cause sodium current deficit and associate with a Brugada syndrome phenotype. *Circulation* 2014, 129, 1092–1103.
- [93] Splawski, I.; Shen, J.; Timothy, K.W.; Lehmann, M.H.; Priori, S.; Robinson, J.L.; Moss, A.J.; Schwartz, P.J.; Towbin, J.A.; Vincent, G.M.; et al. Spectrum of mutations in long-QT syndrome genes. *KVLQT1*, *HERG*, *SCN5A*, *KCNE1*, and *KCNE2*. *Circulation* 2000, 102, 1178–1185.
- [94] Chang, Y.S.; Yang, Y.W.; Lin, Y.N.; Lin, K.H.; Chang, K.C.; Chang, J.G. Mutation Analysis of *KCNQ1*, *KCNH2* and *SCN5A* Genes in Taiwanese Long QT Syndrome Patients. *Int. Heart. J.* 2015, 56, 450–453.
- [95] Yang, P.; Koopmann, T.T.; Pfeufer, A.; Jalilzadeh, S.; Schulze-Bahr, E.; Kaab, S.; Wilde, A.A.; Roden, D.M.; Bezzina, C.R. Polymorphisms in the cardiac sodium channel promoter displaying variant *in vitro* expression activity. *Eur. J. Hum. Genet.* 2008, 16, 350–357.
- [96] Makita, N.; Behr, E.; Shimizu, W.; Horie, M.; Sunami, A.; Crotti, L.; Schulze-Bahr, E.; Fukuhara, S.; Mochizuki, N.; Makiyama, T.; et al. The E1784K mutation in *SCN5A* is associated with mixed clinical phenotype of type 3 long QT syndrome. *J. Clin. Invest.* 2008, 118, 2219–2229.
- [97] Veltmann, C.; Barajas-Martinez, H.; Wolpert, C.; Borggrefe, M.; Schimpf, R.; Pfeiffer, R.; Caceres, G.; Burashnikov, E.; Antzelevitch, C.; Hu, D. Further Insights in the Most Common *SCN5A* Mutation Causing Overlapping Phenotype of Long QT Syndrome, Brugada Syndrome, and Conduction Defect. *J. Am. Heart Assoc.* 2016, 5, e003379.
- [98] Remme, C.A.; Scicluna, B.P.; Verkerk, A.O.; Amin, A.S.; van Brunschot, S.; Beekman, L.; Deneer, V.H.; Chevalier, C.; Oyama, F.; Miyazaki, H.; et al. Genetically determined differences in sodium current characteristics modulate conduction disease severity in mice with cardiac sodium channelopathy. *Circ. Res.* 2009, 104, 1283–1292.
- [99] Remme, C.A.; Verkerk, A.O.; Nuyens, D.; van Ginneken, A.C.; van Brunschot, S.; Belterman, C.N.; Wilders, R.; van Roon, M.A.; Tan, H.L.; Wilde, A.A.; et al. Overlap syndrome of cardiac sodium channel disease in mice carrying the equivalent mutation of human *SCN5A-1795insD*. *Circulation* 2006, 114, 2584–2594.

- [100] Veldkamp, M.W.; Viswanathan, P.C.; Bezzina, C.; Baartscheer, A.; Wilde, A.A.; Balsler, J.R. Two distinct congenital arrhythmias evoked by a multidysfunctional Na⁽⁺⁾ channel. *Circ. Res.* 2000, 86, E91–E97.
- [101] Hu, D.; Barajas-Martinez, H.; Pfeiffer, R.; Dezi, F.; Pfeiffer, J.; Buch, T.; Betzenhauser, M.J.; Belardinelli, L.; Kählig, K.M.; Rajamani, S.; et al. Mutations in *SCN10A* are responsible for a large fraction of cases of Brugada syndrome. *J. Am. Coll. Cardiol.* 2014, 64, 66–79.
- [102] Zhang, L.; Zhou, F.; Huang, L.; Wu, Q.; Zheng, J.; Wu, Y.; Yin, K.; Cheng, J. Association of common and rare variants of *SCN10A* gene with sudden unexplained nocturnal death syndrome in Chinese Han population. *Int. J. Legal Med.* 2017, 131, 53–60.
- [103] Fukuyama, M.; Ohno, S.; Makiyama, T.; Horie, M. Novel *SCN10A* variants associated with Brugada syndrome. *Europace* 2016, 18, 905–911.
- [104] Monasky, M.M.; Micaglio, E.; Vicedomini, G.; Locati, E.T.; Ciconte, G.; Giannelli, L.; Giordano, F.; Crisa, S.; Vecchi, M.; Borrelli, V.; et al. Comparable clinical characteristics in Brugada syndrome patients harboring *SCN5A* or novel *SCN10A* variants. *Europace* 2019, 21, 1550–1558.
- [105] Behr, E.R.; Savio-Galimberti, E.; Barc, J.; Holst, A.G.; Petropoulou, E.; Prins, B.P.; Jabbari, J.; Torchio, M.; Berhet, M.; Mizusawa, Y.; et al. Role of common and rare variants in *SCN10A*: Results from the Brugada syndrome QRS locus gene discovery collaborative study. *Cardiovasc. Res.* 2015, 106, 520–529.
- [106] Zhu, W.; Voelker, T.L.; Varga, Z.; Schubert, A.R.; Nerbonne, J.M.; Silva, J.R. Mechanisms of noncovalent beta subunit regulation of NaV channel gating. *J. Gen. Physiol.* 2017, 149, 813–831.
- [107] Watanabe, H.; Koopmann, T.T.; Le Scouarnec, S.; Yang, T.; Ingram, C.R.; Schott, J.J.; Demolombe, S.; Probst, V.; Anselme, F.; Escande, D.; et al. Sodium channel beta1 subunit mutations associated with Brugada syndrome and cardiac conduction disease in humans. *J. Clin. Invest.* 2008, 118, 2260–2268.
- [108] Sen-Chowdhry, S.; Syrris, P.; McKenna, W.J. Genetics of right ventricular cardiomyopathy. *J. Cardiovasc. Electrophysiol.* 2005, 16, 927–935.
- [109] Elliott, P.M.; Anastakis, A.; Asimaki, A.; Basso, C.; Bauce, B.; Brooke, M.A.; Calkins, H.; Corrado, D.; Duru, F.; Green, K.J.; et al. Definition and treatment of arrhythmogenic cardiomyopathy: An updated expert panel report. *Eur. J. Heart Fail.* 2019, 21, 955–964.
- [110] Huang, L.; Tang, S.; Peng, L.; Chen, Y.; Cheng, J. Molecular Autopsy of Desmosomal Protein Plakophilin-2 in Sudden Unexplained Nocturnal Death Syndrome. *J. Forensic Sci.* 2016, 61, 687–691.
- [111] Kim, C.; Wong, J.; Wen, J.; Wang, S.; Wang, C.; Spiering, S.; Kan, N.G.; Forcales, S.; Puri, P.L.; Leone, T.C.; et al. Studying arrhythmogenic right ventricular dysplasia with patient-specific iPSCs. *Nature* 2013, 494, 105–110.
- [112] Nademanee, K.; Raju, H.; de Noronha, S.V.; Papadakis, M.; Robinson, L.; Rothery, S.; Makita, N.; Kowase, S.; Boonmee, N.; Vitayakritsirikul, V.; et al. Fibrosis, Connexin-43, and Conduction Abnormalities in the Brugada Syndrome. *J. Am. Coll. Cardiol.* 2015, 66, 1976–1986.
- [113] Corrado, D.; Zorzi, A.; Cerrone, M.; Rigato, I.; Mongillo, M.; Bauce, B.; Delmar, M. Relationship Between Arrhythmogenic Right Ventricular Cardiomyopathy and Brugada Syndrome: New Insights from Molecular Biology and Clinical Implications. *Circ. Arrhythm. Electrophysiol.* 2016, 9, e003631.
- [114] Abriel, H. Cardiac sodium channel Na(v)1.5 and interacting proteins: Physiology and pathophysiology. *J. Mol. Cell. Cardiol.* 2010, 48, 2–11.
- [115] Moncayo-Arlandi, J.; Brugada, R. Unmasking the molecular link between arrhythmogenic cardiomyopathy and Brugada syndrome. *Nat. Rev. Cardiol.* 2017, 14, 744–756.
- [116] Vermij, S.H.; Abriel, H.; van Veen, T.A. Refining the molecular organization of the cardiac intercalated disc. *Cardiovasc. Res.* 2017, 113, 259–275.
- [117] Agullo-Pascual, E.; Cerrone, M.; Delmar, M. Arrhythmogenic cardiomyopathy and Brugada syndrome: Diseases of the connexome. *FEBS Lett.* 2014, 588, 1322–1330.

- [118] Catalano, O.; Antonaci, S.; Moro, G.; Mussida, M.; Frascaroli, M.; Baldi, M.; Cobelli, F.; Baiardi, P.; Nastoli, J.; Bloise, R.; et al. Magnetic resonance investigations in Brugada syndrome reveal unexpectedly high rate of structural abnormalities. *Eur. Heart J.* 2009, 30, 2241–2248.
- [119] Coronel, R.; Casini, S.; Koopmann, T.T.; Wilms-Schopman, F.J.; Verkerk, A.O.; de Groot, J.R.; Bhuiyan, Z.; Bezzina, C.R.; Veldkamp, M.W.; Linnenbank, A.C.; et al. Right ventricular fibrosis and conduction delay in a patient with clinical signs of Brugada syndrome: A combined electrophysiological, genetic, histopathologic, and computational study. *Circulation* 2005, 112, 2769–2777.
- [120] Veerman, C.C.; Kosmidis, G.; Mummery, C.L.; Casini, S.; Verkerk, A.O.; Bellin, M. Immaturity of human stem-cell-derived cardiomyocytes in culture: Fatal flaw or soluble problem? *Stem Cells Dev.* 2015, 24, 1035–1052.
- [121] Van den Berg, C.W.; Okawa, S.; Chuva de Sousa Lopes, S.M.; van Iperen, L.; Passier, R.; Braam, S.R.; Tertoolen, L.G.; del Sol, A.; Davis, R.P.; Mummery, C.L. Transcriptome of human foetal heart compared with cardiomyocytes from pluripotent stem cells. *Development* 2015, 142, 3231–3238.
- [122] Devalla, H.D.; Schwach, V.; Ford, J.W.; Milnes, J.T.; El-Haou, S.; Jackson, C.; Gkatzis, K.; Elliott, D.A.; Chuva de Sousa Lopes, S.M.; Mummery, C.L.; et al. Atrial-like cardiomyocytes from human pluripotent stem cells are a robust preclinical model for assessing atrial-selective pharmacology. *EMBO Mol. Med.* 2015, 7, 394–410.
- [123] Protze, S.I.; Liu, J.; Nussinovitch, U.; Ohana, L.; Backx, P.H.; Gepstein, L.; Keller, G.M. Sinoatrial node cardiomyocytes derived from human pluripotent cells function as a biological pacemaker. *Nat. Biotechnol.* 2017, 35, 56–68.
- [124] Nugraha, B.; Buono, M.F.; von Boehmer, L.; Hoerstrup, S.P.; Emmert, M.Y. Human Cardiac Organoids for Disease Modeling. *Clin. Pharmacol. Ther.* 2019, 105, 79–85.
- [125] Sung, J.H.; Wang, Y.I.; Narasimhan Sriram, N.; Jackson, M.; Long, C.; Hickman, J.J.; Shuler, M.L. Recent Advances in Body-on-a-Chip Systems. *Anal. Chem.* 2019, 91, 330–351.
- [126] Iseoka, H.; Miyagawa, S.; Fukushima, S.; Saito, A.; Masuda, S.; Yajima, S.; Ito, E.; Sougawa, N.; Tekeda, M.; Harada, A.; et al. Pivotal Role of Non-cardiomyocytes in Electromechanical and Therapeutic Potential of Induced Pluripotent Stem Cell-Derived Engineered Cardiac Tissue. *Tissue Eng. Part A* 2018, 24, 287–300.
- [127] Goldfracht, I.; Efrain, Y.; Shinnawi, R.; Kovalev, E.; Huber, I.; Gepstein, A.; Arbel, G.; Shaheen, N.; Tiburcy, M.; Zimmermann, W.H.; et al. Engineered heart tissue models from hiPSC-derived cardiomyocytes and cardiac ECM for disease modeling and drug testing applications. *Acta Biomater.* 2019, 92, 145–159.
- [128] Goldfracht, I.; Protze, S.; Shiti, A.; Setter, N.; Gruber, A.; Shaheen, N.; Nartiss, Y.; Keller, G.; Gepstein, L. Generating ring-shaped engineered heart tissues from ventricular and atrial human pluripotent stem cell-derived cardiomyocytes. *Nat. Commun.* 2020, 11, 75.
- [129] Giacomelli, E.; Bellin, M.; Sala, L.; van Meer, B.J.; Tertoolen, L.G.; Orlova, V.V.; Mummery, C.L. Three-dimensional cardiac microtissues composed of cardiomyocytes and endothelial cells co-differentiated from human pluripotent stem cells. *Development* 2017, 144, 1008–1017.
- [130] Sala, L.; Bellin, M.; Mummery, C.L. Integrating cardiomyocytes from human pluripotent stem cells in safety pharmacology: Has the time come? *Br. J. Pharmacol.* 2017, 174, 3749–3765.
- [131] Fermini, B.; Hancox, J.C.; Abi-Gerges, N.; Bridgland-Taylor, M.; Chaudhary, K.W.; Colatsky, T.; Correll, K.; Crumb, W.; Damiano, B.; Erdemli, G.; et al. A New Perspective in the Field of Cardiac Safety Testing through the Comprehensive In Vitro Proarrhythmia Assay Paradigm. *J. Biomol. Screen.* 2016, 21, 1–11.
- [132] Colatsky, T.; Fermini, B.; Gintant, G.; Pierson, J.B.; Sager, P.; Sekino, Y.; Strauss, D.G.; Stockbridge, N. The Comprehensive in Vitro Proarrhythmia Assay (CiPA) initiative—Update on progress. *J. Pharmacol. Toxicol. Methods* 2016, 81, 15–20.

1.10 Supplementary material

Supplementary Table 1-1 Overview of the used reprogramming and differentiation approaches, together with described genetic variants, their identification methods and connected clinical phenotypes and patient history. FB- fibroblasts; Sev – Sendai virus; Retro – retroviral vector; Lenti – lentiviral vector; Episomal – episomal vectors; ML – monolayer-based; EB – EB-based; SC – suspension culture; MxS – matrix sandwich); - G – glucose starvation; LT – lactate treatment; Puro αMHC - puromycin selection of αMHC-Puro containing spheres; M – male; F – female

Reference	Reprogramming		Differentiation				Genetic diagnosis			Patient information			
	Cell type	Vector	Method	Agents	Enrichment	Culture period [days]	Gene	Variant	Method of identification	Sex	Diagnosis	Clinical phenotype	Family history
89	FB	Sev	ML	Activin A, BMP4, CHIR-90021, Xav939 in BPEL medium	N/A	28-32	SCN5A	c.4912C>T (p.R1638X)	Diagnostic screening	M	BrS	34-year old; BrS type 1 ECG and ventricular tachyarrhythmias during electrophysiological investigations	N/A
								c.468G>A (p.W156X)					
68	FB	Sev	ML	CHIR99021, IWR-1	-G	40-60	SCN5A	c.2053G>A (p.R620H) and c.2626G>A (p.R811H)	Diagnostic screening	M	BrS	44 year old; unstable ventricular tachycardia after multiple episodes of recurrent syncope. BrS diagnosis based on BrS type-1 ECG pattern at rest	Sudden death in two paternal uncles and a female cousin
								c.4189delT 4190ΔA/1397 Δ(frameshift)					
90	FB	Retro	ML	CHIR99021, IWR-1	LT	35-45	SCN5A	c.677C>T (p.A226V) and c.4885C>T (p.R1629X)	Genetic screening of SCN5A gene	M	BrS	21-year old, presented with syncopal events since the age of 11 during exercise. Baseline ECG with BrS type-2 pattern and first-degree atrioventricular block and QRS duration of 130 ms. Treadmill testing ECG showed a QRS widening up to 240 ms and a BrS type-1 ECG pattern followed by polymorphic ventricular tachycardia.	Father - p.A226V with ajmaline induced type-1 ECG pattern. Mother - p.R1629X carrier asymptomatic, with baseline ECG showing first-degree AV block at 250 ms, with prolonged QRS duration of 130 ms and a saddle shaped ST elevation in V2 lead. Treadmill challenge revealed QRS prolongation up to 160 ms with no BrS characteristics. Healthy SCN5A variants negative brother and asymptomatic p.A226V carrier sister.
91	FB	Episomal	EB	END-2 conditioned media	N/A	22-31	SCN5A	c.1100G>A (p.R367H)	Familial Arrhythmia Network of Scotland	M	BrS	69-year old; classical ST-segment elevation in the ECG	N/A
			ML	CHIR99021, heparin, IWP2									

56	FB	Retro	SC	CHIR99021, IWP2	N/A	20-46	SCNSA	c.2204C>T (p.A735V)	N/A	N/A	BrS	BrS diagnosis in cases from four different clinical centres	One familial case with multiple mutation carriers with variable phenotypes
			ML										
88	FB	Lenti	EB	END-2 cells co-culture	N/A	50	SCNSA	c.5537insTGA (p.1795insD)	Mutation analysis of SCNSA	M	LQTS3/BrS	Bradycardia, ventricular and atrial conduction slowing, including diagnosed cases of BrS and LQTS	Dutch founder mutation, identified in a large family with multiple individuals presenting variable symptoms
86	FB	Retro	EB	Wnt3a	N/A	30	SCNSA	c.5349G>A (p.E1784K)	Genetic screening of SCNSA gene	M	LQTS3/BrS	20-year old; sudden cardiac arrest while driving a car, successfully resuscitated by external defibrillator, which indicated ventricular fibrillation, while surface ECG showed QT interval prolongation. Piisicalinide administration unmasked coved-shaped ST segment elevation.	No family history of previous syncope or significant QT interval abnormalities
69	FB	Lenti	ML	CHIR99021, IWP2	LT	40-60	SCN10A	c.3749G>A (p.R1250Q) and c.3808G>A (p.R1268Q)	Genetic screening of 8 BrS-associated genes	M	BrS	SCD during ajmaline challenge, no structural abnormalities of the heart	No history of SCD
		Episomal											
		SeV											
70	FB	Lenti	ML	CHIR99021, IWP2	LT	40-60	SCN1B	c.629T>C (p.L210P) and c.637C>A (p.P213T)	Genetic screening of 8 BrS candidate genes	M	BrS	Syncope at rest with BrS type 1 ECG in ajmaline challenge	No history of SCD; mutations carrier son with asymptomatic BrS
		Episomal											
		SeV											
71	FB	SeV	ML (MxS)	tivin A, BMP4, bFGF	N/A	31-35	RRAD	p.Arg211His	WES	M	BrS	Systematic ECG with typical but labile BrS type 1 ECG pattern with a history of palpitations associated with a near syncope and nocturnal agonal respiration. Treated with an ICD implantation	Identification of 4 affected relatives after flecainide challenge and one with BrS type 1 ECG pattern. No relevant symptoms observed in all of those individuals. History of unexplained SCD in probands' 41-year old uncle. RRAD variant present in all affected individuals (4) and 2 unaffected family members.
92	FB	Lenti	EB	Activin A, BMP4, bFGF, DKK1, VERGF, SB-431542	Puro aMHC	60	PKP2	R635Q (c.1904G>A)	Retrospective WES	M	BrS	31-year old; two episodes of syncope at rest with spontaneous BrS type-1 ECG. Implanted ICD with no shocks at follow up	Symptomatic grandfather with sudden death during sleep. Affected mutation-positive father with a history of syncope at rest. Mutation carrier brother with a positive flecainide test

87	FB	Lenti STEMCCA	EB	KY02111, XAV939	LT	42-56	Undefined		NGS sequencing of 12 BrS and 26 arrhythmia- related genes	M	BrS	28-years old; VF arrest at 16-years old, spontaneous BrS-type 1 ECG	Father presenting similar ECG
							Undefined			M	BrS	30-years old; ajmaline induced BrS-type 1 ECG, occasional spontaneous	N/A
							PKP2	c.302G>A (p.R101H)		M	BrS	68-years old; ajmaline induced BrS-type 1 ECG leading to VF; occasional spontaneous	N/A
55	FB	Lenti STEMCCA	ML	CHIR99021, IWP- 4	LT	19	Undefined		Genetic screening of BrS- associated genes	M	BrS	42-year olds; spontaneous BrS type 1 ECG, previous story of syncope, no structural cardiac abnormalities	3 relatives with ajmaline induced BrS ECGs with no history of SCD
							Undefined			M	BrS	67-year old; spontaneous BrS type 1 ECG, previous story of syncope. Diagnosed with BrS during hospital admission for an inferior myocardial infarction	6 relatives with ajmaline induced BrS ECGs, several family members with previous history of SCD
							CACNA1C	int19 position -7		F	BrS	24-year old; spontaneous BrS type 1 ECG, previous history of syncope, no structural cardiac abnormalities. Inducible non- sustained ventricular tachycardias in RVOT followed by ICD implantation. PR- interval prolongation (220 ms) with normal ORS- and QTc.	5 relatives with ajmaline induced BrS ECGs with no history of SCD

Supplementary Table 1-2 AP properties published from BrS iPSC-CM models. RMP/MDP – resting membrane potential/maximum diastolic potential; APA – action potential amplitude; APD20/APD50/APD90 – action potential duration at 20/50/90 % of depolarization; Vmax- upstroke velocity; RT -room temperature.

Reference	Cell line	AP properties										Protocol	In silico I _{K1} injection
		RMP/MDP [mV]	APA [mV]	Overshoot [mV]	APD20 [ms]	APD30 [ms]	APD50 [ms]	APD90 [ms]	Vmax [v/s]	peak to peak duration [ms]	n		
89	hiPSC-CM ^{WT1}	-75±1	105±5				125±20	190±20	56±12		12	Isolated cells recorded on D28-32 of differentiation. APs measured at 37°, elicited at frequency of 1Hz by 3ms	
	hiPSC-CM ^{WT2}	-75±0.5	107±3				205±10	290±15	55±3		12		
	hiPSC-CM ^{R1638X}	-70±0.5	100±2				160±10	205±15	18±2		14		
	hiPSC-CM ^{W156X}	-70±0.5	98±5				150±20	200±20	19±2		16		
68	CON1	-58.9±0.8	106.4±1.0	48.0±0.7				443.5±17.3	15.6±0.8	49.4±5.5	10to25	APs recorded on dissociated cells at day 40-60 at 36-37 degrees	
	CON2												
	BrS1	-58.1±0.7	107.1±1.6	50.1±1.2				459.3±38.2	11.1±0.1	380.4±96.2	10to25		
	BrS2	-56.5±2.0	105.0±2.6	47.8±2.5				396.2±33.4	7.2±1.1	195.5±60.3	10to25		
	BrSp2-GE	-64.2±1.0	109.3±1.5	46.1±0.9				355.8±19.3	17.4±1.2	48.4±7.4	10to25		
90	CON1	- 43.39±2.81	87.5±5.76				204.09±44.01	362.09±56.35	473.64±63.97	17.76±4.59	37.83±5.81	APs recorded at day 35-45 of differentiation at 34°C	Generated in real time in response to CM membrane potential; potentiometer was set to provide a
	BrS_A266V+R1629X	- 49.09±6.12	91.16±8.09				277.46±48.5	430.82±60.84	493.18±62	15.76±4.59	32.57±7.92		
	BrS_A266V+R1629X 1.0 Hz	- 57.83±0.32	73.30±1.53				92.08±5.18	166.10±4.77	221.24±8.58	10.72±0.32	3		

BrS_A266V+R162 9X 1.5 Hz	- 57.87±1.5 4	74.12±0.9 3		88.61±1.82		153.60±5.87	209.77±9.63	9.21±0.09		3	standard outward current peaked at 150 pA at -75 mV
BrS_A266V+R162 9X 0.5 Hz	- 60.72±2.0 2	69.00±1.5 5		95.00±4.82		164.66±9.2	216.36±12.1	14.05±1.8 7		3	
BrS_A266V+R162 9X 0.2 Hz	- 53.52±3.1 7	64.10±5.3 5		87.37±7.43		166.30±6.97	221.25±10.3 1	13.21±0.0 2		3	
CON1 with I _{K1} injection	-84.2±0.4	128.6±1.3	44.4±1.0	126.3±14.2		297.2±25	339.2±26.8	185.1±11		22	
BrS_A266V+R162 9X with I _{K1} injection	-84.4±0.2	115.6±0.9	31.3±0.9	223.8±12.3		318.2±13.9	338±14.3	41.9±5.3		45	
CON1 with I _{K1} injection 1 Hz	-84.2±0.2	128.0±1.4	43.8±1.1	142.6±18.8		302.9±32.8	348.2±31.7	178.9±12. 3		19	
CON1 with I _{K1} injection 0.5 Hz	-84.3±0.2	129.9±1.3	45.5±1.0	186.0±32.6		381.7±53.0	426.3±52.6	193.8±13. 0		19	
CON1 with I _{K1} injection 0.2 Hz	-84.4±0.2	129.9±1.3	45.5±1.1	133.6±46.5		328.4±65.2	367.2±65.1	197.3±13. 9		19	
BrS_A266V+R162 9X with I _{K1} injection non-ER 1 Hz	-84.2±0.4	115.3±0.9	31.10.9	211.7±13.4		310.9±16.1	331.5±16.6	36.9±5.7		33	
BrS_A266V+R162 9X with I _{K1} injection non-ER 0.5 Hz	-84.5±0.4	117.0±1.0	32.7±1.0	308.6±22.8		424.3±26.8	444.2±27.3	40.7±6.4		33	
BrS_A266V+R162 9X with I _{K1} injection non-ER 0.1 Hz	-84.4±0.4	114.1±1.2	29.7±1.2	284.2±29.8		396.0±35.2	414.6±35.8	42.1±6.8		33	
BrS_A266V+R162 9X with I _{K1} injection ER 1 Hz	-85.0±0.3	116.1±2.7	31.1±2.6	173.8±20.4		249.9±17.7	267.4±17.9	36.4±6.9		11	

BrS_A266V+R162 9X with I _{K1} injection ER 0.5 Hz	-84.5±0.4	112.8±2.9	28.3±2.8	148.3±37.0		214.9±39.7	231.8±40.2	36.5±7.4		11
BrS_A266V+R162 9X with I _{K1} injection ER 0.11 Hz	-81.6±0.9	103.5±4.1	21.9±3.6	31.8±8.7		65.7±10.4	87.6±11.4	35.3±7.0		11
CON2 with I _{K1} injection patched at 24°C 1 Hz			40±2				510±100	110±30		9
CON2 with I _{K1} injection patched at 24°C 0.1 Hz			42±2				600±190	130±30		9
BrS2 p.T1620M with I _{K1} injection patched at 24°C 1 Hz			43±1				370±10	190±20		11
BrS2 p.T1620M with I _{K1} injection patched at 24°C 0.1 Hz			44±1				390±20	205±20		11
BrS2 p.T1620M with I _{K1} injection patched at 34°C 1 Hz			55±4				505±20	380±10		6
BrS2 p.T1620M with I _{K1} injection patched at 34°C 0.1 Hz			56±5				610±90	395±5		6
BrS_A266V+R162 9X with I _{K1} injection 0.1 Hz	-82.9±0.9	107.6±4.6	24.7±4.0	53.1±21.3		116.2±31.5	127.5±29.7	60.7±12.4		9
BrS_A266V+R162 9X with I _{K1} injection 0.1 Hz +0.5 mM 4-AP	-83.6±0.6	114.7±1.4	31.1±1.2	405.9±28.18		551.5±23.1	579.2±23.7	52.0±10.0		9

	BrS_A266V+R162 9X with I _{K1} injection 1 Hz	-84.8±0.4	115.6±2.2	30.8±1.9	199.9±18.7		288.9±19.4	308.5±19.7	31.4±7.7		9		
	BrS_A266V+R162 9X with I _{K1} injection 1 Hz +Flecainide	-85.0±0.3	109.6±2.1	24.6±1.8	104.0±10.5		157.4±12.3	170.9±12.4	12.6±2.7		9		
56	WT (average from both controls)	-70±3	108±4				1802±494		23±7		16	Dissociated cells at 37 degrees patched 20- 46 days after the start of differentiation	0 to -100 pA
	WT with I _{K1} injection (average from both controls)	-82±1	135±4				1250±280		121±13		21		
	WT1								140±12		12		
	WT2								98±10		9		
	MUT1								22±4		32		
	MUT2								41±9		29		
	MUT (average from both mutants)	-65±2	104±2				2274±314		7±1		41		
MUT with I _{K1} injection (average from both mutants)	-82±1	120±2				1350±150		31±5		61			
88	hiPSC-CM control	-72.4±0.9	106±3.2		50.7±6.2		89.8±7.9	173.5±12.2	115.7±18. 4		16	Single CMs, after day 50 of differentiation; data from 4 independent differentiations per line. Recordings on quiescent cells that contracted upon field	
	hiPSC-CM het	-71.3±1.3	103.1±3.2		58.7±5.9		109±10.1	217.2±14.9	57.6±14		13		

												stimulation; recordings performed at 36°C; APs elicited at 1,2 or 3 Hz by 3ms, 1.2x threshold current pulses through the patch pipette; average from 10 consecutive AP waveforms	
86	Control	-65±4	99.3±3.9	34.4±2.5			247.3±30.5	416.7±24	15.8±3.8		10	iPSC-CMs after day 30	
	LQTS/BrS	-60±2.8	97.4±4	37.4±1.8			326.1±74.5	563.7±57.1	21.8±10.8		7		
	corrected	-53.8±1.9	93.1±2.9	39.3±1.2			250.9±40	418±29.6	8.6±1.6		10		
69	Control D1	-82±1	138±4				102±13	290±5	42±3		22	Dissociated cells at D40-60 of differentiation, Patching at RT	Yes
	Control D2	-82±1	140±2				142±18	295±5	39±2		21		
	Control D3	-82±1	130±2				98±13	230±5	38±3		22		
	BrS SCN10A	-81±1	125±2				115±15	285±5	23±2		19		
	Control D1 +3 μM ajmaline	-81±1	140±2				90±12	220±5	43±3		11		
	Control D1 +10 μM ajmaline	-81±1	138±2				80±12	219±5	41±3		11		
	Control D1 +30 μM ajmaline	-81±1	135±2				79±12	219±5	36±3		11		
	BrS SCN10A +3 μM ajmaline	-80±1	120±2				116±15	253±7	25±2		15		
	BrS SCN10A +10 μM ajmaline	-81±1	110±2				125±15	280±7	21±2		15		
	BrS SCN10A +30 μM ajmaline	-81±1	108±2				140±15	305±7	20±1		15		

70	Control D1	-82±1	138±4				102±13	290±5	42±3		22	Dissociated cells at D40-60 of differentiation, Patching at RT	Yes
	Control D2	-82±1	140±2				142±18	295±5	39±2		19		
	Control D3	-82±1	130±2				100±13	285±5	38±3		30		
	BrS	-82±1	103±2				150±20	320±10	28±3		17		
71	Ctl1					150±5	200±10	210±90	14±7	500±100	6	Patched on D31-35 with amphotericin-B on single cells at 37°C; cycle length 700ms	
	BrS1					210±10 0	290±120	400±200	9±7	1100±190 0	16		
	Rad WT					250±60	390±200	400±300	16±29	600±600	7		
	Rad R211H ins					500±11 0	580±120	590±110	10±3	1100±800	7		
87	iPS-HS1M	-58±46	90±35					183.0±17.9	17±10		21	APs recorded at D42-56 of differentiation at 22±2°C	
	iBR1-P5M-L1	-50±10	88±37					125.5±12.4	17±10		17		
55	iCtrl 1	-80	115±2		65±6		120±8	155±8	225±13		30	iPSC-CMs after day 19 at 36°C; APs elicited at 0.5-3 Hz by 3-ms, ~1.2x threshold current pulses; average from 10 consecutive APs	Constant 2pA/pF
	iCtrl 2	-80	110±2		85±5		155±8	190±8	200±13		30		
	iBrS 1	-80	118±2		86±5		150±8	175±8	180±20		28		
	iBrS 2	-80	115±2		55±4		100±5	130±5	195±13		30		
	iBrS 3	-78	118±4		80±5		149±8	177±8	260±15		19		
	iSCN5A	-78	126±2		110±5		180±5	240±20	126±25		22		

Supplementary Table 1-3 I_{Na} properties from published BrS iPSC-CM models. κ – slope factor of activation/inactivation curve; $V_{1/2}$ - mid-point of activation/inactivation; τ_f - fast kinetics; τ_s - slow kinetics; I_{NaL} - late/persistent sodium current density; RT – room temperature

Reference	Cell line	Sodium current properties																	Protocol	
		I_{Na} peak density		Activation			Inactivation				Recovery			I_{NaL}		Cell capacitance				
		pA/pF	n	κ	$V_{1/2}$ [mV]	n	κ	$V_{1/2}$ [mV]	τ_f [ms]	τ_s [ms]	n	τ_f [ms]	τ_s [ms]	n	pA/pF	n	pF	n		
89	hiPSC-CM ^{WT1}	-105±15	11																Recordings at RT; cycle length 5s, -5mV hyperpolarizing step from -50 mV	
	hiPSC-CM ^{WT2}	-102±13	21																	
	hiPSC-CM ^{R1638X}	-30±2	11																	
	hiPSC-CM ^{W156X}	-32±3	10																	
68	CON1	-122.8±31.3	10-25															22.2±4	10-25	I_{Na} recordings at RT; cycle length 40ms; holding potential -80 mV
	CON2																			
	BrS1	-33.7±6.3	10-25															27±1.7	10-25	
	BrS2	-36.8±8.6	10-25															24.9±2.2	10-25	
	BrSp2-GE	-63.0±4.3	10-25															21.9±2.6	10-25	
90	CON1	-245.8±32.7	15	4.94±0.4	-35.72±0.46	15	7.55±0.35	-70.26±0.4			15	19.1±0.05	327.4±0.05	14					Patched at RT; cycle length 5s; holding potential -90 mV	
	BrS_A266V+R1629X	-59.2±8.8	21	4.99±0.49	-40.89±0.56	21	6.38±0.19	-73.37±0.22			15	23.3±0.04	380±0.05	14						
91	Beating bodies Control hiPSC-CM	-78.77±5.16	3	5.57±0.33	-44.15±0.37	3	8.94±1.54	-61.64±0.77			3	5.85±1.01	40.38±4.95	3					Measurements at RT; cycle length 50 ms; holding	
	Beating bodies Patient hiPSC-CM	-42.93±3.86	7	5.86±0.28	-36.73±	7	8.7±0.57	-70.15±			7	2.89±0.35	34.45±14.45	6						

					0.32			2.76											potential -80 mV
	Monolayer Control hiPSC-CM	-45.62± 5.37	11	3.94± 0.14	32.96± 0.79	11	6.7± 0.33	-48.8± 0.79			8	2.58± 0.31	46.17± 7.01	5					
	Monolayer Patient hiPSC-CM	-30.51± 3.09	13	5.58± 0.26	- 25.44± 0.78	13	9.59± 0.24	- 54.69± 1.21			10	1.68± 0.18	20.12± 6.76	5					
56	WT (average from both controls)	-279± 53	20		-58± 0.4	20		-77± 0.3			17	2.4± 0.2	62± 28	17					Measurements at RT; cycle length 3s; holding potential -120 mV
	MUT1	-52± 10	31		-31± 2	31		-85± 2			31								
	MUT2	-96± 15	26		-40± 3	26		-84± 2			25								
	MUT (average from both mutants)	-68± 6	57		-35± 0.5	57		-84± 0.1			57	2.7± 0.3	301± 46	57					
88	hiPSC-CM control	-264.4± 57	13												0.5± 0.1	9	36± 3.3	13	Measurements at RT; cycle length 5s; holding potential -90 mV
	hiPSC-CM het	-121.4± 23.8	13												1.8± 0.2	9	31.7± 3.2	13	
86	Control	-200± 10	22												1.8± 0.2	22			Measurements at RT, at rate 0.33 Hz, holding potential of -100 mV
	LQTS/BrS	-180± 20	21												2.5± 0.25	21			
	Control in second experiment with corrected iPSC-CMs	-100± 25	6												0.3± 0.05	6			
	LQTS/BrS in second experiment with corrected iPSC-CMs	-80± 10	13												0.8± 0.1	7			
	corrected	-65± 10	7												0.1± 0.1	13			
69	Control D1	-116.9± 28.7	25												-2.6± 0.3 / inhibited -1.1± 0.1	10/ 10			Measurements at RT; cycle length 4s; holding

	Control D2	-95.4 ± 41.6	12												-2.8 ± 0.4 / inhibited -0.7 ± 0.2	15/24			potential -100 mV	
	Control D3	-94.7 ± 28.3	11												-3.2 ± 0.8 / inhibited -1 ± 0.2	10/10				
	BrS SCN10A	-54.7 ± 9.4	37												-1.1 ± 0.1 / inhibited -0.6 ± 0.1	17/20				
70	Control D1	-116.9 ± 28.7	25		-53.2 ± 2.1	25		-73.3 ± 2.3			25	22 ± 8		25	-0.4 ± 0.06	12			Measurements at RT; cycle length 4s; holding potential -100 mV	
	Control D2	-95.4 ± 41.6	12		-43.3 ± 2.1	12		-80.6 ± 1.5			12	20 ± 2		12	-0.4 ± 0.08	16				
	Control D3	-94.7 ± 28.3	11		-45.1 ± 4.1	11		-77.9 ± 2.6			11	22 ± 2		11	-0.3 ± 0.006	14				
	BrS	-19.3 ± 3.7	22		-37.8 ± 1.8	22		-88.1 ± 1.8			22	75 ± 15		22	-0.2 ± 0.03	14				
71	Ctl1	-58.8 ± 16.5	17	5.3 ± 0.2	-39.4 ± 1.3	17	5.3 ± 0.1	-83.4 ± 1.3	1.1 ± 0.1	2.9 ± 0.3	9	9.7 ± 0.6	109.1 ± 6.8	13	0 ± 1	7	45.7 ± 22.8	51	Measurements at RT; cycle length 50 ms; holding potential -120 mV	
	BrS1	-36.8 ± 16.7	42	5.2 ± 0.2	-36.1 ± 0.7	42	4.5 ± 0.6	-82.9 ± 0.8	1.2 ± 0.1	3.5 ± 0.2	20	6.7 ± 0.4	93.6 ± 3.3	33	-3 ± 5	40	55.5 ± 25.5	68		
	Rad WT	-56.8 ± 35.0	18	7.4 ± 0.1	-34.8 ± 0.6	9	6.9 ± 0.1	-83.3 ± 1.2			9									
	Rad R211H ins	-30.3 ± 14.2	14	8.4 ± 0.1	-28.1 ± 0.4	10	5.7 ± 0.2	-82.7 ± 1.5			10									
92	H9 hESC-CMs	-100 ± 60	7																Measurements at RT; 200 ms pulses; holding potential -120 mV	
	AC patient iPSC-CMs	-20 ± 50	8																	
	AC patient iPSC-CMs + PKP2 WT	-40 ± 20	8																	

	AC patient iPSC-CMs + PKP2-R635Q	-25±15	10																
87	iPS-HS1M	-110±18.7	15																I _{Na} recordings at RT; cycle length 3 s; holding potential -90 mV
	iPS-HS1M +100 μM ajmaline	-15.4±4.4	15																
55	iCtrl 1	-93.6±84.9	36	6.9±0.1	-34.6±0.5	26	6.48±0.2	-78.9±1.4			15	1.5±0.1	5.2±0.5	36					Measurements at RT; cycle length 5s; holding potential -100 mV
	iCtrl 2	-83±83.3	31	7±0.2	-33±0.9	20	7.05±0.3	-85±1			11	1.5±0.1	5.9±0.7	33					
	iBrS 1	-81.7±73.25	37	6.6±0.1	-33.5±0.5	25	6.6±0.2	-83.6±0.9			15	1.52±0.1	6.4±0.7	37					
	iBrS 2	-96.8±70.5	28	7±0.2	-34.7±0.7	20	6.6±0.2	-84.5±1			10	1.55±0.1	7.2±1	31					
	iBrS 3	-151.7±208.5	31	7.2±0.2	-32.1±0.6	29	6.83±0.2	-80±0.9			13	1.68±0.2	7.3±0.8	32					
	iSCN5A	-38.7±55.03	25	6.7±0.2	-31.8±0.9	20	6.9±0.2	-83.7±0.8			10	2.55±0.2	16.5±2	25					

Supplementary Table 1-4 Calcium current (I_{CaL}) properties from published BrS iPSC-CMs. $V_{1/2}$ – mid-point of activation/inactivation; κ – slope factor of activation/inactivation curve; τ_f - fast kinetics; τ_s - slow kinetics; RT – room temperature.

Reference ID nr	Cell line	I_{CaL} properties								Protocol	
		Peak		Activation			Inactivation				
		pA/pF	n	$V_{1/2}$ [mV]	κ	n	τ_f [ms]	τ_s [ms]	$V_{1/2}$ [mV]		n
56	WT (average from both controls)	-5.8±0.5	19							Not specified	
	MUT (average from both mutants)	-8±1	57								
69	Control D1	-9.9 ±1.7	18	-7 ±1.8					-36 ±2.1	18	measurements at RT
	Control D2	-10.1 ±2.8	11	-6.6 ±1.3					-36.2 ±2.2	11	
	Control D3	-6.5 ±1.3	11	-5.5 ±1.5					-34.6 ±1.3	11	
	BrS SCN10A	-3.4 ±1.5	12	12.3 ±4.1					-47.1 ±3.2	12	
70	D1	-8.0±1.4	20	-7±2		20		15±5	-35±2	20	Not specified
	D2	-8.4±1.9	18	-6.5±1.5		18		13±6	-35±3	18	
	D3	-6.5±1.3	11	-5,9±1,1		11		11±5	-33±2	11	
	BrS	-7.4±2.4	13	-5±5.2		12		33±8	-33±9	13	
71	Ctrl1	-26.3±7.1	34	-18.6±0.6	5.5±0.1	34					Not specified
	BrS1	-18.9±6.0	24	-18.6±0.6	5.8±0.1	24					
	Rad WT	-6.1±1.7	6	-14.1±0.6	6.7±0.4	6					
	Rad R211H ins	-1.7±0.5	8	-11.2±0.6	6.2±0.3	8					
55	iCtrl 1	-52±3	21				4.0±0.2	18.2±0.8			measurements at 36°C; cycle lengths 2s
	iCtrl 2	-58±3	21				3.7±0.2	21.5±1.3			
	iBrS 2	-60±3	19				3.6±0.3	21.5±1.4			

Supplementary Table 1-5 Calcium transient properties from published BrS iPSC-CMs. CTD50/75 – calcium transient duration at 50/75% of depolarization.

Reference ID nr	Cell line	CT properties						Protocol
		CTD50 [ms]	CTD 75 [ms]	Beat interval [ms]	Rise rate [ms]	Amplitude [mV]	n	
68	CON1	471.3±12.6		108.3±20.4	92.0±6.6	6±0.3	10-25	CT measured on dissociated cells with 5 μM Fluo-4 AM and 0.02% Pluronic F-127 at 37°C.
	CON2							
	BrS1	1362.7±124.6		1894.7±436.5	10.3±0.9	2.6±0.2	10-25	
	BrS2	541.5±60.2		313.3±59.1	45.2±4.7	2.3±0.2	10-25	
	BrSp2-GE	589.3±27.4		190.7±24.6	72.7±5.0	4.7±0.1	10-25	
71	Ctl1		500±150				5	CT measured on single CMs at 37°C.
	BrS1		790±180				7	
	Rad WT		390±400				22	
	Rad R211H ins		590±400				27	

Supplementary Table 1-6 Field potential properties from published BrS iPSC-CMs. FPD – field potential duration; BPM – beats per minute.

Reference ID	Cell line	FPD						Protocol
		Baseline [ms]	100 nM ajmaline [ms]	1 μ M ajmaline [ms]	10 μ M ajmaline [ms]	100 μ M ajmaline [ms]	Beating rate [BPM]	
86	Control	210 \pm 5					65 \pm 17	Not specified
	LQTS/BrS	350 \pm 50					59 \pm 6	
87	iPS-HS1M	322.3 \pm 19.1	326.0 \pm 19.3	334.4 \pm 19.0	379.8 \pm 29.4	462.1 \pm 47.4		Sampling frequency 10 kHz at 37°C. One minute baseline recordings were taken after minimum 15 min superfusion of basal media, and 1 min drug recordings were taken after 6 min superfusion.
	iBR1-P5M-L1	319.6 \pm 12.8	327.4 \pm 13.6	352.1 \pm 12.6	385.7 \pm 13.3	415.2 \pm 26.1		
	iBR1-P5M-L9	281.3 \pm 15.0	307.7 \pm 13.8	328.7 \pm 15.0	364.8 \pm 16.4	418.7 \pm 23.1		
	iBR1-P3M-N2 (PKP2-R101H)	395.5 \pm 10.9	439.3 \pm 7.9	448.0 \pm 13.9	505.0 \pm 21.8	596.6 \pm 19.5		
	iBR1-P6M-L1	385.4 \pm 32.9	410.1 \pm 32.8	428.7 \pm 29.7	484.0 \pm 30.1	553.0 \pm 27.0		

Supplementary Table 1-7 Ito properties from published BrS iPSC-CMs. V1/2- mid-point of inactivation

Reference ID	Cell line	I _{to} properties					Protocol
		Peak		Inactivation			
		pA/pF	n	Time constant [ms]	V _{1/2}	n	
56	WT (average from both controls)	15±1	18				Not specified
	MUT (average from both mutants)	6±1	59				
70	Control D1	2.7±0.4					Not specified
	Control D2	1.9±0.6					
	BrS	1.7±0.4					
55	iCtrl 1	14.5±2	13	28.1±4.6		13	Measurements at 36 °C; cycle length 10s
	iCtrl 2	11.5±2	13	26±5		13	
	iBrS 2	14.5±2.5	13	27.1±3.3		13	

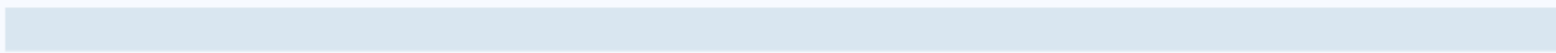
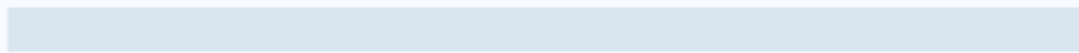
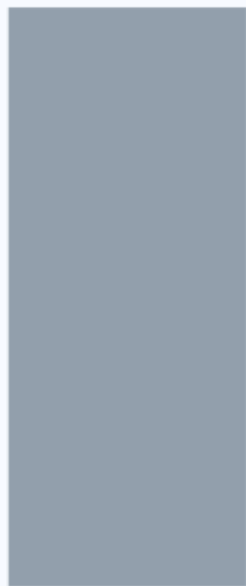
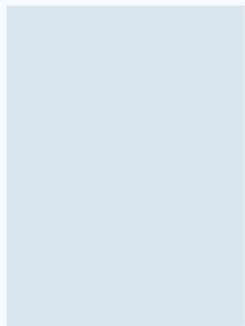
Supplementary Table 1-8 IKr properties from published BrS iPSC-CMs.

Reference ID	Cell line	Peak I _{Kr}				Protocol
		pA/pF	n	pA/pF +100 μM ajmaline	n	
70	Control D1	2.5±0.25	19			Not specified
	Control D2	2.2±0.4	11			
	BrS	1.1±0.2	13			
87	iPS-HS1M	1.7±0.2	8	0.7±0.1	8	Not specified

Supplementary Table 1-9 IKs properties from published BrS iPSC-CMs.

Reference ID	Cell line	Peak I _{Ks}		Protocol
		pA/pF	n	
64	Control D1	1.2±0.2	21	Not specified
	Control D2	1.25±0.25	14	
	BrS SCN10A	0.3±0.2	7	
65	Control D1	0.7±0.2	16	Not specified
	Control D2	0.7±0.3	13	
	Control D3	N/A		
	BrS	0.1±0.09	10	

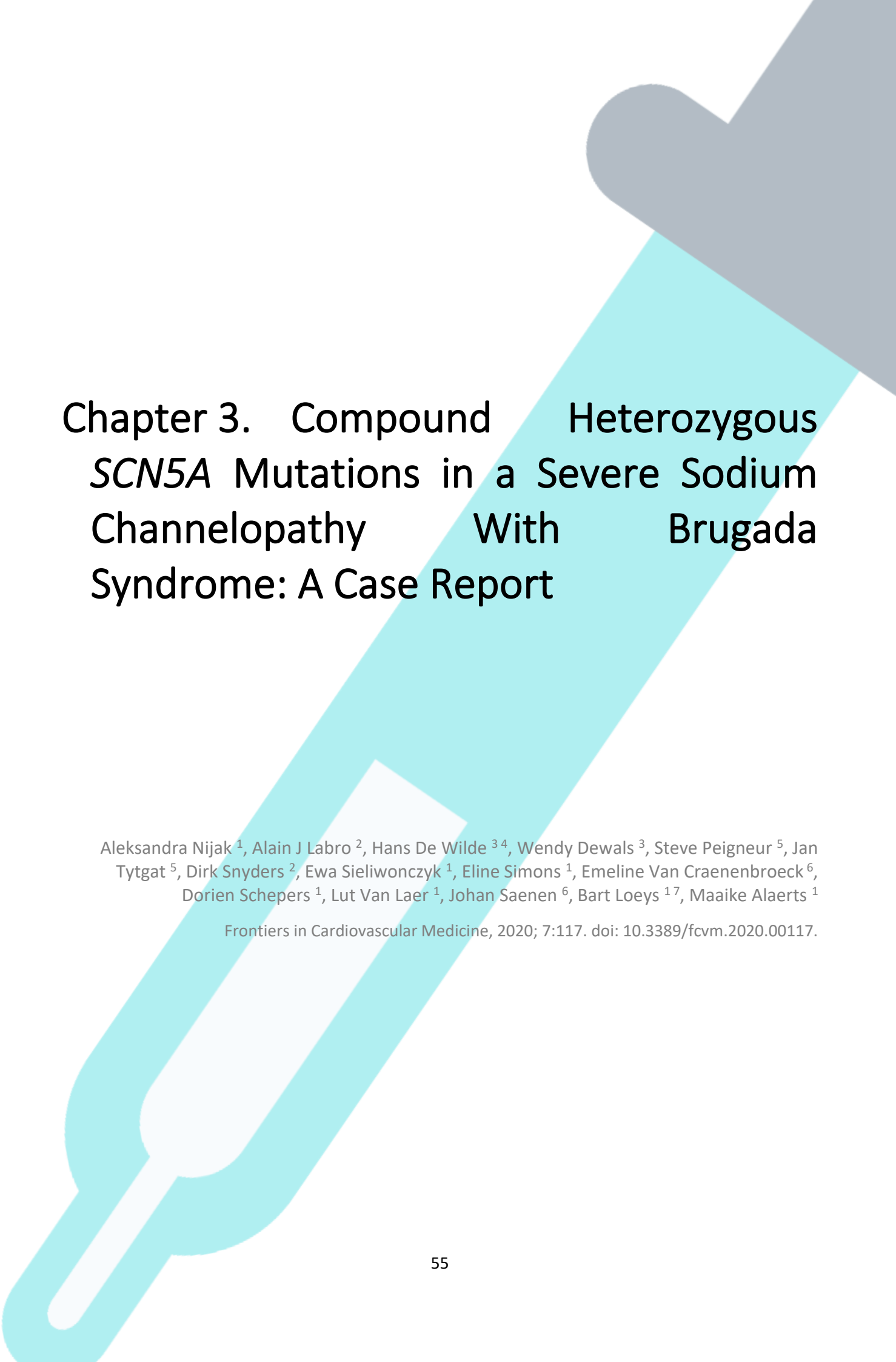
Chapter 2. Aim of the thesis



Brugada syndrome (BrS) disease can stay unnoticed until an event of a sudden cardiac death (SCD), which is predominantly reported in young adults (41±15 years old), who often do not experience any prior symptoms. Contemporary knowledge about the pathomechanisms underlying BrS development is limited and about 70% of the BrS patients remain genetically undiagnosed. Over 20 genes have so far been reported to be involved in BrS development, however, no suitable pharmacological therapies were proposed. Unravelling the genetic basis of the so far unresolved Brugada syndrome cases is of a great importance to contribute to new knowledge on disease mechanisms and potential therapeutic targets and as such formed the general aim of this thesis.

We intend to contribute to this general aim by pursuing the following objectives:

- Identification of the genetic variants involved in Brugada syndrome in three unique and well characterized BrS families, in which no variants were detected in any of the 60 candidate genes tested with an in-house developed cardiac arrhythmia gene panel. This will be achieved by using a combined linkage analysis and whole genome sequencing (WGS) approach. Several research questions will be addressed in this objective:
 - o Do mutations in novel genes (including RNA genes) explain the remaining 70% of molecularly unexplained BrS cases?
 - o Does structural variation contribute to the genetic architecture of BrS?
 - o Is variation in the non-coding regions of known genes explaining part of the missing heritability of BrS?
- Functional characterization of disease phenotype in patient-specific induced pluripotent stem cell-derived cardiomyocytes (iPSC-CMs) in search for genetic explanation. To address this aim, we will use iPSC lines obtained from selected family members and perform functional *in vitro* analysis of the observed phenotype. We will address here the following questions:
 - o Can we model BrS in patient-derived iPSC-CMs?
 - o Can we use iPSC-CMs to investigate the pathophysiological mechanism of potential new variants/genes underlying BrS?



Chapter 3. Compound Heterozygous *SCN5A* Mutations in a Severe Sodium Channelopathy With Brugada Syndrome: A Case Report

Aleksandra Nijak¹, Alain J Labro², Hans De Wilde^{3,4}, Wendy Dewals³, Steve Peigneur⁵, Jan Tytgat⁵, Dirk Snyders², Ewa Sieliwonczyk¹, Eline Simons¹, Emeline Van Craenenbroeck⁶, Dorien Schepers¹, Lut Van Laer¹, Johan Saenen⁶, Bart Loeys^{1,7}, Maaïke Alaerts¹

Frontiers in Cardiovascular Medicine, 2020; 7:117. doi: 10.3389/fcvm.2020.00117.

¹Center of Medical Genetics, Antwerp University Hospital, University of Antwerp, Antwerp, Belgium.

²Laboratory of Molecular, Cellular and Network Excitability, Department of Biomedical Sciences, University of Antwerp, Antwerp, Belgium.

³Department of Paediatric Cardiology, Antwerp University Hospital, Antwerp, Belgium.

⁴Department of Invasive Cardiology and Electrophysiology, Ghent University Hospital, Ghent, Belgium.

⁵Toxicology and Pharmacology, University of Leuven (KU Leuven), Leuven, Belgium.

⁶Department of Cardiology, Antwerp University Hospital, University of Antwerp, Antwerp, Belgium.

⁷Department of Human Genetics, Radboud University Medical Centre, Nijmegen, Netherlands.

3.1 Abstract

Aims

Brugada syndrome (BrS) is an inherited cardiac arrhythmia with an increased risk for sudden cardiac death (SCD). About 20% of BrS cases are explained by mutations in the *SCN5A* gene, encoding the main cardiac sodium $\text{Na}_v1.5$ channel. Here we present a severe case of BrS caused by *SCN5A* compound heterozygous mutations.

We performed genetic analysis of *SCN5A* in a male proband who collapsed during cycling at the age of two. During follow-up, he experienced a new collapse, with left-sided brain stroke at the age of three, and subsequent repetitive collapses during fever. The functional effect of the detected genetic variants was investigated.

Methods and results

Next-generation sequencing allowed detection of two *SCN5A* variants in trans: c.4813+3_4813+6dupGGGT - a Belgian founder mutation - and c.4711 T>C, p.Phe1571Leu. Familial segregation analysis showed the presence of the founder mutation in the proband's affected father and paternal aunt and *de novo* occurrence of the p.Phe1571Leu. The functional effect of the founder mutation was previously described as a loss-of-function. We performed functional analysis of the p.Phe1571Leu variant in HEK293 cells alone or co-expressed with the β_1 -subunit. Compared to the *SCN5A* wild type, p.Phe1571Leu displayed a hyperpolarizing shift in the voltage dependence of inactivation (loss-of-function), while the activation parameters were unaffected. Using the peptide toxin nemertide α -1 the variant's loss-of-function effect could be restored due to a toxin-dependent reduction of channel inactivation.

Conclusion

This is the first report providing support for the pathogenicity of the p.Phe1571Leu *SCN5A* variant, which together with the c.4813+3_4813+6dupGGGT founder mutation, explains the severity of the BrS phenotype in the presented case.

3.2 Introduction

Brugada syndrome (BrS) is an inherited cardiac arrhythmia with significant risk for sudden cardiac death (SCD) and a prevalence of 1:2000 in the general population [1]. The disease is diagnosed based on a specific ECG pattern with distinct ST-segment elevation in the right precordial leads [2; 3]. The disorder is predominantly explained by mutations in *SCN5A* (20-25% of all cases), encoding the α -subunit of the cardiac voltage-gated sodium channel $Na_v1.5$. Currently, over 20 genes encoding other cardiac channels as well as their accessory proteins are linked to BrS. [2; 4; 5].

Cardiac action potential generation and conduction velocity in the ventricles rely primarily on the availability of $Na_v1.5$ channels [3; 6], responsible for a fast depolarization of the cardiomyocyte membrane [7; 8]. $Na_v1.5$ is a pseudo-tetramer consisting of four repetitive transmembrane domains (DI-IV), containing six transmembrane spanning segments each (S1-S6) with segments S1-S4 forming the 'voltage sensing domain (VSD)'. The VSDs of DI to DIII control channel opening and closure (activation process), whereas the VSD of DIV regulates channel inactivation [3; 9; 10]. An accessory β_1 -subunit binds covalently to the α -subunit with variable effects on the activation kinetics [11]. BrS is associated with a loss-of-function of $Na_v1.5$, resulting in a reduced sodium current (I_{Na}), impaired channel kinetics or trafficking [3; 4; 5]. Several reports show that heterozygous *SCN5A* variants cause a BrS phenotype with variable expressivity, ranging from asymptomatic to recurrent arrhythmias and SCD. Interestingly, second-hit mutations in genes encoding auxiliary subunits of $Na_v1.5$ or compound heterozygous mutations in *SCN5A* tend to cause more severe phenotypes [4; 5; 6].

Here we present a patient with a severe BrS phenotype presenting in early childhood due to compound heterozygous *SCN5A* mutations. One of the variants, c.4813+3_4813+6dupGGGT – a Belgian founder mutation causing cardiac conduction defects and/or BrS in 83% of carriers [12], segregates in the paternal family. This splice site mutation results in a deletion of 32 amino acids (1572 to 1604) in S2 and S3 of DIV of $Na_v1.5$ with a loss-of-function of the channel, observed as the absence of sodium current when expressed in human embryonal kidney TSA cells [13; 14]. We hypothesize that the second de novo variant, c.4711T>C (p.Phe1571Leu) located in S2 of DIV, aggravates the phenotype in the proband. In this study we functionally characterize this p.Phe1571Leu variant. We provide evidence for a loss-of-function effect, which in co-occurrence with the Belgian founder mutation most likely explains the severity of the observed phenotype.

3.3 Materials and Methods

3.3.1 Mutation analysis of *SCN5A*

Genomic DNA was extracted from whole blood using standard procedures. Genetic testing of *SCN5A* was performed using an in-house developed cardiac arrhythmia gene panel [15]. Sanger sequencing was used to validate the variants and perform familial segregation analysis. This study was carried out in accordance with the recommendations of Ethics Committee of the Antwerp University Hospital. All subjects gave written informed consent in accordance with the Declaration of Helsinki.

3.3.2 Site-directed mutagenesis and transfection of HEK293 cells

WT human *SCN5A* cDNA was cloned into the pSP64T plasmid, and human *SCN1B* (the β_1 -subunit) cDNA into a pRcCMV plasmid. The p.Phe1571Leu variant was introduced in *SCN5A* using the QuickChange Site-Directed Mutagenesis Kit (Life Technologies) and a primer set that contained the variant (Eurogentec S.A.). The variant *SCN5A* p.Phe1571Leu plasmid was obtained by amplification in XL2 blue cells (Agilent Technologies) and subsequently purified (purification kit, Macherey-Nagel). The presence of the desired and absence of additional mutation(s) was confirmed by sequencing.

HEK293 cells were transiently transfected with WT *SCN5A* (expressing $Na_v1.5$) or the p.Phe1571Leu variant ($Na_v1.5$ -F1571L) alone, or co-expressed in a 1:1 mass ratio with *SCN1B* using Lipofectamine 2000 (Life Technologies). In every condition the pEGFP1-N1 plasmid was co-transfected to visualize transfected

cells for electrophysiological analysis. Cells were grown in DMEM medium supplemented with 10% fetal bovine serum and 1% Penicillin/Streptomycin (Life Technologies). Cells were placed in a 5% CO₂ incubator at 37°C for 48h prior to patch-clamp recordings.

3.3.3 Electrophysiological recordings

Whole-cell patch-clamp recordings were performed at room temperature (20-22°C) using an Axopatch 200B amplifier and a pClamp 10.7/Digidata 1440A acquisition system (Axon Molecular Devices). Patch-pipettes with a resistance between 1 and 1.5 MΩ were pulled from 1.2 mm borosilicate glass capillaries (World Precision Instruments, Inc.) using a P-2000 puller (Sutter Instrument Co.). Pipettes were filled with an intracellular solution containing (in mM): 4 NaCl, 106 KCl, 5 K₂ATP, 2 MgCl₂, 5 K₄BAPTA and 10 HEPES adjusted to pH 7.2 with KOH. The cells were continuously superfused with a bath solution (ECS) containing (in mM): 145 NaCl, 4 KCl, 5.3 CaCl₂, 1 MgCl₂, 10 HEPES, and 10 glucose (pH 7.35 with NaOH). For the toxin experiments, the nemertide 1-α synthetic peptide was directly dissolved in ECS at a concentration of 5 μM and applied near the patched cell using a pressurized fast-perfusion system.

I_{Na} was recorded by step depolarization for 20 ms to different potentials between -120 mV and +40 mV from a holding potential of -130 mV. Current-voltage relations (in pA/pF) were obtained by normalizing the peak I_{Na} amplitude to the cell capacitance and plotting these values as a function of the applied potential. Normalized conductance-voltage (G-V) curves were obtained by approximating the linear part of the current-voltage relation with the function $I = G_{max} * (V_{applied} - V_{reversal})$ to determine maximal conductance G_{max}. Dividing the data points of the current-voltage relation by the calculated maximum current at that voltage, using G_{max}, yielded the G-V relation. Activation and inactivation kinetics were determined by fitting the activating part or decay of I_{Na} with a single exponential function. The voltage dependence of inactivation was determined by stepping after a 500 ms pre-pulse, ranging from -135 mV to -30 mV, to a -10 mV test pulse to determine the amount of channel inactivation. Voltage-dependence of inactivation curves were obtained by plotting the normalized I_{Na} amplitude upon the test pulse against the corresponding pre-pulse potential. The recovery from inactivation was investigated upon a 500 ms conditioning pre-pulse to induce inactivation. The recovery was determined by stepping after the pre-pulse for variable time to -130 mV, a potential that recovers inactivation, followed by -10 mV pulse to evaluate the I_{Na} amplitude, which is a measure for the channels that have recovered. The speed of recovery from inactivation was evaluated by normalizing the I_{Na} elicited upon the -10 mV pulse to the maximum I_{Na}. These normalized values were plotted as a function of the duration at -130 mV and this relation was approximated with a single exponential function.

Currents, after passing a 5 kHz low-pass filter, were digitized at a sampling rate of 10 kHz. Recordings were discarded from analysis if the remaining voltage error, originating from series resistance error, exceeded 5 mV after compensation.

3.3.4 Data analysis

To obtain the midpoint potential (V_{1/2}) and the slope factor (V_s) for the voltage dependence of activation and inactivation, the G-V and voltage dependence of inactivation curves were fitted with a Boltzmann

$$\text{equation: } f(V) = \frac{I_{max}}{1 + e^{-\frac{(V - V_{1/2})}{V_s}}}$$

Data are reported as mean ± standard error of mean (SEM) with n the number of cells analysed. Comparison between the WT and variant was performed with two-tailed Student's t-test. A P-value of ≤ 0.05 indicates statistical significance (Systat Software Inc.).

3.4 Case description and diagnostic assessment

3.4.1 Clinical presentation of index patient and available family members

A 20-months-old boy was admitted to hospital emergency service after a collapse during cycling. Based on the ECG he was diagnosed with sick sinus syndrome (SSS) with junctional escape (**Figure 3-1b**). A DDD-pacemaker was implanted and during the implantation the dilated atria were electrically inactive leading to the diagnosis of atrial standstill. A DNA sample was collected for molecular diagnostics.

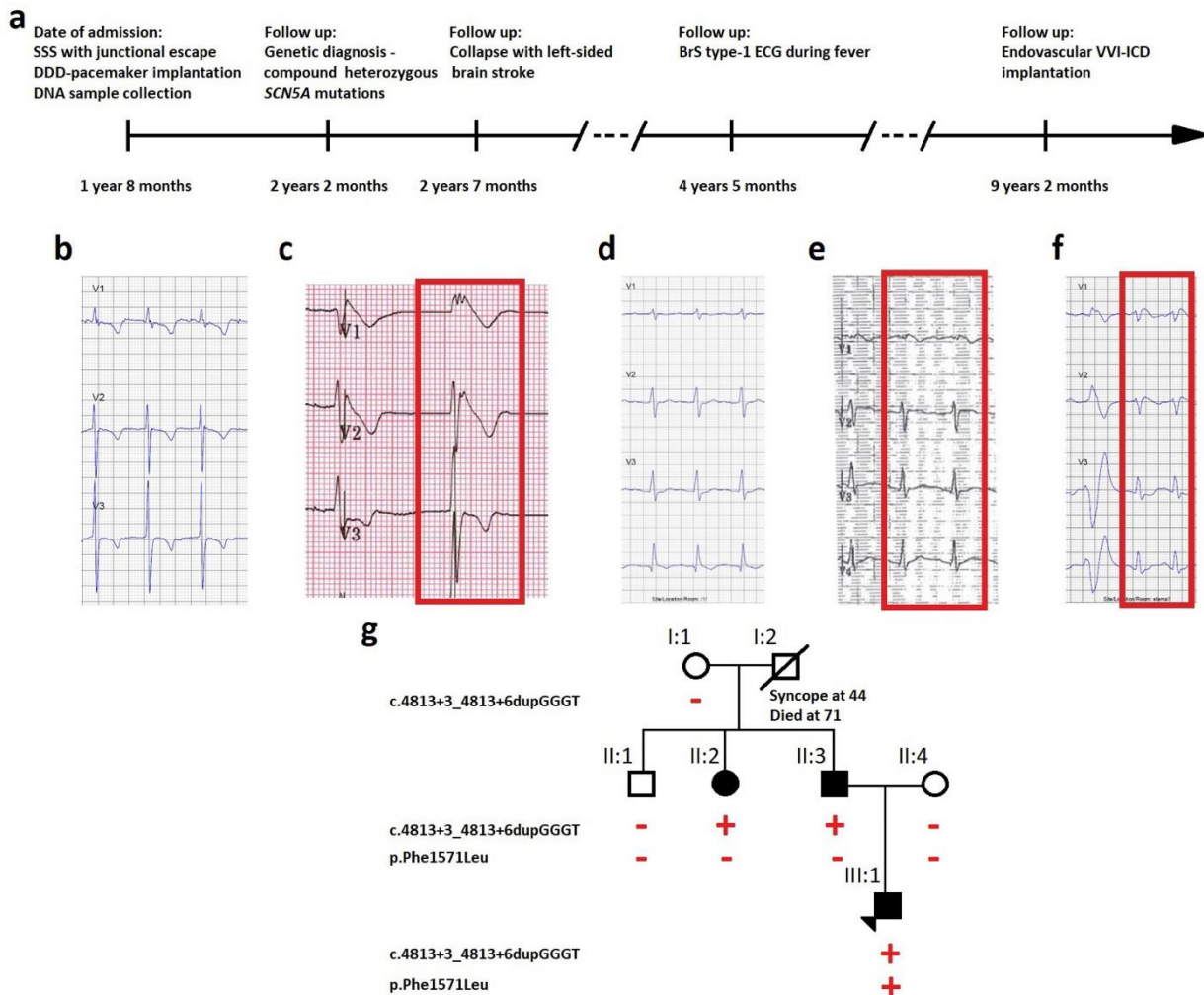


Figure 3-1 (a) Timeline of diagnostic interventions for the described case. ECG traces of (b) the proband on the day of diagnosis with absent atrial activity with junctional escape, (c) repeated during fever 39°C which unmasked BrS ECG pattern with elevated ST-segment, (d) the father carrying the *SCN5A* founder mutation with absent BrS ECG type-1 pattern after ajmaline challenge, but (e) present during fever at 39 °C (visible in lead V1), (f) the asymptomatic aunt carrying the *SCN5A* founder mutation with ECG type-1 pattern after ajmaline challenge. (g) Pedigree of the family showing segregation of the identified variants. Full symbols indicate affected individuals. Red plusses and minuses indicate respectively the presence or absence of the variant indicated on the left side of the pedigree.

During recovery, he experienced a new collapse, caused by a post-implantation thrombus which lead to a left-sided brain stroke. Echocardiography showed left atrial spontaneous echocardiographic contrast but no obvious thrombi. Although during follow up, no ventricular tachyarrhythmias were documented, an ECG taken during fever (39°C) unmasked the characteristic BrS type-1 pattern (**Figure 3-1c**) and the boy received an endovascular VVI-ICD, as there is a high estimated risk of development of ventricular arrhythmias (timeline: **Figure 3-1a**).

The father had a history of syncope at the age of 30. His ajmaline challenge test was negative but an ECG taken during a fever episode showed a BrS coved-shape ECG pattern (**Figure 3-1d-e**). The sister of the father was diagnosed with an ajmaline induced BrS type-1 ECG pattern (**Figure 3-1f**).

3.4.2 Molecular genetics

Two *SCN5A* variants were identified in the index patient: c.4813+3_4813+6dupGGGT, a Belgian founder mutation, and c.4711T>C p.(Phe1571Leu). Their occurrence in *trans* was derived from the sequence reads. Familial segregation analysis revealed the founder mutation in the proband's father (II:3) and paternal aunt (II:2), and de novo occurrence of the p.Phe1571Leu variant in the index patient (III:1) (**Figure 3-1g**).

The founder mutation was previously shown to cause a loss-of-function of the $Na_v1.5$ channel [14]. p.Phe1571Leu is absent from the GnomAD database (gnomad.broadinstitute.org [16]) whereas one carrier is reported in the TOPMED sample collection (dbSNP rs1369632373; nhlbwgs.org), Phenylalanine at position 1571 is highly conserved between species (**Figure 3-2a**) and *in silico* prediction on the functional impact of the variant is possibly damaging/damaging (MutationTaster, SIFT, PolyPhen; ENST00000413689.5). This initially led to the classification of this variant as a variant of uncertain significance (VUS).

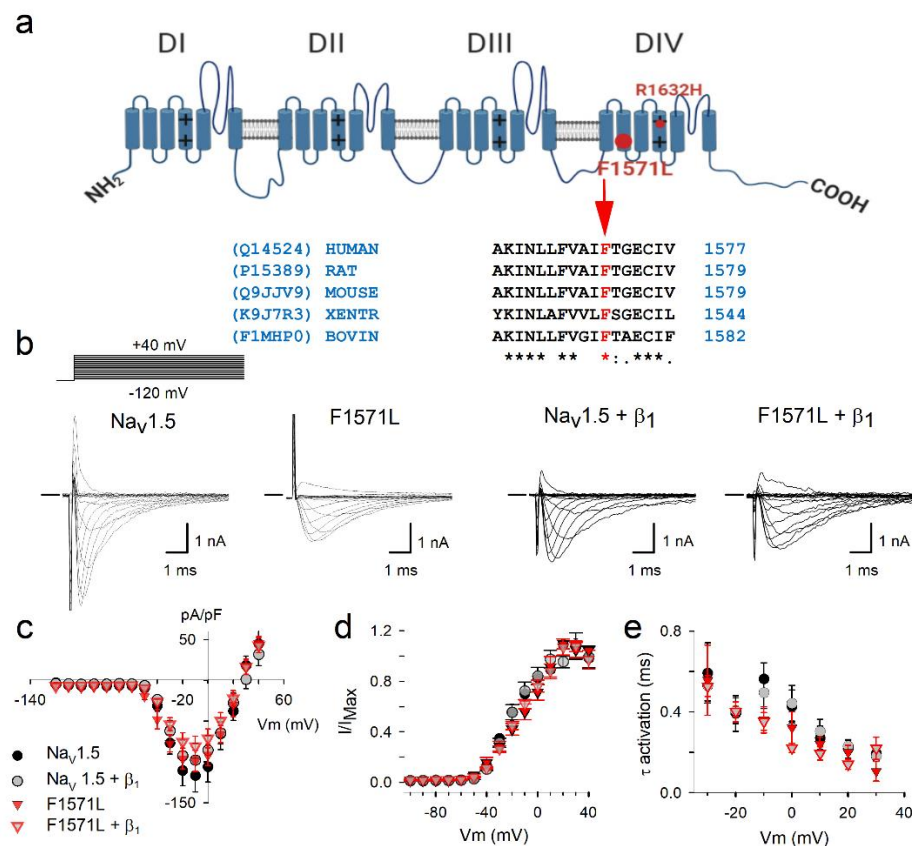


Figure 3-2 (a) Schematic representation of $Nav1.5$ structure [10] with location of p.Phe1571Leu variant (big full red circle) and p.Arg1632His (small red circle). The alignment shows conservation of Phe at position 1571 in *SCN5A* amino acid sequence between species. Accession numbers for the UniProt database are indicated on the left side. (b) Electrophysiological properties of WT $Nav1.5$ and $Nav1.5$ -F1571L alone or co-expressed with β_1 . Displayed from left to right are representative whole cell ionic current recordings of WT $Nav1.5$, $Nav1.5$ -F1571L, WT $Nav1.5 + \beta_1$, and $Nav1.5$ -F1571L + β_1 . The Na^+ selective currents were elicited with the pulse protocol shown on the left above the traces. Horizontal bar at the beginning of the traces indicates the zero current level. (c) Current density of WT $Nav1.5$ (black circles, $n = 8$), WT $Nav1.5 + \beta_1$ (grey circles, $n = 9$), $Nav1.5$ -F1571L (full red inverted triangles, $n = 7$) and $Nav1.5$ -F1571L + β_1 (open red inverted triangles, $n = 9$) were obtained by normalizing the peak current amplitudes, from pulse protocols shown in panel b, to the cell capacitance. (d) Voltage dependence of channel activation, $G-V$ curves, are represented for WT $Nav1.5$, $Nav1.5$ -F1571L, WT $Nav1.5 + \beta_1$, and $Nav1.5$ -F1571L + β_1 (e) Voltage-dependent kinetics of channel activation are shown as means \pm S.E.M.

3.5 Electrophysiological characteristics

To determine if this VUS contributes to the severe phenotype observed in our index patient, the Na_v1.5 WT and Na_v1.5-F1571L variant, and combinations with the WT β₁-subunit (Na_v1.5 + β₁ and Na_v1.5-F1571L + β₁) were expressed in HEK293 cells to assess the functional effect of the variant. The current-voltage (I-V) relationship showed that the current densities for the Na_v1.5 and Na_v1.5-F1571L, either expressed alone or in presence of β₁, did not differ (**Figure 3-2b-c**). The activation kinetics as well as the voltage dependence of channel activation (G-V curves) did not show significant differences yielding a V_{1/2} of -13.8 ± 1.7 mV and -14.9 ± 0.9 mV with slope factors of 14.5 ± 2.4 mV and 14 ± 1.3 mV for Na_v1.5 and Na_v1.5-F1571L, respectively (**Figure 3-2d-e**). These values did not change significantly in presence of β₁ yielding G-V curves with a V_{1/2} of -12 ± 0.8 mV and -14.7 ± 1.1 mV with slope factors of 16.1 ± 1 mV and 11.7 ± 1.7 mV for Na_v1.5 + β₁ and Na_v1.5-F1571L + β₁ respectively.

We subsequently analysed the kinetics of inactivation, voltage dependence of inactivation and the recovery from inactivation (**Figure 3-3a-e**). From the inactivation time constant, we observed a 3-fold slower inactivation (P < 0.001) for the variant (1.96 ± 0.12 ms at 0 mV, n = 7) compared to Na_v1.5 WT (0.67 ± 0.08 ms at 0 mV, n = 8) (**Figure 3-3b**). Co-expression with β₁ did not compensate this slowing and Na_v1.5-F1571L + β₁ (2.25 ± 0.16 ms at 0 mV, n = 9) displayed 3.6-fold slower inactivation kinetics compared to WT (0.63 ± 0.02 ms at 0 mV, n = 9) (P < 0.001).

Interestingly, the Na_v1.5-F1571L variant displayed a significant 18 mV hyperpolarizing shift in the voltage dependence of inactivation compared to WT (P = 0.001), yielding inactivation curves with a V_{1/2} of -104 ± 3 mV (n = 9) and -86 ± 3 mV (n = 5), combined with a slope factor of 7.6 ± 0.8 mV and 5.4 ± 0.7 mV for Na_v1.5-F1571L and Na_v1.5, respectively (**Figure 3-3c**). Co-expression with the β₁ subunit did not rescue the effect of the variant, and Na_v1.5-F1571L + β₁ displayed a significant 8.3 mV hyperpolarizing shift compared to Na_v1.5 + β₁ (P = 0.003) yielding inactivation curves with a V_{1/2} of -93 ± 2 mV (n = 12) and -84 ± 2 mV (n = 12), combined with a slope factor of 7.2 ± 0.5 mV and 5.8 ± 0.5 mV, respectively (P = 0.04).

As the onset of inactivation was slowed in the variant, we observed also a slowed recovery from inactivation. Time constants of recovery from inactivation revealed slower recovery for the variant channel compared to WT (P < 0.001), which was not rescued by co-expression with the β₁ subunit (P < 0.001) (Na_v1.5: 7.4 ± 0.1 ms (n = 6); Na_v1.5-F1571L: 15.2 ± 0.1 ms (n = 12); Na_v1.5 + β₁: 5.2 ± 0.2 ms (n = 10); Na_v1.5-F1571L + β₁: 13 ± 0.1 ms (n = 15)) (**Figure 3-3d-e**).

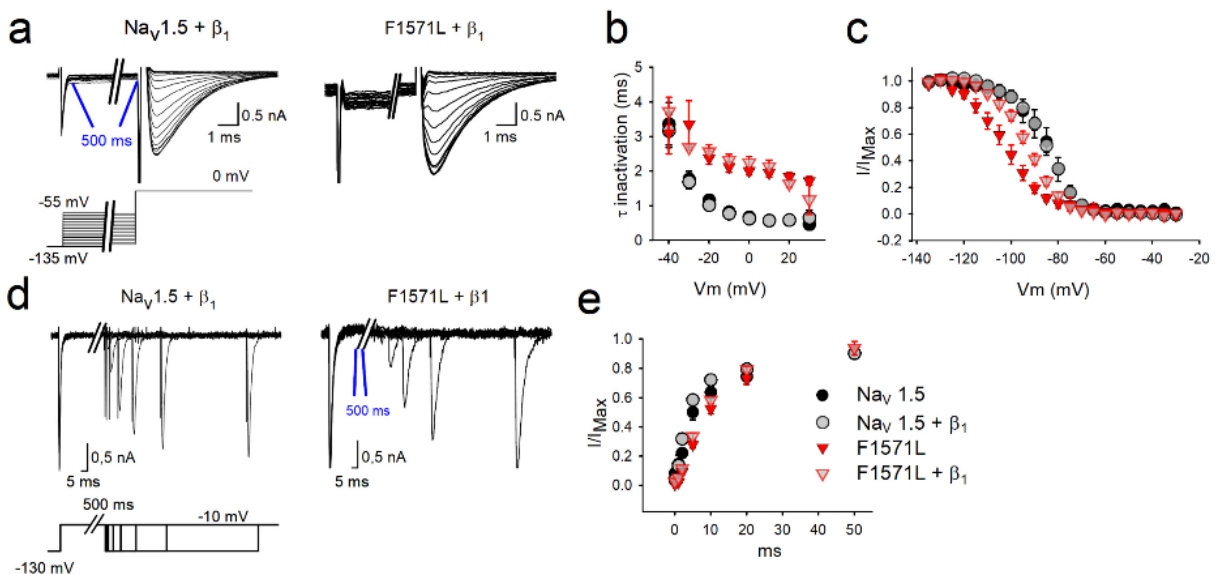


Figure 3-3 Inactivation properties of WT Na_v1.5 and Na_v1.5-F1571L alone or co-expressed with β₁. (a) Displayed from left to right are representative whole cell inactivation recordings of WT Na_v1.5 + β₁ and Na_v1.5-F1571L + β₁. The I_{No} were elicited with the pulse protocol shown underneath the traces. (b) Panel displays the time constants of channel inactivation for WT Na_v1.5 (black circles,

$n = 5$), WT $Na_v1.5 + \beta_1$ (grey circles, $n = 12$), $Na_v1.5$ -F1571L (full red inverted triangles, $n = 9$) and $Na_v1.5$ -F1571L + β_1 (open red inverted triangles, $n = 12$). Shown values are the means \pm S.E.M. (c) Voltage dependence of channel inactivation obtained by plotting the normalized current amplitudes at -10 mV, elicited after 500 ms conditioning pre-pulse depolarization, as a function of the pre-pulse potential. (d) Displayed from left to right are representative whole cell recordings of recovery from inactivation of WT $Na_v1.5 + \beta_1$ and $Na_v1.5$ -F1571L + β_1 . The used protocol is shown underneath the traces. (e) Graph represents the recovery from inactivation, sampled after 500 ms induction of inactivation. As this patient's severe phenotype seems to be associated with $Na_v1.5$ -F1571L displaying a hyperpolarizing shift in the voltage dependence of inactivation, we explored if we could restore the variant's voltage dependence of inactivation towards WT values by drug/toxin addition. The peptide toxin nemertide α -1 seemed a good candidate as it was reported to have a decelerating effect on the inactivation process of human sodium channels without influencing parameters of activation and I_{Na} density [17]. Two minutes perfusion of $5 \mu\text{M}$ of nemertide α -1 induced a steady-state modification of I_{Na} inactivation of both $Na_v1.5 + \beta_1$ and the variant p.F1571L + β_1 (Figure 3-4a). Upon this nemertide α -1 addition we observed a 16-fold slowing in the inactivation kinetics of $Na_v1.5 + \beta_1$, at 0 mV the time constant of inactivation slowed from 0.47 ± 0.04 ms in absence of nemertide α -1 to 7.62 ± 1.18 ms with nemertide α -1 ($n = 6$; $P = 0.0002$). The variant $Na_v1.5$ -F1571L + β_1 also reported a significant 3-fold slowing of inactivation ($P = 0.002$) displaying at 0 mV a time constant of 2.22 ± 0.57 ms in absence of nemertide α -1 and 5.82 ± 0.68 ms in its presence ($n = 6$) (Figure 3-4b). Next we investigated the voltage dependence of inactivation and observed no significant changes in the $V_{1/2}$ upon toxin addition for both $Na_v1.5 + \beta_1$ and $Na_v1.5$ -F1571L + β_1 ($P > 0.5$). In contrast, the slope factors became significantly shallower and amounted after toxin modification to 10.6 ± 0.8 mV ($n = 6$) and 12.3 ± 1.3 mV ($n = 6$) for $Na_v1.5 + \beta_1$ and $Na_v1.5$ -F1571L + β_1 respectively (Figure 3-4c-d). Due to the shallower slope, the amount of $Na_v1.5$ -F1571L + β_1 channel inactivation is reduced at the physiological relevant resting membrane potential (i.e. around -85 mV) upon nemertide α -1 addition.

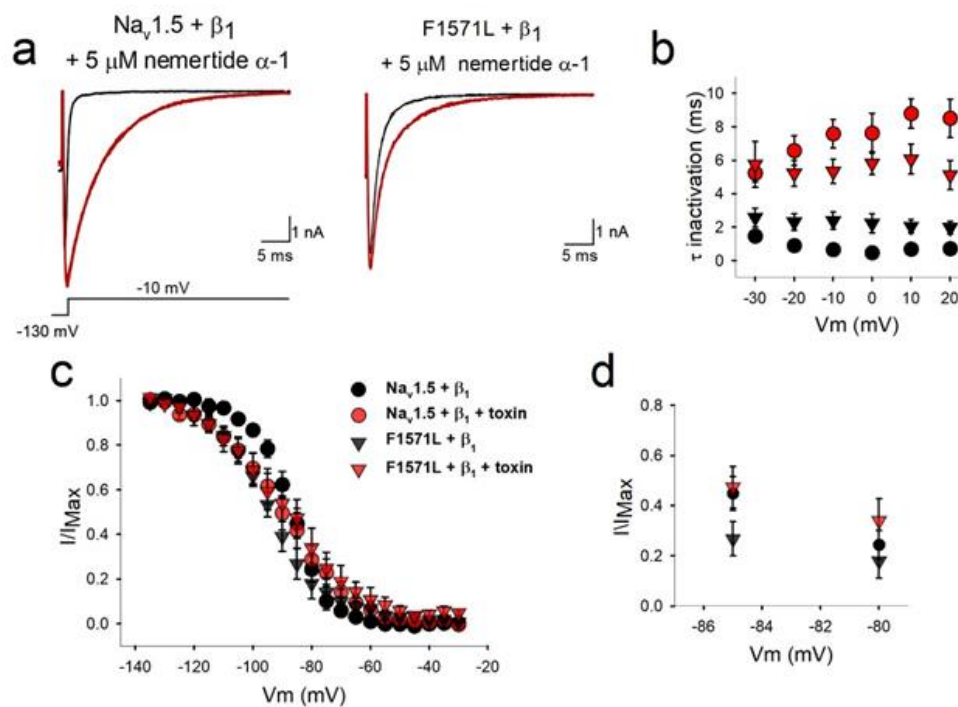


Figure 3-4 Inactivation properties of WT $Na_v1.5 + \beta_1$ and $Na_v1.5$ -F1571L + β_1 in the presence of nemertide α -1. (a) Displayed from left to right are representative whole cell recordings of WT $Na_v1.5 + \beta_1$ and $Na_v1.5$ -F1571L + β_1 in control conditions (black tracings) and upon steady-state modification by $5 \mu\text{M}$ nemertide α -1 (red tracings). Currents were elicited with the pulse protocol shown underneath the traces. Steady-state toxin modulation was achieved after approximately 2 minutes. (b) Kinetics of channel inactivation for WT $Na_v1.5 + \beta_1$ (circles) and $Na_v1.5$ -F1571L + β_1 (inverted triangles) in control conditions (black) and upon steady-state modification by nemertide α -1 (red) are shown. Values are the means \pm S.E.M. (c) Voltage dependence of channel inactivation for WT $Na_v1.5 + \beta_1$ (black symbols) and $Na_v1.5$ -F1571L + β_1 (red) in control conditions (circles) and upon steady-state modification by nemertide α -1 (inverted triangles) is shown. (d) Scaled-up view of the voltage dependence of channel inactivation in the physiological range of resting membrane potentials, with a focus on in comparison to the WT $Na_v1.5 + \beta_1$. Note, in the presence of nemertide α -1 the amount of inactivated $Na_v1.5$ -F1571L + β_1 channels (red inverted triangles) is similar to the WT in control conditions (black circles).

3.6 Discussion

Single heterozygous loss-of-function variants in *SCN5A* cause BrS with variable penetrance. When *SCN5A* is affected by two compound variants, this can result in a significant aggravation of the disease severity and/or earlier disease onset [5; 18; 19; 20; 21]. This was also observed in our proband, who experienced his first syncope during physical activity around the age of two, probably caused by the brady-arrhythmia in the setting of atrial standstill. Most of the similarly published patients presented with sinus node dysfunction [5; 18; 19; 21], only Sacilotto et al. reported a patient presenting initially with atrial flutter and recurrent syncopes without spontaneous ventricular arrhythmia and who similarly to our case presented a spontaneous BrS type-1 ECG pattern during follow-up [18]. Clinical interventions mostly encompassed implantation of a pacemaker [5; 18; 19; 21], with additional low dose aspirin [19] or oral quinidine [18], and single patient received β -blockers without pacemaker implantation [20].

In the presented family, heterozygous carriers of the *SCN5A* Belgian founder mutation showed characteristic BrS type-1 ECG pattern either after sodium channel blocker challenge (II:2) or during fever conditions (II:3), but presented no symptoms (II:2) or syncope at the age of 30 (II:3). The proband's second variant, p.Phe1571Leu, is a missense variant that we functionally modelled in HEK293 cells. Our experiments showed that p.Phe1571Leu does not affect current density, voltage dependence of channel activation or activation kinetics (**Figure 3-2c-e**). However, it did impair the inactivation properties, as could be expected from the localization of the variant in the VSD of DIV, which is known to regulate channel inactivation [9]. On the one hand, the variant slows down inactivation (**Figure 3-3b**), which would suggest a gain-of-function of the variant. This effect would rather be predicted to lead to a long-QT syndrome type 3 phenotype [4]. But on the other hand, the voltage dependence of inactivation of p.Phe1571Leu displays a significant hyperpolarizing shift (**Figure 3-3c**) which in physiological conditions results in a reduction of over 40 % in the availability of $\text{Na}_v1.5$ channels at rest (i.e. at -85 mV) and impairment of the recovery from inactivation (**Figure 3-3e**), which further reduces the remaining availability of the channel. This leads obviously to a loss-of-function of I_{Na} , explaining the (aggravated) BrS phenotype in the patient.

Interestingly, an almost identical electrophysiological effect was reported for the *SCN5A* p.Arg1632His (R1632H) variant [5; 21], located in DIV S4 (**Figure 3-2a**) in proximity to p.Phe1571Leu. Slower inactivation kinetics, delayed recovery from inactivation and a hyperpolarizing shift in voltage dependence of inactivation of similar magnitude (20.7mV) as we observed (18mV) were described [21]. Heterozygous carriers of this variant had no symptoms, SSS, ajmaline induced BrS [5] or 1st degree AV block [21], while compound heterozygous carriers (with second *SCN5A* variant) presented with early-onset SSS [5; 21]. This supports the likely pathogenicity of the p.Phe1571Leu variant characterized in this study, and its causal role in aggravating the phenotype of the presented case.

Our experiments with the toxin nemertide α -1 showed that the WT channels were responding as expected, as inactivation kinetics were slowed down. However, no depolarizing shift in the voltage dependence of inactivation was observed for the WT $\text{Na}_v1.5+\beta_1$, as was observed for $\text{Na}_v1.5$ expressed in *Xenopus laevis* oocytes [17]. This might be because of a different cell type and/or the addition of the β_1 -subunit, which seems to protect the cells from fluctuations in the voltage dependence of inactivation. Nevertheless, toxin addition resulted in a shallower voltage dependence of inactivation (i.e. larger slope factor value) such that the amount of inactivated $\text{Na}_v1.5$ -F1571L channels is reduced at the physiological resting membrane potential (**Figure 3-4c-d**). I.e. in the presence of toxin, the amount of available non-inactivated $\text{Na}_v1.5$ -F1571L + β_1 channels rises from 18 % without toxin to approximately 36 % (at -85 mV), which is similar to the amount of available WT $\text{Na}_v1.5$ + β_1 channels. To our knowledge, this is the first report in which the use of a sodium channel activator toxin is proposed as a potential remedy for the pathogenic effect of an *SCN5A* variant.

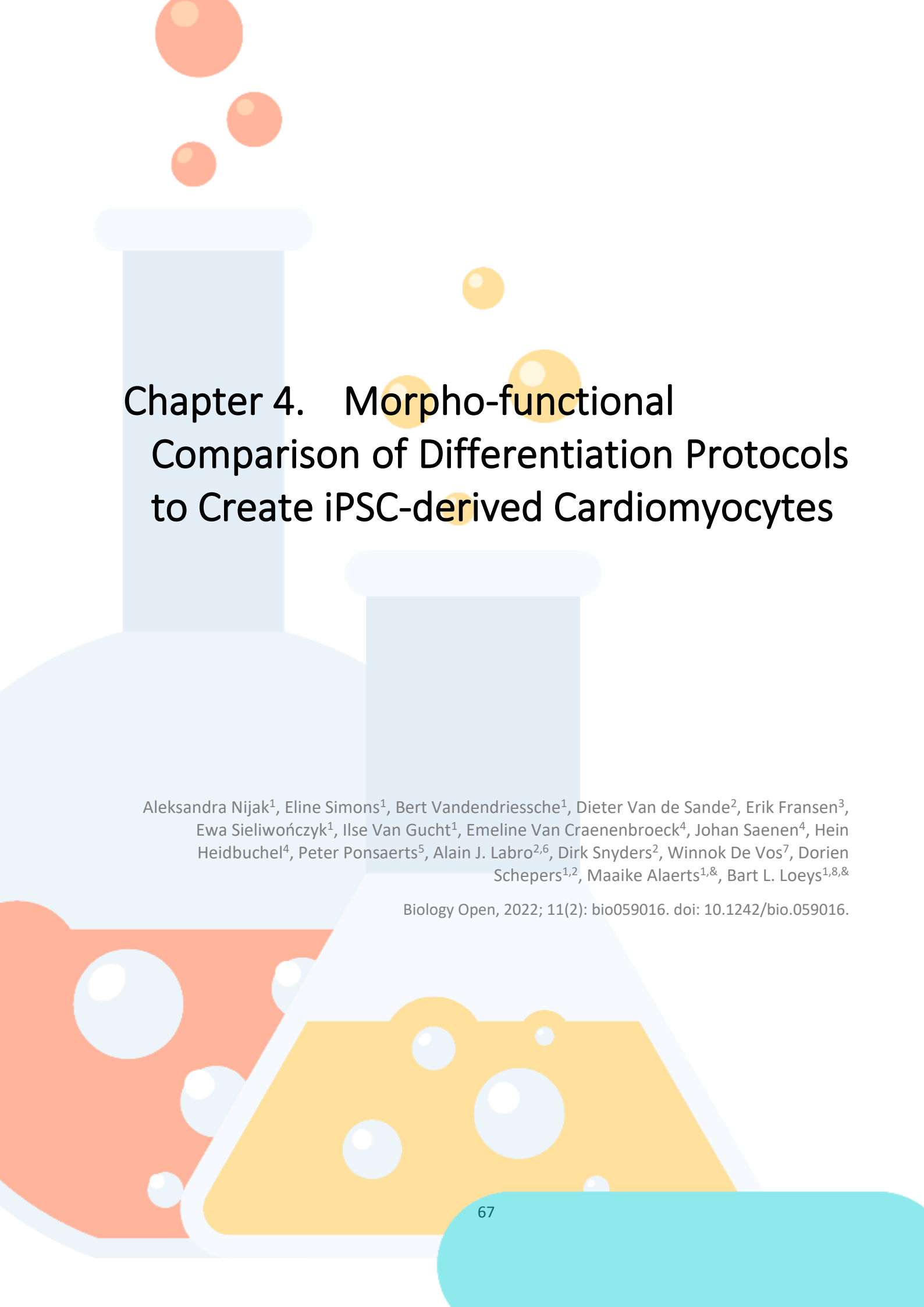
Based on these functional experiments we conclude that the described p.Phe1571Leu variant is likely pathogenic and in the presented case its *de novo* occurrence, together with the *SCN5A* Belgian founder mutation explains the severe BrS phenotype.

3.7 References

- [1] Postema, P.G. About Brugada syndrome and its prevalence. *Europace* 14 (2012) 925-928.
- [2] Antzelevitch, C. J wave syndromes: Brugada and early repolarization syndromes. *Heart Rhythm* 12 (2015) 1852-66.
- [3] Bartos, D. C.; Ripplinger, C. M. Ion channels in the heart. *Comprehensive Physiology* 5 (2015) 1423-64.
- [4] Bezzina, C. R.; Priori, S. G. Genetics of Sudden Cardiac Death. *Circulation Research* 116 (2015) 1919-1936.
- [5] Robyns, T.; Van Casteren, L.; Corveleyn, A.; De Ravel, T.; Heidbuchel, H.; Willems, R. Reduced penetrance and variable expression of *SCN5A* mutations and the importance of co-inherited genetic variants: case report and review of the literature. *Indian Pacing and Electrophysiology Journal* 14 (2014) 133-49.
- [6] Baroni, D. On the multiple roles of the voltage gated sodium channel B1 subunit in genetic disease. *Frontiers in Pharmacology* 6 (2015).
- [7] Priest, B. T. Cardiac ion channels. *Channels (Austin)* 9 (2015) 352-9.
- [8] Medeiros-Domingo, A.; Iturralde Torres, P.; Tester, D. J.; Luna, T. T.; Makielski, J. C.; Ackerman, M. J. Unique mixed phenotype and unexpected functional effect revealed by novel compound heterozygosity mutations involving *SCN5A*. *Heart Rhythm* 6 (2009) 1170-1175.
- [9] Detta, N.; Salvatore, F. The multi-faced aspects of the complex cardiac Nav1.5 protein in membrane function and pathophysiology. *Biochimica et Biophysica Acta (BBA) - Proteins and Proteomics* 1854 (2015) 1502-1509.
- [10] Jiang, D.; Tonggu, L.; El-Din, T.M.G.; Lenaeus, M.J.; Zhao, J.; Yoshioka, C.; Zheng, N.; Catterall, W.A. Structure of the cardiac sodium channel. *Cell* 180 (2020) 122-134.
- [11] Zhu, W.; Varga, Z.; Schubert, A. R.; Nerbonne, J. M.; Silva, J. R. Mechanisms of noncovalent B subunit regulation of Nav channel gating. *The Journal of General Physiology* (2017).
- [12] Sieliwończyk, E.; Robyns, T.; Schepers, D.; Claes, C.; Van Craenenbroeck, E.; Simons, E.; Nijak, A.; Vandendriessche, B.; Mortier, G.; Vrints, C.; et al. Clinical characterization of the first Belgian *SCN5A* founder mutation cohort. *Europace* submitted (2020).
- [13] Rossenbacker, T.; Kuiperi, C.; de Ravel, T. J. L.; Devriendt, K.; Matthijs, G. et al., Unconventional intronic splice site mutation in *SCN5A* associates with cardiac sodium channelopathy. *Journal of Medical Genetics* 42 (2005).
- [14] Hong, K.; Pollevick, G. D.; Dumaine, R.; de Zutter, M.; Burashnikov, E.; Wu, Y.S.; Brugada, J.; Brugada, P.; Brugada, R. Cryptic 5' splice site activation in *SCN5A* associated with Brugada syndrome. *Journal of Molecular and Cellular Cardiology* 38 (2005) 555-60.
- [15] Proost, D.; Vanderweyer, G.; Rotthier, A.; Alaerts, M.; Van Craenenbroeck, E.M.; Van Crombruggen, J.; Mortier, G.; Wuyts, W.; Vrints, C.; Del Favero, J.; et al. Targeted next-generation sequencing of 51 genes involved in primary electrical disease. *The Journal of Molecular Diagnostics* 19 (2017) 445-459.
- [16] Karczewski, L.C.; Francioli, G.; Tiao, B.B.; Cummings, J.; Alfoldi, Q.; Wang, R.L.; Collins, K.M.; Laricchia, A.; Ganna, D.P. Birnbaum, L.D.; et al. Variation across 141,456 human exomes and genomes reveals the spectrum of loss-of-function intolerance across human protein-coding genes. *bioRxiv* (2019) 531210.
- [17] Jacobsson, E.; Strand, M.; Peigneur, S.; Eriksson, C.; Loden, H.; Shariatgorji, M.; Andren, P.E.; Lebbe, E.K.M.; Rosengren, K.J.; Tytgat, J.; et al. Peptide ion channel toxins from the bootlace worm, the longest animal on Earth. *Nature Scientific Reports* 8 (2017).
- [18] Sacilotto, L.; Darrieux, F.C.; Wulkan, F.; Oliveira, T.G.; Hachul, D.T.; Pereira, A.D.; Scanavacca, M.I. Compound heterozygous *SCN5A* mutations in a toddler - are they associated with a more severe phenotype? *Arquivos brasileiros de cardiologia* 108 (2017) 70-73.
- [19] Baskar, S.; Clements, D.; Mayuga, K.A.; Aziz, P.F. Compound heterozygous mutations in the *SCN5A*-encoded Nav1.5 cardiac sodium channel resulting in atrial standstill and His-Purkinje system disease. *The Journal of Pediatrics* 165 (2014) 1050-1052.

[20] Bezzina, C. R.; Groenewegen, W. A.; Herfst, L. J.; van der Wal, A. C.; Lam, J.; Jongsma, H. J.; Wilde, A. A.; Mannens, M. M. Compound heterozygosity for mutations (W156X and R225W) in *SCN5A* associated with severe cardiac conduction disturbances and degenerative changes in the conduction system. *Circulation Research* 92 (2003) 159-68.

[21] Benson, D.W.; Dymont, M.; Knilans, T.K.; Fish, F.A.; Strieper, M.J.; Rhodes, T.H.; George, A.L. Jr. Congenital sick sinus syndrome caused by recessive mutations in the cardiac sodium channel gene (*SCN5A*). *J Clin Invest* 112 (2003) 1019-1028.

The background features two stylized laboratory flasks. The flask on the left is light blue and contains an orange liquid with several white bubbles. The flask on the right is light blue and contains a yellow liquid with several white bubbles. Above the flasks, there are several floating bubbles in shades of orange and yellow. The overall style is clean and modern, typical of a scientific publication cover.

Chapter 4. Morpho-functional Comparison of Differentiation Protocols to Create iPSC-derived Cardiomyocytes

Aleksandra Nijak¹, Eline Simons¹, Bert Vandendriessche¹, Dieter Van de Sande², Erik Fransen³, Ewa Sieliwończyk¹, Ilse Van Gucht¹, Emeline Van Craenenbroeck⁴, Johan Saenen⁴, Hein Heidbuchel⁴, Peter Ponsaerts⁵, Alain J. Labro^{2,6}, Dirk Snyders², Winnok De Vos⁷, Dorien Schepers^{1,2}, Maaïke Alaerts^{1,&}, Bart L. Loeys^{1,8,&}

Biology Open, 2022; 11(2): bio059016. doi: 10.1242/bio.059016.

¹Center of Medical Genetics, Faculty of Medicine and Health Sciences, University of Antwerp & Antwerp University Hospital, Antwerp, Belgium

²Laboratory of Molecular Biophysics, Cellular and Network Excitability, Department of Biomedical Sciences, University of Antwerp, Antwerp, Belgium

³StatUa Center of Statistics, University of Antwerp, Antwerp, Belgium

⁴Department of Cardiology, Faculty of Medicine and Health Sciences, University of Antwerp and Antwerp University Hospital, Antwerp, Belgium

⁵Laboratory of Experimental Hematology, Vaccine & Infectious Disease Institute, Department of Biomedical Sciences, University of Antwerp, Antwerp, Belgium

⁶Department of Basic and Applied Medical Sciences, Faculty of Medicine and Health Sciences, Ghent University, Ghent, Belgium

⁷Laboratory of Cell Biology and Histology, Faculty of Veterinary Sciences, University of Antwerp, Antwerp, Belgium

⁸Department of Human Genetics, Radboud University Medical Centre, Nijmegen, The Netherlands

& equally contributed

4.1 Abstract

Cardiomyocytes derived from induced pluripotent stem cells (iPSC-CMs) offer an attractive platform for cardiovascular research. Patient-specific iPSC-CMs are very useful for studying disease development, and bear potential for disease diagnostics, prognosis evaluation and development of personalized treatment. Several monolayer-based serum-free protocols have been described for the differentiation of iPSCs into cardiomyocytes, but data on their performance are scarce.

In this study, we evaluated two protocols that are based on temporal modulation of the Wnt/ β -catenin pathway for iPSC-CM differentiation from four iPSC lines, including two control individuals and two patients carrying an *SCN5A* mutation. The *SCN5A* gene encodes the cardiac voltage-gated sodium channel ($Na_v1.5$) and loss-of-function mutations can cause the cardiac arrhythmia Brugada syndrome. We performed molecular characterization of the obtained iPSC-CMs by immunostaining for cardiac specific markers and by expression analysis of selected cardiac structural and ionic channel protein-encoding genes with qPCR. We also investigated cell growth morphology, contractility and survival of the iPSC-CMs after dissociation. Finally, we performed electrophysiological characterization of the cells, focusing on the action potential (AP) and calcium transient (CT) characteristics using patch-clamping and optical imaging, respectively.

Based on our comprehensive morpho-functional analysis, we concluded that both tested protocols result in a high percentage of contracting CMs. Moreover, they showed acceptable survival and cell quality after dissociation (>50% of cells with a smooth cell membrane, possible to seal during patch-clamping). Both protocols generated cells presenting with typical iPSC-CM AP and CT characteristics, although one protocol (that involves sequential addition of CHIR99021 and Wnt-C59) rendered iPSC-CMs, which were more accessible for patch-clamp and calcium transient experiments and showed an expression pattern of cardiac-specific markers more similar to this observed in human heart left ventricle samples.

4.2 Introduction

A major challenge for contemporary cardiac research is acquisition of tissue specific cells for *in vitro* modeling. As it is not routine to obtain cardiomyocytes from a patient, induced pluripotent stem cells (iPSCs) serve as an attractive alternative source for derivation of cardiomyocytes (CMs, iPSC-CMs; **Figure 4-1a**). The first attempts to differentiate pluripotent stem cells into CMs employed a suspension culture of human embryonic stem cells (hESCs) in medium containing serum, to form so-called embryoid bodies (EB) [1]. However, this approach resulted in low numbers of hESC-CM (5–10%). Later on, the suspension protocol was improved with the use of defined serum-free media, supplemented with growth factors involved in normal human embryological heart development, like activin A, bone morphogenetic proteins (BMPs), fibroblast growth factor 2 (FGF2), vascular endothelial growth factor (VEGF), Dickkopf-related protein (DKK) and Wnt agonists and antagonists [2-6]. Although those protocols showed improved CM yield to about 40–90%, the 3D EB clusters hamper even diffusion of the growth factors in the cell culture, having an impact on reproducibility of the procedure [7]. To overcome the obstacles of suspension protocols, an application of monolayer cell culture with addition of the aforementioned growth factors was proposed. Multiple monolayer-based differentiation approaches have been reported, with high efficiency (80–99% estimated based on the proportion of troponin T or cardiac α -actinin positive cells in flow cytometric measurements) and reproducibility tested in multiple laboratories [8-13].

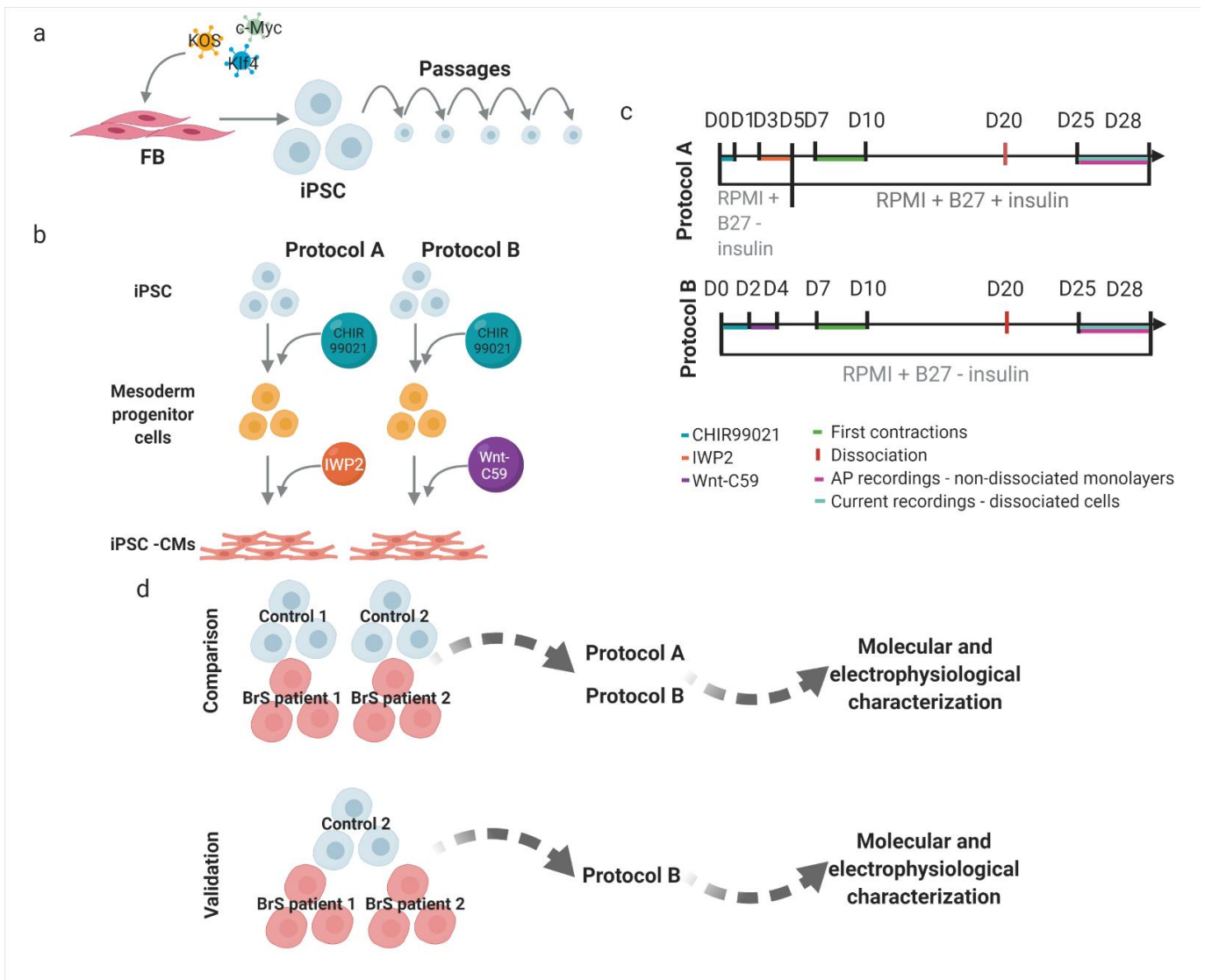


Figure 4-1 Schematic presentation of the workflow and experimental design. (A) Reprogramming of the fibroblasts into iPSC. (B) Derivation of cardiomyocytes. (C) Timelines for the tested differentiation protocols with addition of small molecules, first observed

contractions, time point of dissociation of the cells as well as time window for patch-clamping experiments indicated. (D) Experimental design used for comparison assessment of the selected differentiation protocols (created with biorender.com, August 2021).

Based on the fact that iPSC-CMs express cardiac specific structural and ion channel proteins, they can be used for modeling cardiac activity *in vitro*. The first reported use of iPSC-CMs as a model for arrhythmias concerned long QT syndrome (LQTS) [14]. The study showed that iPSC-CMs enable the investigation of an arrhythmic phenotype, based on differences in action potential duration (APD) and decrease in potassium current density when patient iPSC-CMs were compared to control iPSC-CMs. Further on, iPSC-CM models for other inherited cardiac arrhythmias, including Brugada syndrome (BrS) have been successfully characterized [15-20]. Electrophysiological characterization of these models is typically performed using patch-clamping experiments, however, alternate more high-throughput data acquisition techniques such as intracellular Ca²⁺ transient (CT) recordings using optical dyes or field potential recordings have also been successfully applied [19, 20].

To date, available reports on comparison of differentiation protocols focus on performance of 3D versus monolayer-based approaches from a single control donor. The aim of this report is to compare two selected differentiation protocols based on (i) their overall performance in generation of iPSC-CMs from iPSC clones from several donors and (ii) the morpho-functional characteristics of the created iPSC-CMs. We compared two monolayer-based serum-free differentiation protocols, which adopt a two-step procedure: mesoderm induction through activation of the Wnt/ β -catenin pathway using medium supplemented with a GSK3 inhibitor small molecule – CHIR99021, followed by cardiac-fate determination through inhibition of the canonical Wnt pathway using media supplemented with IWP2 (protocol A [10]) and Wnt-C59 (protocol B [11]) (**Figure 4-1b**). In order to select the best performing differentiation protocol, we followed the subsequent experimental outline: one iPSC clone from four individuals (Control 1 and 2, BrS patient 1 and 2) was used, each differentiated in four or six replicates (one well on a six-well plate=one replicate) using protocol A and B (**Figure 4-1d**). We investigated growth morphology, contracting area, survival after dissociation, expression of cardiac specific proteins and mRNA expression level of cardiac structural and ion channel proteins. As in subsequent studies we aim to model cardiac arrhythmias, for the evaluation of the best performing protocol we looked at electrophysiological properties of the obtained cells. In patch-clamp experiments we characterized action potential (AP) properties, including APD, action potential amplitude (APA), resting membrane potential (RMP) and beating rate (beats per minute, BPM). In addition, we used optical dyes to characterize CT properties: calcium transient duration (CTD), time of rise and decay and beating rate. In this report we do not address *SCN5A* expression, nor sodium currents and AP upstroke velocity, since we expect these to be different in patient iPSC-CMs based on the mutation status of the selected patient donors and these are beyond the scope of this paper.

4.3 Results

4.3.1 Reprogrammed iPSC clones express pluripotency markers and show appropriate iPSC morphology

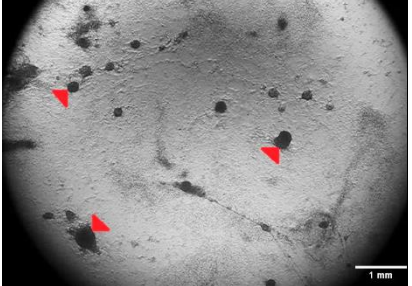
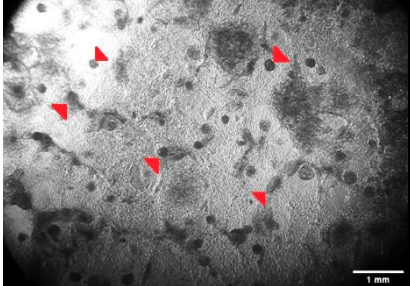
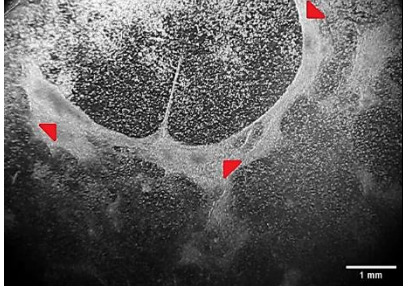
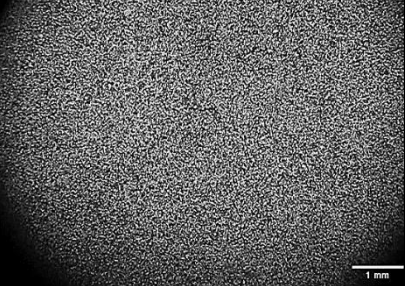
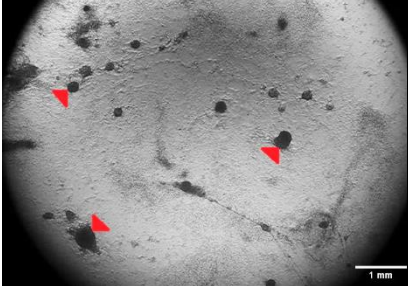
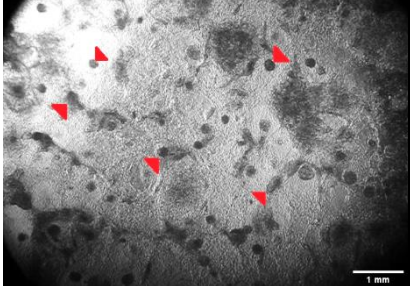
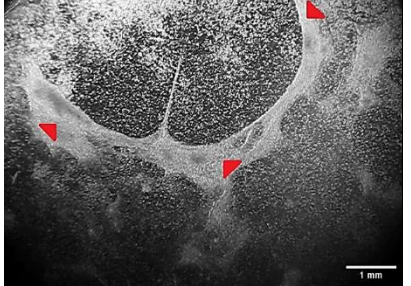
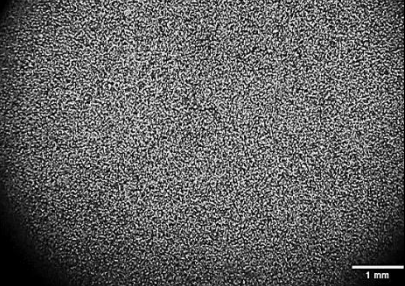
We derived 10–12 iPSC clones from each individual fibroblast line and validated three of them. All of the validated clones selected for the experiments presented good iPSC colony morphology (bright small round cells forming compact colonies with smooth, defined edges), showed expected expression of all of the tested pluripotency markers and presented no relevant novel genomic aberrations (CNVs >100 kb, affecting genes involved in cardiomyocyte function or development) after the reprogramming process (**Supplementary Figure 4-1** and **Supplementary Table 4-1**).

4.3.2 Protocol comparison: iPSC-CMs obtained with protocol B show higher similarity in transcript expression in comparison to ventricular tissue, and show less 3D clumps morphology

The first observable features of differentiating iPSC-CMs are changes in cell morphology, which in the end lead to the development of spontaneously contracting cells. We collected light microscopy images of contracting cell cultures and observed three types of growth morphology: full flat monolayer, patches of monolayer and 3D cell clumps. Representative examples of growth morphology are presented in **Table 4-1**. Both protocols generated contracting CMs from Control 1 and 2 and BrS patient 2 iPSCs, while for BrS patient 1 only protocol B was successful (**Table 4-1**). We noted morphology of 3D clumps in iPSC-CMs generated with protocol A but not with protocol B. Overall, protocol A generated contracting cells in 7 out of 18 and protocol B in 15 out of 18 replicates, with on average larger contracting area in iPSC-CMs generated with protocol B (11±1% and 33±5.6% average contracting area for protocols A and B, respectively).

All of the generated contracting iPSC-CMs showed expression of all tested cardiac protein markers (cACT, cTNNI and Nkx2.5) in ICC staining for protocol A and B (**Figure 4-2a-b**). The iPSC-CMs differentiated using protocol A showed less organization of cTNNI, where generated cells showed cTNNI expression mainly around the nucleus and not presenting cytoskeletal structures visible in the cells obtained with protocol B (**Figure 4-2b; Supplementary Figure 2**). Average differentiation efficiency calculated from ICC staining of cACT was similar for iPSC-CMs generated using both protocols (protocol A: 90.2±4.1%; protocol B: 95.9±4.1%) (**Figure 4-2a; Table 4-1; Supplementary Table 4-2**), although for BrS patient 1 protocol A did not produce CMs. We evaluated mRNA levels of selected cardiac markers in iPSC-CMs for both protocols (except for control 2 for which insufficient RNA concentration was obtained). Results showed significant differences in the expression levels for five of the markers (*GJA1*, *KCNJ2*, *MYH7*, *RYR2*, *TNNI3*) between the used protocols (**Figure 4-3a; Supplementary Table 4-3**). We observed significantly lower relative expression of *KCND3*, *KCNQ1*, *RYR2*, *TNNI3* and *TNNT2* in iPSC-CMs obtained using both protocols, in comparison to left ventricular (LV) cardiac tissue (**Figure 4-3a; Supplementary Figure 4-3a; Supplementary Table 4-3**) as a reference. Additionally, cells generated with protocol A showed significantly lower relative expression of *KCNH2*, *KCNJ8*, *MYH6* and *MYH7*, as well as higher relative expression of *KCNJ2* and *GJA1*, while cells generated with protocol B showed significantly higher relative expression of *MYH6* compared with the reference tissue. Although both protocol A and B show differences in expression compared to LV tissue, protocol B showed more similar expression levels of each of the tested genes in comparison to LV tissue (**Supplementary Figure 4-3a**).

Table 4-1 Summary of morphology observations and immunofluorescence staining for cell lines differentiated comparing protocol A and B with example images.

	3D clumps				Patchy monolayer		Monolayer	
								
Used protocol	Protocol A				Protocol B			
Cell line	Control 1	Control 2	BrS patient 1	BrS patient 2	Control 1	Control 2	BrS patient 1	BrS patient 2
Morphology of the contracting iPSC-CMs	3D clumps/ patchy monolayer	Patchy monolayer with 3D clumps	-	3D clumps	Patchy monolayer	Patchy monolayer	Monolayer	Patchy monolayer
Number of wells with contracting cells	3/6	2/4	0/4	2/4	5/6	4/4	2/4	4/4
Contracting areas [%]	5±1.98	35±1.27	0	3±0.92	17±2.21	26±2.6	70±6.04	19±11.61
Differentiation efficiency	80	89.5	-	100	100	83.65	100	100
ICC stainin g	cACT	+	+	-	+	+	+	+
	cTNNI	+	+	-	N/A	+	+	N/A
	Nkx2.5	+	+	-	N/A	+	+	N/A

Red arrow heads indicate the 3D clumps and patchy monolayer, respectively. differentiation efficiency was calculated from ICC images for cACT.

N/A - No cTNNI or Nkx2.5 staining was performed on iPSC-CMs from BrS patient 2 due to low amount of contracting areas on coverslips, which were used for electrophysiological tests and ICC staining for cACT.

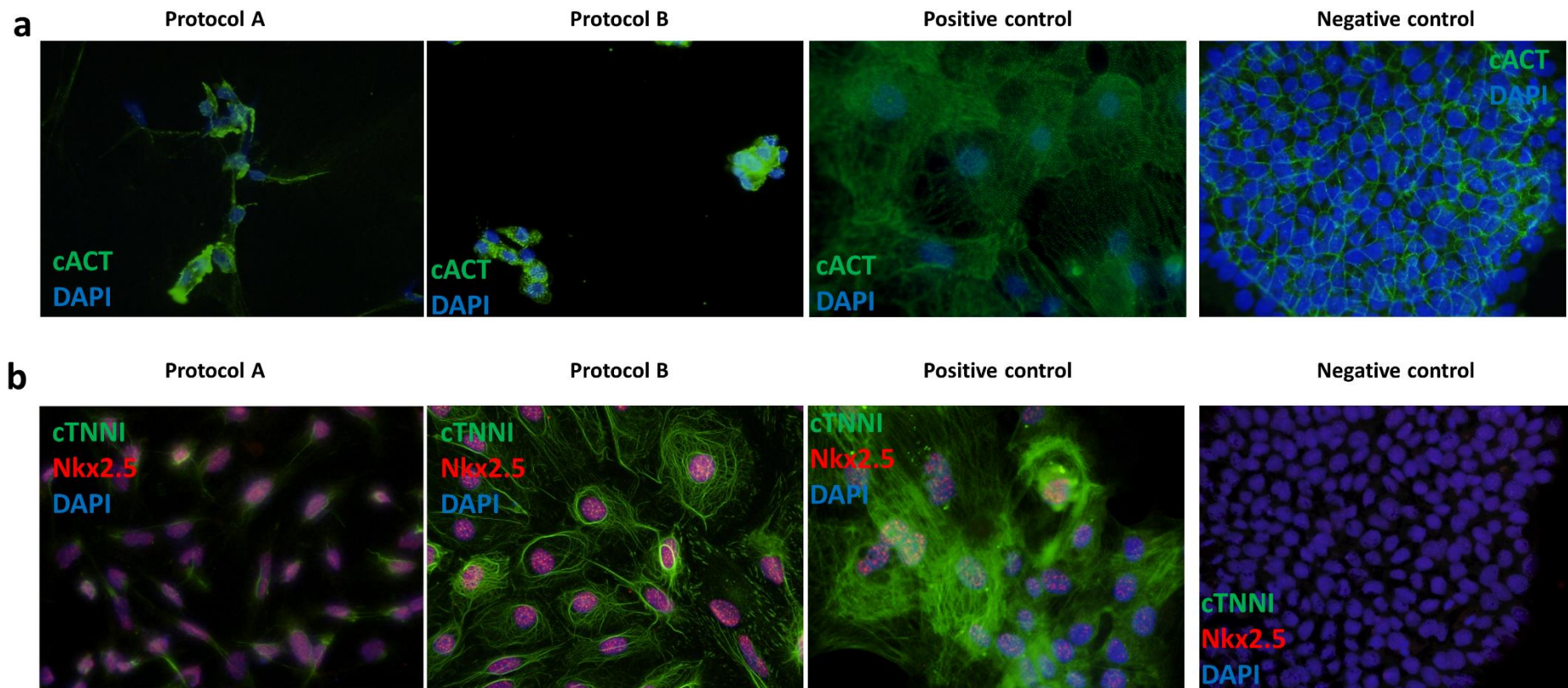
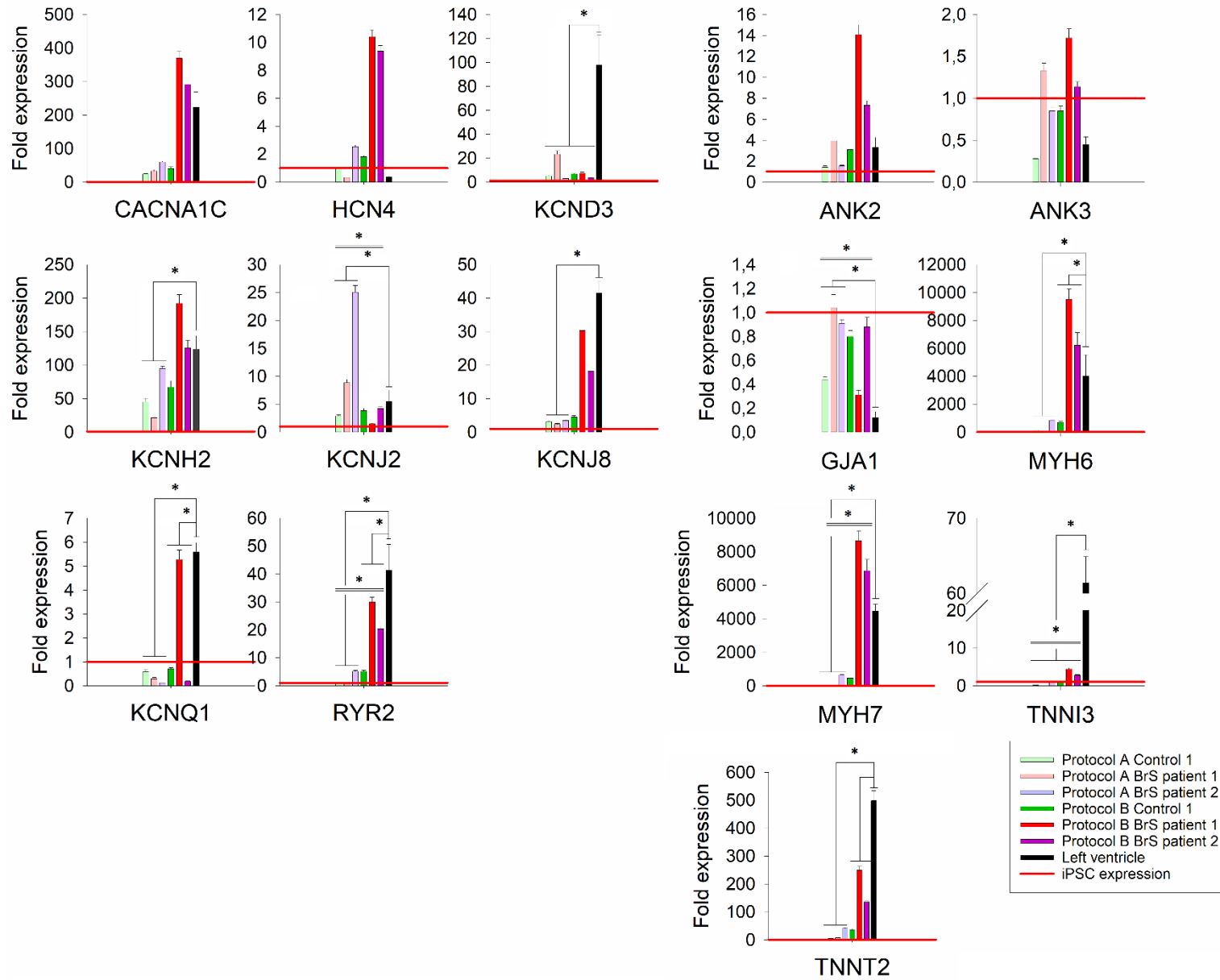


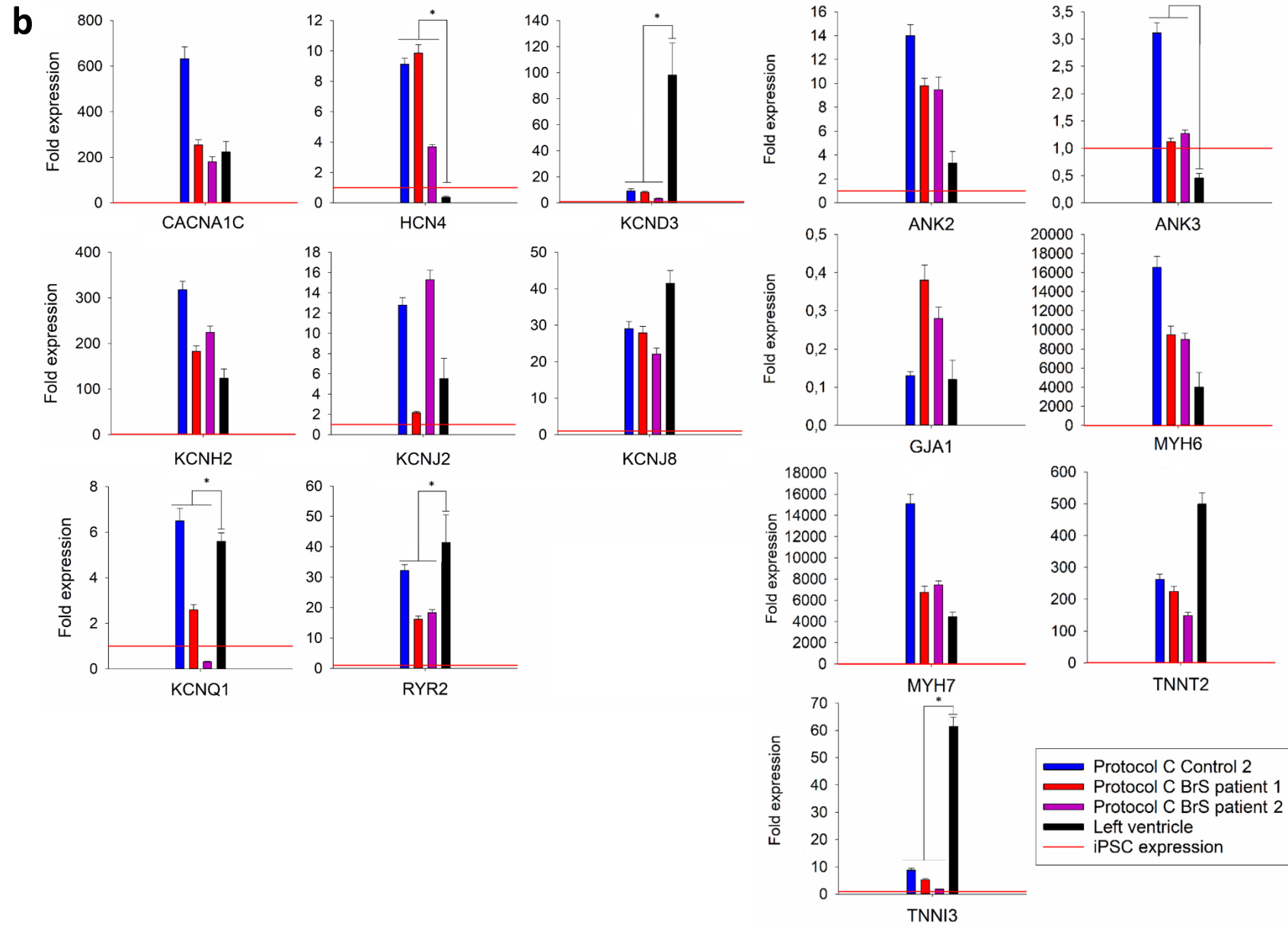
Figure 4-2 Representative immunofluorescence staining of cardiac markers and patch-clamping experiment results for iPSC-CMs in the comparison of protocol A and B. (A) Staining of cardiac α -actinin (cACT) on dissociated and (B) cardiac troponin I (cTNNI) and Nkx2.5 on non-dissociated iPSC-CMs. Nuclei were visualized using DAPI. A positive (commercial iPSC-CMs) and negative (iPSC) control staining results are shown for both tested antibody combinations.

An important feature of the created iPSC-CMs is proper survival after dissociation to allow single-cell patch-clamp recordings, especially required for characterization of specific ionic currents. After dissociation we saw that cells obtained with both protocols showed sufficient survival (>50% of single cells attached to the cover slips were round with smooth cell membrane). For AP characterization, we performed AP recordings on a non-dissociated monolayer, as these reflect a more physiologically relevant condition [21]. We were able to obtain AP recordings for three of the differentiated cell lines (Control 2, BrS patient 1 and 2), however their quality impacted the number of recordings which could be analysed (**Supplementary Table 4-4**). Based on the numbers of recordings per cell line (average 6.7 for protocol A and 10.7 for protocol B; **Supplementary Table 4-4**), the cells generated with protocol B were more approachable (flatter and more elongated) for patch-clamp experiments than those obtained with protocol A. Due to inappropriate RMP (above -50 mV, while physiological RMP ranges from -80 to -90 mV; and iPSC-CMs RMP ranges from -40 to -70 mV), absence of spontaneous activity and/or declining seal quality (due to vivid contractions), we obtained a sufficient number of good quality AP recordings from iPSC-CMs created only by protocol B (BrS patient 1 and 2, n=4 and 2, respectively) (**Supplementary Table 4-4**).

In conclusion, only the application of protocol B led to successful differentiation of all four lines into contracting iPSC-CMs. Protocol A resulted predominantly in 3D morphology, which was not observed in cells obtained with protocol B. Both protocols showed similar differentiation efficiency based on ICC staining, and generated iPSC-CMs expressing all the tested cardiomyocyte-specific markers at the RNA as well as the protein level. However, the expression pattern of cells generated with protocol B resembled that of adult left ventricle more closely and they presented better expression and organization of cTNNI in ICC staining. Finally, the cells generated by protocol B showed a more physiological flatter and more elongated morphology, and were more amenable for patch-clamping, while 3D clumps observed in iPSC-CMs obtained with protocol A impaired their electrophysiological characterization. As such, for future experiments, we opted to focus on further validation of protocol B.

*Figure 4-3 Transcript levels of selected cardiac ion channel and structural genes in generated iPSC-CMs as fold expression compared to iPSCs. (A) Relative expression levels of tested cardiac markers for cells differentiated with protocols A and B: in light green Control 1, in light red BrS patient 1, in light purple BrS patient 2; protocol B: in green Control 1, in red BrS patient 1, in purple BrS patient 2. (B) Relative expression levels of tested cardiac markers for: Control 2 presented in blue, BrS patient 1 in red and BrS patient 2 in purple, obtained in validation experiment of protocol B. The graphs show the average \pm s.d. values from triplicates obtained from the tested samples. In each panel, measured expression levels of the analysed cardiac markers in left ventricle tissue of a healthy donor (in black) are indicated next to the expression measured in the analysed iPSC-CM samples. Relative transcript expression level in iPSC is indicated with red horizontal line for each of the tested markers (fold expression=1). Statistically significant differences in relative transcript expression between the tested protocols and in relation to LV tissue are indicated (respectively) with a double or a single line and a * above the graphs. Calculated P-values for each tested marker between two groups (protocol A versus protocol B) and in relation to the LV tissue are listed in **Supplementary Table 4-3**.*

a



4.3.3 Protocol validation: iPSC-CMs generated with protocol B are suitable for patch-clamping and intracellular Ca²⁺ imaging

Since protocol B was the best performing protocol, we decided to perform a more detailed electrophysiological validation of the generated iPSC-CMs. All tested cell lines differentiated in a contracting/patchy monolayer in all of the replicates for Control 2, three out of six replicates for BrS patient 1 and two out of six replicates for BrS patient 2 (**Table 4-2**). Average contracting areas for Control 2 amounted to 97±0.01%, for BrS patient 1 to 19±10.5% and BrS patient 2 to 80±2.2% (**Table 4-2**).

Table 4-2 Morphological observations and differentiation efficiency from validation experiment of protocol B.

Cell line	Control 2	BrS patient 1	BrS patient 2
Morphology	Monolayer	Patchy monolayer	Monolayer
Number of wells with contracting cells	6/6	3/6	2/6
Contracting areas [%]	97±0.01	19±10.47	80±2.16
Differentiation efficiency [%]	99.7	74.7	N/A*

* no iPSC-CMs left for ICC staining

Differentiation efficiency was calculated from cACT staining (Control 2: 99.7%; BrS patient 1: 74.7%; no ICC was performed for BrS patient 2 as due to obtaining contracting cells in only two out of six replicates those cells were used for AP recordings and RNA extraction; **Table 4-2**). We did observe expression of all cardiac markers (cACT, cTNNI and Nkx2.5) on protein level (**Figure 4-4a**; unmerged images of cACT and cTNNI staining are presented in **Supplementary Figure 4-4**). Expression levels of six of the tested markers (*ANK3*, *HCN4*, *KCND3*, *KCNQ1*, *RYR2* and *TNNI3*) showed significant differences in comparison with the LV tissue (**Figure 4-3b**, **Supplementary Table 4-3**).

We recorded APs from two out of three differentiated iPSC-CM lines (Control 2 and BrS patient 2) (**Figure 4-4b**; **Supplementary Table 4-5**). For BrS patient 1 we mostly obtained contracting iPSC-CMs formed on sides of the coverslips, which were not accessible for patch-clamping experiments. iPSC-CMs from both cell lines showed similar RMP values (-56.3±3.4 and -60.9±4.1 for Control 2 and BrS patient 2, respectively; P=0.76) and amplitude (94±4 for BrS patient 2 and 93.9±8.4 mV for Control 2; P=0.992). We observed that APD was shortened for BrS patient 2 at both 90% and 50% of repolarization [twofold shortening for both APD50 (P=0.0023) and APD90 (P=0.025)] (**Figure 4-4b**; **Supplementary Table 4-5**).

In this validation experiment, we performed calcium imaging on the iPSC-CMs, an additional more high-throughput electrophysiological characterization. We collected CT recordings from Control 2 and BrS patient 1 (the contracting cells of BrS patient 2 were used for AP characterization and RNA extraction; **Figure 4-4c**). Similar to our observations from AP recordings, CTD values for BrS patient 1 were about threefold shorter in comparison to those from Control 2 (P≤0.001) (exact values provided in **Supplementary Table 4-5**). We could also see that BrS patient 1 showed shorter rise time and shorter transient decay in comparison to Control 2 [rise time: 202.3±17.9 ms versus 824.3±24.6 ms versus (P≤0.001); RC: 380.3±28.9 ms versus 1108.1±43.4 ms (P≤0.001), respectively] (**Supplementary Table 4-5**).

Based on the obtained results we conclude that iPSC-CMs generated with selected protocol B are amenable for patch-clamping as well as more high-throughput calcium imaging characterization. Moreover, with the applied techniques we were able to detect differences in both APD and CTD between tested patient and control iPSC-CMs.

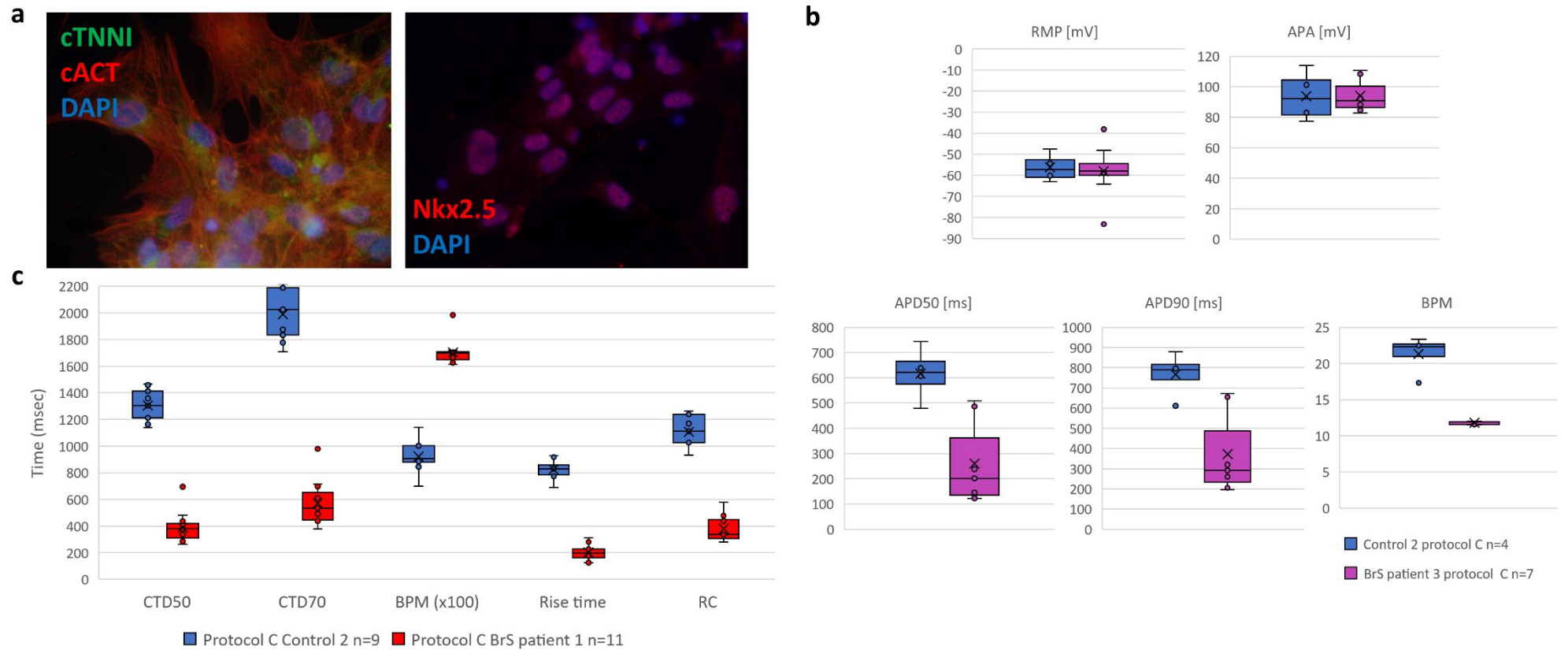


Figure 4-4 Results obtained from iPSC-CM in the validation experiment of protocol B. (A) Representative immunofluorescence staining of cardiac markers cTNNI, cACT and Nkx2.5 on non-dissociated iPSC-CMs; nuclei were visualized using DAPI. (B) AP properties of obtained iPSC-CMs. Displayed from left to right are box plots presenting the range of values for RMP, APA, APD90 and APD50 and BPM with indicated average (x), median (vertical line) and SEM (straight error bar) values for: Control 2 in blue (n=4) and BrS patient 2 in purple (n=7). (C) CT properties of obtained iPSC-CMs. Displayed from left to right are the box plots showing ranges of values for CTD50, CTD70, BPM, rise time and RC with indicated average (x), median (vertical line) and SEM (straight error bar) for Control 2 in blue (n=9) and BrS patient 1 in red (n=11).

4.4 Discussion

Generation of appropriate iPSC-CMs is an important step towards cellular modeling of cardiac arrhythmias. Multiple monolayer-based differentiation protocols have been reported, but to date the comparative performance of such protocols in generating iPSC-CMs from several iPSC cell lines from different individuals was not tested. In this report we selected two protocols with addition of the same small molecule (CHIR99021) to induce mesoderm formation, whilst cardiac lineage differentiation was obtained with the use of different Wnt pathway inhibitors: IWP2 in protocol A and Wnt-C59 in protocol B, respectively (**Figure 4-1b**). In addition, protocol A switched from supplementation of media with B27 supplement lacking insulin to B27 supplement with insulin on day 5 of differentiation, while in protocol B B27 supplement without insulin was used throughout the entire differentiation (**Figure 4-1c**).

We generated iPSC lines from fibroblasts of two healthy donors as well as two BrS patients, and derived iPSC-CMs using the two selected protocols. In a comparison experiment, protocol A led to derivation of cells with a mixed patchy monolayer and 3D clumps morphology (**Table 4-1**). Cells generated with protocol B showed better organization of cTNNI on protein level (**Figure 4-2; Supplementary Figure 4-2**).

In 2017, Jeziorowska et al. published a report in which they compared efficiencies of two monolayer-based differentiation protocols (implementing 6 μ M CHIR99021 and 5 μ M IWP2 or 2.5 μ M IWR1, similar to our protocol A which involved addition of IWP2) with further maintenance in RPMI supplemented with B27 without insulin on three independent iPSC clones derived from a single control fibroblast line [22]. They observed first contractions on day 8 and patchy monolayer morphology in iPSC-CMs obtained with both protocols. In our hands, first contractions occurred starting from day 7 in both protocols A (IWP2) and B (Wnt-C59), while the observed morphology was more protocol specific and varied from monolayer/patchy monolayer to 3D cell clumps (**Figure 4-1c and Table 4-1**) but with the best monolayer formation in our protocol B.

We obtained contracting iPSC-CMs with comparable differentiation efficiency. Jeziorowska et. al. also observed that both tested monolayer-based protocols performed with similar differentiation efficiency (54 \pm 20% and 54 \pm 22% of cTNNI positive iPSC-CMs for IWP2 and IWR1, respectively) but lower than what we observed (\geq 90% of cardiac α -actinin positive iPSC-CMs; **Table 4-1 and Supplementary Table 4-2**) [22]. Nonetheless, in our hands, iPSC-CMs produced by protocol B were of better quality and more accessible for patch-clamp experiments. This was not only observed in the number of analysed recordings with RMP $<$ -50 mV, but as well in the total number of obtained AP recordings (**Supplementary Table 4-4**). This could be explained by the presence of 3D structures formed in iPSC-CMs generated with protocol A, which hampered electrophysiological characterization, as in our experiment AP recordings were obtained from small undissociated clusters of cells (i.e. patches of monolayers). This way we mimicked better the physiological conditions, where cell-cell connections are intact and connecting proteins are structurally similar to that in cardiac tissue, as opposed to an isolated cell [21]. We checked if the obtained AP characteristics of iPSC-CMs from protocol B fall within the normal ranges, based on the AP properties described for iPSC-CMs in seven previous literature reports, where differentiation protocols and patch-clamping conditions similar to our report were used [22-28]. Either commercially available or in-house differentiated control iPSC-CMs were characterized (summarized in **Supplementary Table 4-6**). In these seven studies the following ranges for the analysed AP parameters were observed: RMP -75 to -41.6 mV; APA 64 to 121 mV; APD50 280 to 991 ms and APD90 135 to 1216 ms. We concluded that although published iPSC-CMs were characterized on slightly later time points (0-7 days later; **Figure 4-1c**) all of the obtained AP parameters from our iPSC-CMs fell within the published AP parameter ranges (irrespective of the used differentiation protocol or disease status) (**Figure 4-4b, Supplementary Tables 4-4 and 4-5**).

Although iPSC-CMs show expression of cardiac markers, their relative level differs from this observed in mature cardiomyocytes. Expression pattern of iPSC-CMs usually resembles the pattern observed in human fetal/embryonic cardiomyocytes [29, 30]. We compared relative transcript expression of the selected cardiac markers in our iPSC-CMs with their expression in left ventricular tissue. Five of the

markers: *KCND3*, *KCNQ1*, *RYR2*, *TNNI3* and *TNNT2* showed reduced relative expression in iPSC-CMs from both protocols (**Figure 4-3a; Supplementary Table 4-3; Supplementary Figure 4-3**). Similarly, Jeziorowska et al. reported about 70% reduced relative expression of *RYR2* in their iPSC-CMs derived using monolayer-based protocols. We observed reduced relative expression of *KCNH2*, *KCNJ8*, *MYH6* and *MYH7* and increased expression of *KCNJ2* and *GJA1* in iPSC-CMs generated with protocol A (**Figure 4-3; Supplementary Figure 4-3a; Supplementary Table 4-3**). Those observations suggest immaturity of the obtained iPSC-CMs, as those cardiac markers (*GJA1*, *KCND3*, *KCNH2*, *KCNJ8*, *KCNQ1*, *MYH7*, *RYR2*, *TNNI3*, *TNNT2*) have been reported to be expressed at higher levels in mature iPSC-CMs, obtained during long term culture or after hormonal maturation treatment [31-35]. In iPSC-CMs obtained in our validation experiment, we detected increased relative expression of *HCN4*, in comparison with the reference tissue (**Figure 4-3b; Supplementary Figure 4-3b**). High expression of *HCN4* is a known characteristic of iPSC-CMs, which explains their high spontaneous beating ability (automaticity) [36]. Although overall the expression pattern of cells generated with protocol B implies still incomplete maturity, it resembled that of adult left ventricle more closely in comparison with the tested protocol A.

To understand the underlying cause of the different performance of the tested similar differentiation approaches, we looked at the differences between the protocols. A different small molecule was used for cardiac fate determination, IWP2 in protocol A and Wnt-C59 in protocol B. The mechanism of action of both molecules is based on inhibition of a membrane-bound O-acyltransferase porcupine (PORCN) activity, to prevent Wnt ligand palmitoylation and its subsequent secretion [37]. Although both molecules show different potency (IC₅₀ of 27 nM for IWP2 and 74 pM for Wnt-C59), the concentrations of each molecule used to obtain the inhibitory effect on PORCN in the tested protocols account for this difference (5 μM of IWP2; 2 μM of Wnt-C59). Thus, the differences in performance between the protocols is most likely not attributable to the used small molecules. The remaining differences between the protocols included: (i) inclusion of a rest day before the cardiac fate determination (present in protocol A, absent in protocol B) and (ii) insulin switch (in protocol A) or absence (in protocol B). It was previously shown that insulin presence has an inhibitory effect on cardiomyocyte differentiation at early stages (between day 1–5 of differentiation) by its inhibitory effect on cardiac mesoderm formation, while its presence at later stages of differentiation promotes the oxidative metabolism, characteristic for mature cardiomyocytes [12, 38, 39]. This is why in the tested differentiation protocol A, Lian et al. proposed an insulin switch on day 5 of differentiation [10]. Thus, the included rest day and introduction of insulin in the tested protocol A are the potential critical points in terms of the differences in the iPSC-CM morphology as well as molecular profile of the cells, in comparison to protocol B.

Finally, with results collected in an independent validation experiment we proved that protocol B generated iPSC-CMs with similar morphology and contracting cells from all of the tested cell lines, with efficiency ≥94% (**Table 4-2**). As calcium handling plays an important role in the electromechanical coupling of the human heart, we decided to implement calcium imaging in our experimental pipeline in the validation experiments. Intracellular calcium (Ca²⁺) modulates Na⁺ current density without changing its kinetics in freshly isolated ventricular myocytes [40]. Hwang et al. showed that iPSC-CMs derived from different iPSC lines reprogrammed using different approaches have similar calcium handling properties. Their CT properties are relatively mature around day 21 post differentiation and comparable to those of human native CMs [19]. We compared our CT parameters with those previously published in six independent reports [41-43] (summarized in **Supplementary Table 4-7**). These six papers revealed the following ranges for CT parameters: CTD90 1093–2897.5 ms; CTD50 459–1633 ms; rise time 85–500 ms and transient decay 230–2937 ms. The CT values (CTD50, rise time and transient decay) obtained from our iPSC-CMs generated from both Control 2 and BrS patient 1 iPSC-CMs fitted within the range of previously published data (**Figure 4-4c; Supplementary Table 4-5**). It has previously been shown that calcium transient duration is usually longer than APD (1.2–2 times longer) [44] and this property was also noted in our electrophysiological data for Control 2 iPSC-CMs (**Figure 4-4c; Supplementary Table 4-5**). We noticed significant APD and CTD shortening for BrS patient lines in comparison to our Control 2 iPSC-CMs [twofold shorter APD50 (P=0.0023) and 3.4-fold shorter CTD50 (P≤0.001)] and we also observed a shorter

rise time ($P \leq 0.001$) and slower transient decay ($P \leq 0.001$) in CT recordings of BrS patient 1 in comparison to Control 2 (**Figure 4-4b-c**). Additional patch clamp, sodium current measurement and calcium imaging experiments on BrS patients with the identical *SCN5A* founder mutation are needed in the prospective experiments to confirm these observations.

In the methodology of differentiations used in this report we focused on comparison of basic differentiation conditions. As the expression profile of the tested cardiac markers of our iPSC-CMs suggests their immaturity, for future experiments additional maturation strategies will be applied on the cells, such as triiodothyronine and/or glucocorticoid hormone treatment, micropatterning, electrical and/or mechanical stimulation or addition of specific miRNAs [45-49].

In conclusion, we were able to generate functional iPSC-CMs using both selected protocols. Both protocols A and B show similar efficiency of differentiation and produce CMs with electrophysiological parameters falling within the range of previously reported values for control iPSC-CMs. Moreover, both protocols generate cells expressing all of the tested cardiac markers on protein and RNA level. For our prospective experiments, we decided to further optimize protocol B based on the findings that the obtained iPSC-CMs showed (i) more consistent cardiac markers expression between the differentiation batches, with a closer resemblance of that observed in the left ventricle, (ii) better sarcomeric protein organization, (iii) >50% survival after dissociation and (iv) monolayers that were more amenable for patch clamp and calcium transient experiments.

4.5 Materials and methods

4.5.1 Fibroblast reprogramming to iPSCs and validation

Commercial fibroblasts – BJ (ATCC®CRL-2522™) (referred to as Control 1) were thawed and cultured for 8 days prior to reprogramming. Skin biopsies from one healthy control donor (Control 2) and two BrS patients (BrS patient 1 and 2 –carrying the same *SCN5A* variant: a Belgian BrS founder mutation c.4813+3_4813+6dupGGGT [47]) were obtained using standard procedures and processed on the day of collection as follows: after mechanical cutting, sample underwent enzymatic digestion in 37°C in a mixture of trypsin (Life Technologies) and collagenase type IV (Sigma-Aldrich) (1:1) for 1 h. Cells were brought to culture in a T25 flask (Corning) in fibroblast culture media consisting of RPMI1640 media (Life Technologies) supplemented with 10% FBS (Life Technologies), 1% of Penicillin/Streptomycin (Life Technologies), 1% of sodium pyruvate (Sigma-Aldrich) and 0.1% of primocin (InvivoGen Europe), and cultured in 5% CO₂ humidified conditions in 37°C up to 3 weeks.

Before transduction, cells were tested for absence of Mycoplasma DNA (LookOut® Mycoplasma PCR Detection Kit, Sigma-Aldrich) according to the supplier's protocol. Cells were cultured on tissue culture treated dishes (CORNING CoStar) in 37°C with 5% CO₂. Reprogramming of the fibroblasts was performed using the CytoTune™-iPS 2.0 Sendai Reprogramming Kit and Essential 8 Flex media (Life Technologies), according to the protocol provided by the supplier for feeder-free cell culture. iPSC colonies were selected manually throughout ten passages [five passages using single colony picking and further on at least five passages were performed using Versene EDTA solution (Lonza) according to suppliers' protocol], from day 21 onwards on plates coated with extracellular matrix (Matrigel, CORNING) diluted in DMEM F12 media (Life Technologies) according to the suppliers' protocol (**Figure 4-1a**) [51].

The obtained iPSCs were validated confirming the presence of pluripotency markers [Nanog (Cell Signaling Technology), Oct 3/4 (Cell Signaling Technology), Tra 1-60 (Life Technologies), Tra 1-81 (Life Technologies)] with immunofluorescence staining on non-dissociated iPSC colonies fixed on passage 10 (P10) (**Supplementary Figure 4-1; Supplementary Tables 4-8 and 4-9**), performing a qPCR analysis to prove absence of Sendai virus vectors and running SNP arrays to confirm retention of genomic integrity, using protocols described below. For long term preservation in liquid nitrogen, cells were frozen down in KnockOut Serum Replacement (Life Technologies) supplemented with 10% DMSO (Sigma-Aldrich).

4.5.2 Immunofluorescence staining

iPSCs/iPSC-CMs for immunofluorescence staining were grown on glass coverslips (Saillart Glass Atelier). iPSCs on P10 or iPSC-CMs on D20-30 were fixed by incubation with 98% ice cold methanol (Sigma-Aldrich) for 20 min in -20°C and washed afterwards with PBS (Life Technologies). Permeabilization of the cells was carried out for 15 min with PBS supplemented with 0.1% Triton X-100 (Sigma-Aldrich). Subsequently cells were incubated with the blocking solution at room temperature for 30 min for iPSCs and 1 h for iPSC-CMs. Primary antibodies were diluted in DAKO real diluent (DAKO) and cells were incubated overnight at 4°C . Secondary antibodies were diluted in DAKO Real antibody diluent and cells were incubated for 1 h to stain pluripotency markers [Nanog (Life Technologies), Oct 3/4 (Santa Cruz Biotechnology), Tra 1-60 (Cell Signaling Technology), Tra 1-81 (Cell Signaling Technology)] or cardiac specific markers [cardiac α -actinin (cACT) (Abcam), cardiac troponin I (cTNNI) (Abcam) and Nkx2.5 (Abcam)] at room temperature. The composition of blocking solutions and dilutions of each antibody used are listed in detail in **Supplementary Table 4-8** for pluripotency and **Supplementary Table 4-9** for cardiomyocyte markers. Nuclei were visualized by 5 min incubation with DAPI (Life Technologies) in a 1 in 1000 dilution in PBS. Before imaging, cells were mounted with mounting solution Fluoromount-G (Life Technologies). Fluorescent images were acquired at room temperature using an Olympus BX51 fluorescence microscope equipped with an Olympus DP71 digital camera. cellSens software was used for image acquisition and processing.

4.5.3 Sendai vectors presence test

Prior to the differentiation experiments, selected clones were validated for the absence of the reprogramming vectors. The cell pellets containing 5×10^5 – 1×10^6 cells were collected on day 0 of reprogramming (Sendai negative control), day 7 of reprogramming (Sendai positive control) and passage 10 during reprogramming from each of the validated clones for each reprogrammed cell line. Pellets were resuspended in RNA lysis buffer and frozen down in -80°C prior to extraction. RNA was extracted using RNA extraction kit (Zymo) and cDNA was prepared using Super Script III First Strand Synthesis kit (Life Technologies) according to the manufacturer's protocols.

Sendai virus presence PCR was carried out using primers from the sequences provided by the supplier in User Guide: Cyto Tune™-iPS 2.0 Sendai Reprogramming Kit using Taq Polymerase and Buffer (Life Technologies) using the PCR protocol described in **Supplementary Table 4-10**. The iPSC clone was considered Sendai negative when primers for Sendai virus backbone and at least two out of three other primer pairs showed a negative result.

4.5.4 Genomic integrity test using SNP array

DNA sample was collected from: fibroblasts on D0 of reprogramming and iPSC clones on passage 10 before differentiation to CMs. DNA was extracted using an automatic DNA extraction system Maxwell® RSC with Maxwell® RSC Cultured Cells DNA Kit (Promega), following the supplier's protocol. Briefly, 5×10^5 – 1×10^6 cells were collected from cell culture dishes and centrifuged at 120 rcf for 5 min at room temperature. The supernatant was discarded, and cell pellet was frozen down in -20°C until the day of extraction. Cell pellet was thawed at room temperature and resuspended in the media residues present in the sample. One Maxwell® RSC Cultured Cells DNA Cartridge was used per sample. First well of the DNA Cartridge was loaded with the cell sample and mixed by pipetting with the lysis buffer in the well. Elution tubes on the deck tray were filled with 100 μl of Elution Buffer. Extraction was carried out using Maxwell RSC Instrument using the Cultured Cells DNA method and DNA sample was stored at $+4^{\circ}\text{C}$ after extraction.

HumanCytoSNP-12 array (Illumina) was run according to the supplier's protocol for the automated Infinium HD Assay Ultra. Genome Studio (Illumina) software was used to visualize results and confirm identity between the iPSC clones and original fibroblast line. Results were further analysed with CNV-WebStore, an in-house developed online available CNV Analysis tool (<http://cnv-webstore.ua.ac.be>).

Large novel CNVs (>100 kb) detected in the used iPSC clones, which were absent in the original fibroblast cell lines are presented in **Supplementary Table 4-1**.

4.5.5 Cardiomyocyte differentiation

Prior to differentiation, cells underwent two to three expansion passages using Versene/EDTA 0.02% solution (Lonza) and final passage on six-well cell culture treated plates (CORNING CoStar) with glass coverslips (Saillart, Glass Atelier), coated with Matrigel (Corning). iPSCs were cultured in an incubator with humidified conditions at 37°C and 5% CO₂ until they reached 80–90% confluency before starting the differentiation procedure. Both differentiation protocols started on day 0 with RPMI1640 (Life Technologies) media supplemented with 2% B27 supplement without insulin (Life Technologies) and CHIR99021 (6 µM, Axon Medchem) to induce mesodermal differentiation (**Figure 4-1b-c**). The next steps for each protocol were as follows:

Protocol A – previously reported by Lian et al. [10], briefly: on day 3 of differentiation, RPMI1640 medium with 2% B27 supplement without insulin and IWP2 (5 µM, SelleckChem) was added to the cells for 48 hours. Cells were subsequently cultured in RPMI1640 medium with 2% B27 supplement with insulin (**Figure 4-1c**).

Protocol B – previously described by Burridge et al. [11], briefly: on day 2 of differentiation cells were cultured in RPMI1640 medium with 2% B27 supplement without insulin and Wnt-C59 (2 µM, SelleckChem) for the next 48 hours. Cells were subsequently cultured in RPMI1640 medium with 2% B27 supplement without insulin (**Figure 4-1c**).

From day 0 of differentiation, cells were cultured in an incubator with humidified atmosphere at 37°C and 5% CO₂. Cells were cultured until D20 of differentiation before performing further experiments. For RNA collection and single-cell patch-clamp recordings, dissociation of iPSC-CMs was performed using Accumax or TrypLE (Life Technologies) according to the suppliers' protocol.

Undissociated cells were fixed on D20-25 of differentiation and immunofluorescence staining for cardiac specific markers [cardiac α -actinin (cACT), cardiac troponin I (cTNNI) and Nkx2.5] was performed according to the protocol described in detail in the Immunofluorescence staining section of the Materials and Methods. Analysis of iPSC-CMs quality was performed based on the expression of cardiac specific markers on RNA level, as well as expression and organization of the sarcomeric proteins based on immunofluorescence staining. Electrophysiological properties were characterized from AP/CT recordings to investigate signal propagation in iPSC-CMs and their general electrophysiological activity.

4.5.6 Electrophysiological experiments

Perforated-patch AP recordings were performed 25-28 days after the start of differentiation at room temperature (20-22°C) on non-dissociated cells (unless stated otherwise) grown on glass coverslips using the current clamp mode of the Axopatch 200B amplifier and a pClamp 10.7/Digidata 1440A acquisition system (Axon Molecular Devices). Patch-pipettes with a resistance of approximately 2 M Ω were pulled from 1.2 mm borosilicate glass capillaries (World Precision Instruments, Inc.) using a P-2000 puller (Sutter Instrument Co.). Pipettes were filled with an intracellular solution containing (in mM): 4 NaCl, 106 KCl, 5 K₂ATP, 2 MgCl₂, 5 K₄BAPTA and 10 HEPES adjusted to pH 7.2 with KOH and addition of 0.72 ng/mL amphotericin B (A9528, Sigma Aldrich). The cells were continuously superfused at 1mL/min rate with an extracellular solution (ECS) containing (in mM): 150 NaCl, 5.4 KCl, 1.8 CaCl₂, 1 MgCl₂, 15 HEPES, 15 glucose, 1 Na-pyruvate adjusted to pH 7.4 with NaOH. Junction potentials were compensated prior to sealing of the cell before the patch pipette made contact with the cell membrane.

AP waveforms were recorded using the current clamp mode under the whole-cell perforated patch configuration without pacing. Spontaneous APs were recorded over 10s per sweep. Recordings were carried out for maximum 10 minutes after obtaining perforated cell access.

Intracellular Ca²⁺ transients (CT) were registered from cell populations on an epifluorescent microscope setup using a Photomax 200 detection system (DAGAN). The iPSC-CMs were loaded with 5 μM Cal-520 AM (Abcam, ab171868) fluorogenic calcium sensitive dye and 1% Pluronic™ F-127 (20% solution in DMSO, Life Technologies, P300MP) supplemented to the culture medium. After incubation for 60-90 min (37°C, 5% CO₂), the cells were washed with pre-warmed ECS and incubated for 30 min to allow recovery before imaging. Experiments were performed on non-dissociated cells at D25-28 on glass coverslips using the same ECS solution as for AP recordings.

Electrophysiological data was analysed using PClamp10 software (Axon CNS Molecular devices). For each cell recording, AP and CT values were calculated as a mean of five subsequent waveforms and data are presented as a mean ± SEM of the means for each single cell of the 'n' cells analysed. The following parameters were analysed: APA, RMP, APD50 and APD90. The time between two AP peaks was presented as BPM (60/time in seconds). APD correction related to beating rate was not performed, as the obtained iPSC-CMs were all beating slower than 60 BPM. The amplitudes of Ca²⁺ transients are presented as a pseudo difference $\Delta F = F - F_{\text{base}}$ where the F and F_{base} are the measured fluorescence intensity at the peak and before/after the CT. To determine the rate constant of decay (RC), the slope after the ΔF_{max} to F_{base} was fitted using standard exponential function: $f(t) = \sum_{i=1}^n A_i e^{-t/\tau_i} + C$. Comparisons between groups were performed using one-way ANNOVA (Systat Software Inc.). A p-value of ≤0.05 is considered statistically significant.

4.5.7 qPCR

RNA was extracted from iPSC-CMs on D20-25 of differentiation, using RNA Extraction Kit (Zymo) and cDNA was prepared using Super Script III First Strand Synthesis kit (Life Technologies) according to the manufacturer's protocols. Quantitative RT-PCR of cardiac markers: *ANK2*, *ANK3*, *CACNA1C*, *GJA1* (*CNX43*), *HCN4*, *KCND3*, *KCNH2*, *KCNJ2*, *KCNJ8*, *KCNQ1*, *MYH6*, *MYH7*, *RYR2*, *TNNT2*, *TNNI3* was performed using in-house designed primers listed in **Supplementary Table 4-11** and qPCR MasterMix Plus for SYBR Assay No-ROX (Tebu-bio N.V.). Each reaction was performed in triplicate and fold changes in gene expression were determined using the comparative CT method ($\Delta\Delta\text{Ct}$) with normalization to three reference genes: *GAPDH*, *ECHS1* and *RPL13A* and relative to the expression in iPSCs. Results were analysed using QBase 3.2 (Biogazelle). As ventricular cardiomyocytes are the cell type of interest to study inherited arrhythmia disorders, healthy human heart donor left ventricle (LV) tissue expression is shown as a reference in relative expression graphs and the expression profile of iPSC-CMs generated with each protocol was statistically compared with the reference tissue.

Comparison of the normalized Ct values between the groups (protocols and reference tissue) was performed with a linear mixed model, having the protocol as fixed effect and the normalized Ct value as dependent variable. The nonindependence between observations within the same cell line was accounted for using a random intercept for cell line, and a random slope for protocol. Pairwise comparisons between the protocols and/or reference tissue were carried out using a post hoc analysis with Tukey's correction for multiple hypothesis testing. Analyses were carried out in the software package R version 4.0.2, and the add on packages lme4 and multcomp. A p-value of ≤ 0.05 is considered statistically significant.

4.5.8 Imaging data analysis

The light microscopy images of contracting iPSC-CMs were acquired at a rate of 20 frames per second using cellSens software (Olympus LS) and converted to TIFF images for analysis using Fiji image analysis freeware [49], with manual indication of the areas of contracting cell monolayer, based on the movements of the pixels in the generated stacks of images. The calculated contracting area sizes were measured in mm² and divided by the area of the whole image of the culture surface (approximately 96 mm²).

Differentiation efficiency was calculated based on in total four randomly taken immunofluorescence staining images for cACT for each tested iPSC-CM line. Fluorescence images were analysed using CellBlocks, a Fiji script for cell-based analysis [53]. In brief, individual nuclei were detected using

a Laplacian operator and automatic thresholding on the DAPI-channel. After particle analysis and dilation of the nuclear objects, the resulting regions of interest were used to measure the signal intensities in the cACT on the GFP channels within 50 μM around the nuclei. User-defined thresholds were set to classify cells as being positive for either marker, calibrated to commercial hSC-CMs [54] as a positive control and negative fibroblast cACT expression. Efficiency is presented as percentage of cells positive for cACT.

4.6 References

- [1] Kehat, I.; Snir, M.; Segev, H.; Amit, M.; Gepstein, A.; Livne, E.; Binah, O.; Itskovitz-Eldor, J.; Gepstein, L. Human embryonic stem cells can differentiate into myocytes with structural and functional properties of cardiomyocytes. *The Journal of Clinical Investigation*. 2001;108(3):407-14.
- [2] Zhang, J.; Wilson, G.F.; Herman, A.M.; Lian, X.; Raval, K.K.; Barron, M.R.; Hou, L.; Soerens, A.G.; Yu, J.; et al. Extracellular matrix promotes highly efficient cardiac differentiation of human pluripotent stem cells: the matrix sandwich method. *Circulation Research*. 2012;111(9):1125-36.
- [3] Yang, L.; Adler, E.D.; Roepke, T.K.; Kattman, S.J.; Kennedy, M.; Henckaerts, E.; Bonham, K.; Abbott, G.W.; Linden, R.M.; Field, L.J.; et al. Human cardiovascular progenitor cells develop from a KDR+ embryonic-stem-cell-derived population. *Nature*. 2008;453(7194):524-8.
- [4] Burridge, P.W.; Millrod, M.A.; Weinberg, S.; Yuan, X.; Peters, A.; Mahairaki, V.; Koliatsos, V.E.; Tung, L.; Zambidis, E.T. A universal system for highly efficient cardiac differentiation of human induced pluripotent stem cells that eliminates interline variability. *Plos One*. 2011;6(4).
- [5] Lian, X.; Wilson, G.; Zhu, K.; Hazeltine, L.B.; Azarin, S.M.; Raval, K.K.; Zhang, J.; Kamp, T.J.; Palecek, S.P. Robust cardiomyocyte differentiation from human pluripotent stem cells via temporal modulation of canonical Wnt signaling. *Proceedings of the National Academy of Sciences of the United States of America*. 2012;109(27):1848-57.
- [6] Minami, I.; Otsuji, T.G.; Yamamoto, T.; Shen, Y.; Otsuka, S.; Kadota, S.; Morone, N.; Barve, M.; Asai, Y.; Tenkova-Heuser, T.; Heuser, J.E.; Uesugi, M.; et al. A small molecule that promotes cardiac differentiation of human pluripotent stem cells under defined, cytokine- and xeno-free conditions. *Cell Reports*. 2012;2(5):1448-60.
- [7] Correia, C.; Serra, M.; Espinha, N.; Sousa, M.; Brito, C.; Burkert, K.; et al. Combining hypoxia and bioreactor hydrodynamics boosts induced pluripotent stem cell differentiation towards cardiomyocytes. *Stem Cell Rev Rep*. 2014;10(6):786-801.
- [8] Bhattacharya, S.; Burridge, P.W.; Kropp, E.M.; Chuppa, S.L.; Kwok, W.M.; Wu, J.C.; et al. High efficiency differentiation of human pluripotent stem cells to cardiomyocytes and characterization by flow cytometry. *J Vis Exp*. 2014(91):52010.
- [9] D'Amour, K.A.; Agulnick, A.D.; Eliazar, S.; Kelly, O.G.; Kroon, E.; Baetge, E.E. Efficient differentiation of human embryonic stem cells to definitive endoderm. *Nat Biotechnol*. 2005;23(12):1534-41.
- [10] Lian, X.; Azarin, S. M.; Zhu, K.; Hazeltine, L. B.; Bao, X.; Hsiao, C.; Kamp, T. J.; Palecek, S. P. Directed cardiomyocyte differentiation from human pluripotent stem cells by modulating Wnt/b-catenin signaling under fully defined conditions. *Nature Protocols*. 2013;8(1):162-75.
- [11] Burridge, P. W.; Shukla, P.; Lin, Z. C.; Churko, J. M.; Ebert, A. D.; Lan, F.; Diecke, S.; Huber, B.; Mordwinkin, N. M.; Plews, J. R.; Abilez, O. J.; et al. Chemically defined generation of human cardiomyocytes. *Nature Methods*. 2014;11(8):855-64.
- [12] Lian, X.; Zhang, J.; Zhu, K.; Kamp, T.J.; Palecek, S.P. Insulin inhibits cardiac mesoderm, not mesendoderm, formation during cardiac differentiation of human pluripotent stem cells and modulation of canonical Wnt signaling can rescue this inhibition. *Stem Cells*. 2013;31(3):447-57.
- [13] Ren, Y.; Lee, M.Y.; Schliffke, S.; Paavola, J.; Amos, P.J.; Ge, X.; et al. Small molecule Wnt inhibitors enhance the efficiency of BMP-4-directed cardiac differentiation of human pluripotent stem cells. *J Mol Cell Cardiol*. 2011;51(3):280-7.
- [14] Moretti, A.; Bellin, M.; Welling, A.; Jung, C.B.; Lam, J.T.; Bott-Flugel, L.; et al. Patient-specific induced pluripotent stem-cell models for long-QT syndrome. *N Engl J Med*. 2010;363(15):1397-409.
- [15] Yazawa, M.; Jia, X.; Pasca, A.M.; Bernstein, J.A.; Hallmayer, J.; Dolmetsch, R.E. Using induced pluripotent stem cells to investigate cardiac phenotypes in Timothy syndrome. *Nature*. 2011;471(7337):230-4.
- [16] Jung, C.B.; Mederos y Schnitzler, M.; Iop, L.; Storch, U.; Bellin, M.; Dorn, T.; Ruppenthal, S.; Pfeiffer, S.; Goedel, A.; Dirschinger, R.J.; Seyfarth, M.; et al. Dantrolene rescues arrhythmogenic RYR2 defect in a patient-specific stem cell model of catecholaminergic polymorphic ventricular tachycardia. *EMBO Molecular Medicine*. 2012;4(3):180-91.

- [17] Kim, C.; Wen, J.; Wang, S.; Wang, C.; Spiering, S.; Kan, N.G.; Forcales, S.; Puri, P.L.; Leone, T.C.; Marine, J.E.; et al. Studying arrhythmogenic right ventricular dysplasia with patient-specific iPSCs. *Nature*. 2013;494(7435):105-10.
- [18] Cerrone, M.; Zhang, M.; Agullo-Pascual, E.; Pfenniger, A.; Chkourko Gusky, H.; Novelli, V.; Kim, C.; Tirasawadichai, T.; Judge, D.P.; Rothenberg, E.; Chen, H.S.; et al. Missense mutations in plakophilin-2 cause sodium current deficit and associate with a Brugada syndrome phenotype. *Circulation*. 2014;129(10):1092-103.
- [19] Hwang, H.S.; Kryshal, D.O.; Feaster, T.K.; Sanchez-Freire, V.; Zhang, J.; Kamp, T.J.; et al. Comparable calcium handling of human iPSC-derived cardiomyocytes generated by multiple laboratories. *J Mol Cell Cardiol*. 2015;85:79-88.
- [20] Nijak, A.; Saenen, J.; Labro, A.J.; Schepers, D.; Loeys, B.L.; Alaerts, M. iPSC-Cardiomyocyte Models of Brugada Syndrome - Achievements, Challenges and Future Perspectives. *International Journal of Molecular Sciences*. 2021;22(6):2825.
- [21] Van de Sande, D.V.; Kopljak, I.; Alaerts, M.; Teisman, A.; Gallacher, D.J.; Loeys, B.; et al. The resting membrane potential of hSC-CM in a syncytium is more hyperpolarised than that of isolated cells. *Channels (Austin)*. 2021;15(1):239-52.
- [22] Jeziorowska, D.; Fontaine, V.; Jouve, C.; Villard, E.; Dussaud, S.; Akbar, D.; et al. Differential Sarcomere and Electrophysiological Maturation of Human iPSC-Derived Cardiac Myocytes in Monolayer vs. Aggregation-Based Differentiation Protocols. *Int J Mol Sci*. 2017;18(6).
- [23] Bett, G.C.; Kaplan, A.D.; Lis, A.; Cimato, T.R.; Tzanakakis, E.S.; Zhou, Q.; et al. Electronic "expression" of the inward rectifier in cardiocytes derived from human-induced pluripotent stem cells. *Heart Rhythm*. 2013;10(12):1903-10.
- [24] Gibson, J.K.; Yue, Y.; Bronson, J.; Palmer, C.; Numann, R. Human stem cell-derived cardiomyocytes detect drug-mediated changes in action potentials and ion currents. *J Pharmacol Toxicol Methods*. 2014;70(3):255-67.
- [25] Meijer van Putten, R.M.; Mengarelli, I.; Guan, K.; Zegers, J.G.; van Ginneken, A.C.; Verkerk, A.O.; et al. Ion channelopathies in human induced pluripotent stem cell derived cardiomyocytes: a dynamic clamp study with virtual IK1. *Front Physiol*. 2015;6:7.
- [26] Lopez-Redondo, F.; Kurokawa, J.; Nomura, F.; Kaneko, T.; Hamada, T.; Furukawa, T.; et al. A distribution analysis of action potential parameters obtained from patch-clamped human stem cell-derived cardiomyocytes. *J Pharmacol Sci*. 2016;131(2):141-5.
- [27] Herron, T.J.; Rocha, A.M.; Campbell, K.F.; Ponce-Balbuena, D.; Willis, B.C.; Guerrero-Serna, G.; et al. Extracellular Matrix-Mediated Maturation of Human Pluripotent Stem Cell-Derived Cardiac Monolayer Structure and Electrophysiological Function. *Circ Arrhythm Electrophysiol*. 2016;9(4):e003638.
- [28] Feaster, T.K.; Cadar, A.G.; Wang, L.; Williams, C.H.; Chun, Y.W.; Hempel, J.E.; et al. Matrigel Mattress: A Method for the Generation of Single Contracting Human-Induced Pluripotent Stem Cell-Derived Cardiomyocytes. *Circ Res*. 2015;117(12):995-1000.
- [29] Zhou, Y.; Wang, L.; Liu, Z.; Alimohamadi, S.; Yin, C.; Liu, J.; et al. Comparative Gene Expression Analyses Reveal Distinct Molecular Signatures between Differentially Reprogrammed Cardiomyocytes. *Cell Rep*. 2017;20(13):3014-24.
- [30] Karakikes, I.; Ameen, M.; Termglinchan, V.; Wu, J.C. Human induced pluripotent stem cell-derived cardiomyocytes: insights into molecular, cellular, and functional phenotypes. *Circ Res*. 2015;117(1):80-8.
- [31] Zhao, Z.; Lan, H.; El-Battrawy, I.; Li, X.; Buljubasic, F.; Sattler, K.; et al. Ion Channel Expression and Characterization in Human Induced Pluripotent Stem Cell-Derived Cardiomyocytes. *Stem Cells Int*. 2018;2018:6067096.
- [32] Lewandowski, J.; Rozwadowska, N.; Kolanowski, T.J.; Malcher, A.; Zimna, A.; Rugowska, A.; et al. The impact of *in vitro* cell culture duration on the maturation of human cardiomyocytes derived from induced pluripotent stem cells of myogenic origin. *Cell Transplant*. 2018;27(7):1047-67.
- [33] Sottas, V.; Wahl, C.M.; Trache, M.C.; Bartolf-Kopp, M.; Cambridge, S.; Hecker, M.; et al. Improving electrical properties of iPSC-cardiomyocytes by enhancing Cx43 expression. *J Mol Cell Cardiol*. 2018;120:31-41.

- [34] Bedada, FB.; Wheelwright, M.; Metzger, JM. Maturation status of sarcomere structure and function in human iPSC-derived cardiac myocytes. *Biochim Biophys Acta*. 2016;1863(7 Pt B):1829-38.
- [35] Garg, P.; Garg, V.; Shrestha, R.; Sanguinetti, MC.; Kamp, TJ.; Wu, JC. Human Induced Pluripotent Stem Cell-Derived Cardiomyocytes as Models for Cardiac Channelopathies: A Primer for Non-Electrophysiologists. *Circ Res*. 2018;123(2):224-43.
- [36] Goversen, B.; van der Heyden, MAG.; van Veen, TAB.; de Boer, TP. The immature electrophysiological phenotype of iPSC-CMs still hampers *in vitro* drug screening: Special focus on IK1. *Pharmacol Ther*. 2018;183:127-36.
- [37] Chen B, Dodge ME, Tang W, Lu J, Ma Z, Fan CW, et al. Small molecule-mediated disruption of Wnt-dependent signaling in tissue regeneration and cancer. *Nat Chem Biol*. 2009;5(2):100-7.
- [38] Freund C, Ward-van Oostwaard D, Monshouwer-Kloots J, van den Brink S, van Rooijen M, Xu X, et al. Insulin redirects differentiation from cardiogenic mesoderm and endoderm to neuroectoderm in differentiating human embryonic stem cells. *Stem Cells*. 2008;26(3):724-33.
- [39] Zhao M, Tang Y, Zhou Y, Zhang J. Deciphering Role of Wnt Signalling in Cardiac Mesoderm and Cardiomyocyte Differentiation from Human iPSCs: Four-dimensional control of Wnt pathway for hiPSC-CMs differentiation. *Sci Rep*. 2019;9(1):19389.
- [40] Casini, S.; Verkerk, AO.; van Borren, MM.; van Ginneken, AC.; Veldkamp, MW.; de Bakker, JM.; et al. Intracellular calcium modulation of voltage-gated sodium channels in ventricular myocytes. *Cardiovasc Res*. 2009;81(1):72-81.
- [41] Shah, D.; Virtanen, L.; Prajapati, C.; Kiamehr, M.; Gullmets, J.; West, G.; et al. Modeling of LMNA-Related Dilated Cardiomyopathy Using Human Induced Pluripotent Stem Cells. *Cells*. 2019;8(6).
- [42] Shah, D.; Prajapati, C.; Penttinen, K.; Cherian, RM.; Koivumaki, JT.; Alexanova, A.; et al. hiPSC-Derived Cardiomyocyte Model of LQT2 Syndrome Derived from Asymptomatic and Symptomatic Mutation Carriers Reproduces Clinical Differences in Aggregates but Not in Single Cells. *Cells*. 2020;9(5).
- [43] Liang, P.; Sallam, K.; Wu, H.; Li, Y.; Itzhaki, I.; Garg, P.; et al. Patient-Specific and Genome-Edited Induced Pluripotent Stem Cell-Derived Cardiomyocytes Elucidate Single-Cell Phenotype of Brugada Syndrome. *J Am Coll Cardiol*. 2016;68(19):2086-96.
- [44] Prajapati, C.; Polonen, RP.; Aalto-Setälä, K. Simultaneous recordings of action potentials and calcium transients from human induced pluripotent stem cell derived cardiomyocytes. *Biol Open*. 2018;7(7).
- [45] White, MC.; Pang, L.; Yang, X. MicroRNA-mediated maturation of human pluripotent stem cell-derived cardiomyocytes: Towards a better model for cardiotoxicity? *Food Chem Toxicol*. 2016;98(Pt A):17-24.
- [46] Yang, X.; Rodriguez, M.; Pabon, L.; Fischer, KA.; Reinecke, H.; Regnier, M.; et al. Tri-iodo-L-thyronine promotes the maturation of human cardiomyocytes-derived from induced pluripotent stem cells. *J Mol Cell Cardiol*. 2014;72:296-304.
- [47] Ulmer, BM.; Stoehr, A.; Schulze, ML.; Patel, S.; Gucek, M.; Mannhardt, I.; et al. Contractile Work Contributes to Maturation of Energy Metabolism in hiPSC-Derived Cardiomyocytes. *Stem Cell Reports*. 2018;10(3):834-47.
- [48] Nunes, SS.; Miklas, JW.; Liu, J.; Aschar-Sobbi, R.; Xiao, Y.; Zhang, B.; et al. Biowire: a platform for maturation of human pluripotent stem cell-derived cardiomyocytes. *Nat Methods*. 2013;10(8):781-7.
- [49] Parikh, SS.; Blackwell, DJ.; Gomez-Hurtado, N.; Frisk, M.; Wang, L.; Kim, K.; et al. Thyroid and Glucocorticoid Hormones Promote Functional T-Tubule Development in Human-Induced Pluripotent Stem Cell-Derived Cardiomyocytes. *Circ Res*. 2017;121(12):1323-30.
- [50] Sieliwarczyk, E.; Alaerts, M.; Robyns, T.; Schepers, D.; Claes, C.; Corveleyn, A.; et al. Clinical characterization of the first Belgian SCN5A founder mutation cohort. *Europace*. 2020.
- [51] Santostefano, KE.; Hamazaki, T.; Biel, NM.; Jin, S.; Umezawa, A.; Terada, N. A practical guide to induced pluripotent stem cell research using patient samples. *Lab Invest*. 2015;95(1):4-13.
- [52] Schindelin, J.; Arganda-Carreras, I.; Frise, E.; Kaynig, V.; Longair, M.; Pietzsch, T.; et al. Fiji: an open-source platform for biological-image analysis. *Nat Methods*. 2012;9(7):676-82.

[53] De Vos, WH.; Van Neste. L.; Dieriks, B.; Joss, GH.; Van Oostveldt, P. High content image cytometry in the context of subnuclear organization. *Cytometry A*. 2010;77(1):64-75.

[54] Van de Sande, DV.; Kopljar, I.; Teisman, A.; Gallacher, DJ.; Snyders ,DJ.; Lu, HR.; et al. Pharmacological Profile of the Sodium Current in Human Stem Cell-Derived Cardiomyocytes Compares to Heterologous Nav1.5+beta1 Model. *Front Pharmacol*. 2019;10:1374.

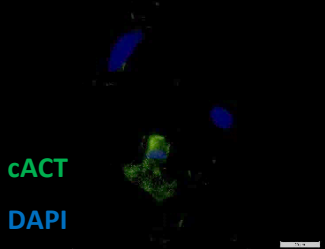
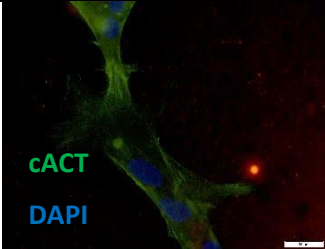
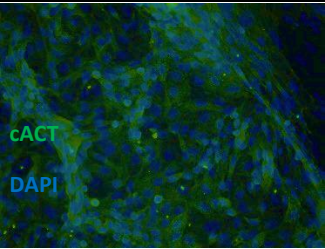
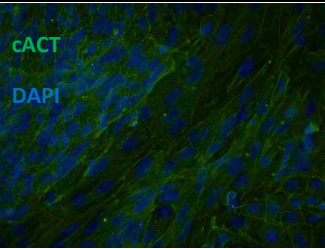
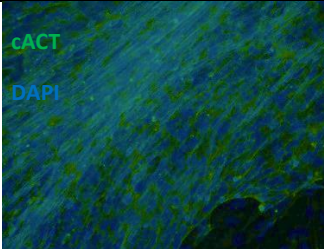
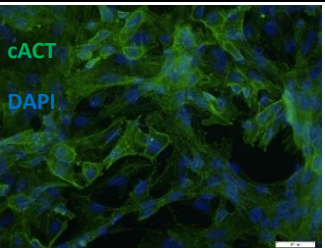
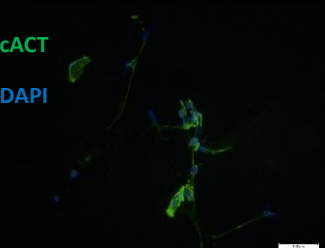
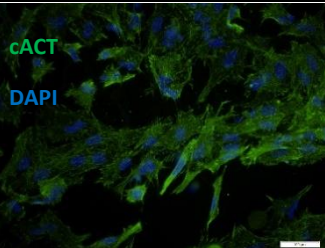
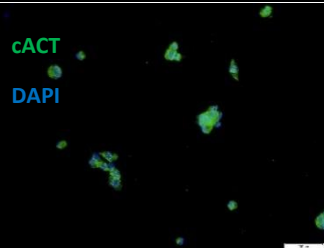
4.7 Supplementary material

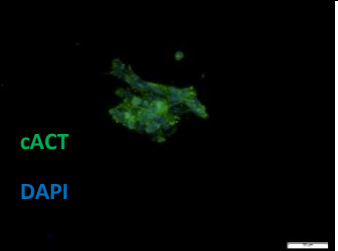
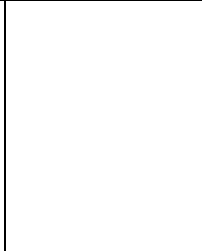
Supplementary Table 4-1 CNVs (larger than 100kb) detected in the used iPSC-lines.

Cell line	CNV type	CNV minimal region	CNV size (bp)	Genes in the region
Control 1	del	Chr1:1,030,565-1,266,041	235477	<i>ACAP3, mir429, TTLL10</i>
	del	Chr1:2,532,899-2,745,883	212985	<i>MMEL1</i>
	del	Chr1:191,618,129-191,875,752	257624	
	del	Chr4:994,414-1,188,049	193636	<i>FGFRL1</i>
	del	Chr4:34,049,908-34,423,079	373172	<i>LINC02484</i>
	del	Chr4:43,363,694-43,526,808	163115	<i>LINC02383</i>
	del	Chr4:113,294,328-113,779,891	485564	<i>ALPK1, mir367</i>
	del	Chr6:27,002,406-27,194,072	191667	<i>HIST1H2AG</i>
	del	Chr8:78,359,134-78,510,649	151516	<i>LOC102724874</i>
	del	Chr8:144,669,392-144,861,985	192594	<i>BREA2, PYCR3</i>
	del	Chr8:144,998,779-145,268,000	269222	<i>CYC1, MROH1</i>
	dup	Chr10:54,002,021-54,141,652	139632	<i>DKK1</i>
	del	Chr11:39,066,761-39,266,095	199335	
	del	Chr14:105,285,159-105,395,204	110046	<i>CEP170B</i>
	del	Chr19:1,341,509-1,497,060	155552	<i>APC2</i>
	del	Chr19:1,566,043-1,712,898	146856	<i>MBD3</i>
	dup	ChrX:71,284,941-71,411,659	126719	<i>FLI44635</i>
dup	ChrX:91,685,124-92,178,902	493779	<i>PCDH11X</i>	
Control 2	del	Chr16:32,624,879-32,855,389	230511	<i>TP53TG3</i>
	dup	Chr19:54,737,010-54,841,732	104723	<i>LILRA3</i>
	dup	ChrX:48,645,256-48,746,726	101471	<i>ERAS</i>
	dup	ChrX:153,051,907-153,197,130	145224	<i>ARHGAP4</i>
BrS patient 1	-	-	-	-
BrS patient 2	dup	Chr9:2,407,101-2,618,969	211869	<i>VLDLR-AS1</i>
	del	Chr10:68,196,544-68,517,908	321365	<i>CTNNA3</i>
	del	Chr11:90,802,950-90,926,931	123982	
	del	Chr16:32,564,812-32,959,259	394448	<i>SLC6A10P</i>
	del	ChrX:7,564,428-7,736,547	172120	

Del = deletion, dup = duplication

Supplementary Table 4-2 Differentiation efficiency based on immunofluorescence staining for cACT (comparison experiment).

	Protocol A		Efficiency	Protocol B		Efficiency
	Dissociated iPSC-CMs			Dissociated iPSC-CMs		
Control 1			80%			100%
	Non-dissociated monolayer			Non-dissociated monolayer	Non-dissociated monolayer	
Control 2			89.5 %			83.65 %
	Non-dissociated monolayer	Dissociated iPSC-CMs		Non-dissociated monolayer	Dissociated iPSC-CMs	
BrS patient 1			91.2 %			100 %
	Dissociated iPSC-CMs			Dissociated iPSC-CMs		

BrS patient 2			100 %			100 %
---------------	--	---	-------	--	---	-------

Supplementary Table 4-3 Calculated *p* values for the tested cardiac markers for qPCR data on samples from the comparison between the two protocols and in relation to the reference tissue (left ventricle of a healthy human heart donor).

Tested gene	Protocol A vs. Protocol B	Protocol A/B vs. reference tissue		
	Comparison round	Comparison experiment		Validation experiment
		Protocol A	Protocol B	Protocol B
<i>ANK2</i>	0.155	0.059	0.414	0.323
<i>ANK3</i>	0.985	0.505	0.652	1.7*E-6*
<i>CACNA1C</i>	0.349	0.087	0.699	0.115
<i>GJA1</i>	7.5*E-5*	3.6*E-5*	0.239	0.6
<i>HCN4</i>	0.453	0.439	0.776	4.6*E-6*
<i>KCND3</i>	0.057	1*E-6* [^]	2.2*E-6*	1.1*E-9*
<i>KCNH2</i>	0.570	0.010*	0.539	0.176
<i>KCNJ2</i>	7.8*E-4*	8.9*E-5*	0.983	0.413
<i>KCNJ8</i>	0.288	1.1*E-16*	0.081	0.504
<i>KCNQ1</i>	0.491	5.2*E-6*	0.002*	0.027*
<i>MYH6</i>	0.105	0.016*	0.013*	0.285
<i>MYH7</i>	0.015*	0.002*	0.171	0.539
<i>RYR2</i>	0.042*	2.8*E-6*	9.9*E-4*	4.87*E-5*
<i>TNNI3</i>	0.026*	5.6*E-7*	0.0023*	0.035*
<i>TNNT2</i>	0.138	1.7*E-4*	0.037*	0.175

Supplementary Table 4-4 Action potential properties for iPSC-CMs generated in the comparison experiment.

Used protocol	Protocol A			Protocol B		
	Control 2	BrS patient 1	BrS patient 2	Control 2	BrS patient 1	BrS patient 2
Number of AP recordings	4	8	8	10	9	13
Number of analysed AP recordings	0*	0*/†	1	0*/‡	4	2
APD50 [ms]	-	-	422.08	-	351.51± 24.84	273.7± 40.83
APD90 [ms]	-	-	501.8	-	509.95± 27.91	422.3± 10.9
APA [mV]	-	-	114.5	-	90.8± 5.1	86.7± 17.3
RMP [mV]	-	-	-59.3	-	-59.6± 3.1	-58.3± 5.4
BPM	-	-	8	-	17± 1.12	27± 3

*Recordings with RMP >-40 mV; †Recordings with proper RMP but cells did not fire AP; ‡Declined seal quality due to vivid beating

**No proper recordings were obtained from Control 1 for both tested protocols.

Supplementary Table 4-5 Action potential and calcium transient properties for iPSC-CMs generated in validation experiment.

	Protocol B		
	Control 2	BrS patient 1	BrS patient 2
Number of analysed AP recordings	4	0	7
APD50 [ms]	617.2± 54.5	-	260.7± 59
APD90 [ms]	767.6± 56.4	-	371.5± 72.3
APA [mV]	93.9± 8.4	-	94± 4
RMP [mV]	-56.3± 3.4	-	-60.9± 4.1
BPM	21± 1	-	11± 0.3
Number of analysed CT recordings	9	11	0
CTD50 [ms]	1305.3± 41.9	389.7± 36.5	-
CTD70 [ms]	1988.9± 65.6	571.7± 52.1	-
BD [s]	6.62± 0.31	3.53± 0.06	-
BPM	9± 0.4	17± 0.3	-
Rise time [ms]	824.3± 24.6	202.3± 17.9	-
RC [ms]	1108.1± 43.4	380.3± 28.9	-

Supplementary Table 4-6 Previously reported AP properties from commercial iPSC-CMs and iPSC-CMs differentiated using monolayer-based protocols

Reference	Differentiation protocol	Culture duration	Patching temperature	AP parameters				
				RMP	APA	APD50	APD90	n
Bett et. al. (2013)[1]	Commercial iCell CMs		RT	-63±5.8	83±11		955±103	25
Gibson et.al. (2014) [2]	Commercial iCell CMs		RT	-68±9	103±9		427±65	8
Meijer Van Puten et. al. (2015) [3]	Monolayer-based with CHIR 99021 and IWP4	30 days	36±1	-56±4	73±9		162±27	9
Lopez-Redondo et. al. (2016) [4]	Commercial iCell CMs		36±1	-43.3±1.7	79.4±2.9	309.4±29.5		54
Jezirowska et. al. (2016) [5]	Monolayer-based using CHIR99021 and IWP2/IWR1	28-35 days	37	-69.5±9.5	96.6±15.5	586.8±404.3	726±489.6	156
Herron et. al. (2016) [6]	Commercial iCell CMs		37	-59.3±1.7	105±5			6
Feaster et. al. (2016) [7]	Monolayer-based with CHIR99021 and IWR1 + B27	30-35 days	RT	-74±1	118±3	326±13	378±14	53

Supplementary Table 4-7 Previously reported CT properties from iPSC-CMs differentiated using monolayer-based protocols.

Reference	Differentiation protocol	Culture duration	Imaging temperature	CT parameters				
				CTD90 [ms]	CTD50 [ms]	Rise time [ms]	Decay [ms]	n
Paci et. al. (2020) [8]	Commercial iCell ² CMs		21±1	1826.2±1071.3	920.1±456.3			42
Shah et. al. (2020) [9]	END-2 co-culture	30 days	36±1	1900±100		480±20	250±20	68
Shah et. al. (2019) [10]	END-2 co-culture	30 days	36±1			251±29	2261±676	34
Higgins et. al. (2019) [11]	Monolayer-based with CHIR99021 and IWP2	60 days	36±1		1533±100		2790±50	200
Ahola et. al. (2017) [12]	END-2 co-culture	Not specified	36±1	1663±570	797±227			13
Liang et. al. (2016) [13]	Monolayer-based with CHIR99021 and IWR1	40-60 days	36±1		471.3±12.6	92±6.6		10-25

Supplementary Table 4-8 Immunofluorescence blocking buffers and dilutions of used antibodies for pluripotency markers

Blocking buffer	PBS (Life Technologies)	Goat serum (Jackson Immunotechnologies; 5%)		
Primary antibodies	Nanog (PA1-097, Life Technologies; dilution 1:500)	Tra1-81 (4745S, Cell Signaling Technology dilution 1:200)	Oct3/4 (sc-9081, SantaCruz Biotechnology dilution 1:100)	Tra1-60 (4746S, Cell Signaling Technology dilution 1:200)
Matching secondary antibody	Goat anti-rabbit Alexa Fluor 488 (A-11034, Life Technologies; dilution 1:500)	Goat anti-mouse (IgM) Alexa Fluor 555 (A-21426, Life Technologies; dilution 1:500)	Goat anti-rabbit Alexa Fluor 488 (A-11034, Life Technologies; dilution 1:500)	Goat anti-mouse (IgM) Alexa Fluor 555 (A-21426, Life Technologies; dilution 1:500)

Supplementary Table 4-9 Immunofluorescence blocking buffer and dilutions of used antibodies for cardiac markers.

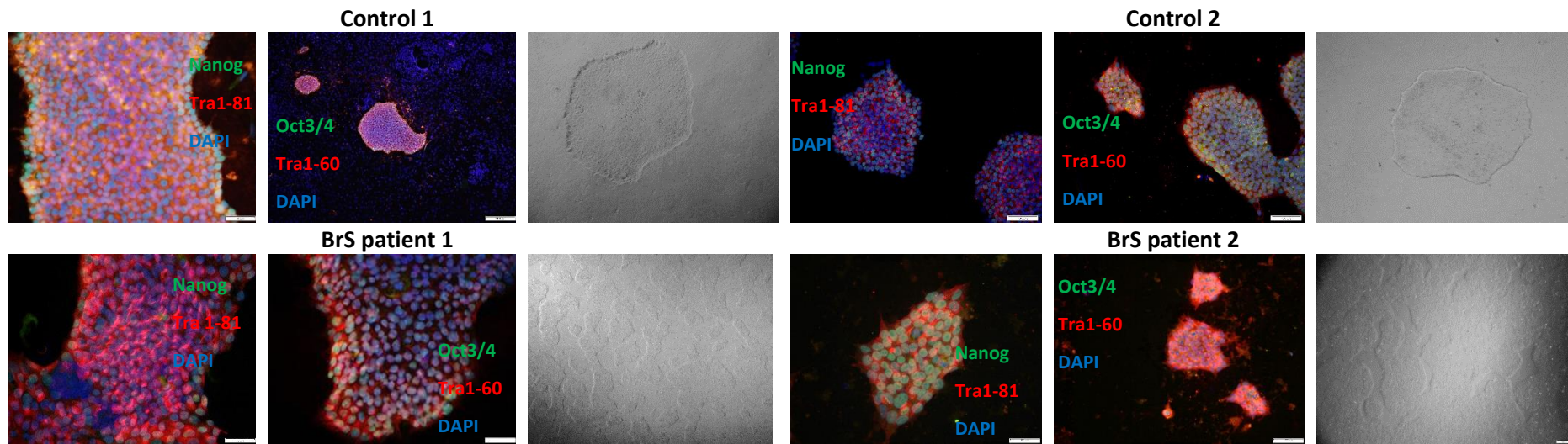
Blocking buffer CM markers	Goat serum (Jackson Immunotechnologies; 5%)	PBS (Life Technologies)	
Primary antibodies	Cardiac α -actinin (Abcam; dilution 1:300)	Cardiac troponin I (Abcam; dilution 1:100)	Nkx2.5 (Abcam; dilution 1:200)
Matching secondary antibodies	Goat anti rabbit (Life Technologies; dilution 1:500)	Goat anti rabbit (Life Technologies; dilution 1:500)	Goat anti mouse IgG (Life Technologies; dilution 1:500)

Supplementary Table 4-10 Sendai vectors presence test - PCR reaction protocol

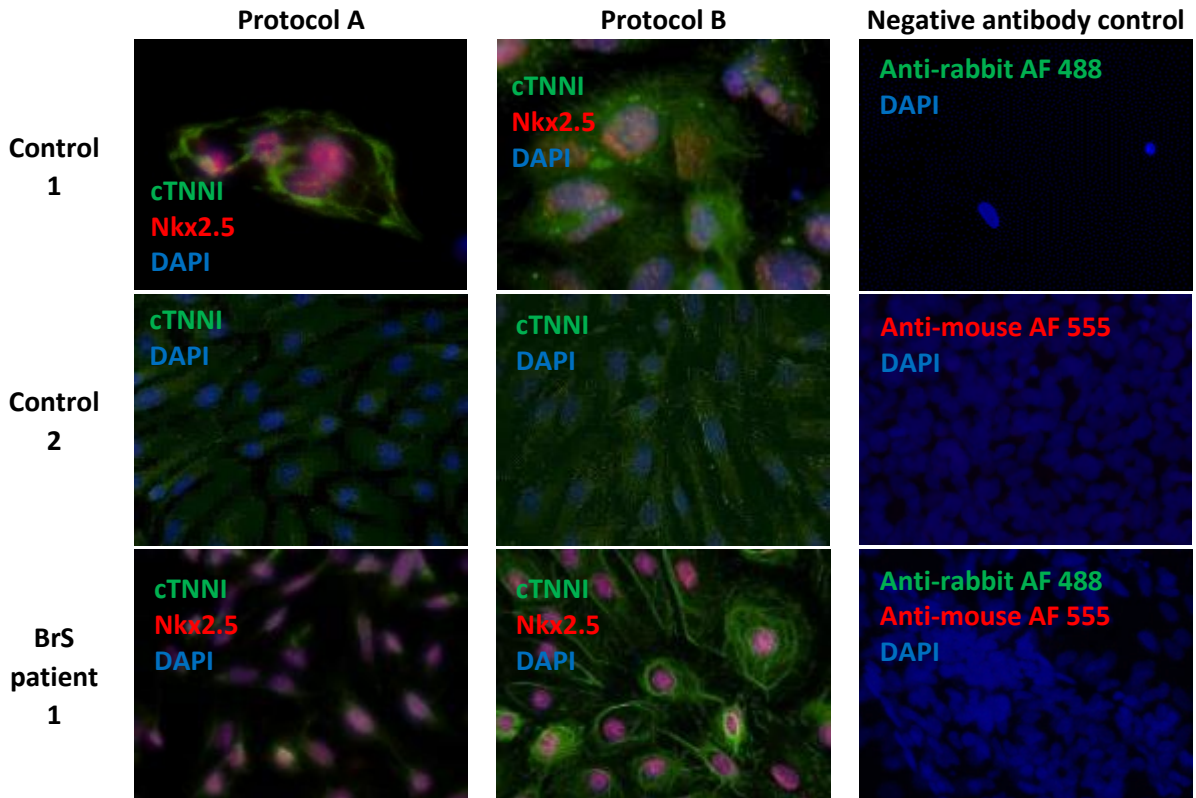
Initialization	94°C	5 min	
Denaturation	94°C	15 sec	34x
Annealing	60°C	30 sec	
Elongation	72°C	45 sec	
Final elongation	72°C	10 min	
Final hold	10°C	1 min	

Supplementary Table 4-11 Cardiac markers qPCR primers

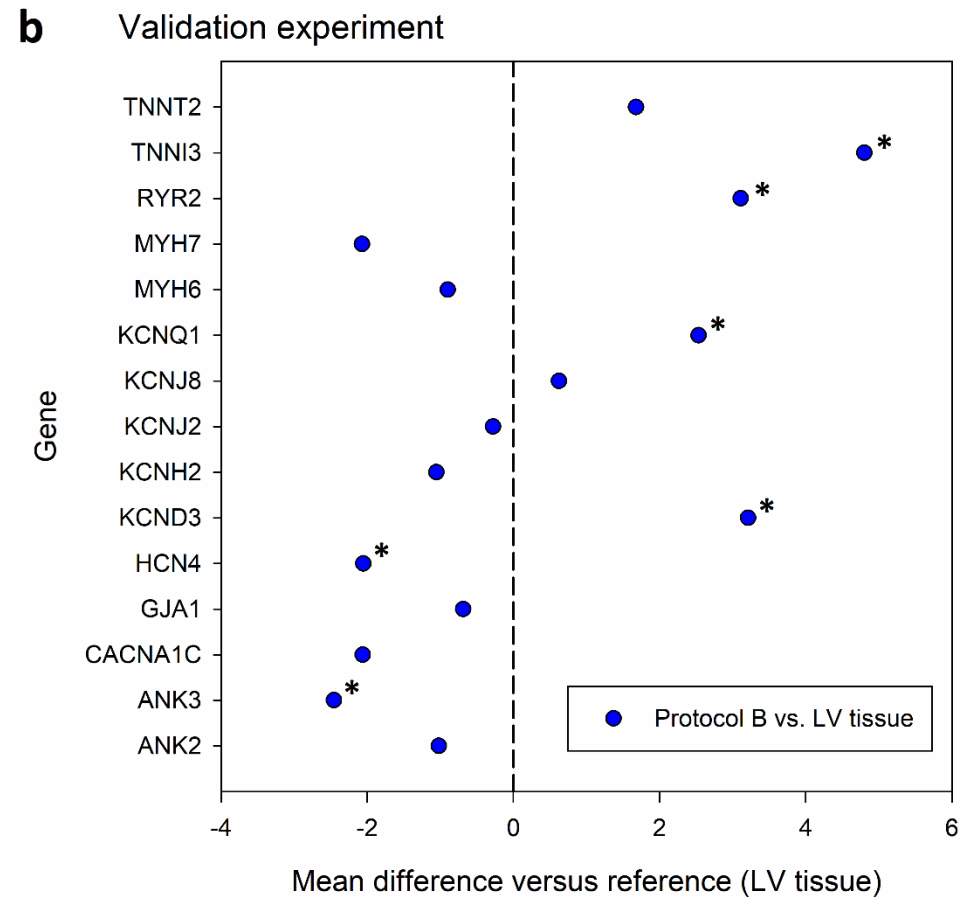
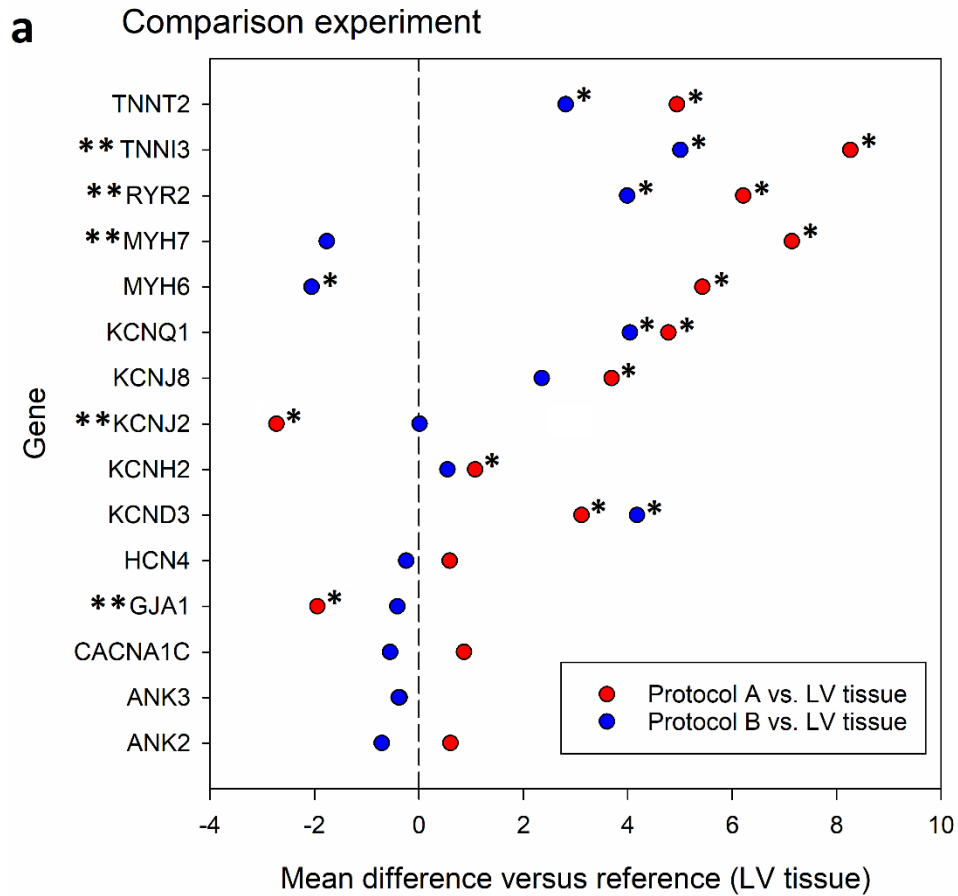
	FORWARD 5'-3'	REVERSE 5'-3'
REFERENCE GENES		
GAPDH	TGCACCACCAACTGCTTAGC	GGCATGGACTGTGGTCATGAG
ECHS1	AAGGCCCTCAATGCACCTTG	ACTCAGGTTCTGCATTTCTTG
RPL13A	CCTGGAGGAGAAGAGGAAAGAGA	TTGAGGACCTCTGTGATTTGTCAA
TARGET GENES		
ANK2	TGGACTTCACAGCCAGGAAT	GCCTCGATCCAGTAAGAGCT
ANK3	ACCAAAGGAGGACAGCAACT	GAAAAGACAGACGACCACAGG
CACNA1C	TGACATCGAGGGAGAAAACCT	ACATTAGACTTGACTGCGGC
GJA1 (CX43)	GGTACTGGAGCGCCTTAG	GCGCACATGAGAGATTGGGA
HCN4	ACCCATGCTACAGGACTTCC	GAAGAGCGCGTAGGAGTACT
KCND3	AAACAATCACAGGGACTGGC	ACACCATTGTCACCATGACC
KCNH2	TCCTTCTCCATCACACCTC	AAATCGCCTTCTACCGGAAA
KCNJ2	GTGCGAACCAACCGCTACA	CCAGCGAATGTCCACACAC
KCNJ8	AGTGGAATGGAGAAAAGTGGT	TCCTCTGTCATCATCTCCC
KCNQ1	ACAAAGTACTGCATGCGTCG	CATGAGAACCAACAGCTTCG
MYH6	GATAGAGAGACTCCTGCGGC	CCGTCTCCATTCTCGTT
MYH7	TCGTGCCTGATGACAAACAGGAGT	ATACTCGGTCTCGGCAGTGACTTT
RYR2	CATCGAACACTCCTCTACGGA	GGACACGCTAACTAAGATGAGGT
TNNI3	TGTGGACAAGGTGGATGAAG	CCGCTTAACTTGCCTCGAA
TNNT2	GGAGGAGCTCGTTTCTCTCA	CCTCCTGTTCTCCTCCTCT



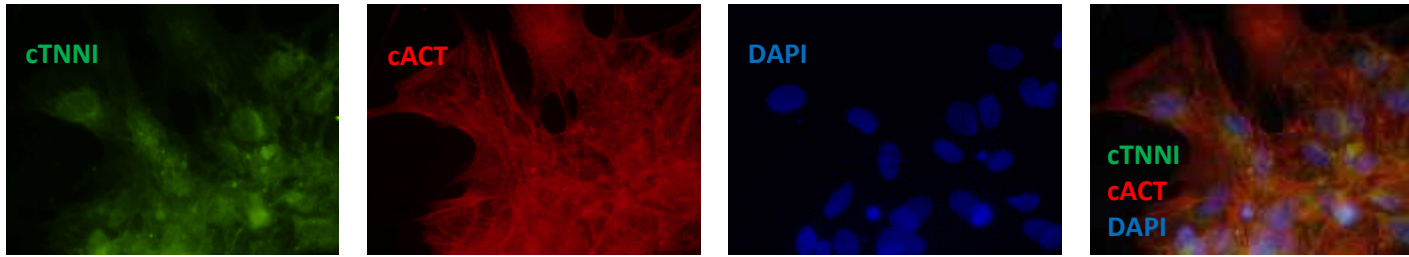
Supplementary Figure 4-1 Representative immunofluorescence staining of pluripotency markers of iPSCs of Control1, Control 2, BrS patient 1, BrS patient 2 and BrS patient 3.



Supplementary Figure 4-2 Immunofluorescence staining of cTNNI of iPSC-CMs of Control 1, 2 and BrS patient 1 generated with protocol A and B in the comparison experiment. No cTNNI or Nkx2.5 staining was performed on iPSC-CMs from BrS patient 2 due to low amount of contracting areas on coverslips, which were used for electrophysiological tests and ICC staining for cACT. Negative secondary antibody controls (anti-rabbit Alexa Fluor 488 and/or anti-mouse Alexa Fluor 555) are shown in the right column).



Supplementary Figure 4-3 Measured Ct values for all tested genes in iPSC-CMs generated using protocol A (in red) and protocol B (in blue) in relation to left ventricle (0 level on the x axis) from samples obtained in the comparison (a) and validation (b) experiment. The figures show graphical overview of the difference in the measured mean Ct values. Values for iPSC-CMs generated with protocol B in comparison experiment show closer resemblance to those in the reference tissue in comparison to iPSC-CMs generated with protocol A. * $p \leq 0.05$ for Ct comparison between the used protocol versus reference tissue (left ventricle of the healthy donor heart); ** $p \leq 0.05$ for Ct comparison between protocols A and B.



Supplementary Figure 4-4 Unmerged immunofluorescence staining images of cardiac markers cACT and cTNNI obtained from iPSC-CMs in the validation experiment (merged images are presented in Figure 4-4a).

4.8 References

- [1] Bett, G.C.; Kaplan, A.D.; Lis, A.; Cimato, T.R.; Tzanakakis, E.S.; Zhou, Q.; Morales, M.J.; Rasmusson, R.L. Electronic "expression" of the inward rectifier in cardiocytes derived from human-induced pluripotent stem cells. *Heart Rhythm* 10 (2013) 1903-10.
- [2] Gibson, J.K.; Yue, Y.; Bronson, J.; Palmer, C.; Numann, R. Human stem cell-derived cardiomyocytes detect drug-mediated changes in action potentials and ion currents. *J Pharmacol Toxicol Methods* 70 (2014) 255-67.
- [3] Meijer van Putten, R.M.; Mengarelli, I.; Guan, K.; Zegers, J.G.; van Ginneken, A.C.; Verkerk, A.O.; Wilders, R. Ion channelopathies in human induced pluripotent stem cell derived cardiomyocytes: a dynamic clamp study with virtual I_{K1} . *Front Physiol* 6 (2015) 7.
- [4] Lopez-Redondo, F.; Kurokawa, J.; Nomura, F.; Kaneko, T.; Hamada, T.; Furukawa, T.; Yasuda, K. A distribution analysis of action potential parameters obtained from patch-clamped human stem cell-derived cardiomyocytes. *J Pharmacol Sci* 131 (2016) 141-5.
- [5] Jeziorowska, D.; Fontaine, V.; Jouve, C.; Villard, E.; Dussaud, S.; Akbar, D.; Letang, V.; Cervello, P.; Itier, J.M.; Pruniaux, M.P.; et al. Differential Sarcomere and Electrophysiological Maturation of Human iPSC-Derived Cardiac Myocytes in Monolayer vs. Aggregation-Based Differentiation Protocols. *Int J Mol Sci* 18 (2017).
- [6] Herron, T.J.; Rocha, A.M.; Campbell, K.F.; Ponce-Balbuena, D.; Willis, B.C.; Guerrero-Serna, G.; Liu, Q.; Klos, M.; Musa, H.; Zarzoso, M.; et al. Extracellular Matrix-Mediated Maturation of Human Pluripotent Stem Cell-Derived Cardiac Monolayer Structure and Electrophysiological Function. *Circ Arrhythm Electrophysiol* 9 (2016) e003638.
- [7] Feaster, T.K.; Cadar, A.G.; Wang, L.; Williams, C.H.; Chun, Y.W.; Hempel, J.E.; Bloodworth, N.; Merryman, W.D.; Lim, C.C.; Wu, J.C.; et al. Matrigel Mattress: A Method for the Generation of Single Contracting Human-Induced Pluripotent Stem Cell-Derived Cardiomyocytes. *Circ Res* 117 (2015) 995-1000.
- [8] Paci, M.; Passini, E.; Klimas, A.; Severi, S.; Hyttinen, J.; Rodriguez, B.; Entcheva, E. All-Optical Electrophysiology Refines Populations of In Silico Human iPSC-CMs for Drug Evaluation. *Biophys J* 118 (2020) 2596-2611.
- [9] Shah, D.; Prajapati, C.; Penttinen, K.; Cherian, R.M.; Koivumaki, J.T.; Alexanova, A.; Hyttinen, J.; Aalto-Setälä, K. hiPSC-Derived Cardiomyocyte Model of LQT2 Syndrome Derived from Asymptomatic and Symptomatic Mutation Carriers Reproduces Clinical Differences in Aggregates but Not in Single Cells. *Cells* 9 (2020).
- [10] Shah, D.; Virtanen, L.; Prajapati, C.; Kiamehr, M.; Gullmets, J.; West, G.; Kreutzer, J.; Pekkanen-Mattila, M.; Helio, T.; et al. Modeling of LMNA-Related Dilated Cardiomyopathy Using Human Induced Pluripotent Stem Cells. *Cells* 8 (2019).
- [11] Higgins, E.M.; Bos, J.M.; Dotzler, S.M.; John Kim, C.S.; Ackerman, M.J. MRAS Variants Cause Cardiomyocyte Hypertrophy in Patient-Specific Induced Pluripotent Stem Cell-Derived Cardiomyocytes: Additional Evidence for MRAS as a Definitive Noonan Syndrome-Susceptibility Gene. *Circ Genom Precis Med* 12 (2019) e002648.
- [12] Ahola, A.; Polonen, R.P.; Aalto-Setälä, K.; Hyttinen, J. Simultaneous Measurement of Contraction and Calcium Transients in Stem Cell Derived Cardiomyocytes. *Ann Biomed Eng* 46 (2018) 148-158.
- [13] Liang, P.; Sallam, K.; Wu, H.; Li, Y.; Itzhaki, I.; Garg, P.; Zhang, Y.; Vermglinchan, V.; Lan, F.; Gu, M.; et al. Patient-Specific and Genome-Edited Induced Pluripotent Stem Cell-Derived Cardiomyocytes Elucidate Single-Cell Phenotype of Brugada Syndrome. *J Am Coll Cardiol* 68 (2016) 2086-2096.

Chapter 5. Electrophysiological Characterization of a Brugada Syndrome *SCN5A* Belgian Founder Mutation Modeled in Induced Pluripotent Stem Cell Derived Cardiomyocytes

Aleksandra Nijak ¹, Eline Simons ¹, Bert Vandendriessche ¹, Dieter Van de Sande ², Ewa Sieliwończyk ¹, Erik Fransen ³, Peter Ponsaerts ⁴, Alain J. Labro ^{2,5}, Dirk Snyders ², Emeline Van Craenenbroeck ⁶, Johan Saenen ⁶, Dorien Schepers ^{1,2}, Lut Van Laer ¹, Bart Loeys ^{1,7}, Maaïke Alaerts ¹

This chapter is a collection of preliminary data from Belgian *SCN5A* founder mutation iPSC-CMs lines, which is still a work in progress after the completion of this thesis.

¹Center of Medical Genetics, Faculty of Medicine and Health Sciences, University of Antwerp & Antwerp University Hospital, Antwerp, Belgium

²Laboratory of Molecular Biophysics, Cellular and Network Excitability, Department of Biomedical Sciences, University of Antwerp, Antwerp, Belgium

³StatUa Center of Statistics, University of Antwerp, Antwerp, Belgium

⁴Laboratory of Experimental Hematology, Vaccine & Infectious Disease Institute, Department of Biomedical Sciences, University of Antwerp, Antwerp, Belgium

⁵Department of Basic and Applied Medical Sciences, Faculty of Medicine and Health Sciences, Ghent University, Ghent, Belgium

⁶Department of Cardiology, Faculty of Medicine and Health Sciences, University of Antwerp and Antwerp University Hospital, Antwerp, Belgium

⁷Department of Human Genetics, Radboud University Medical Centre, Nijmegen, The Netherlands

5.1 Abstract

The *SCN5A* gene encodes the voltage-gated cardiac sodium channel α -subunit $\text{Na}_v1.5$. Loss-of-function mutations in $\text{Na}_v1.5$ are identified in about 20% of patients with BrS, an inherited cardiac arrhythmia that predisposes to ventricular fibrillation and SCD.

We have identified an *SCN5A* BrS founder mutation (c.4813+3_4813+6dupGGGT) in 25 different Belgian families. The variant leads to a loss-of-function of $\text{Na}_v1.5$. Mutation carriers show variable expression of the phenotype: from asymptomatic to cardiac conduction defects, characteristic BrS ECG, abrupt syncope and SCD. We used iPSC-CMs to investigate the underlying pathophysiology of the phenotypes.

Dermal fibroblasts from skin biopsies of three patients with different phenotypic severity, and two unrelated healthy control individuals were reprogrammed, and iPSC-CMs were differentiated following a previously published protocol. T3 hormone addition was tested to improve maturity of the cells, and lactate treatment was tested to obtain more purified iPSC-CM cultures. We performed several differentiation rounds of selected lines and investigated expression of cardiac markers using qPCR and immunocytochemistry analysis, as well as electrophysiological properties using patch-clamping and calcium imaging, to characterise action potentials (AP), sodium current (I_{Na}) and calcium transients (CT).

We established iPSC-CM models for a unique Belgian *SCN5A* founder mutation. All differentiated lines expressed selected cardiac markers. However, our electrophysiological data display signal variability between clones generated from one donor. Addition of T3 improved organization of the sarcomeres, while a combination of T3 and lactate treatments did not further improve tested properties. We prove that T3 addition improves the maturity of the cells. Despite observed variability in the obtained electrophysiological characteristics, we could detect differences in electrophysiological properties of patient cells compared to controls.

5.2 Introduction

Over the past decade, iPSC-CM modeling of cardiac arrhythmias became an attractive alternative to the conventional electrophysiological (EP) characterization of the channelopathies using heterologous expression models. A major advantage of the iPSC-CMs over the conventional models is the presence of the complete genetic background of the donor. This hallmark is particularly interesting when studying diseases with variable phenotypes connected with a single genetic variant, to study the influence of potential genetic modifiers. Moreover, iPSC-CMs express the full repertoire of the cardiac ion channels, which undergo the “normal” tissue specific post-translational modifications [1]. Although their main drawback remains their immaturity and mixed cell population in the obtained differentiated cell cultures, multiple methods were tested and implemented to address these issues [2].

One of the most used approaches to improve the maturity of the cells (in addition to a prolonged cell culture time) is addition of triiodothyronine (T3) to cell culture during differentiation [3; 4]. T3 maturation improves the contractile force as well as calcium release and reuptake in iPSC-CMs, through the effect on gene transcription. T3 promotes expression of cardiac specific genes like cardiac troponin I (*TNNI*), α -myosin heavy chain (α -MHC; *MYH6*), and voltage-gated potassium channels: $K_v1.5$ (*KCNA5*), $K_v4.2$ (*KCND2*) or $K_v4.3$ (*KCND3*), and inhibits expression of genes that can suppress the contractile function of cardiomyocytes (e.g. β -myosin heavy chain (β -MHC; *MYH7*)) [3; 4; 5]. This regulatory function of the T3 hormone relies on its binding to the thyroid hormone (TH) receptors. Repression of the transcription of the target genes in absence of T3 hormone results from recruitment of co-repressors by TH receptors (inactive aporeceptors), while activation of transcription of the target genes is achieved through switch to an active TH holoreceptor by exchange of co-repressors to co-activators as a consequence of ligation of T3 to TH receptor [5]. It has been previously reported that genomic changes obtained by the hormonal stimulation with T3 and/or glucocorticoid dexametasone (Dex) can promote the development of T-tubules due to advancement of cytoskeletal maturation, resulting in more organized cytoskeleton and elongated cell morphology [3]. The human heart is composed of several cell types, and likewise are the iPSC-CM cultures obtained with the available differentiation protocols, as was observed in the reported electrophysiological recordings of action potentials. Indeed, in iPSC-CM cultures atrial-, nodal- and ventricular-like AP waveforms can be identified [1; 6]. As mature cardiomyocytes can produce energy not only from glucose, but also from lactate through oxidative phosphorylation, this metabolic characteristic is utilized in enrichment techniques for iPSC-CM cultures [7]. Cell culture with the media without glucose but supplemented with 4 mM lactate purifies the iPSC-CM culture by the selection of those cells which are able to metabolise this energy source, which ultimately leads to enhanced contractions, more uniform rod-shaped morphology, as well as better EP characteristics in the obtained iPSC-CM cultures [7; 8; 9]. This effect is thought to be achieved by the enrichment of the cell culture in iPSC-CMs expressing higher levels of genes present in mature CMs (e.g. *RYR2*, cardiac troponin T (*TNNT2*)), as well as improved excitation-contraction coupling of the obtained cells.

The *SCN5A* gene is the major monogenic cause in BrS pathophysiology. Mutations in this gene explain about 20-25% of the known BrS cases, and usually they lead to a loss-of-function of the cardiac voltage-gated sodium channel ($Na_v1.5$). BrS *SCN5A* founder mutations have been identified in two regions in the Netherlands: Maastricht (c.4850_4852delTCT, p.(Phe1617del)) and provinces of Groningen and Friesland (c.1795insD) [10; 11], as well as in Belgium (c.4813+3_4813+6dupGGGT) [12]. In this study, we investigated the functional phenotypes of three Belgian *SCN5A* BrS founder mutation carriers: two asymptomatic carriers (with ajmaline induced BrS type-1 ECG pattern) and one severely affected carrier (symptomatic with syncope/sudden cardiac death (SCD)).

5.3 Aims and objectives

We performed several differentiation experiments of both the patient and control iPSC-CMs with the **basic differentiation** protocol (without additional maturation and/or purification procedures) (**Chapter 4 [1]**) as well as **optimized differentiation** protocol with addition of T3 (to improve the maturity of the obtained iPSC-CMs) and/or lactate treatment (to enrich the cell culture in properly differentiated cardiomyocytes).

We evaluated the differentiation performance based on the number of replicate wells containing contracting cells and the observed surface area sizes of contracting cells. In addition, we calculated the proportion of α -actinin positive cells within the obtained contracting replicates. Next, we carried out molecular characterization of the transcript expression of a panel of selected cardiac markers in the obtained iPSC-CMs. Finally, we performed electrophysiological characterization of the obtained iPSC-CMs, investigating sodium current (I_{Na}), action potential (AP) and calcium transient (CT) recordings. We looked at EP properties obtained with different differentiation protocols, as well as the differences between patients and controls. To minimize the bias of the obtained phenotypic observations due to the preferential clonal selection, use of several iPSC clones in modeling of genetic disorders is considered a good practice. To investigate this, we also looked at the differences between the clones obtained from a single donor.

Based on the collected results, we were able to answer the following three main questions:

- (i) is the T3 with lactate treatment improving cell maturity (based on both morphological, molecular and electrophysiological properties) compared to T3 treatment only (paragraph 5.5.1);
- (ii) what is the intra- (paragraph 5.5.2) and inter-clonal (paragraph 5.5.3) variability of a single clone/donor. Further on, we compared the performance of basic and T3 differentiation protocols (paragraph 5.5.4);
- (iii) can we detect phenotypic differences between iPSC-CMs from patients and controls in each differentiation approach (paragraph 5.5.5), and differences between patients with different disease severity (paragraph 5.5.5 section 4)?

5.4 Materials and methods

5.4.1 Patients, control individuals and cell lines

We selected five individuals for iPSC generation: two unrelated unaffected control individuals (M45-50, F25-30) and three BrS patients carrying a Belgian *SCN5A* founder mutation: two asymptomatic (BrS1, BrS8) and one severely affected (BrS3) patient. Phenotypic information on these individuals is described below:

- M45-50: unrelated unaffected control male, age 47, for whom the genetic testing with a diagnostic cardiac primary electrical disease (PED) and a cardiomyocyte-specific gene panel was negative.
- F25-30: unrelated unaffected control female, age 29, for whom the genetic testing with a diagnostic PED and cardiomyocyte-specific gene panel was negative.
- BrS1: 37-year-old female, asymptomatic with flecainide-induced BrS type-1 ECG. Founder mutation identified in familial mutation testing after incidental finding of BrS type-1 ECG pattern and founder mutation through genotyping with diagnostic PED gene panel in her asymptomatic daughter (at the age of eight). No history of SCD was reported in first and second degree relatives.
- BrS3: patient presented with SCD at the age of 10, which led to patient's death. Molecular autopsy using PED panel on patient's fibroblasts led to identification of the founder mutation. The variant was inherited from the asymptomatic mother, and BrS was also diagnosed in a maternal aunt who presented with syncope and received an ICD.

- BrS8: 38-year-old male, asymptomatic mutation carrier with normal baseline and ajmaline induced BrS type-1 ECG. Variant was identified in a pre-symptomatic screening for the Belgian *SCN5A* founder mutation, due to the variant's presence in the maternal nephew. There was no history of SCD in patient's family.

We performed two to four differentiations of seven iPSC clones: two clones of M45-50: clone 9 (C9) and clone 15 (C15); one clone of F25-30 clone 3 (C3); one clone of BrS1 clone 1 (C1), one clone of BrS3 clone 2 (C2) and two clones of BrS8: clone 2 (C2) and clone 3 (C3).

5.4.2 iPSC culture and differentiation to iPSC-CMs

iPSC clones were derived and cultured for several passages according to our previously published standard protocol (**Chapter 4** [1]). Briefly, iPSCs on 80-90% of confluency were incubated on day 0 of differentiation with RPMI1640 media containing 6 μ M CHIR99021 and 1% B27 supplement without insulin (differentiation medium DM1) for 48h. On day 2 cells were incubated with RPMI1640 media containing 5 μ M Wnt-C59 and 1% B27 supplement without insulin (DM2) for 48h. On day 4 of differentiation cells were supplemented with RPMI1640 media with 1% B27 supplement without insulin (DM3) and media was changed every other day, cells were kept in an incubator at 37°C, 80% humidity, 5% CO₂ and 5% O₂. From the day of first visible contractions, cells were supplemented with DM3 or RPMI1640 media with 1% B27 supplement without insulin with addition of triiodothyronine (T3) (20 ng/mL) (DM4) and cells were transferred to an incubator with normoxic conditions the day after the start of T3 treatment (37°C, 80% humidity, 5% CO₂). A metabolic enrichment using RPMI1640 media without glucose (Life Technologies) supplemented with 5 mM lactate (Sigma Aldrich), human serum albumin (500 μ g/mL; Life Technologies) and L-ascorbic-acid (5 mM; Sigma Aldrich) (DM5) was used from day 11 to day 16 of differentiation to homogenize the cell culture for further experiments. Cells were supplemented with DM3 or DM4 refreshed every other day, until the end of functional experiments (day 35-40). Cells were dissociated on day 20-35 of differentiation using TrypLE (Life Technologies) for functional characterization. Each differentiation was performed in 6-well plates, where one well is treated as a single technical replicate.

5.4.3 Molecular characterization

RNA samples and ICC staining with cardiomyocyte markers was performed on day 25-40 according to our previously reported protocols (**Chapter 4** [1]). Cardiac marker expression (*ANK2*, *ANK3*, *TNNI3*, *TNNT2*, *GJA1*, *MLC2 α* , *MLC2 ν* , *MYH6*, *MYH7*, *HCN4*, *KCND3*, *KCNH2*, *KCNJ2*, *KCNJ8*, *KCNQ1*, *CACNA1C*, *RYR2*, *SCN5A*) was assessed on RNA level using previously published qPCR primers. Fold changes in gene expression were determined using the comparative Ct method ($\Delta\Delta$ Ct) with normalization to three housekeeping genes: *GAPDH*, *ECHS1* and *RPL13A*, and in relation to the expression in iPSC. Healthy donor left ventricle (LV) tissue expression was used as a reference in the presented graphs. Expression on protein level was assessed using primary antibodies for: cardiac α -actinin (cACT), cardiac troponin I (cTNNI) and Na_v1.5 according to the protocols reported in **Chapter 4** [1]. Non-dissociated, contracting monolayers were fixed on coverslips on D25-40 of differentiation and three to four random fluorescent images were taken for each antibody staining.

5.4.4 Electrophysiological recordings

Electrophysiological (EP) experiments were performed 25-40 days after the start of differentiation. Perforated-patch AP and intracellular Ca²⁺ transient (CT) recordings were carried out at room temperature (RT; 21 \pm 1°C) on non-dissociated (monolayer) cells grown on glass cover slips, while ruptured-patch I_{Na} recordings were performed at RT, according to the protocol reported previously in **Chapter 4** [1]. The cells were continuously superfused at 1mL/min rate with an extracellular solution (ECS) containing (in mM): 150 NaCl, 5.4 KCl, 1.8 CaCl₂, 1 MgCl₂, 15 HEPES, 15 glucose and 1 Na-pyruvate adjusted to pH 7.4 with NaOH. Junction potentials were compensated before sealing of the cell when the patch pipette made contact with the cell membrane.

5.4.5 Data analysis

The light microscopy images of contracting iPSC-CMs and fluorescence images for immunocytochemistry were acquired using cellSens software (Olympus LS) and analysed using Fiji image analysis freeware [13], and differentiation efficiency was calculated from ICC staining for cardiac α -actinin, according to the protocol previously described in **Chapter 4** [1]. Transcript expression level results were analysed as previously described in **Chapter 4** [1].

I_{Na} , AP and CT data were analysed using PClamp10 software (Axon CNS Molecular devices) as previously described in **Chapter 3** [14] and **Chapter 4** [1]. I_{Na} data are presented as a mean \pm SEM with 'n' as the number of cells analysed. For each cell recording, AP and CT values are calculated as a mean of five subsequent waveforms and data are presented as a mean \pm SEM for each single cell of the 'n' cells analysed. The following parameters were analysed: AP amplitude (APA), resting membrane potential (RMP), upstroke velocity (dV/dT_{max}), action potential duration at 50% (APD50) and 90% (APD90) of repolarization; calcium transient duration at 50% (CTD50), and 70% (CTD70) of repolarization, rise time and decay rate (RC). The beating frequency (BPM) was calculated from the time difference between two AP or CT peaks. No APD correction to the beating rate was performed. AP recordings with RMP >-40 mV or BPM <10 ; and CT recordings with BPM <10 were excluded from the analysis, to obtain the closest representation of the physiological conditions (RMP -80 to -90mV and 60 BPM) in the obtained results for phenotype analysis. Concerning the RMP, in the graphs we represent all RMP values for completeness, but in the analysis of the other AP characteristics cells with RMP above -40mV were excluded.

Comparison of the I_{Na} , AP, and CT properties between the used differentiation conditions as well as case-control analysis was performed using one-way ANOVA test, with Tukey's correction for AP and I_{Na} parameters. Comparison of the SD values between the tested conditions for the analysis of the tested EP characteristics was carried out using paired t-test. A p-value of ≤ 0.05 is considered statistically significant (Systat Software Inc.). Comparison of the normalized $\Delta\Delta Ct$ values between the groups (used treatments and reference tissue) was performed with a linear mixed model, having the protocol as fixed effect and the normalized Ct value as dependent variable. The nonindependence between observations within the same cell line was accounted for using a random intercept for cell line, and a random slope for protocol. Pairwise comparisons between the differentiation conditions and/or reference tissue were carried out using a post hoc analysis with Tukey's correction for multiple hypothesis testing. Comparison of the $\Delta\Delta Ct$ values between the clones obtained from the same donor was performed using the Mann-Whitney test, testing the null hypothesis that median $\Delta\Delta Ct$ value is equal between the two clones. Analyses were carried out in the software package R version 4.0.2, and the add on packages lme4 and multcomp. A p-value of ≤ 0.05 is considered statistically significant.

5.5 Results

5.5.1 Comparison of T3 versus T3+lactate treatment

We studied the effect on the differentiation efficiency and contracting areas in the iPSC-CMs obtained with either T3 or T3+lactate treatment: M45-50 C15, F25-30 C3, BrS3 C2 and BrS8 C3 (**Table 5-1**). We did not see significant differences in the number of contracting replicates, size of contracting areas or differentiation efficiency in T3 combined with lactate treatment conditions in comparison to T3 treatment only (**Table 5-1**). There was no visible difference in organization of cytoskeleton in T3+lactate treated iPSC-CMs in comparison to T3 treatment only (**Figure 5-1**). ICC of $Na_v1.5$ showed that all the generated cell lines expressed the protein in a similar way (**Figure 5-1**). We did not see differences in measured AP and I_{Na} characteristics in obtained iPSC-CMs (**Table 5-1**). As we did not observe significant differences between T3 only and combined T3+lactate treatment in all evaluated characteristics, further on in this report we pooled data from iPSC-CMs of each cell line generated with T3 only and combined T3+lactate treatments **together in one 'T3 protocol'**.

Table 5-1 Obtained morpho-functional characteristics of iPSC-CMs obtained with T3 treatment and T3 + lactate treatment differentiation protocol: number of replicates with visible contractions, contracting areas, calculated differentiation efficiency, obtained AP (RMP, APA, APD90, APD50 and dV/dT_{max}) and I_{Na} (sodium current density, $V_{1/2}$ of inactivation, recovery from inactivation) characteristics. p-values for comparison of each characteristic between the tested conditions (basic vs. treatment protocol) are listed in the right column. Comparison of the contracting areas, number of replicates with visible contractions and differentiation efficiency was performed using one-way ANOVA. Comparison of the I_{Na} and AP properties between the groups was carried out using one-way ANOVA with Tukey's correction.

Treatment Cell line	T3 treatment				T3 + lactate treatment				p-value for comparison between the treatments
	M45-50 C15	F25-30 C3	BrS3 C2	BrS8 C3	M45-50 C15	F25-30 C3	BrS3 C2	BrS8 C3	
Number of replicates with visible contractions/total number of replicates	18/18	14/16	4/4	12/14	6/8	9/9	6/8	8/8	0.739
Contracting areas [%]*	74 ±10	66 ±2	59 ±2	50 ±11	74 ±7	70 ±12	59 ±4	50 ±6	0.917
Differentiation efficiency [% of cACT positive cells]	93 ±4	92 ±8	98 ±2	99 ±1	93 ±5	85 ±15	97 ±3	98 ±2	0.761
RMP [mV]	-63 ±5.1	-47.8 ±10	-62.4 ±4	-45.4 ±9.1	-49.9 ±2.8	-49.8 ±3.3	-69.7 ±2.3	-45.4 ±2.6	0.60008
APA [mV]	94.4 ±7.5	98.4 ±4.2	77.3 ±10	89.5 ±5.7	96.5 ±4.2	110.5 ±5.4	104 ±5	109.2 ±2.7	0.072
APD90 [ms]	402.1 ±14	380.5 ±51	371.7 ±19.6	346.6 ±15.2	509.1 ±43.3	354 ±25.9	382.7 ±13.1	397.7 ±28.6	0.67618
APD50 [ms]	291.1 ±21.8	242.4 ±31.5	212 ±6.6	208.1 ±32.4	234.5 ±14.7	218.2 ±11.3	229.3 ±16.9	281.5 ±27.2	0.9931
dV/dT_{max} [V/s]	21.2 ±7.3	8.47 ±2.3	19.8 ±9.4	13.4 ±4.5	10.9 ±3.9	28.2 ±8.3	30.1 ±8.1	23.3 ±4.1	0.0865
Number of analysed AP recordings	5	3	4	4	4	10	6	16	-
I_{Na} [mV]	-310 ±118	-356 ±71	-245 ±63	-262 ±49	-114 ±28	-343 ±90	-179 ±30	-140 ±46	(controls only) 0.195
n	2	2	9	6	6	23	11	10	
$V_{1/2}$ of inactivation [mV]	-81.9 ±2.0	-87.9 ±3.3	-91.2 ±2.8	-97.9 ±2.3	-80.7 ±3.4	-85.7 ±2.5	-92.2 ±2.9	-42.7 ±9.7	(controls only) 0.447
n	8	14	10	10	6	16	27	9	
Recovery from inactivation [ms]	30.4 ±2.9	18.6 ±5.4	41.6 ±3.0	35.4 ±1.9	34.1 ±1.8	26.0 ±2.0	20.0 ±2.2	34.4 ±3.0	(controls only) 0.24
n	6	5	5	6	6	22	6	7	

*Average of the contracting areas in wells with visible contractions.

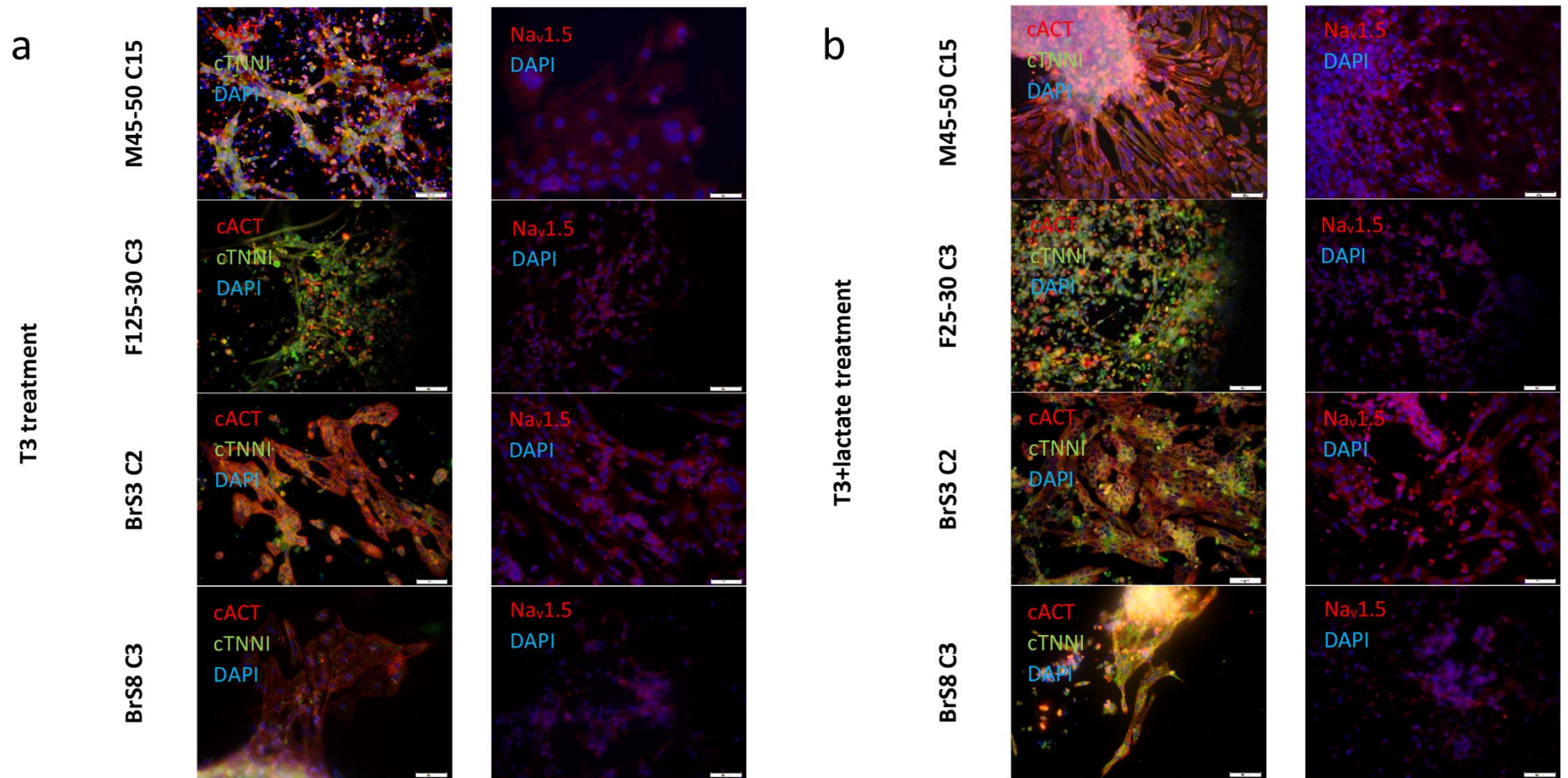


Figure 5-1 Example ICC staining results for the obtained iPSC-CMs with differentiation protocol with addition of T3 treatment (a) and T3 combined with lactate treatment (b). cACT – cardiac α -actinin; cTNNI – cardiac troponin I; Nav_v1.5 – cardiac sodium channel; DAPI – nuclear staining.

5.5.2 Obtained iPSC-CMs show low intra-clonal (batch-to-batch) differentiation variability

We looked at differences in molecular and EP characteristics in the obtained iPSC-CMs between different differentiation batches of the cell lines: M45-50 C9 and C15, F25-30 C3, BrS3 C2, BrS8 C2 and C3.

1. Basic differentiation protocol

There were no statistically significant differences in size of contracting areas between the batches for BrS8 C3, while the difference for M45-50 C9, F25-30 C3, BrS3 C2 and BrS8 C2 was statistically significant (**Table 5-2**). There were no significant differences in differentiation efficiency, sodium current densities and AP properties between the batches for any of the tested cell lines (**Table 5-2**).

2. T3 protocol

We also compared differences between batches for the T3 treated iPSC-CMs: significant difference in contracting areas between the batches for BrS8 C3 (**Table 5-2**) was observed. There were no significant differences in differentiation efficiencies and tested EP characteristics between batches in any of the tested cell lines obtained with T3 treatment (**Table 5-2**).

Disregarding the contracting area as a very variable and thus potentially unreliable parameter (also supported by our other comparisons in this chapter), we were able to combine the data from several differentiation batches for each of the cell lines in our further analyses.

*Table 5-2 Statistical analysis of batch-to-batch differences (intra-clonal variability) in morphological and EP characteristics (AP and peak I_{Na} density) in the obtained iPSC-CMs. Statistically significant differences are indicated with *. Comparison of the I_{Na} and AP properties between the groups was carried out using one-way ANOVA with Tukey's correction. Comparison of the contracting areas and differentiation efficiency was performed using one-way ANOVA.*

Culture conditions		Tested characteristic																	
		M45-50 C9		P value	M45-50 C15		P value	F25-30 C3		P value	BrS3 C2		P value	BrS8 C2		P value	BrS8 C3		P value
Basic protocol	Tested characteristic	Batch I	Batch II		Batch I	Batch II		Batch I	Batch II		Batch I	Batch II		Batch I	Batch II		Batch I	Batch II	
		Basic protocol	Contracting areas [%]	97 ±0.01	62 ±11.2	0.009*	-	-	-	45 ±0.1	68 ±0.2	<0.001*	4 ±2.0	36	0.003*	80 ±2.2	0.002*	21 ±7.2	22 ±13.9
Differentiation efficiency [%]	99.9 ±0.1		100	0.667	-	-	-	93.1 ±11.2	75.8 ±20.8	0.444	69.6 ±37.1	46.6 ±24.7	0.764	96.8 ±4.6	N/A	-	99.5 ±0.7	61.7 ±48.8	0.397
RMP [mV]	-56.3 ±3.4		-58.4 ±2.8	0.656	-	-	-	-68.1 ±0.5	-66.6 ±5.0	0.789	-57.9 ±2.8	-51.4 ±4.3	0.285	-58.3 ±5.4	-60.9 ±4.1	0.733	-51.7 ±2.4	-55.5 ±3.2	0.385
APA [mV]	93.85 ±22.21		72.2 ±10.7	0.425	-	-	-	103.4 ±42.2	101.5 ±23.3	0.972	62 ±19.4	45.6 ±12.3	0.508	86.7 ±37.4	94.0 ±13.2	0.879	53.6 ±12.2	89.5 ±22.4	0.209
APD90 [ms]	767.6 ±178.5		664.2 ±82.5	0.625	-	-	-	484.2 ±197.7	422.2 ±94.7	0.812	324.4 ±78.3	602.9 ±185.0	0.268	422.3 ±172.6	371.5 ±87.1	0.823	392.5 ±100.8	531.0 ±108.4	0.381
APD50 [ms]	617.2 ±145.9		407.4 ±66.3	0.256	-	-	-	309.1 ±127.4	300.6 ±69.2	0.96	180.1 ±41.1	303.8 ±96.8	0.332	273.7 ±115.4	260.9 ±68.0	0.933	211.0 ±52.6	361.6 ±89.8	0.196
dV/dT _{max} [V/s]	4.3 ±1.2		1.7 ±0.4	0.119	-	-	-	11.8 ±5.7	9.9 ±2.8	0.802	2.0 ±0.6	2.7 ±0.4	0.302	6.3 ±3.6	4.2 ±0.7	0.665	1.1 ±0.3	5.8 ±2.3	0.105
BPM	21.3 ±4.9		29.3 ±5.9	0.326	-	-	-	22.8 ±9.4	19.4 ±4.5	0.783	20.4 ±6.8	12.3	0.34	23.9 ±10.5	11.4 ±2.1	0.442	17.6 ±4.9	18.5 ±4.5	0.894
Number of analysed AP recordings	4		8	-	-	-	-	2	4	-	2	2	-	2	7	-	6	3	-
I _{Na} [pA/pF]	-50.7 ±12.6		-34.4 ±12.3	0.497	-	-	-	-69.1 ±13.1	-38.1 ±13.9	0.124	-20.8 ±3.6	-21.4 ±7.3	0.953	-47.7	-36.6 ±16.0	0.803	-64.8 ±14.2	-119.5 ±27.4	0.086
Number of analysed I _{Na} recordings	12		4	-	-	-	-	9	9	-	9	14	-	1	6	-	7	22	-
T3 protocol	Contracting areas [%]	74	74	1.0	81	59	0.401	64 ±0.2	66 ±0.1	0.009	-	-	-	-	-	44 ±0.1	63	<0.001*	
	Differentiation efficiency [%]	N/A	93.1 ±7.4	-	74 ±10	N/A	-	91.7 ±14.3	84.5 ±16.5	0.766	-	-	-	-	-	99.2 ±1.1	98.3 ±1.5	0.698	
	RMP [mV]	-68.6 ±3.1	-63.4 ±6.2	0.55	-68.2 ±1.3	-67.9 ±6.2	0.971	-63.2 ±0.1	-63.0	0.577	-	-	-	-	-	-	-62.2	-66.5 ±3.7	0.666
	APA [mV]	100.9 ±7.9	96.9 ±7.9	0.746	98.7 ±6.9	91.5 ±12.7	0.655	96.6 ±6.5	102.0	0.718	-	-	-	-	-	-	72.7	94.3 ±7.4	0.34
	APD90 [ms]	645.6 ±82.2	784.2 ±195.2	0.599	383.2 ±34.4	414.8 ±7.6	0.524	330.6 ±18.4	480.1	0.133	-	-	-	-	-	-	373.0	333.4 ±21.5	0.481
	APD50 [ms]	519.1 ±76.9	509.5 ±42.5	0.92	256.5 ±51.2	314.1 ±6.3	0.461	221.5 ±40.9	284.2	0.538	-	-	-	-	-	-	139.9	225.2 ±43.0	0.457
	dV/dT _{max} [V/s]	7.3 ±2.4	3.6 ±1.6	0.297	20.6 ±15.8	21.4 ±9.6	0.97	9.0 ±3.9	7.3	0.843	-	-	-	-	-	-	26	10.9 ±5.8	0.353
	BPM	34.8 ±9.4	22.5 ±4.5	0.339	24.0 ±14.3	52.6	0.244	20.1 ±4.8	23.9	0.732	-	-	-	-	-	-	37.6	48.5 ±3.9	0.353
	Number of analysed AP recordings	2	2	-	3	2	-	13	1	-	-	-	-	-	-	-	1	3	-
	I _{Na} [pA/pF]	-86.7 ±48.8	-8.1 ±0.4	0.343	-19.8 ±3.9	-295.7 ±117.3	0.245	-356.1 ±71.0	-377.3 ±140.5	0.913	-	-	-	-	-	-	-261.9 ±49.0	-139.5 ±45.7	0.084
	Number of analysed I _{Na} recordings	3	3	-	2	6	-	9	15	-	-	-	-	-	-	-	6	10	-

*a p-value <0.05 is considered statistically significant

5.5.3 Inter-clonal variability of a single donor

1. Basic differentiation protocol

We compared morpho-functional characteristics between two different iPSC lines obtained from two individuals: M45-50 C9 and C15, and BrS8 C2 and C3. There were no significant differences in the size of contracting areas between clones obtained from M45-50, while for clones from BrS8 this difference was significant. We observed significant differences in I_{Na} density between the two clones obtained from M45-50, while the difference for both BrS8 clones was not statistically significant (**Table 5-3**). There were no significant differences in $V_{1/2}$ of I_{Na} inactivation between the clones of both cell lines (**Table 5-3**). We did not observe significant differences between two clones from each cell line for RMP, APA, APD as well as dV/dT_{max} (**Table 5-3**).

*Table 5-3 Inter-clonal variability of the molecular and EP characteristics for clones obtained from M45-50 and BrS8 using basic differentiation protocol. Statistically significant differences are indicated with *. Comparison of the I_{Na} and AP properties between the groups was carried out using one-way ANOVA with Tukey's correction. Comparison of the contracting areas and differentiation efficiency was performed using one-way ANOVA.*

Cell line		M45-50		P-value	BrS8		P-value
		C9	C15		C2	C3	
Contracting areas [%]		80±24	55±37	0.636	19±12	73±10	0.008*
Differentiation efficiency [%]		96±3	90±7	0.506	97±5	85±14	0.543
I_{Na}	Peak current density [pA/pF]	-44.5 ±8.6	-166.3 ±32.5	<0.001*	-22.8 ±8.8	-62.6 ±14.5	0.630
	$V_{1/2}$ of inactivation [mV]	-79.5 ±3.2	-87.1 ±3.2	0.261	-85.5 ±7.4	-82.7 ±4.2	0.630
AP	RMP [mV]	-48.1 ±3.9	-34.1 ±10.3	0.33	-50.4 ±4.5	-43.4 ±4.5	0.35
	APA [mV]	79.4 ±6	83.6 ±17.3	0.95	92.3 ±4.5	73.6 ±11.1	0.26
	APD50 [ms]	477.4 ±46.6	461.1 ±71.2	0.73	263.7 ±48.7	294.7 ±45.9	0.73
	APD90 [ms]	698.7 ±28.8	646.1 ±37.8	0.45	382.8 ±59.5	469.4 ±44.2	0.19
	dV/dT_{max} [V/s]	2.7 ±0.5	4.4 ±1.8	0.37	4.7 ±0.8	3.7 ±1.4	0.14

2. T3 protocol

For the cells obtained with additional T3 treatment, we did not see differences in the size of contracting areas and differentiation efficiency for M45-50 clones, while we observed significant difference in size of contracting areas between BrS8 clones (**Table 5-4**). We observed no differences in I_{Na} density between the two BrS8 clones, while in M45-50 this was significantly reduced in C9 compared to C15 (**Table 5-4**), similar to our observation using the basic protocol. We did not notice significant differences in $V_{1/2}$ of I_{Na} inactivation for M45-50 clones, while in BrS8 clones the difference for this parameter was statistically significant. We observed no significant inter-clonal differences in APA, APD and dV/dT_{max} (**Table 5-4**). Although for both M45-50 clones we did not see significant differences in BPM, this characteristic differed significantly in both BrS8 clones (**Table 5-4**).

Table 5-4 Inter-clonal variability of the molecular and EP characteristics for clones obtained from M45-50 and BrS8 using T3 differentiation protocol. Statistically significant differences are indicated with *. Comparison of the I_{Na} and AP properties between the groups was carried out using one-way ANOVA with Tukey's correction. Comparison of the contracting areas and differentiation efficiency was performed using one-way ANOVA.

Cell line		M45-50		P-value	BrS8		P-value
		C9	C15		C2	C3	
Contracting areas [%]		74	74±10	1	80±2.2	50±8.5	0.02*
Differentiation efficiency [%]		93±7	93±4	1	-	99±1	-
I_{Na}	Peak current density [pA/pF]	-30.7 ±17.9	-237.2 ±98.7	0.008*	-51.3 ±36.5	-157.9 ±39.3	0.345
	$V_{1/2}$ of inactivation [mV]	-77.9 ±4.2	-81.9 ±2.0	0.312	-72.0 ±3.9	-84.9 ±3.5	<0.001*
AP	RMP [mV]	-42.9 ±8.8	-63.0 ±5.1	0.165	-57.9 ±2.0	-45.4 ±9.1	0.05
	APA [mV]	100.9 ±7.9	101.5 ±3.2	1	96.2 ±3.3	89.5 ±5.7	0.177
	APD50 [ms]	519.1 ±76.9	282.1 ±25.6	0.1	213.9 ±16.2	208.1 ±32.4	0.537
	APD90 [ms]	645.6 ±82.1	401.5 ±118.0	0.1	334.7 ±19.8	346.6 ±15.2	0.247
	dV/dT_{max} [V/s]	7.3 ±2.4	25.5 ±7.5	0.1	4.5 ±0.8	13.4 ±4.5	0.429
	BPM	34.8 ±9.4	38.3 ±14.3	1	12.9 ±1.0	45.0 ±2.8	0.016*

3. Inter-clonal effect on the gene transcript expression

We looked at the differences in expression pattern of the tested cardiac markers between clones of M45-50 obtained with basic differentiation protocol and BrS8 obtained with both basic and T3 differentiation protocols (**Table 5-5; Figure 5-2**). We could observe significant differences in transcript levels of *CACNA1C*, *HCN4*, *KCNH2*, *KCNJ8*, *MYH7*, *SCN5A*, *TNNI3* and *TNNT2* between the M45-50 clones (**Table 5-5**). In BrS8 iPSC-CMs obtained with basic protocol, we observed significant difference between the clones in the measured transcript levels of only *KCNQ1* (**Table 5-5**). Meanwhile, in BrS8 iPSC-CMs obtained with T3 protocol, the measured transcript levels of *ANK2*, *GJA1*, *KCND3*, *KCNJ8*, *KCNQ1*, *MYH6*, *RYR2*, *SCN5A*, *TNNI3* and *TNNT2* differed significantly between the clones.

4. Inter-clonal variability conclusion

Because of the observed statistically significant inter-clonal differences in some characteristics, in the rest of the report the clones are analysed separately.

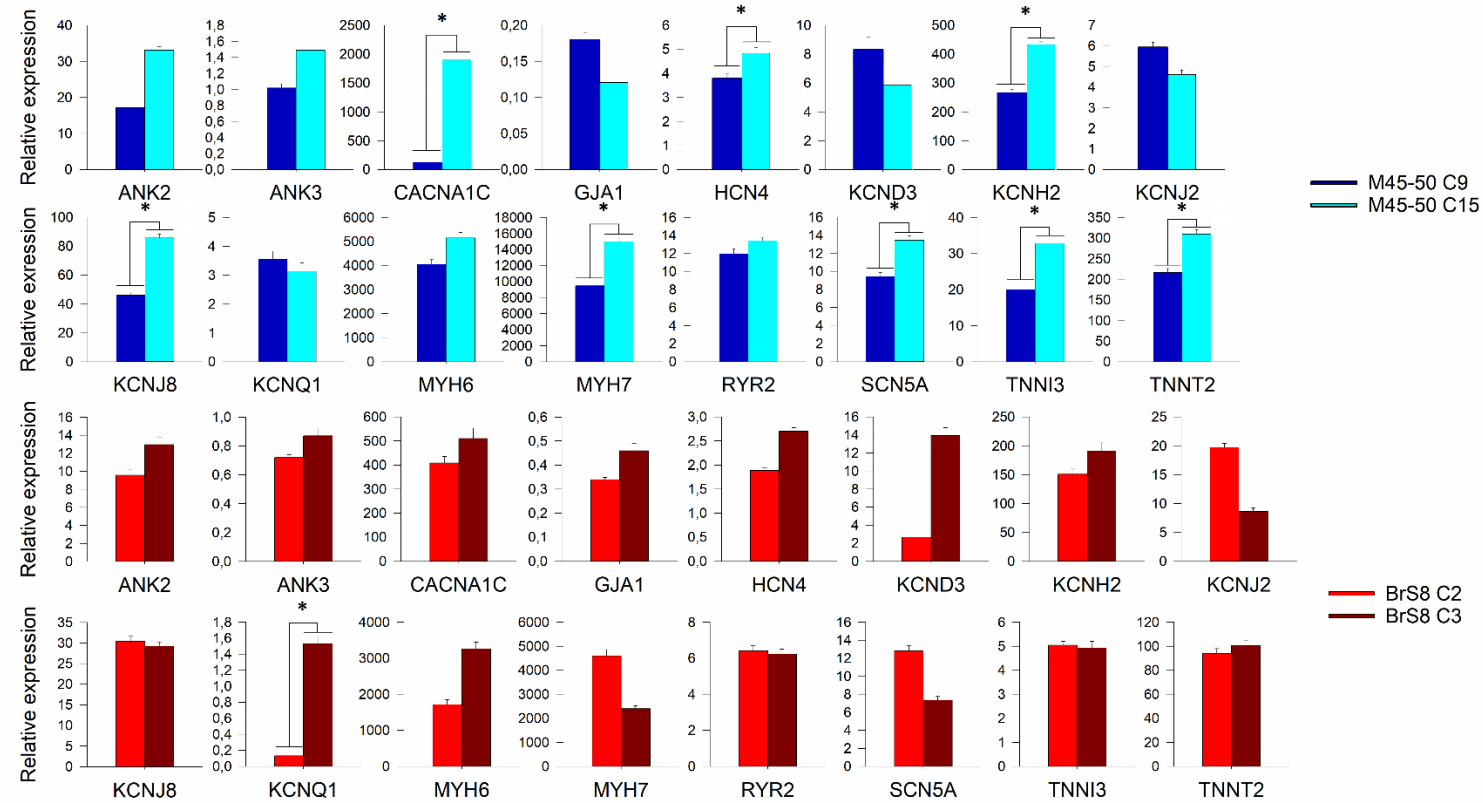
Table 5-5 Calculated p values for the qPCR data obtained from M45-50 and BrS8. Tests were carried out using the Mann-Whitney U test, testing the null hypothesis that median $\Delta\Delta\text{Ct}$ value is equal between the two clones (statistically significant p-values ≤ 0.05 are indicated in bold and with a *).

Tested gene	Difference in mean $\Delta\Delta\text{Ct}$ values		
	M45-50	BrS8	BrS8 T3
ANK2	1	0.517	0.013*
ANK3	0.482	0.388	0.126
CACNA1C	0.018*	0.388	0.692
GJA1	0.482	0.114	0.006*
HCN4	0.009*	1	0.365
KCND3	0.727	0.138	0.022*
KCNH2	0.036*	1	0.365
KCNJ2	0.497	0.776	0.233
KCNJ8	0.012*	0.491	0.004*
KCNQ1	0.727	0.0007*	0.022*
MYH6	0.373	0.755	0.004*
MYH7	0.036*	0.607	0.945
RYR2	0.482	1	0.004*
SCN5A	0.012*	N/A	0.024*
TNNI3	0.009*	0.573	0.004*
TNNT2	0.009*	1	0.004*

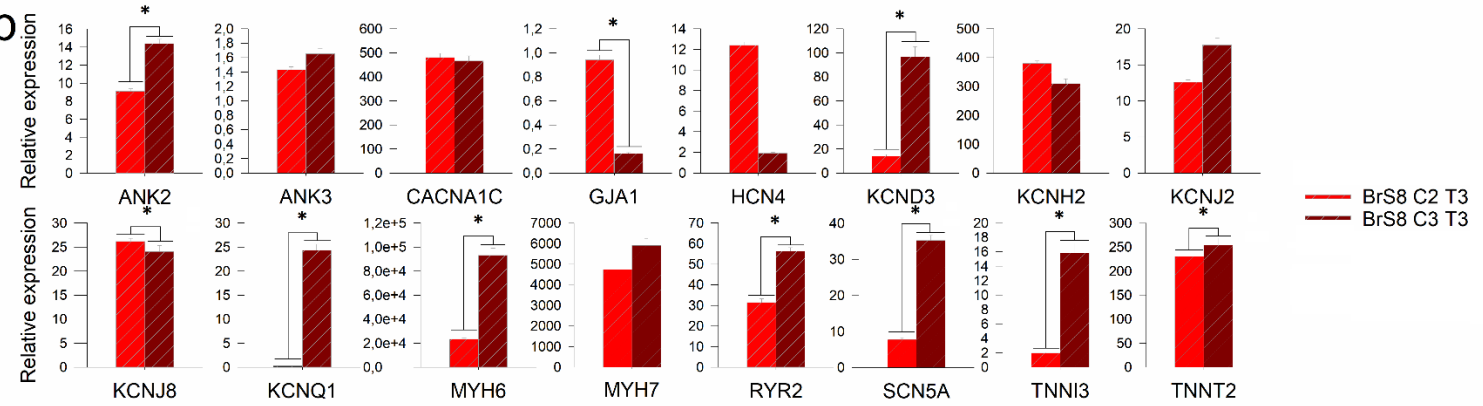
N/A – lack of power of the analysis due to a small number of tested replicates

Figure 5-2 Measured relative expression levels for the selected cardiomyocyte markers in iPSC-CMs obtained for M45-50 and BrS8 clones with basic protocol (a) and BrS8 clones obtained with T3 protocol (b). Statistically significant differences in $\Delta\Delta\text{Ct}$ between the clones are indicated with a *.

a



b



5.5.4 Overall comparison of basic versus T3 protocol

1. T3 protocol increases size of contractions and improves organization of cardiac α -actinin and troponin I

Looking at the number of contracting replicates, we did not see significant differences in the average performance between the protocols ($89.3 \pm 4.3\%$ and $88.2 \pm 3.5\%$ of contracting replicates for basic and treatment protocol, respectively). However, we observed a general improvement (not statistically significant) in the size of contracting areas in treated iPSC-CMs in comparison to those obtained with the basic differentiation protocol (from the average of $51 \pm 15.2\%$ in basic to $60 \pm 6.4\%$ in treatment protocol) (**Table 5-6**). Nonetheless, as mentioned before this showed to be in general quite a variable characteristic. A similar trend was observed for differentiation efficiency – cell lines generated with basic differentiation protocol showed lower differentiation efficiency calculated based on cACT ICC staining in comparison to those obtained with the T3 protocol (average differentiation efficiency of $84.7 \pm 10.7\%$ for basic conditions and $93.3 \pm 4.2\%$ for T3 treatment). Because the T3 protocol is aiming to improve maturation of the cells, we expected to observe differences in localization or organization of the sarcomeric proteins in ICC staining. We indeed noticed better organization of sarcomeres in T3 treated iPSC-CMs, based on the available cACT and cTNNI staining results (visible and regularly arranged striation pattern (cACT staining) as well as visible cytoskeletal structures instead of undefined shape of cytoplasmatic expression of the cTNNI) (**Figure 5-3**).

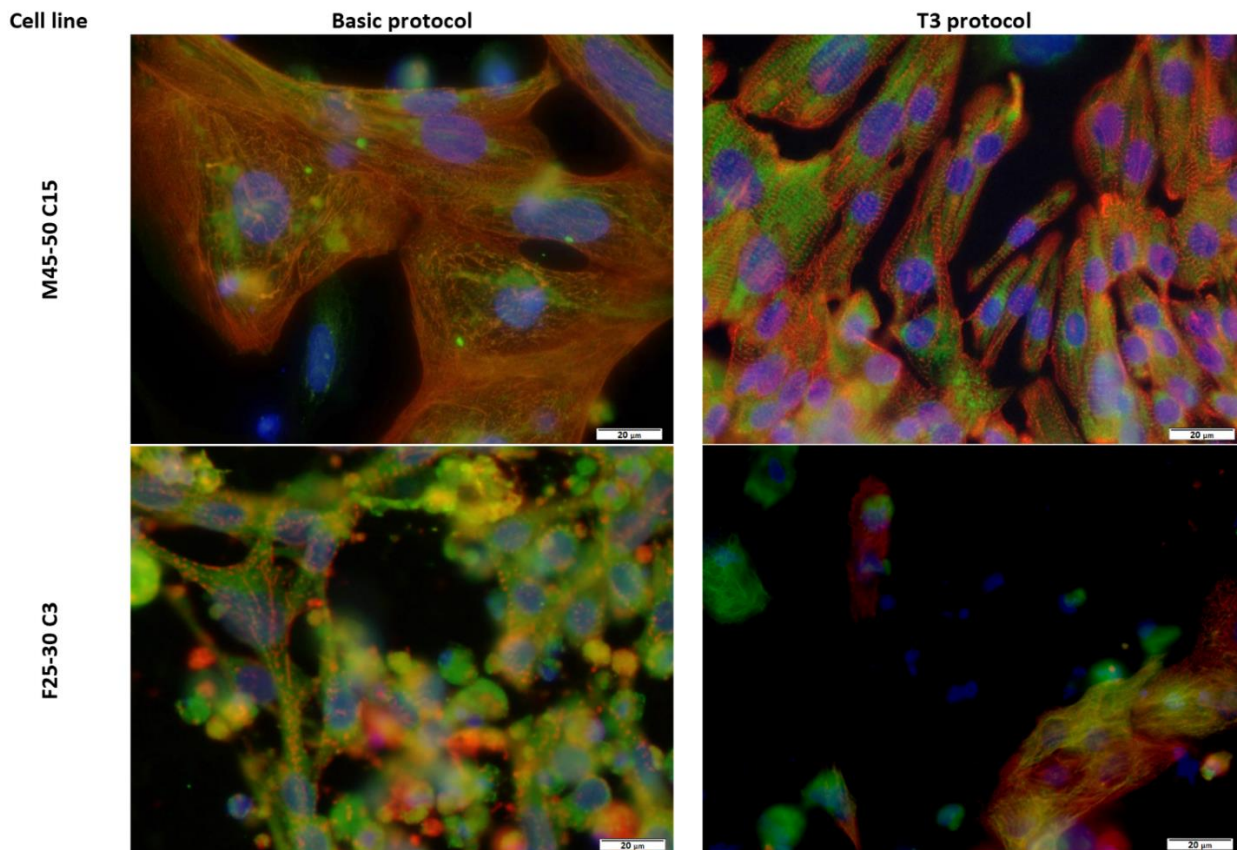


Figure 5-3 Example cACT and cTNNI staining images obtained from control lines derived using basic and T3 conditions.

Table 5-6 Obtained morpho-functional characteristics of iPSC-CMs obtained with basic and T3 differentiation protocol: number of replicates with visible contractions, contracting areas, calculated differentiation efficiency, obtained AP (RMP, APA, APD90, APD50 and dV/dT_{max}) and I_{Na} (sodium current density, $V_{1/2}$ of inactivation, recovery from inactivation) characteristics. *p*-values for comparison of each characteristic between the tested conditions (basic vs. treatment protocol) are listed in the right column. Comparison of the I_{Na} and AP properties between the groups was carried out using one-way ANOVA with Tukey's correction. Comparison of the contracting areas, differentiation efficiency and CT properties was performed using one-way ANOVA..

Treatment	Basic protocol							T3 protocol							p-value
Cell line	M45-50 C9	M45-50 C15	F25-30 C3	BrS1 C1	BrS3 C2	BrS8 C2	BrS8 C3	M45-50 C9	M45-50 C15	F25-30 C3	BrS1 C1	BrS3 C2	BrS8 C2	BrS8 C3	
Number of replicates with visible contractions/total number of replicates	9/12	14/16	8/8	4/4	4/4	6/8	7/8	3/4	18/18	23/25	5/6	10/12	3/4	20/22	0.207
Contracting areas [%]	80 ±24	55 ±37	56 ±17	70 ±6	4 ±0.6	19 ±12	73 ±10	74 ±5	74 ±10	68 ±7	18 ±4	59 ±4	80 ±2.2	50 ±8.5	0.688
Differentiation efficiency [% of cACT positive cells]	96 ±3	90 ±7	76 ±21	91 ±9	58 ±16	97 ±3	85 ±14	93 ±7	93 ±4	89 ±12	85 ±3	98 ±3	N/A [†]	99 ±1	0.485
RMP [mV]	-48.1 ±3.9	-34.1 ±10.3	-56.0 ±5.2	-42.4 ±6.5	-44.1 ±3.8	-50.4 ±4.5	-43.4 ±4.5	-42.9 ±8.8	-63.0 ±5.1	-49.4 ±3.3	-55.8 ±5.0	-65.2 ±1.8	-57.9 ±2.0	-45.4 ±9.1	0.1404
APA [mV]	79.4 ±6	83.6 ±17.3	102.1 ±3.9	79.2 ±9.8	52.6 ±6.4	92.3 ±4.5	73.6 ±11.1	100.9 ±7.9	101.5 ±3.2	107.9 ±4.5	105.8 ±4.2	100.4 ±4.0	96.2 ±3.3	89.5 ±5.7	0.0214*
APD90 [ms]	698.7 ±28.8	646.1 ±37.8	442.9 ±14.3	496.2 ±24.6	443.8 ±65.9	382.8 ±59.5	469.4 ±44.2	645.6 ±82.1	401.5 ±118.0	332.6 ±21.2	370.6 ±46.2	374.2 ±9.7	334.7 ±19.8	346.6 ±15.2	<0.001**
APD50 [ms]	477.4 ±46.6	461.1 ±71.2	303.5 ±13.6	313.8 ±27.5	233.1 ±31.8	263.7 ±48.7	294.7 ±45.9	519.1 ±76.9	282.1 ±25.6	219.8 ±13.2	254.4 ±32.9	219.1 ±12.6	213.9 ±16.2	208.1 ±32.4	0.0910
dV/dT _{max} [V/s]	2.7 ±0.5	4.4 ±1.8	10.5 ±1.8	3.9 ±1	1.5 ±0.3	4.7 ±0.8	3.7 ±1.4	7.3 ±2.4	25.5 ±7.5	20.1 ±9.2	19.5 ±8.3	29.5 ±5.8	4.5 ±0.8	13.4 ±4.5	0.0365*
Number of analysed AP recordings	12	3	6	4	7	9	9	3	4	14	5	9	12	4	
Peak I _{Na} [mV]	-44.5 ±8.6	-166.3 ±32.5	-56.7 ±10.1	-50.7 ±11.6	-46.4 ±20.2	-22.8 ±8.8	-62.6 ±14.5	-30.7 ±18	-237.2 ±98.7	-343.1 ±90.4	-96.8 ±27.9	-198.6 ±28.3	-51.3 ±36.5	-157.9 ±39.3	(controls only) 0.592
n	16	9	18	21	22	7	19	5	8	25	26	20	3	16	
V _{1/2} of inactivation [mV]	-79.5 ±3.2	-87.1 ±3.2	-93.6 ±2.5	-75.5 ±2.8	-75.8 ±1.8	-85.5 ±7.4	-82.7 ±4.2	-77.9 ±4.2	-81.9 ±2.0	-87.5 ±2.0	-84.1 ±6.5	-92.0 ±2.2	-72.0 ±3.9	-84.9 ±3.5	(controls only) 0.0403*
n	19	6	13	13	20	4	20	5	8	38	29	37	4	17	
Recovery from inactivation [ms]	8.6 ±0.7	52.9 ±4.4	70.1 ±17.7	30.3 ±6.2	N/A	N/A	25.3 ±8.9	N/A	30.4 ±2.9	36.1 ±2.4	26.4 ±9.5	41.3 ±3.9	N/A	30.5 ±4.5	(controls only) 0.009**
n	5	6	8	6	N/A	N/A	10	N/A	6	21	7	11	N/A	23	
CTD50 [ms]	N/A	583.6 ±45.2	577.9 ±24.5	428.4 ±35.8	445.8 ±32.6	300.5 ±32.6	496.4 ±38.3	N/A	339.0 ±35.7	428.5 ±13.7	377.7 ±13.9	245.9 ±6.7	N/A	472.3 ±60.9	0.024*
CTD70 [ms]	N/A	572.6 ±220.1	824.1 ±108.8	581.9 ±52.4	585.2 ±76.9	436.4 ±56.2	687.5 ±95.2	N/A	496.4 ±52.2	639.6 ±20.6	566.1 ±21.7	353.4 ±9.4	N/A	732.3 ±99.0	0.543
BPM	N/A	23.3 ±6.9	20.0 ±3.3	19.1 ±0.8	15.6 ±1.4	17.8 ±0.9	16.1 ±0.1	N/A	46.2 ±5.5	32.7 ±1.3	23.0 ±0.5	68.0 ±1.1	N/A	8.9 ±3.7	<0.001**
Rise time [ms]	N/A	370.0 ±110.5	441.5 ±18.7	223.9 ±29.2	244.4 ±25.4	181.0 ±33.7	266.8 ±41.4	N/A	197.1 ±23.6	221.2 ±9.6	188.3 ±9.8	159.2 ±5.6	N/A	309.5 ±45.9	0.078
RC [ms]	N/A	475.6 ±30.8	565.6 ±41.8	366.8 ±24.5	408.6 ±26.2	285.7 ±39.8	472.8 ±29.7	N/A	260.1 ±26.3	383.6 ±16.6	321.7 ±14.2	169.1 ±4.5	N/A	414.5 ±56.4	0.003*
n	N/A	3	7	16	8	5	8	N/A	25	20	10	8	N/A	19	

[†]Obtained cells were used for EP characterization and RNA extraction for transcript expression analysis. Significance codes: *<0.05; **<0.001

2. T3 treatment improves transcript expression of tested cardiac markers

To confirm our observations from ICC staining, we examined the expression patterns of the selected structural cardiac markers in obtained iPSC-CMs (**Figure 5-4 top panel**). We noticed significant increase in expression levels of *MYH6*, which could have been expected based on the reported effect of T3 on iPSC-CMs [4] (p values are listed in **Table 5-7** “Basic vs. T3 protocol”). We also looked at expression of the main ion channel genes (**Figure 5-4 bottom panel**). Expression levels of *KCNQ1* and *RYR2* were increased in all tested cell lines with the use of T3 (**Table 5-7**). We did not see significant differences in *SCN5A* in the measured transcript levels when applying the T3 protocol.

We also compared the expression profile of the tested cardiac markers in iPSC-CMs generated with basic as well as T3 protocol in relation to LV tissue. We noticed significant differences in transcript levels of nine genes in cells generated with basic differentiation protocol and five genes in cells generated with T3 protocol (**Figure 5-4; Table 5-7** “Basic/T3 protocol vs. LV tissue”). For *ANK2*, *ANK3*, *CACNA1C* and *HCN4* the transcript levels in iPSC-CMs obtained with basic conditions were increased, while for *KCND3*, *MLC2v*, *RYR2*, *SCN5A* and *TNNI3* – transcript levels were significantly lower in comparison to the reference tissue. In cells obtained with T3 protocol, we observed increased mean expression levels of *KCND3*, *RYR2*, *SCN5A* and *TNNI3* compared to basic conditions and more similar to levels in LV tissue, while *ANK2*, *ANK3*, *CACNA1C*, *HCN4* and *MLC2v* remained significantly different from the levels observed in LV tissue (**Figure 5-4; Table 5-7**).

Table 5-7 Calculated p values for the tested cardiac markers for qPCR data on samples from the obtained iPSC-CMs between the two tested differentiation conditions and in relation to a reference tissue (left ventricle of a healthy human heart donor). Statistically significant p-values of ≤ 0.05 are indicated with a * and in bold.

Tested gene	Basic vs. T3 protocol	Basic/T3 protocol vs. LV tissue	
		Basic protocol	T3 protocol
<i>ANK2</i>	0.457	<2e⁻¹⁶*	<2e⁻¹⁶*
<i>ANK3</i>	0.492	<0.001*	<0.001*
<i>CACNA1C</i>	0.467	0.023*	0.033*
<i>GJA1</i>	0.988	0.366	0.511
<i>HCN4</i>	0.799	<0.001*	0.0015*
<i>KCND3</i>	0.287	<0.001*	0.339
<i>KCNH2</i>	0.111	0.583	0.383
<i>KCNJ2</i>	0.336	0.413	0.413
<i>KCNJ8</i>	0.460	0.113	0.113
<i>KCNQ1</i>	<0.001*	0.149	0.996
<i>MLC2a</i>	0.998	0.337	0.337
<i>MLC2v</i>	0.344	<0.001*	0.0063*
<i>MYH6</i>	0.032*	0.858	0.289
<i>MYH7</i>	0.0555	0.462	0.832
<i>RYR2</i>	0.010*	<0.001*	0.843
<i>SCN5A</i>	0.176	0.031*	0.913
<i>TNNI3</i>	0.409	<0.001*	0.090
<i>TNNT2</i>	0.102	0.433	0.950

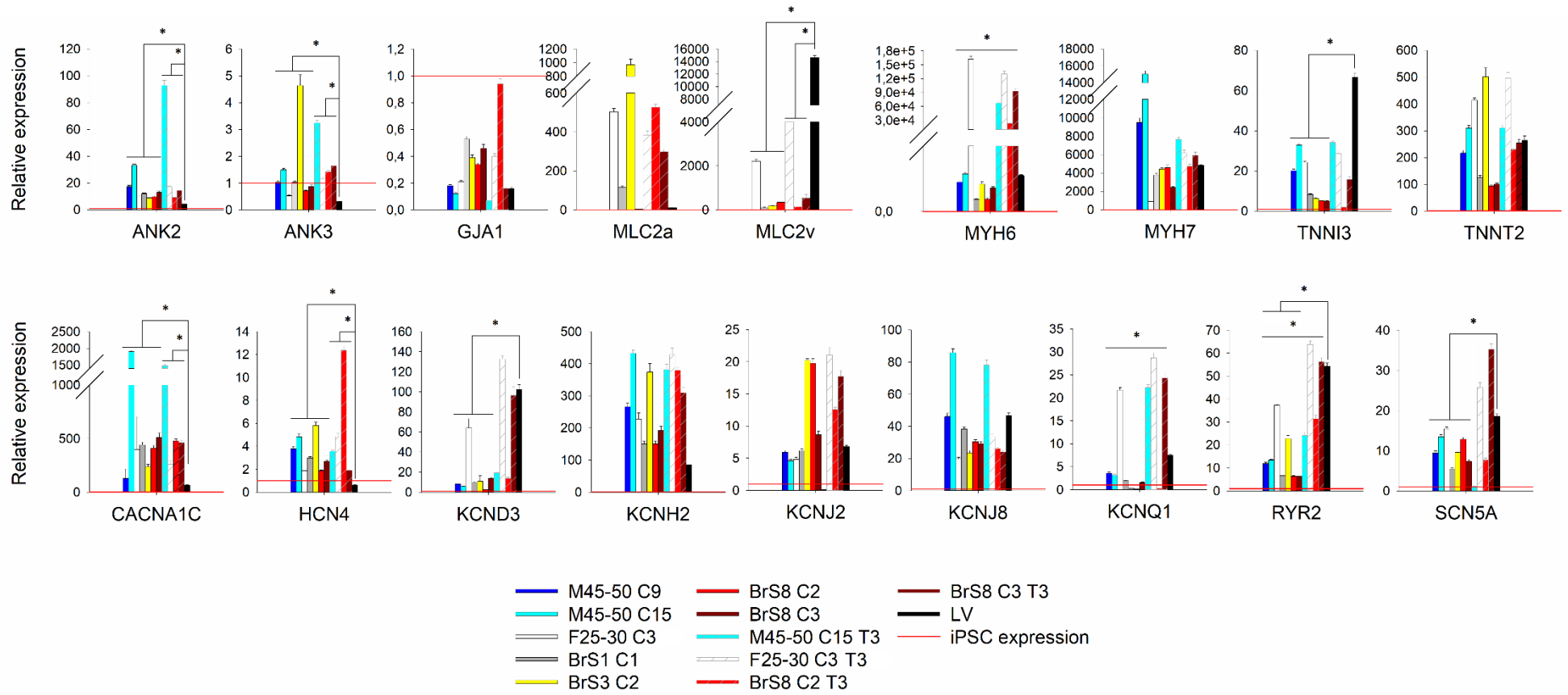


Figure 5-4 Measured relative expression levels for the selected cardiomyocyte markers in obtained iPSC-CMs. LV – healthy donor heart left ventricle. Statistically significant differences are indicated with a *.

3. T3 protocol improves sodium current characteristics in the obtained iPSC-CMs

Investigating the peak sodium current density of the control iPSC-CMs obtained with basic protocol, we could observe a higher peak I_{Na} density in M45-50 C15 in comparison to the other two controls ($p < 0.001$ and $p = 0.001$ in comparison to M45-50 C9 and F25-30 C3 respectively) (measured I_{Na} characteristics are summarised in **Table 5-8** and the p values for comparison in **Table 5-9**). The reported values for peak I_{Na} from control iPSC-CMs range from -99.9 ± 14.9 to -159.1 ± 18.5 pA/pF (values reported in literature discussed in [15]). Both of our control lines: F25-30 C3 and M45-50 C9 iPSC-CMs showed low I_{Na} (in the range of analysed BrS iPSC-CMs; -44.5 ± 8.6 pA/pF and -56.7 ± 10.1 pA/pF for M45-50 C9 and F25-30 C3, respectively). Only M45-50 C15 showed peak current density (-166.3 ± 32.5) in the range of previously reported peak I_{Na} densities from control iPSC-CMs. We looked at $V_{1/2}$, kinetics and recovery from inactivation, where we did not see differences between M45-50 C15 and F25-30 C3, while for M45-50 C9 we reported a significant positive 14.1 mV shift of $V_{1/2}$ of inactivation, slower kinetics of inactivation (τ) and accelerated recovery from inactivation in comparison to F25-30 C3 ($p = 0.006$; $p = 0.037$; $p = 0.017$, respectively). We did not see differences in $V_{1/2}$ and recovery from inactivation between two M45-50 clones (**Table 5-8, 5-9**). We did not observe differences in slope factor of inactivation (κ) between tested control iPSC-CMs.

We noticed an increase in peak I_{Na} density in our recordings from T3 treated iPSC-CMs in comparison to those obtained with basic differentiation protocol in all of the cell lines, except for M45-50 C9 (**Table 5-8**). Average I_{Na} density of M45-50 C9 was -30.7 ± 17.9 pA/pF, while this of M45-50 C15 and F25-30 C3 was now -237.2 ± 98.7 and -349.6 ± 55.0 mV (**Table 5-8**). Our results for peak I_{Na} density were higher than those reported previously in literature reports, where the peak I_{Na} density values obtained from iPSC-CMs with T3 protocol range from -53.1 to -278.5 pA/pF. We did not observe differences in slope factors of inactivation between the tested control lines. We did not see significant differences in $V_{1/2}$ of inactivation between the tested lines obtained with T3 protocol, on the contrary to the results from the basic protocol (**Table 5-9**). Nevertheless, we could still detect slower kinetics of inactivation in M45-50 C9 and accelerated recovery from inactivation in M45-50 C15 compared to F25-30 C3 ($p = 0.035$ and $p = 0.010$, respectively) (**Table 5-8, 5-9**).

Table 5-8 Summary of I_{Na} properties recorded from obtained control iPSC-CMs. The difference in variability of the tested parameters between the tested treatments was calculated using paired t-test.

		Peak current density			Inactivation				Recovery			
		[pA/pF]	SD	n	τ [ms]	$v_{1/2}$ [mV]	SD	κ	SD	n	τ [ms]	n
Basic protocol	M45-50 C9	-44.5 ±8.6	37.6	16	1.4 ±0.2	-79.5 ±3.2	13.8	11.0 ±1.5	6.3	19	8.6 ±0.7	5
	M45-50 C15	-166.3 ±32.5	97.6	9	0.9 ±0.1	-87.1 ±3.2	9.5	12.3 ±0.8	2.3	6	52.9 ±4.4	6
	F25-30 C3	-56.7 ±10.1	39.25	18	0.8 ±0.02	-93.6 ±2.5	7.1	9.5 ±0.9	2.4	13	70.1 ±17.7	8
T3 protocol	M45-50 C9	-30.7 ±17.9	40.1	5	0.7 ±0.2	-77.9 ±4.2	9.4	9.8 ±1.3	27.4	5	N/A	N/A
	M45-50 C15	-237.2 ±98.7	75.9	8	1.1 ±0.2	-81.9 ±2.0	5.7	12.1 ±0.7	2.0	8	30.4 ±2.9	6
	F25-30 C3	-349.6 ±55.0	197.9	16	1.3 ±0.1	-87.5 ±2.0	12.3	8.7 ±0.5	2.5	38	36.1 ±2.4	21
Difference in SD between the tested conditions (p-value)			0.497				0.778		0.750			

Table 5-9 P-values obtained for comparison of the tested I_{Na} parameters between the tested control iPSC-CMs. N/A – comparison was not possible due to lacking data; indicated in red are the comparisons which are not considered in the text due to a possible problem with the $Na_v1.5$ function in the control cell lines, where the measured peak I_{Na} was lower than in previously reported iPSC-CMs. Comparison of the I_{Na} properties between the groups was carried out using one-way ANOVA.

Protocol	Tested characteristic	Peak I_{Na}			τ of inactivation			$V_{1/2}$ of inactivation			κ of inactivation			Recovery from inactivation		
		Cell line	M45-50 C9	M45-50 C15	F25-30 C3	M45-50 C9	M45-50 C15	F25-30 C3	M45-50 C9	M45-50 C15	F25-30 C3	M45-50 C9	M45-50 C15	F25-30 C3	M45-50 C9	M45-50 C15
Basic protocol	M45-50 C9	-	<0.001*	0.529	-	0.191	0.037*	-	0.318	0.006*	-	0.640	0.452	-	0.089	0.017*
	M45-50 C15	<0.001*	-	0.001*	0.191	-	0.751	0.318	-	0.265	0.640	-	0.069	0.089	-	0.358
	F25-30 C3	0.529	<0.001*	-	0.037*	0.751	-	0.006*	0.265	-	0.452	0.069	-	0.017*	0.358	-
T3 protocol	M45-50 C9	-	0.0647	0.119	-	0.241	0.035*	-	0.423	0.093	-	0.245	0.943	--	0.010*	N/A
	M45-50 C15	0.0647	-	0.749	0.241	-	0.994	0.423	-	0.137	0.245	-	0.799	N/A	-	0.010*
	F25-30 C3	0.119	0.749	-	0.035*	0.994	-	0.093	0.137	-	0.943	0.799	-	N/A	0.010*	-

4. T3 protocol improves EP properties, however it does not reduce their variability

We compared the basic with the T3 differentiation protocol (**Table 5-6, Figure 5-5**) and observed statistically significant differences in $V_{1/2}$ of I_{Na} inactivation, as well as recovery from inactivation, while the other tested parameters did not differ between the tested conditions. To assess the influence of the applied T3 protocol on the variability of the obtained results we looked at the SD of the I_{Na} parameters in the tested control iPSC-CMs (**Table 5-8**). We did not observe differences in variability of the tested I_{Na} parameters between the tested protocol conditions (**Table 5-8**).

T3 protocol significantly changed measured APD90, improved the measured dV/dT_{max} , as well as APA, which now reached more physiological levels (100.4 ± 4.7 mV compared to 80.4 ± 8.4 mV in basic protocol; APA reported in native CMs ranges from 102 to 107 mV) (**Table 5-6**). iPSC-CMs are characterized by a more depolarized RMP in comparison to the physiological conditions in mature cardiomyocytes (RMP ~ -80 to -90 mV). Still, we decided to use a RMP cut-off of below -40 mV for the cells to be included in further analysis, to exclude physiologically not relevant AP recordings. In **Figure 5-6a** and **5-6h** we present the full range of the recorded RMP, with RMP cut off indicated as a red line. We observed a high variability in the recorded AP characteristics in all tested conditions (**Figure 5-5**). Nevertheless, T3 treatment resulted in reduced variability in APD50, while for dV/dT_{max} parameters variability increased in at least two out of five cell lines in comparison to those characteristics recorded from iPSC-CMs obtained using basic protocol (M45-50 C9 and C15, F25-30 C3, BrS8 C2 and C3) (**Figure 5-6; Table 5-10**).

Tested CT characteristics (beat rate, CTD50, rise time and RC) became more similar to physiological values obtained from native CMs [16] with the T3 protocol. The beat rate calculated from CT recordings of T3 treated iPSC-CMs was faster in comparison to this in basic conditions in four out of five tested cell lines (basic: 18.7 ± 2.2 ; T3 protocol: 39.8 ± 2.4) (**Table 5-6**). We observed a significant reduction in CTD50 and RC in three out of five tested cell lines obtained with T3 protocol, while other parameters did not change in comparison to basic differentiation conditions (**Table 5-6**). Similar to observations from AP recordings, we obtained highly variable CT parameter measurements in both differentiation approaches (**Figure 5-7; Table 5-11**). However, this variability was not improved in any of the tested CT parameters in iPSC-CMs obtained with T3 protocol in comparison to basic protocol (**Table 5-11**).

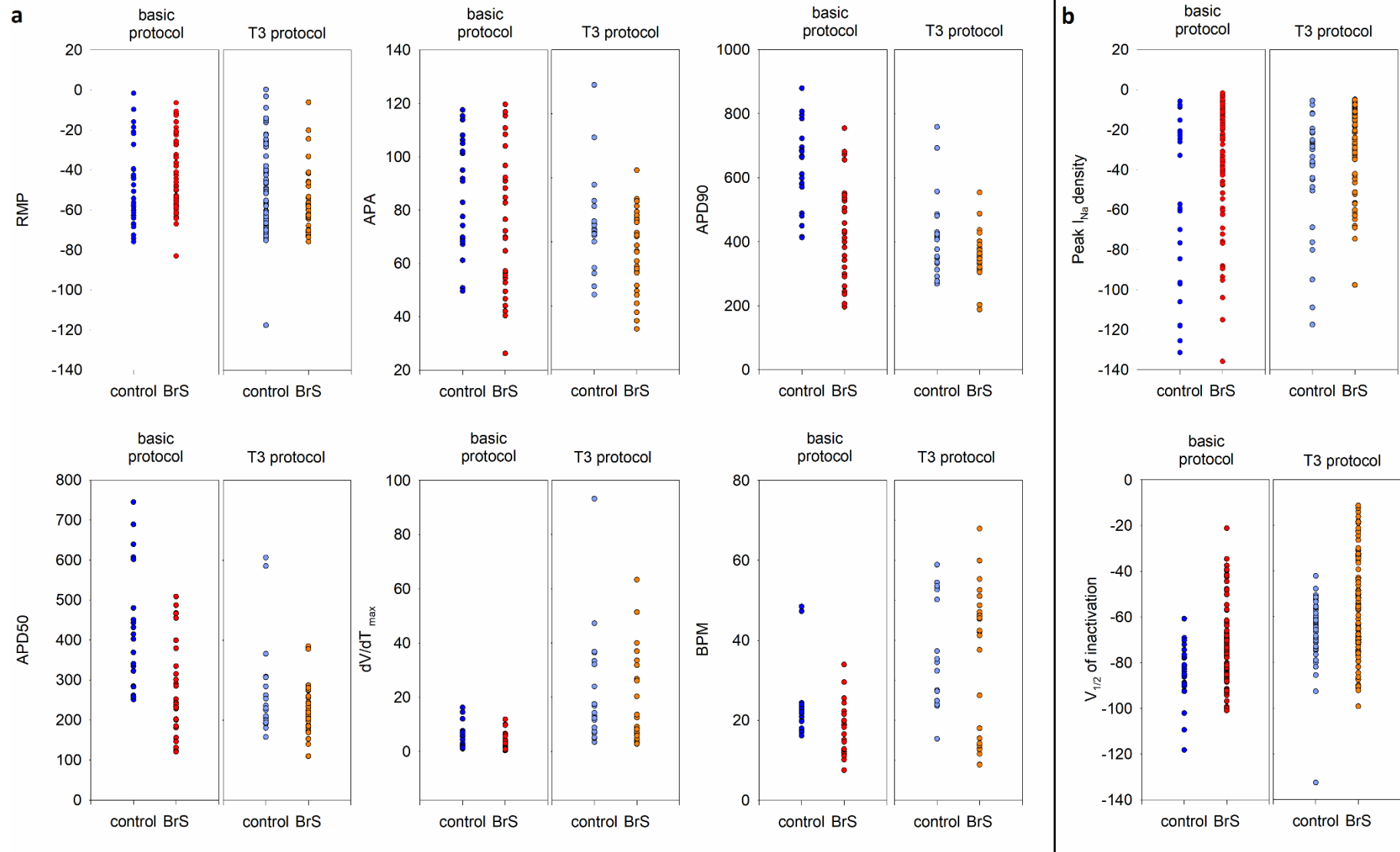


Figure 5-5 Scatter plots for the AP (a) and I_{Na} (b) data used for statistical analysis of the differences between basic conditions and T3 protocol. For AP analysis, cells with RMP >-40 mV were included only in RMP graph to show the spread and excluded for the other AP characteristics.

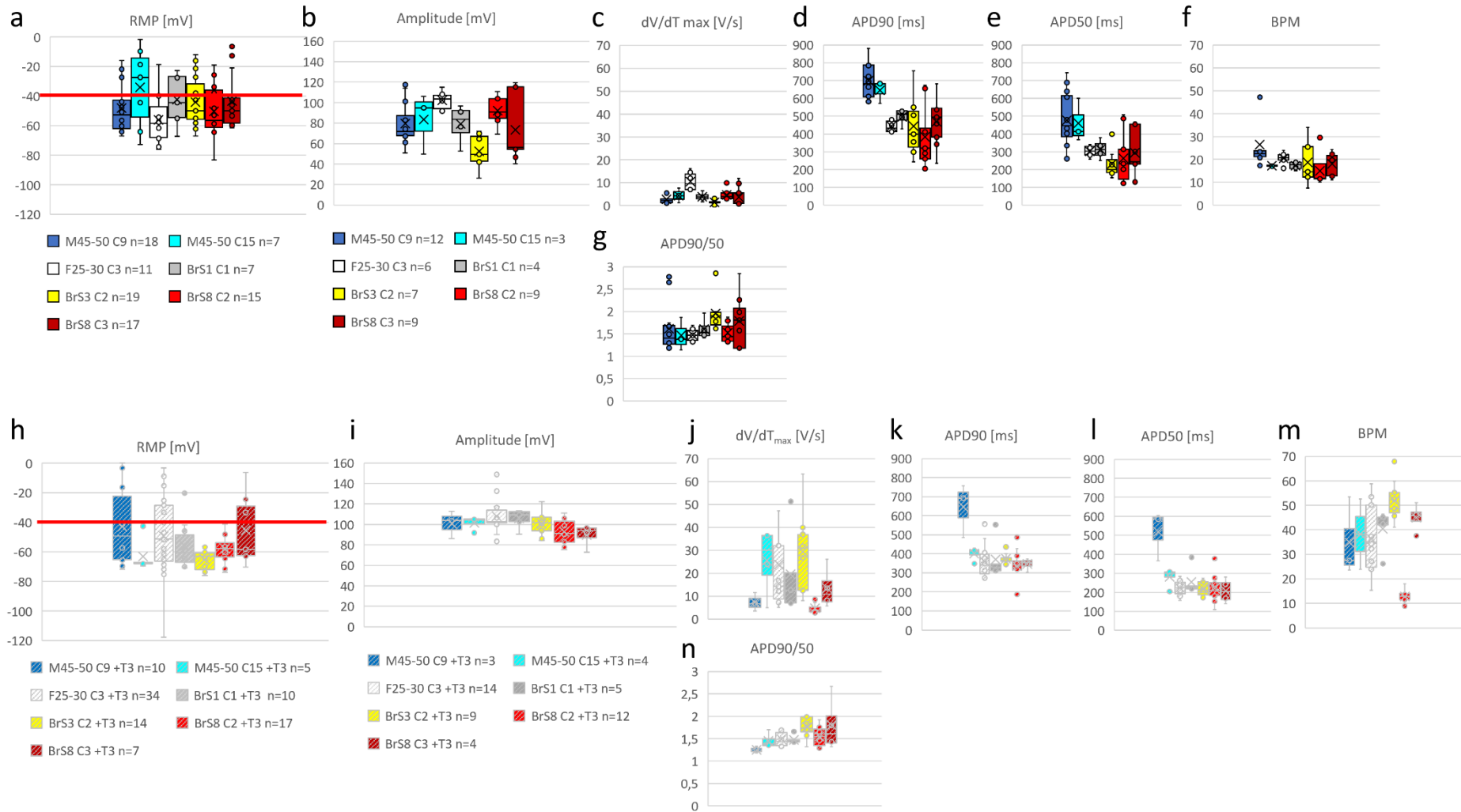


Figure 5-6 AP properties recorded from iPSC-CMs derived using basic differentiation protocol (top panel) and T3 protocol (bottom panel) for: M45-50 C9 (in blue), M45-50 C15 (in cyan), F25-30 C3 (in white), BrS1 C1 (in grey), BrS3 C2 (in yellow), BrS8 C2 (in red) and BrS8 C3 (in dark red). Displayed from left to right are box plots for RMP (a, g), action potential amplitude (APA) (b, h), upstroke velocity (dV/dT_{max}) (c, i), APD90 (d, j), APD50 (e, k), and APD90/50 ratio (f, k).

Table 5-10 AP parameters obtained from iPSC-CMs derived using basic and T3 differentiation protocols. The difference in variability of the tested parameters between the tested treatments was calculated using paired t-test.

	Cell line	RMP [mV]	n	RMP after selection [mV]	SD	APA [mV]	SD	APD90 [ms]	SD	APD50 [ms]	SD	APD90/50	dV/dT _{max} [v/s]	SD	BPM	SD	n
Basic protocol	M45-50 C9	-48.1 ±4.0	18	-57.7 ±2.1	16.5	79.4 ±6	20.9	698.7 ±28.8	99.9	477.4 ±46.6	161.6	1.6 ±0.2	2.7 ±0.5	1.7	26.4 ±3.2	10.8	12
	M45-50 C15	-34.1 ±10.3	7	-60.4 ±8.4	27.1	83.6 ±17.3	30	646.1 ±37.8	65.5	461.1 ±71.2	123.4	1.5 ±0.2	4.4 ±1.8	3.2	17.3 ±0.3	0.6	3
	F25-30 C3	-56.0 ±5.2	11	-67.1 ±3.2	17.3	102.1 ±3.9	9.5	442.9 ±14.3	35.1	303.5 ±13.6	33.4	1.5 ±0.1	10.5 ±1.8	4.3	20.5 ±1	2.7	6
	BrS1 C1	-42.4 ±6.5	7	-55.1 ±4.7	17.3	79.2 ±9.8	19.6	496.2 ±24.6	49.2	313.8 ±27.5	55.0	1.6 ±0.1	3.9 ±1	2.0	17.3 ±0.9	1.9	4
	BrS3 C2	-44.1 ±3.8	19	-55.1 ±2.6	16.6	52.6 ±6.4	16.9	443.8 ±65.9	174.3	233.1 ±31.8	84.1	2.0 ±0.2	1.5 ±0.3	0.8	18.8 ±4.8	10.7	7
	BrS8 C2	-50.4 ±4.5	15	-60.4 ±3.3	17.4	92.3 ±4.5	13.4	382.8 ±59.5	178.6	263.7 ±48.7	146.1	1.5 ±0.1	4.7 ±0.8	2.9	15.0 ±2.6	6.9	9
	BrS8 C3	-43.4 ±4.5	17	-52.8 ±2.1	18.7	73.6 ±11.1	33.2	469.4 ±44.2	132.6	294.7 ±45.9	137.7	1.8 ±0.2	3.7 ±1.4	4.3	18.0 ±1.8	5.1	9
T3 protocol	M45-50 C9	-42.9 ±8.8	10	-61.7 ±4.6	27.7	100.9 ±7.9	13.6	645.6 ±83.6	142.3	519.1 ±76.9	133.2	1.3 ±0.01	7.3 ±2.4	4.1	34.8 ±9.4	16.2	3
	M45-50 C15	-63.0 ±5.1	5	-63.0 ±5.1	11.4	101.5 ±3.2	6.5	401.5 ±18.0	36.1	282.1 ±25.6	51.3	1.5 ±0.1	25.5 ±7.5	15.0	38.3 ±14.3	20.3	4
	F25-30 C3	-49.4 ±3.3	34	-62.9 ±2.6	22.5	107.9 ±4.5	16.7	332.6 ±21.2	83.6	219.8 ±13.2	39.6	1.5 ±0.1	20.1 ±9.2	24.3	36.1 ±5.2	13.8	14
	BrS1 C1	-55.8 ±5.0	10	-59.8 ±3.4	15.8	105.8 ±4.2	9.5	370.6 ±46.2	103.3	254.4 ±32.9	73.5	1.5 ±0.1	19.5 ±8.3	18.6	40.5 ±3.7	8.2	5
	BrS3 C2	-65.2 ±1.8	14	-65.2 ±1.8	6.6	100.4 ±4.0	12.0	374.2 ±9.7	29.0	219.1 ±12.6	37.8	1.8 ±0.1	29.5 ±5.8	17.2	51.9 ±2.7	8.1	9
	BrS8 C2	-57.9 ±2.0	17	-57.88 ±2.03	8.5	96.2 ±3.3	12.1	334.7 ±19.8	83.1	213.9 ±16.2	69.6	1.6 ±0.1	4.5 ±0.8	2.3	12.9 ±1.0	2.9	12
	BrS8 C3	-45.4 ±9.1	7	-63.38 ±2.49	24.1	89.5 ±5.7	11.5	346.6 ±15.2	30.4	208.1 ±32.4	64.9	1.8 ±0.3	13.4 ±4.5	9.0	45.0 ±2.8	5.6	4
Difference in SD between tested conditions (p-value)					0.640		0.077		0.340		0.039*			0.015*		0.149	

Significance code: *≤0.05

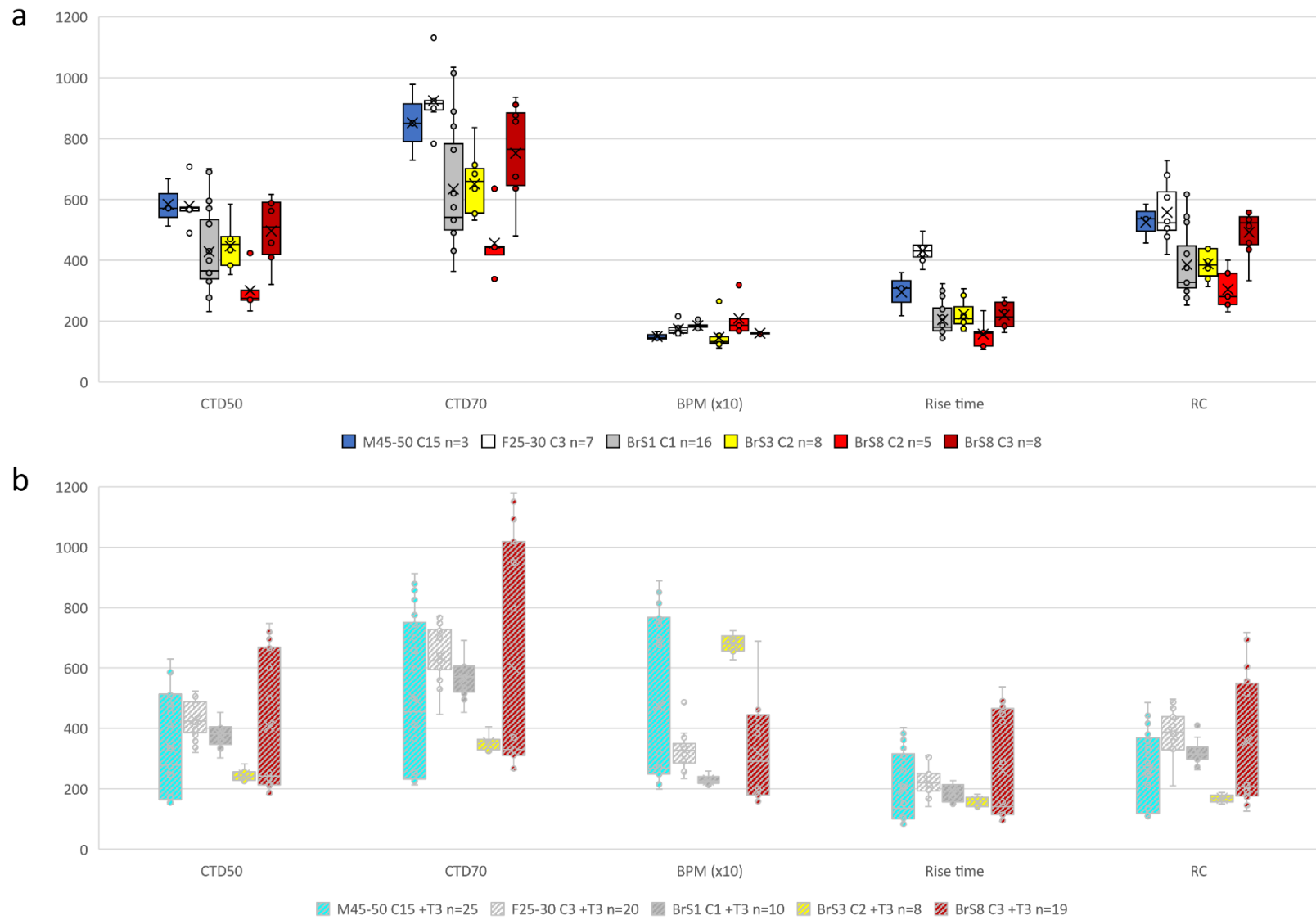


Figure 5-7 CT properties measured from iPSC-CMs obtained with basic (a) and T3 protocol (b) for: M45-50 C9 (in blue), M45-50 C15 (in cyan), F25-30 C3 (in white), BrS1 C1 (in grey), BrS3 C2 (in yellow), BrS8 C2 (in red) and BrS8 C3 (in dark red).

Table 5-11 CT properties. The difference in variability of the tested parameters between the tested treatments was calculated using paired t-test.

	Cell line	CTD50 [ms]	SD	CTD70 [ms]	SD	BPM	SD	Rise time [ms]	SD	RC [ms]	SD	n
Basic protocol	M45-50 C15	583.6 ±45.2	78.2	572.6 ±220.1	381.2	23.3 ±6.9	11.9	370.0 ±110.5	191.5	475.6 ±30.8	53.3	3
	F25-30 C3	577.9 ±24.5	64.8	824.1 ±108.8	287.7	20.0 ±3.3	9.3	441.5 ±18.7	49.5	565.6 ±41.8	110.9	7
	BrS1 C1	428.4 ±35.8	143.3	581.9 ±52.4	209.7	19.1 ±0.8	3.0	223.9 ±29.2	116.9	366.8 ±24.5	105.9	16
	BrS3 C2	445.8 ±32.6	74.2	585.2 ±76.9	217.5	15.6 ±1.4	4.4	244.4 ±25.4	71.8	408.6 ±26.2	74.2	8
	BrS8 C2	300.5 ±32.6	73.0	436.4 ±56.2	125.6	17.8 ±0.9	1.9	181.0 ±33.7	75.3	285.7 ±39.8	89.0	5
	BrS8 C3	496.4 ±38.3	108.2	687.5 ±95.2	269.2	16.1 ±0.1	0.2	266.8 ±41.4	117.0	472.8 ±29.7	83.9	8
T3 protocol	M45-50 C15	339.0 ±35.7	182.3	496.4 ±52.2	266.0	46.2 ±5.5	27.3	197.1 ±23.6	119.7	260.1 ±26.3	134.5	25
	F25-30 C3	428.5 ±13.7	61.2	639.6 ±20.6	92.1	32.7 ±1.3	5.8	221.2 ±9.6	42.8	383.6 ±16.6	74.3	20
	BrS1 C1	377.7 ±13.9	44.0	566.1 ±21.7	68.5	23.0 ±0.5	1.6	188.3 ±9.8	31.1	321.7 ±14.2	45.0	10
	BrS3 C2	245.9 ±6.7	18.8	353.4 ±9.4	26.7	68.0 ±1.1	3.2	159.2 ±5.6	15.9	169.1 ±4.5	12.6	8
	BrS8 C3	472.3 ±60.9	233.9	732.3 ±99.0	376.5	28.9 ±3.7	16.1	309.5 ±45.9	178.1	414.5 ±56.4	221.1	19
Difference in SD between the tested conditions (p-value)			0.761		0.127		0.813		0.301		0.787	

5.5.5 Patient-control differences are dependent on the used differentiation protocol

Finally, we compared morpho-functional characteristics between patient and control iPSC-CMs.

1. Differentiation efficiency

In basic differentiation conditions, we observed no differences in contracting area size and differentiation efficiency between the patient and control groups. In iPSC-CMs obtained with T3 protocol we noticed significant reduction in contracting area size in BrS iPSC-CMs, while there were no differences in differentiation efficiency between the groups (**Table 5-12**). As mentioned before this contracting area size is too variable to be a reliable parameter for comparisons.

Table 5-12 Morpho-functional characteristics of control and patient iPSC-CMs obtained with basic and T3 differentiation protocol: number of replicates with visible contractions, contracting areas, calculated differentiation efficiency. Comparison of the contracting areas and differentiation efficiency was performed using one-way ANOVA.

Treatment Cell line	Basic protocol		P value	T3 protocol		P value
	Controls	Patients		Controls	Patients	
Number of replicates with visible contractions/total number of replicates	31/36	21/24	0.841	44/47	38/44	0.357
Contracting areas [%]*	63.7 ±26	41.5 ±7.2	0.426	72 ±7.3	51.8 ±4.7	0.031*
Differentiation efficiency [% of cACT positive cells]	87.3 ±10.3	82.8 ±10.5	0.762	91.7 ±7.7	94 ±2.3	0.779

Significance codes: *<0.05

2. RNA expression of cardiac markers

In basic differentiation conditions, patient iPSC-CMs showed significant increase in transcript levels of *CACNA1C* and *GJA1*, while the measured expression of *KCNJ8*, *KCNQ1*, *MLC2v* and *TNNI3* was reduced in comparison to tested control iPSC-CMs (**Table 5-13**). In patient iPSC-CMs obtained with T3 protocol, the differences in transcript expression levels of the aforementioned genes in comparison to controls became insignificant. Although we noticed differences in *SCN5A* expression in BrS cell lines in comparison to controls (all of the patient cell lines showed lower *SCN5A* expression in basic protocol and lower or higher expression in T3 protocol; **Figure 5-4**), those changes were not statistically significant (**Table 5-13**).

Table 5-13 Calculated *p* values for the comparison of transcript expression levels between patients and controls. To test if the mean $\Delta\Delta Ct$ was different between BrS cases and controls within each treatment, linear mixed models were fitted with the $\Delta\Delta Ct$ as outcome, case-control status as fixed effect and cell line as random effect, to account for the dependency between observations from the same cell line.

Tested gene	Patients vs. controls	
	Basic conditions	T3 protocol
<i>ANK2</i>	0.052	0.949
<i>ANK3</i>	0.597	0.315
<i>CACNA1C</i>	0.0088*	0.444
<i>GJA1</i>	3.33e^{-10*}	0.104
<i>HCN4</i>	0.338	0.113
<i>KCND3</i>	0.985	0.358
<i>KCNH2</i>	0.221	0.32
<i>KCNJ2</i>	0.094	0.358
<i>KCNJ8</i>	0.047*	0.141
<i>KCNQ1</i>	0.017*	0.613
<i>MLC2a</i>	0.326	0.399
<i>MLC2v</i>	1.07e^{-10*}	0.071
<i>MYH6</i>	0.053	0.862
<i>MYH7</i>	0.075	0.101
<i>RYR2</i>	0.072	0.255
<i>SCN5A</i>	0.946	0.079
<i>TNNI3</i>	4.39e^{-9*}	0.143
<i>TNNT2</i>	0.071	0.262

3. EP characteristics

In the **basic differentiation protocol**, we observed significant reduction in I_{Na} density in all of the tested patient iPSC-CMs in comparison to M45-50 C15 (**Table 5-14, 5-15 Basic protocol**). We did not detect significant difference in $V_{1/2}$ of inactivation in BrS iPSC-CMs in comparison to M45-50 C15 (**Figure 5-8b,f; Table 5-14, 5-15**). Concerning recovery from inactivation we noticed accelerated recovery for BrS1 C1 ($p < 0.001$) and BrS8 C3 ($p = 0.026$) in comparison to M45-50 C15 (**Figure 5-9d; Table 5-14, 5-15**) (52.9 ± 4.4 ms; 30.3 ± 6.2 ms; 25.3 ± 8.9 ms for M45-50 C15, BrS1 C1 and BrS8 C3, respectively). We did not compare I_{Na} characteristics of patient iPSC-CMs with M45-50 C9 due to the extremely low measured I_{Na} density and more positive $V_{1/2}$ of inactivation and F25-30 C3 due to extremely low measured I_{Na} density, deviating from previously reported values for control iPSC-CMs.

Looking at AP properties, we did not see significant differences in RMP and BPM in all tested patient iPSC-CMs in comparison to the tested controls (**Figure 5-6; Table 5-16**). In all tested BrS iPSC-CMs we observed APD90 reduction in comparison with M45-50 C9, and dV/dT_{max} reduction in comparison to F25-30 C3. We measured significant reduction in APA in BrS3 C2 in comparison to F25-30 C3, and significant APD50 reduction in comparison to M45-50 C9 (**Table 5-16**). BrS8 C2 iPSC-CMs showed reduced APD90 in comparison to M45-50 C15, while both BrS8 clones showed reduced APD50 in comparison to M45-50 C9. We saw also significant reduction in CTD50 ($p = 0.024$) in BrS8 C2 iPSC-CMs, in comparison to both tested controls (M45-50 C15, F25-30 C3), while the rest of the tested parameters were not statistically different ($p > 0.1$) in comparison to M45-50 C15 iPSC-CMs (**Figure 5-7a**). All BrS iPSC-CMs showed rise time reduction, while RC was reduced in BrS1 C1, BrS3 C2 and BrS8 C2 RC in comparison to F25-30 C3 (**Table 5-17**).

In the **T3 protocol**, we looked at the I_{Na} properties in BrS lines in comparison to two tested control lines M45-50 C9 C15 and F25-30 C3. We did not compare I_{Na} characteristics of patient iPSC-CMs with M45-50 C9 due to the extremely low measured I_{Na} density, deviating from previously reported values for control iPSC-CMs. BrS1 C1 and BrS8 C2 showed significant I_{Na} density reduction in comparison to both controls, while BrS8 C3 showed I_{Na} reduction compared to F25-30 C3 only (**Table 5-14, 5-15; Figure 5-8 T3 protocol**). We observed no difference in $V_{1/2}$ of inactivation in BrS1 C1 and BrS8 C3, while for BrS3 C2 we observed a significant negative shift in midpoint of inactivation in comparison to both controls (10.11 and 4.51 mV in comparison to M45-50 C15 and F25-30 C3, respectively) (**Figure 5-8f; Table 5-14 to 5-15**). BrS8 C2 iPSC-CMs showed a significant positive shift in $V_{1/2}$ of inactivation in comparison to both controls (9.9 and 15.5 mV in comparison to M45-50 C15 and F25-30 C3, respectively). There was no significant difference in recovery from inactivation of T3 treated patient iPSC-CMs in comparison to the tested controls (except for BrS1 C1 compared to F25-30 C3) (**Figure 5-8h; Table 5-14 to 5-15**).

We did not see differences in RMP, APA and dV/dT_{max} in BrS lines in comparison to tested controls (dV/dT_{max} reduction was observed only in BrS3 C2 in comparison to one tested control – M45-50 C9) (**Table 5-16 T3 protocol**). All tested patient iPSC-CMs showed APD90 and APD50 reduction in comparison with M45-50 C9 iPSC-CMs. BrS8 C2 iPSC-CMs showed significantly slower beating rate in comparison with F25-30 C3 (**Figure 5-6; Table 5-16**). We did not see differences in CTD50 in patient iPSC-CMs in relation to all tested controls (**Figure 5-7; Table 5-17**). We observed reduced beat rate in BrS1 C1 in comparison to M45-50 C9, while BrS3 C2 showed increased beat rate in comparison to both M45-50 C15 and F25-30 C3. Moreover, in BrS3 C2 we observed reduced RC in comparison to F25-30 C3. BrS8 C3 showed CTD70, rise time and RC prolongation, as well as reduced beat rate in comparison with M45-50 C15 (**Figure 5-7; Table 5-17**).

Table 5-14 Summary of I_{Na} properties recorded from obtained iPSC-CMs.

		Peak current density			Inactivation				Recovery			
		[pA/pF]	SD	n	τ [ms]	$V_{1/2}$ [mV]	SD	κ	SD	n	τ [ms]	n
Basic protocol	M45-50 C15	-166.3 ±32.5	97.6	9	0.9 ±0.1	-87.1 ±3.2	9.5	12.3 ±0.8	2.3	6	52.9 ±4.4	6
	BrS1 C1	-50.7 ±11.6	52.9	21	1.5 ±0.4	-75.5 ±2.8	11.2	9.5 ±0.8	3.1	13	30.3 ±6.2	6
	BrS3 C2	-46.4 ±20.2	96.7	22	1.4 ±0.2	-75.8 ±1.8	7.7	10.8 ±4.4	19.8	20	N/A	N/A
	BrS8 C2	-22.8 ±8.8	33.2	7	1.4 ±0.4	-85.5 ±7.4	14.7	16.1 ±7.3	14.5	4	N/A	N/A
	BrS8 C3	-62.6 ±14.5	45	19	1.5 ±0.1	-82.7 ±4.2	10.5	10.0 ±1.4	2.1	20	25.3 ±8.9	10
T3 protocol	M45-50 C15	-237.2 ±98.7	75.9	8	1.1 ±0.2	-81.9 ±2.0	5.7	12.1 ±0.7	2.0	8	30.4 ±2.9	6
	F25-30 C3	-349.6 ±55.0	197.9	16	1.3 ±0.1	-87.5 ±2.0	12.3	8.7 ±0.5	2.5	38	36.1 ±2.4	21
	BrS1 C1	-96.8 ±27.9	142.4	26	1.1 ±0.1	-84.1 ±6.5	22.4	7.9 ±1.7	5.8	29	26.4 ±9.5	7
	BrS3 C2	-198.6 ±28.3	137.7	20	1.1 ±0.1	-92.0 ±2.2	15.1	7.0	9.5	37	41.3 ±3.9	11
	BrS8 C2	-51.3 ±36.5	60.8	3	0.8 ±0.2	-72.0 ±3.9	7.7	9.6 ±1.3	2.6	4	N/A	N/A
	BrS8 C3	-157.9 ±39.3	171.4	16	1.1 ±0.1	-84.9 ±3.5	0.7	9.3 ±0.4	0.3	17	30.5 ±4.5	23

Table 5-15 P-values obtained for case-control comparison of the tested I_{Na} parameters between the tested iPSC-CMs. N/A – comparison was not possible due to lacking data. Comparison of the I_{Na} properties between the groups was carried out using one-way ANOVA.

Protocol	Tested characteristic	Peak I_{Na}		$V_{1/2}$ inactivation		Recovery	
	Cell line	M45-50 C15	F25-30 C3	M45-50 C15	F25-30 C3	M45-50 C15	F25-30 C3
	BrS1 C1	<0.001*	-	0.162	-	<0.001*	-
	BrS3 C2	<0.001*	-	0.098	-	N/A	-
	BrS8 C2	<0.001*	-	0.833	-	N/A	-
	BrS8 C3	0.002*	-	0.414	-	0.026*	-
	BrS1 C1	<0.001*	<0.001*	0.781	0.781	0.698	0.035*
	BrS3 C2	0.835	0.120	0.016*	0.012*	0.329	0.329
	BrS8 C2	<0.001*	<0.001*	0.03*	0.03*	N/A	N/A
	BrS8 C3	0.820	0.031*	0.644	0.622	0.590	0.590

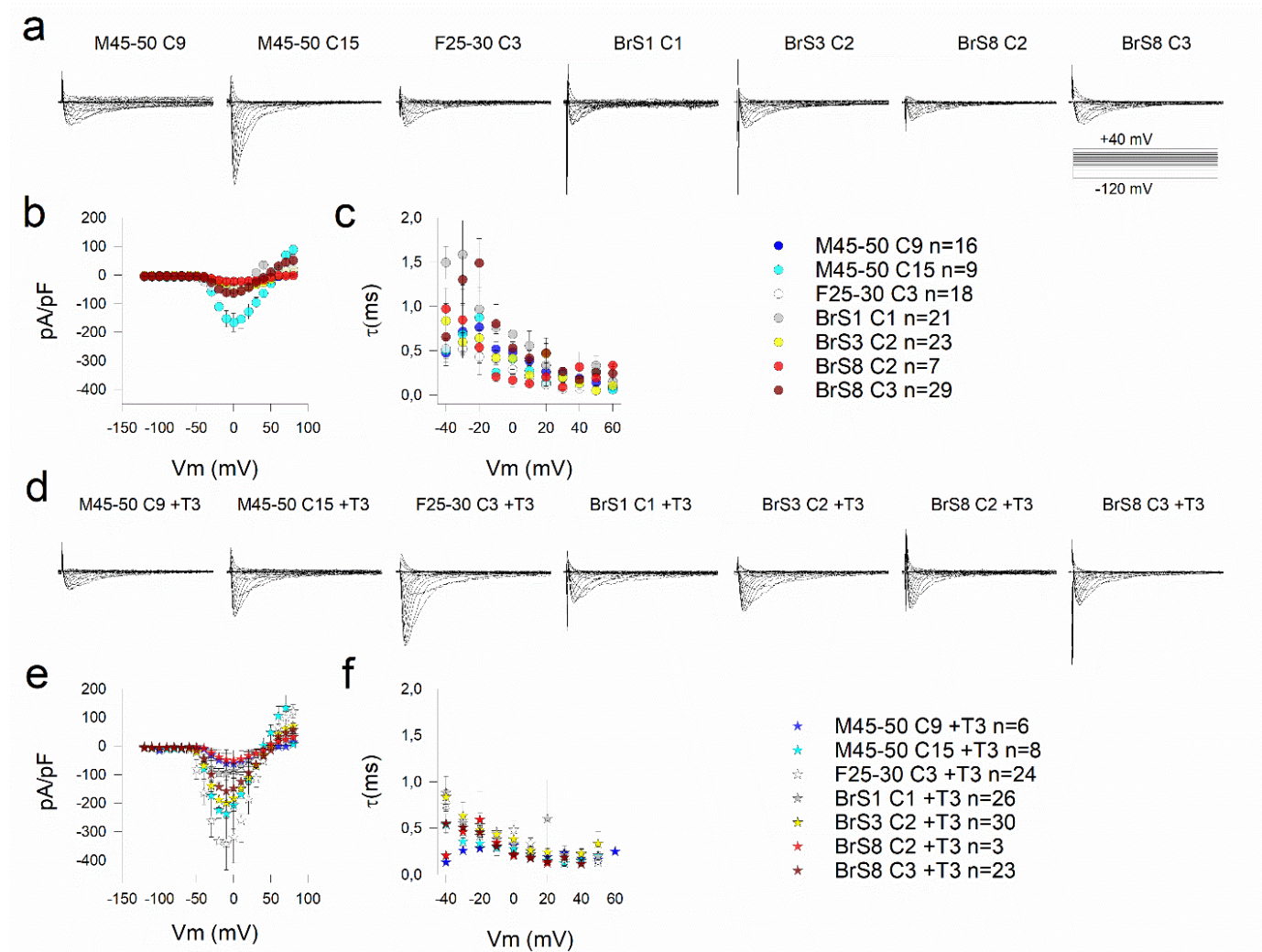


Figure 5-8 Sodium current density and activation properties. (a) From left to right displayed are representative sodium current recordings for M45-50 C9, M45-50 C15, F25-30 C3, BrS1 C1, BrS3 C2, BrS8 C2 and BrS8 C3 obtained using normal differentiation protocol. The top panel shows current-voltage relationship (b) and voltage-dependence of activation (c) plots for: M45-50 C9 (blue circles), M45-50 C15 (cyan circles), F25-30 C3 (white circles), BrS1 C1 (grey circles), BrS3 C2 (yellow circles), BrS8 C2 (red circles) and BrS8 C3 (dark red circles). (d) From left to right displayed are representative sodium current recordings for M45-50 C9, M45-50 C15, F25-30 C3, BrS1 C1, BrS3 C2, BrS8 C2 and BrS8 C3 obtained using differentiation protocol with T3 treatment. The bottom panel shows current-voltage relationship (e), activation kinetics (f) and voltage-dependence of activation (g) plots for: M45-50 C9 (blue stars), M45-50 C15 (cyan stars), F25-30 C3 (white stars), BrS1 C1 (grey stars), BrS3 C2 (yellow stars), BrS8 C2 (red stars) and BrS8 C3 (dark red stars).

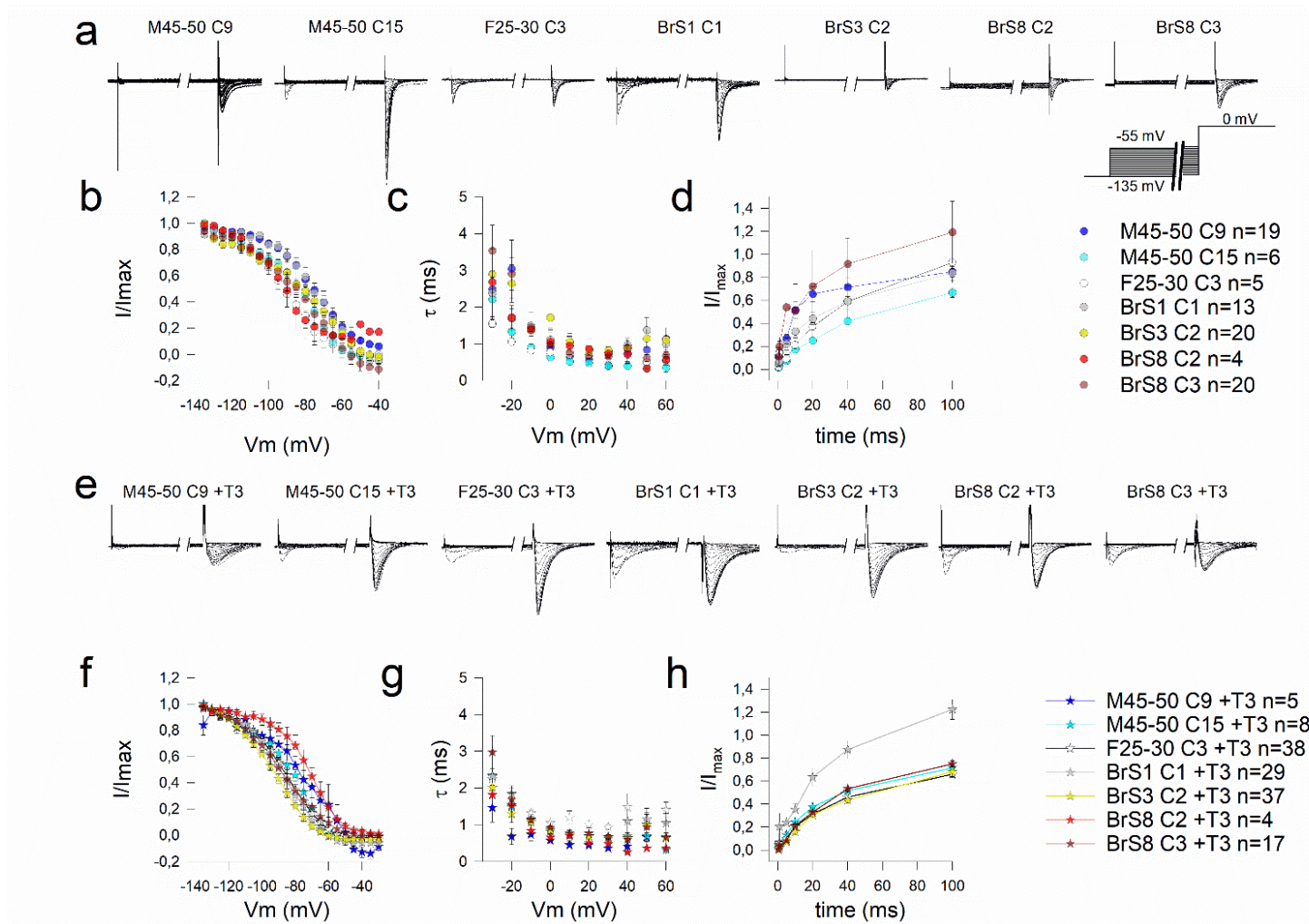


Figure 5-9 Sodium current inactivation properties. (a) From left to right displayed are representative sodium current traces of: M45-50 C9, M45-50 C15, F25-30 C3, BrS1 C1, BrS3 C2, BrS8 C2 and BrS8 C3 obtained using normal differentiation protocol. The top panel shows voltage dependence of inactivation graph (b), inactivation kinetics (c) and recovery from inactivation (d) for: M45-50 C9 (blue circles), M45-50 C15 (cyan circles), F25-30 C3 (white circles), BrS1 C1 (grey circles), BrS3 C2 (yellow circles), BrS8 C2 (red circles) and BrS8 C3 (dark red circles) obtained with a normal differentiation. (e) From left to right displayed are representative sodium current traces of: M45-50 C9, M45-50 C15, F25-30 C3, BrS1 C1, BrS3 C2, BrS8 C2 and BrS8 C3 obtained using T3 differentiation protocol. The bottom panel shows voltage dependence of inactivation graph (f), inactivation kinetics (g) and recovery from inactivation (h) for: M45-50 C9 (blue stars), M45-50 C15 (cyan stars), F25-30 C3 (white stars), BrS1 C1 (grey stars), BrS3 C2 (yellow stars), BrS8 C2 (red stars) and BrS8 C3 (dark red stars) obtained with T3 differentiation protocol.

Table 5-16 Calculated p values for the observed AP characteristics between tested patient and control iPSC-CMs. Comparison of the AP properties between the groups was carried out using one-way ANOVA. Statistically significant differences are indicated in bold with a *.

Protocol	Tested characteristic Cell line	RMP (before selection)			APA			APD90			APD50			dV/dT _{max}			BPM		
		M45-50 C9	M45-50 C15	F25-30 C3	M45-50 C9	M45-50 C15	F25-30 C3	M45-50 C9	M45-50 C15	F25-30 C3	M45-50 C9	M45-50 C15	F25-30 C3	M45-50 C9	M45-50 C15	F25-30 C3	M45-50 C9	M45-50 C15	F25-30 C3
Basic	BrS1 C1	>0.9			0.987	0.957	0.750	0.005*	0.822	0.988	0.379	0.829	0.901	0.978	0.994	0.015*	>0.1		
	BrS3 C2	>0.9			0.216	0.515	0.004*	0.003*	0.342	0.990	0.005*	0.197	0.981	0.987	0.857	<0.001*	>0.1		
	BrS8 C2	>0.9			0.894	0.982	0.982	<0.001*	0.060*	0.978	0.009*	0.331	0.997	0.834	0.985	0.007*	>0.1		
	BrS8 C3	>0.9			0.991	0.991	0.259	0.004*	0.451	0.972	0.041*	0.556	0.989	0.98	0.993	<0.001*	>0.1		
T3	BrS1 C1	0.792	0.973	0.924	>0.1			<0.001*	0.998	0.979	<0.001*	0.991	0.941	0.018*	>0.2		0.995	0.967	0.997
	BrS3 C2	0.052	0.808	0.098	>0.1			<0.001*	0.990	0.932	<0.001*	0.683	0.978	<0.001*	>0.2		0.682	0.808	0.186
	BrS8 C2	0.451	0.984	0.781	>0.1			<0.001*	0.827	0.942	<0.001*	0.559	0.998	0.178	>0.2		0.280	0.058	0.003*
	BrS8 C3	0.947	0.766	0.969	>0.1			<0.001*	0.977	0.995	<0.001*	0.656	1.0	0.072	>0.2		0.987	0.997	0.972

Table 5-17 Calculated p values for the observed CT characteristics between tested patient and control iPSC-CMs. Comparison of the CT properties between the groups was carried out using one-way ANOVA. Statistically significant differences are indicated in bold with a *.

Protocol	Tested characteristic Cell line	CTD50		CTD70		BPM		Rise time		RC	
		M45-50 C15	F25-30 C3	M45-50 C15	F25-30 C3	M45-50 C15	F25-30 C3	M45-50 C15	F25-30 C3	M45-50 C15	F25-30 C3
Basic	BrS1 C1	0.231	0.059	>0.1		>0.1		0.276	<0.001*	0.378	<0.001*
	BrS3 C2	0.419	0.260	>0.1		>0.1		0.542	0.010*	0.635	0.023*
	BrS8 C2	0.017*	0.002*	>0.1		>0.1		0.176	0.002*	0.073	<0.001*
	BrS8 C3	0.690	0.660	>0.1		>0.1		0.733	0.029*	0.964	0.373
T3	BrS1 C1	0.535	0.678	0.475	0.716	0.005*	0.399	0.845	0.927	0.596	0.474
	BrS3 C2	0.529	0.080	0.546	0.079	0.015*	<0.001*	0.944	0.773	0.420	0.006*
	BrS8 C3	0.087	0.798	0.034*	0.609	0.010*	0.500	0.028*	0.155	0.006*	0.509

4. BrS phenotype subgroups are visible in iPSC-CMs obtained with T3 protocol

In our experiments we used cell lines from BrS donors who presented different phenotype severity – BrS3 is severely affected, BrS1 and BrS8 are asymptomatic – so we looked for a correlation with iPSC-CM EP characteristics. We observed a significant difference between severity groups in contracting area size of the iPSC-CMs obtained with basic protocol, but not in cells obtained with the T3 protocol (**Table 5-6**). Nevertheless, we deemed this characteristic to be unreliable, thus those observations should be taken cautiously. There was no significant difference in differentiation efficiency between the severity groups in both basic and treatment protocols (**Table 5-6**). There were no significant differences in sodium current density and $V_{1/2}$ of inactivation between symptomatic and asymptomatic patients in basic differentiation protocol (**Table 5-18**). Although there was a significant reduction in APA in the severe class iPSC-CMs, no significant differences were observed in other AP and CT parameters between tested phenotype classes in iPSC-CMs obtained with basic protocol (**Figure 5-6, 5-7; Table 5-10, 5-18**).

In T3 protocol conditions we observed significant peak I_{Na} density increase as well as a significant 11.7 mV negative shift in $V_{1/2}$ of inactivation in the severe patient in comparison to the average I_{Na} and $V_{1/2}$ obtained from asymptomatic patient iPSC-CMs (**Figure 5-6, Table 5-18**). In iPSC-CMs obtained with T3 protocol we observed significant increase in dV/dT_{max} and beat rate in iPSC-CMs of symptomatic patient in comparison with those from asymptomatic patients (**Table 5-18**). Similarly, we observed the beat rate increase measured from CT recordings from symptomatic patient iPSC-CMs in comparison with that of asymptomatic patients. Moreover, we observed a reduction in CTD50, CTD70 and RC in symptomatic patient iPSC-CMs (**Table 5-18**).

Table 5-18 P-values obtained for comparison of the average values for the tested EP parameters between the characterized symptomatic and asymptomatic patient iPSC-CMs. Comparison of the EP properties between the groups was carried out using one-way ANOVA. Statistically significant differences are indicated with * and in bold.

Protocol	Tested characteristic												
	I_{Na} properties			AP properties					CT properties				
	Peak I_{Na}	$V_{1/2}$ inactivation	Recovery	APA	APD 90	APD 50	dV/dT_{max}	BPM	CTD50	CTD70	BPM	Rise time	RC
Basic	0.962	0.289	N/A	<0.001*	0.952	0.503	0.245	0.637	0.599	0.904	0.136	0.765	0.591
T3	0.035*	0.026*	0.117	0.569	0.581	0.883	0.040*	0.001*	0.018*	0.015*	<0.001*	0.103	0.006*

N/A – comparison was not possible due to lacking data.

5.6 Discussion

iPSC-CM modeling has been successfully applied in research of cardiac arrhythmias. Despite the undeniable successes in disease modeling, there is still a discussion about the maturity of the obtained cells as well as potential preferential selection of the clonal iPSC lines and their influence on the obtained results. We performed investigation of the intra- as well as inter-clonal variability of the morpho-functional properties of iPSC-CMs obtained from control individuals and Belgian *SCN5A* founder mutation carriers, obtained using a basic differentiation protocol as well as the same protocol with T3 or T3 combined with lactate treatments to address maturation and culture purity issues. While we saw significant improvement in investigated molecular as well as electrophysiological parameters in T3 treated iPSC-CMs in comparison to basic conditions, we did not see incremental improvement of the tested parameters with addition of lactate treatment, thus we decided to combine the results from iPSC-CMs cultured with T3 and T3 with lactate treatments for the comparisons of sodium current, AP and CT properties.

Optimized differentiation protocol ("T3 protocol") has an impact on the observed parameters and variability of the results

We investigated if the T3 protocol is improving the outcome in comparison to basic differentiation conditions. We observed contracting cells in all of the tested lines in over 85% of differentiated replicates, regardless of the used differentiation approach (**Table 5-6**). Calculation of the contracting surface areas showed overall similar contracting regions between T3 treated iPSC-CMs and those from the basic protocol, amounting to on average 60% compared to 51% respectively throughout the tested cell lines. However, this contracting surface area showed a very high variability between cell lines and differentiations, and could not always be correlated to the electrophysiological quality of the cells in downstream assays. So we considered it an unreliable parameter to determine the quality of the differentiation performance. It has been previously shown that T3 promotes contractile function of the iPSC-CMs [3; 4; 5], based on specialized contractility assays performed on iPSC-CMs or engineered heart tissue where contour movement recognition was applied using traction force microscopy with fluorescent beads or intracellular calcium fluorescent indicator dyes. As such, we conclude that the size of contracting areas is not reliably reflecting the contractile function of the obtained iPSC-CMs, and more precise contractility assays should be considered to determine differences in contractility of our iPSC-CMs between basic and T3 treatment conditions.

As during maturation, the expression profile of cardiac-specific markers in iPSC-CMs undergoes changes, we performed immunocytochemistry staining and transcript expression analysis of cardiac-specific markers and looked at differences in expression between the used protocols (**Figure 5-4, 5-5**). It was previously shown that T3 promotes expression of *TNNI3*, *MYH6*, *KCNA5*, *KCND2* or *KCND3* and inhibits expression of *MYH7* and *NCX*, while lactate treatment results in higher levels of *RYR2* and *TNNT2* expression in obtained cultures. Those changes improve excitation-contraction coupling and are visible as enhanced contractions. *MYH7*, alongside *TNNT2*, are the sarcomeric-related proteins, expressed in adult human (ventricular) cardiomyocytes [6; 7; 8; 9]. As expected, we noticed better organization of sarcomeric proteins cACT and cTNNI as well as significant increase in *RYR2* transcript expression in obtained cells after T3 treatment, which is a hallmark of maturation of iPSC-CMs (**Figure 5-4, 5-5**). Interestingly, we observed the opposite effect of T3 treatment on the *MYH6/MYH7* isoforms expression. While in adult human ventricular cardiomyocytes, an isoform switch from α -MHC (*MYH6*) to β -MHC (*MYH7*) occurs [16], in our T3 protocol derived iPSC-CMs we observed more prominent increase in expression of *MYH6* compared to *MYH7*. Similar observation was reported by Huang et al. [16] as well as Yang et al. [3] in their iPSC-CMs, where the explanation for this phenomenon was attributed to the enhancing function of T3 on the α -MHC promoter and miRNA208a expression, a miRNA previously shown to inhibit β -MHC expression. Thus in the applied T3 treatment *MYH6* levels can remain higher than *MYH7* expression, despite the other observed features of cell maturation [3; 16]. *MYH6* and *MLC2a* are expressed at higher levels in early stages of embryonic cardiomyocyte development, and in adult atria, while *MYH7* and *MLC2v* are the

predominant adult isoforms in ventricular cardiomyocytes [5; 16; 18; 19; 20]. With the improved maturation in iPSC-CMs obtained with T3 protocol, we had hoped to observe increase in expression of *MLC2v*. However, the expression of *MLC2v* remained low in T3 protocol iPSC-CMs, compared to the adult human ventricle tissue (**Figure 5-5**). Thus, the observed high expression of *MYH6* and *MLC2a*, together with the low expression of *MLC2v* in T3 treated iPSC-CMs suggests still incomplete maturation of the obtained CMs.

Experiments performed on iPSC-CMs require several rounds of differentiation ('differentiation batches') to obtain a sufficient number of observations and prove the consistency of the results. Thus, it is important that the batch-to-batch difference in the obtained results is minimal. We looked at batch-to-batch differences (intra-clonal) in the characterized parameters. Measured differentiation efficiency as well as EP parameters did not differ between batches (**Table 5-2**). Taking into account the small variability in the remaining parameters, we are able to pool the data from separate differentiation batches.

iPSC lines are derived from selection of best performing colonies, which present as compact homogenous groups of cells with defined edges and flat appearance. This type of high-quality morphology traits ensures preservation of the pluripotency characteristics, observed in indefinite self-renewal without spontaneous differentiation. To minimize the bias of the functional observations due to the clonal selection, it is a good practice to compare results obtained from minimum two iPSC cell lines obtained from a single donor. We looked at the inter-clonal variability in iPSC-CMs from two clones for one control and one asymptomatic BrS patient (**Table 5-3, 5-4**). We did not see differences in differentiation efficiency between two clones from both cell lines generated with basic or T3 protocol. Looking at the I_{Na} properties of obtained cells, we noticed a significant difference in peak current density measured in both clones of the control line (M45-50 C9 and C15, where C9 showed significant I_{Na} reduction), while there was no difference in this characteristic in both clones obtained from the patient in both basic and T3 protocols (**Table 5-3, 5-4**). We did not see differences in AP properties between both control clones in both basic and T3 protocols, while for BrS8 clones we saw a significant difference in BPM and RMP in basic differentiation protocol (**Table 5-3**). The observed difference in BPM and RMP in BrS8 clones was reduced with application of T3 protocol (**Table 5-4**). To understand the origin of the observed inter-clonal differences, we looked at the transcript levels of the cardiac markers (**Table 5-3, 5-4; Figure 5-2**). However, we were not able to correlate the observed transcript expression levels with the aforementioned electrophysiological properties. Nevertheless, T3 treatment improved I_{Na} density in M45-50 C9 (**Figure 5-8**), though it did not contribute to reduction of the inter-clonal differences in I_{Na} characteristics in this cell line (**Table 5-3, 5-4**). Interestingly, despite low I_{Na} density, M45-50 C9 iPSC-CMs showed AP characteristics (including APA and dV/dT_{max}) falling within the range of characteristics from previously reported control iPSC-CMs (**Chapter 4**) (**Table 5-6; Figure 5-6**).

In literature, T3 treatment was shown to improve EP properties of the iPSC-CMs, through improved maturation status of the ionic channels and cytoskeleton of the obtained cells, which contributes to measurement of lower RMP and longer APD in comparison to less mature cells, as well as reducing the CTD and rise time [4; 10]. In our hands, T3 treated cells displayed higher I_{Na} densities in comparison to those obtained from the same cell lines with basic protocol (**Figure 5-8b,e; Table 5-14**). We also noticed reduced difference in the peak I_{Na} density between T3 treated controls (M45-50 C15 and F25-30 C3), in comparison to those obtained in basic conditions (**Table 5-9**). Treated control cells showed no difference in the voltage dependence from inactivation. Improved I_{Na} density goes in line with the improvement of APA and dV/dT_{max} values in all of the tested lines cultured with T3 protocol (**Figure 5-10**). Nevertheless, our results presented with persistent issue of signal variability, regardless of the used differentiation approach (except for the APD50 values, which showed reduced variability in 5 out of 7 tested cell lines in T3 protocol).

Comparison of the measured EP properties in the T3 protocol to reported EP values in the literature

It was previously shown, that the molecular and EP properties of iPSC-CMs resemble those of fetal cardiomyocytes [6; 11; 12; 13; 15]. To overcome this issue, prolonged cell culture time as well as maturation protocols with addition of T3 and/or dexamethasone hormones have been used, showing improved cardiac marker expression profiles, cell structure and growth morphology, as well as EP characteristics [3; 4]. We summarized the reported measured value ranges for I_{Na} , AP and CT characteristics of iPSC-CMs from in total 20 reports in **Table 5-19** [21; 22; 23; 24; 25; 26; 27; 28; 29; 30; 31; 32; 33; 34; 35; 36; 37; 38; 39; 40]. Native ventricular cardiomyocytes (VMCs) show RMP within the range of -78.8 to -88.2 mV; APA of 102 to 108.1 mV; APD50 of 129.9 to 159.1 ms; APD90 of 159.2 to 365 ms and dV/dT_{max} of 169 to 262 V/s. Meanwhile, in control iPSC-CMs those ranges fall much lower. The RMP ranges from -40 to -77 mV, which has a direct impact on the other AP characteristics, where the more depolarized RMP, the more 'immature' the other AP properties are. Van de Sande et al. reported more negative RMP values for AP recordings obtained from small patches of monolayers, where the cells were forming a syncytium. They hypothesized that the preserved gap junctions play a role in this, presenting a more native setting in comparison to isolated cells [27]. As such, we also performed our AP recordings on small monolayers of iPSC-CM. The higher the availability of the sodium channels, the faster the upstroke velocity and larger APA. Upstroke velocity recorded from iPSC-CMs is usually much slower, compared to native VMCs. We observed this in the dV/dT_{max} reaching only 7% or 16% of that measured in native VMCs in iPSC-CMs obtained with basic differentiation protocol or T3 protocol respectively (**Table 5-19**).

AP recordings obtained from iPSC-CMs derived with T3 protocol showed (on average) higher APA, shorter APD, faster BPM and higher dV/dT_{max} . Despite the improved beat rate and significantly faster dV/dT_{max} , the values for the measured upstroke velocity were still much slower in comparison with those values reported from native ventricular CMs (**Table 5-19**). This can be explained with still too positive RMP (**Figure 5-6**), in which most of the available sodium channels remain inactivated. This can also be deduced from the obtained inactivation curves, where $V_{1/2}$ of inactivation falls between -85 mV for basic conditions to -80 mV for T3 treated iPSC-CMs from all of the tested cell lines (**Figure 5-9b,f**). With the RMP cut off of -40 mV we are far from the physiological RMP value at which all of the available sodium channels would be active. This will have an influence on the functional characterization of BrS phenotype. However it can be overcome with application of in silico I_{K1} injection, which will lower the RMP level in the patched iPSC-CMs, improving the availability of $Na_v1.5$ channels [41]. In monolayer setting, iPSC-CMs retain their cell-to-cell connections which has beneficial impact on their rhythmicity as well as propagation of the electrical signals. Electrical signal propagation in CMs depends on a proper development of calcium handling in the cells. Thus, we added imaging of calcium transients to the experimental pipeline on the iPSC-CMs to investigate calcium handling in the obtained cells. We measured CTD50 ranges from 538 to 629 ms in basic conditions and 303 to 442 ms in T3 conditions; rise time from 259.5 to 481 ms in basic conditions and from 174 to 231 ms in T3 conditions; decay rate of 445 to 607 ms in basic conditions and 234 to 400 ms in T3 conditions in our control iPSC-CMs, which were falling within the previously reported CT value ranges (**Table 5-19**). Similar to our observations for AP recordings, we observed a faster beat rate in T3 treated iPSC-CMs (31.4-51.7 BPM in comparison to 16.5-30.2 BPM in basic conditions), which had a positive impact on difference in CTD70, rise time and decay rate between the tested controls (**Figure 5-7; Table 5-11**).

Table 5-19 Summary of AP, CT and I_{Na} properties from literature review.

Reference	Differentiation protocol	Patching temperature	AP parameters					n
			RMP [mV]	APA [mV]	APD50 [ms]	APD90 [ms]	dV/dT_{max} [V/s]	
Basic differentiation conditions								
Ma et. al. [22]	CHIR99021, IWR1	36±1	-58.9±0.8	106.4±1.0		443.5±17.3	15.6±0.8	10-25
Treatment differentiation protocol								
Bett et. al. (2013)[23]	Commercial iCell CMs	RT	-63±5.8	83±11		955±103		25
Gibson et. al. (2014) [24]	Commercial iCell CMs	RT	-68±9	103±9		427±65		8
Lopez-Redondo et. al. (2016) [25]	Commercial iCell CMs	36±1	-43.3±1.7	79.4±2.9	309.4±29.5			54
Herron et. al. (2016) [26]	Commercial iCell CMs	37	-59.3±1.7	105±5				6
Kussauer et. al. [27]	CHIR99021, IWR1	34	-43.4±2.8	87.5±5.8	362.1±56.4	473.6±64.0	17.8±4.6	11
Van de Sande et. al. [28]	Commercial hSC-CMs Cor.4U	RT isolated cells	-49.3±2.3	85.3±3.1		381±17.8	7.7±2	16
		RT monolayer	-68.1±1.4	118±3.2		530±13	77.2±9	20
Hoekstra et. al. [40]	Native ventricular CMs	37	-81.8±3.3	106.7±1.4		213±7	215±33	
		37	-87.1±1.1	105±2		330±16	234±28	
		37	-86±1	104±2		351±14	228±11	
Goodrow et. al. [29]	Native ventricular CMs		-87.3±		144.5±14.6	172.2±13	183.3±14.3	3
CT parameters								
Reference	Differentiation protocol	Imaging temperature	CT parameters			n		
			CTD90 [ms]	CTD50 [ms]	Rise time [ms]		Decay [ms]	
Basic differentiation conditions								
Paci et. al. (2020) [30]	Commercial iCell ² CMs	21±1	1826.2±1071.3	920.1±456.3				42
Shah et. al. (2020) [31]	END-2 co-culture	36±1	1900±100		480±20	250±20		68
Shah et. al. (2019) [32]	END-2 co-culture	36±1			251±29	2261±676		34
Higgins et. al. (2019) [33]	Monolayer-based with CHIR99021 and IWP2	36±1		1533±100		2790±50		200
Ma et. al. [22]	Monolayer based with CHIR99021 and IWR1	37	471.3±12.6		92.0±6.6			10-25
Ahola et. al. (2017) [34]	END-2 co-culture	36±1	1663±570	797±227				13

Liang et. al. (2016) [41]	Monolayer-based with CHIR99021 and IWR1	36±1		471.3±12.6	92±6.6		10-25	
Pioner et. al. (2019) [21]	Monolayer-based with CHIR99021 and Wnt-C59	36±1		340±4	234±3		336	
	Native left ventricular CMs	36±1		2505±26	95±9		27	
I_{Na} properties								
Reference	Differentiation protocol	Imaging temperature	I _{Na} properties				n	
			Peak density [pA/pF]	V _{1/2} of activation [mV]	V _{1/2} of inactivation [mV]	Recovery from inactivation [ms]		
Basic differentiation conditions								
Ma et. al. [22]	CHIR99021, IWR1	RT	-122.8±31.3				10-25	
de la Roche et. al. [35]	CHIR99021, IWP2	RT	-279±53	-58±0.4	77± 0.3	62±28	20	
Treatment differentiation protocol								
Kussauer et. al. [27]	CHIR99021, IWR1	RT	-245.8±32.7	-35.7± 0.5	-70.3± 0.4	19.1±0.1	15	
Selga et. al. [36]	CHIR99021, IWP2	RT	-116.9±28.7				25	
			-95.4±41.6				12	
			-94.7±28.3				37	
Davis et. al. [37]	CHIR99021, IWP2	RT	-116.9±28.7	-53.2±2.1	-73.3±2.3	22±8	25	
			-95.4±41.6	-43.3±2.1	-80.6±1.5	20±2	12	
			-94.7±28.3	-45.1±4.1	-77.9±2.6	22±2	11	
Veerman et. al. [38]	CHIR99021, IWP4	RT	-93.6±84.9	-34.6±0.5	-78.9±1.4	5.2±0.5	36	
			-83±83.3	-33±0.9	-85±1	5.9±0.7	31	
Sakakibara et. al. [39]	Native human ventricular CMs	RT	-20.2±2.2	-42.4±3	-100.3±2.1		34	
Goodrow et. al. [29]	Native human ventricular CMs	RT	-70.4±9.3	-43.4±0.4	-74.4±0.2	42.6±2.5	14	

iPSC-CM differences between BrS patients and controls

The final and most important question we tried to answer was if we can detect differences between BrS patient and control iPSC-CMs. As reviewed in [15], the main effect of the I_{Na} loss-of-function in BrS iPSC-CMs is observed as a reduction in peak I_{Na} density. If the defective channels are trafficked to the plasma membrane, a negative shift in voltage dependence of channel inactivation, which contributes to lower availability of conductive (active) channels; a positive shift in the voltage dependence of activation, which leads to a requirement of a more depolarized cell membrane to activate the channels, and less commonly – a delayed time of recovery from inactivation, which prolongs the inactivation of the channels can be observed. We report significant inter-clonal differences in $V_{1/2}$ of inactivation in iPSC-CMs obtained from two clones from a single BrS donor, which were not reduced with application of T3 protocol (**Table 5-3, 5-4**). In case-control comparison for $V_{1/2}$ of inactivation those ranges amounted from 2 to 18 mV and 2 to 16 mV in basic and T3 protocols, respectively (**Table 5-14, 5-15**). Based on generally more physiological properties obtained in T3 treated iPSC-CMs, the changes in $V_{1/2}$ of inactivation in these cells should be considered as relevant. We observed a loss-of-function of I_{Na} in BrS3 C2 and BrS8 C2 (reduced I_{Na} density, leading to lower availability of the channels) and a mixed loss- and gain-of-function phenotype for BrS1 C1 and BrS8 C3 (reduced I_{Na} density and accelerated recovery from inactivation (reduced availability and prolonged inactivation of the channels)) iPSC-CMs derived with basic differentiation protocol. Meanwhile, in iPSC-CMs obtained with T3 treatment we observed a loss-of-function effect on I_{Na} properties in two of the tested patient lines (BrS1 C1: reduced I_{Na} in comparison to both controls (M45-50 C15 and F25-30 C3); BrS3 C2: negative shift in $V_{1/2}$ of inactivation in comparison to both controls (M45-50 C15, F25-30 C3)) (**Figure 5-8b; Figure 5-9c,d**). In BrS8 C2 iPSC-CMs we observed a gain-of-function effect on $V_{1/2}$ of channel inactivation in comparison to both controls M45-50 C15 and F25-30 C3 (positive shift) and a loss-of-function effect on I_{Na} density, while in BrS8 C3 we observed I_{Na} reduction in comparison to only one control (F25-30 C3). Interestingly, the changes in recovery from inactivation observed in iPSC-CMs from basic conditions were not detected in T3 treated BrS iPSC-CMs (**Figure 5-9h**). Those observations can point out improved cytoskeleton structure, which was confirmed by increased expression levels of structural markers in T3 treated cells in comparison to basic conditions and better organization of sarcomeres visible in our ICC results (**Figure 5-4, 5-5**). Those expression changes suggest better maturation of the obtained iPSC-CMs which is necessary for proper channel protein delivery to the cell surface. Based on those observations, we conclude that the phenotype characteristics observed in iPSC-CMs obtained with basic conditions are not reliable due to the possible high immaturity of the obtained cells, and as such the effect of the investigated *SCN5A* founder mutation should be further explored in iPSC-CMs obtained with treatment conditions, which was shown to produce cells with closer to physiological electrophysiological characteristics.

We saw a significant APD reduction in all of the tested BrS iPSC-CMs obtained with basic as well as T3 protocol, in comparison to one control – M45-50 C9 (**Figure 5-6**). We reported dV/dT_{max} reduction in all tested BrS iPSC-CMs obtained with basic protocol in comparison to F25-30 C3, while in the T3 treated cells, this difference was reduced and became insignificant (**Table 5-16**). Similarly, in CT recordings we observed rise time reduction in all BrS patient iPSC-CMs obtained with basic protocol in comparison with F25-30 C3, while in T3 protocol those changes became insignificant (**Figure 5-7; Table 5-17**). It is possible that the differences in channel properties and AP/CT traces observed in iPSC-CMs obtained with basic differentiation protocol were attributed more to the molecular immaturity of the cells than to the real effect of the mutant channel, thus we suspect that the electrophysiological observations from our iPSC-CMs obtained with T3 protocol are more reliable.

Differences between the BrS severity groups

As we tested BrS iPSC-CMs obtained from donors with different phenotype severity (ajmaline-induced BrS type-1 ECG in asymptomatic patients BrS1 and BrS8; SCD in BrS3), we tried to correlate this to EP characteristics of our iPSC-CM models (**Table 5-19**). As reported in our recent review [15], we could expect to observe in iPSC-CMs of the severely affected patient: reduced peak I_{Na} density, negative shift in $V_{1/2}$ of

inactivation, reduced dV/dT_{max} and APA, as well as reduced rise time of CT. Meanwhile, in the less severely affected patient iPSC-CMs we could expect to see reduced peak I_{Na} density with or without less pronounced changes in other sodium current properties, but not necessarily changes in APA or dV/dT_{max} , as the ECG abnormalities in those donors were only unmasked in a sodium channel blocker challenge. We did not see a correlation between phenotype severity and *SCN5A* expression, I_{Na} density or dV/dT_{max} in our results from basic protocol, while in T3 protocol those properties became significantly higher in symptomatic patient iPSC-CMs in comparison to the asymptomatic group (**Table 5-18**), which is not what we could expect based on the previous literature reports. While in basic protocol we observed no difference in $V_{1/2}$ of inactivation between the severity groups, in T3 protocol this value was more negative in the symptomatic patient iPSC-CMs (**Table 5-14, 5-18**), consistent with previous reports from BrS iPSC-CM models. Moreover, we observed expected APA reduction in a more severe patient iPSC-CMs in basic protocol, while in T3 conditions the difference in APA between the severity classes became insignificant, showing that the observed differences in phenotype classes are treatment dependent. In the obtained CT recordings severe patient iPSC-CMs showed increased beating rate, as well as reduced CTD, rise time and RC in comparison to asymptomatic patient iPSC-CMs which is in line with what could be expected (**Table 5-18**).

BrS phenotype modeling in iPSC-CM – future considerations

Based on the discussed results, a question arises: if we notice such variability in sodium current properties from two clones obtained from a single control donor, as well as between two independent control donors (M45-50 and F25-30 C3), is it possible to pick up the subtle differences in phenotype between patients and controls and even more subtle between patients with different disease severity? And what would be the best practice – discard the results from the worse performing control line based on a single phenotype characteristic, or rather compare the results from patients versus each control line separately? In this report we opted for inclusion of the tested control lines in most of the comparisons, where the average values of the tested parameters from all tested controls were used, except for the sodium current characteristics. For these the two clones from one control line showed significant differences (with M45-50 C9 underperforming in comparison to C15; **Figures 5-9, 5-9, Tables 5-8, 5-9**). Based on molecular characteristics and AP properties, there were no reasons to discard M45-50 C9 from further analysis (**Figure 5-5, 5-6, 5-7**).

Concerning characterization of the Belgian *SCN5A* founder mutation, in reported transient expression experiments electrophysiological characterization was performed only for cells expressing homozygous mutant $Na_v1.5$ [42], thus it is possible that in the context of heterozygous expression of WT and mutant channels the effect of the variant could be different than the sole I_{Na} reduction. As observed in the reported results, in T3 treated Belgian BrS *SCN5A* founder mutation iPSC-CMs, where co-expression of WT and mutant $Na_v1.5$ exists, a reduced peak I_{Na} density and/or changes in channel inactivation were observed (**Table 5-14; Figure 5-8, 5-9**). Similar observation was made by Selga et. al., where the heterologous expression of a p.(Arg367His) *SCN5A* variant in tSA cells revealed only the I_{Na} reduction, while the iPSC-CM model of the variant additionally revealed negative shift in voltage dependence of inactivation of the channel [36]. Nonetheless, the defective mutant mRNA may be undergoing nonsense mediated decay, so that the mutant channel protein could be not translated and hence not trafficked to the plasma membrane [42]. In this way, the mutant channels would not be influencing the kinetics of channel opening and closing in our iPSC-CMs. Therefore, to determine if the changes in channel kinetics we observed are a true effect of the mutant and not an artifact generated by the immaturity and the drawbacks of the iPSC-CMs model (e.g. variability), it would be interesting to investigate the expression and potential localization of the Belgian BrS *SCN5A* founder mutation mutant proteins in the obtained cardiomyocytes to determine their impact on the signal propagation. Despite the observed characteristic BrS ECG abnormalities in our donors, as well as measured I_{Na} abnormalities in iPSC-CMs, we were not able to recapitulate the expected disease phenotype in our AP recordings, even from iPSC-CMs obtained with T3 protocol, which showed more mature molecular and EP phenotype (**Figure 5-6**). Further electrophysiological tests of the obtained iPSC-CMs with the presence of sodium channel blocker, like e.g.

ajmaline or quinidine, should be performed to investigate if the $\text{Na}_v1.5$ block can unmask the expected characteristic BrS AP changes in the reported iPSC-CM lines. For the characterization of this genetic variant in the current state of the art of generation of the iPSC-CM models, it would be interesting to develop an isogenic control iPSC line for the Belgian *SCN5A* founder mutation. This would enable the most objective comparison of the phenotype of the donor and corrected cell line to study the true effect of the mutation. However, it is still questionable if when one did not observe expected AP changes in donor iPSC-CMs one would be able to reproduce BrS AP changes in the isogenic cell line.

Conclusions

In conclusion, we obtained iPSC-CMs from BrS Belgian *SCN5A* founder mutation carriers who presented with different disease severity. Our molecular and electrophysiological characterization of the derived iPSC-CMs showed importance of the application of the maturation agent T3 hormone in the differentiation process, to obtain iPSC-CMs which resemble the phenotype of mature cardiomyocytes more closely. Nevertheless, we show that the obtained EP results present variability between two clones obtained from the same donor (e.g. M45-50 C9 and C15) as well as between the independent unaffected control donors (M45-50 and F25-30 C3). Based on the obtained results, we were not able to recapitulate a clear loss-of-function phenotype in the tested iPSC-CMs obtained from BrS donors, showing that the characterization of subtle changes in the functional phenotype might be difficult in current iPSC modeling approaches. This should be taken into account when interpreting the results and trigger further improvement and standardization of the iPSC-CMs differentiation procedures.

5.7 References

- [1] Nijak, A.; Simons, E.; Vandendriessche, B.; Van de Sande, D.; Fransen, E.; Seliwonczyk, E.; Van Gucht, I.; Van Craenenbroeck, E.; Saenen, J.; Heidbuchel, H.; et al., Morpho-functional comparison of differentiation protocols to create iPSC-derived cardiomyocytes. *Biol Open* (2021).
- [2] Parikh, S.; Blackwell, D.J.; Gomez-Hurtado, N.; Frisk, M.; Wang, L.; Kim, K.; Dahl, C.P.; Fiane, A.; Tonnessen, T.; Kryshstal, D.O.; et al., Thyroid and Glucocorticoid Hormones Promote Functional T-Tubule Development in Human-Induced Pluripotent Stem Cell-Derived Cardiomyocytes. *Circ Res* 121 (2017) 1323-1330.
- [3] Yang, X.; Rodriguez, M.; Pabon, L.; Fischer, K.A.; Reinecke, H.; Regnier, M.; Sniadecki, N.J.; Ruohola-Baker, H.; Murry, C.E., Tri-iodo-L-thyronine promotes the maturation of human cardiomyocytes-derived from induced pluripotent stem cells. *J Mol Cell Cardiol* 72 (2014) 296-304.
- [4] Li, S.E.; Iismaa, M.; Naqvi, N.; Nicks, A.; Husain, A.; Graham, R.M.; Thyroid hormone action in postnatal heart development. *Stem Cell Res* 13 (2014) 582-91.
- [5] Karakikes, I.; Ameen, M.; Termglinchan, V.; Wu, J.C., Human induced pluripotent stem cell-derived cardiomyocytes: insights into molecular, cellular, and functional phenotypes. *Circ Res* 117 (2015) 80-8.
- [6] Lewandowski, J.; Rozwadowska, N.; Kolanowski, T.J.; Malcher, A.; Zimna, A.; Rugowska, A.; Fiedorowicz, K.; Labeledz, W.; Kubaszewski, L.; Chojnacka, K.; et al., The impact of *in vitro* cell culture duration on the maturation of human cardiomyocytes derived from induced pluripotent stem cells of myogenic origin. *Cell Transplant* 27 (2018) 1047-1067.
- [7] Doss, M.X.; Di Diego, J.M.; Goodrow, R.J.; Wu, Y.; Cordeiro, J.M.; Nesterenko, V.V.; Barajas-Martinez, H.; Hu, D.; Urrutia, J.; Desai, M.; et al., Maximum diastolic potential of human induced pluripotent stem cell-derived cardiomyocytes depends critically on I_{Kr} . *PLoS One* 7 (2012) e40288.
- [8] Kolanowski, T.J.; Antos, C.L.; Guan, K., Making human cardiomyocytes up to date: Derivation, maturation state and perspectives. *Int J Cardiol* 241 (2017) 379-386.
- [9] Lee, Y.K.; Ng, K.M.; Chan, Y.C.; Lai, W.H.; Au, K.W.; Ho, C.Y.; Wong, L.Y.; Lau, C.P.; Tse, H.F.; Siu, C.W., Triiodothyronine promotes cardiac differentiation and maturation of embryonic stem cells via the classical genomic pathway. *Mol Endocrinol* 24 (2010) 1728-36.
- [10] Goversen, B.; van der Heyden, M.A.G.; van Veen, T.A.B.; de Boer, T.P., The immature electrophysiological phenotype of iPSC-CMs still hampers *in vitro* drug screening: Special focus on I_{K1} . *Pharmacol Ther* 183 (2018) 127-136.
- [11] Honda, M.; Kiyokawa, J.; Tabo, M.; Inoue, T., Electrophysiological characterization of cardiomyocytes derived from human induced pluripotent stem cells. *J Pharmacol Sci* 117 (2011) 149-59.
- [12] van den Heuvel, N.H.; van Veen, T.A.; Lim, B.; Jonsson, M.K., Lessons from the heart: mirroring electrophysiological characteristics during cardiac development to *in vitro* differentiation of stem cell derived cardiomyocytes. *J Mol Cell Cardiol* 67 (2014) 12-25.
- [13] van den Berg, C.W.; Okawa, S.; Chuva de Sousa Lopes, S.M.; van Iperen, L.; Passier, R.; Braam, S.R.; Tertoolen, L.G.; del Sol, A.; Davis, R.P.; Mummery, C.L., Transcriptome of human foetal heart compared with cardiomyocytes from pluripotent stem cells. *Development* 142 (2015) 3231-8.
- [14] Nijak, A.; Labro, A.J.; De Wilde, H.; Dewals, W.; Peigneur, S.; Tytgat, J.; Snyders, D.; Seliwończyk, E.; Simons, E.; Van Craenenbroeck, E.; et al. Compound Heterozygous *SCN5A* Mutations in Severe Sodium Channelopathy With Brugada Syndrome: A Case Report. *Front Cardiovasc Med.* (2020) 7:117.
- [15] Nijak, A.; Saenen, J.; Labro, A.J.; Schepers, D.; Loeys, B.L.; Alaerts, M., iPSC-Cardiomyocyte Models of Brugada Syndrome - Achievements, Challenges and Future Perspectives. *International Journal of Molecular Sciences* 22 (2021) 2825.
- [16] Guo, Y.; Pu, W.T., Cardiomyocyte Maturation: New Phase in Development. *Circ Res* 126 (2020) 1086-1106.

- [17] Huang, C.Y.; Peres Moreno Maia-Joca, R.; Ong, C.S.; Wilson, I.; DiSilvestre, D.; Tomaselli, G.F.; Reich, D.H., Enhancement of human iPSC-derived cardiomyocyte maturation by chemical conditioning in a 3D environment. *J Mol Cell Cardiol* 138 (2020) 1-11.
- [18] Lewandowski, J.; Rozwadowska, N.; Kolanowski, T.J.; Malcher, A.; Zimna, A.; Rugowska, A.; Fiedorowicz, K.; Labeledz, W.; Kubaszewski, L.; Chojnacka, K.; et al., The impact of *in vitro* cell culture duration on the maturation of human cardiomyocytes derived from induced pluripotent stem cells of myogenic origin. *Cell Transplant* 27 (2018) 1047-1067.
- [19] Kane, C.; Terracciano, C.M.N., Concise Review: Criteria for Chamber-Specific Categorization of Human Cardiac Myocytes Derived from Pluripotent Stem Cells. *Stem Cells* 35 (2017) 1881-1897.
- [20] Cyganek, L.; Tiburcy, M.; Sekeres, K.; Gerstenberg, K.; Bohnenberger, H.; Lenz, C.; Henze, S.; Stauske, M.; Salinas, G.; Zimmermann, W.H.; et al., Deep phenotyping of human induced pluripotent stem cell-derived atrial and ventricular cardiomyocytes. *JCI Insight* 3 (2018).
- [21] Pioner, J.M.; Santini, L.; Palandri, C.; Martella, D.; Lupi, F.; Langione, M.; Querceto, S.; Grandinetti, B.; Balducci, V.; Benzoni, P.; et al., Optical Investigation of Action Potential and Calcium Handling Maturation of hiPSC-Cardiomyocytes on Biomimetic Substrates. *Int J Mol Sci* 20 (2019).
- [22] Ma, D.; Liu, Z.; Loh, L.J.; Zhao, Y.; Li, G.; Liew, R.; Islam, O.; Wu, J.; Chung, Y.Y.; Teo, W.S.; et al., Identification of an I_{Na} -dependent and I_{to} -mediated proarrhythmic mechanism in cardiomyocytes derived from pluripotent stem cells of a Brugada syndrome patient. *Sci Rep* 8 (2018) 11246.
- [23] Bett, G.C.; Kaplan, A.D.; Lis, A.; Cimato, T.R.; Tzanakakis, E.S.; Zhou, Q.; Morales, M.J.; Rasmusson, R.L., Electronic "expression" of the inward rectifier in cardiomyocytes derived from human-induced pluripotent stem cells. *Heart Rhythm* 10 (2013) 1903-10.
- [24] Gibson, J.K.; Yue, Y.; Bronson, J.; Palmer, C.; Numann, R., Human stem cell-derived cardiomyocytes detect drug-mediated changes in action potentials and ion currents. *J Pharmacol Toxicol Methods* 70 (2014) 255-67.
- [25] Lopez-Redondo, F.; Kurokawa, J.; Nomura, F.; Kaneko, T.; Hamada, T.; Furukawa, T.; Yasuda, K., A distribution analysis of action potential parameters obtained from patch-clamped human stem cell-derived cardiomyocytes. *J Pharmacol Sci* 131 (2016) 141-5.
- [26] Herron, T.J.; Rocha, A.M.; Campbell, K.F.; Ponce-Balbuena, D.; Willis, B.C.; Guerrero-Serna, G.; Liu, Q.; Klos, M.; Musa, H.; Zarzoso, M.; et al., Extracellular Matrix-Mediated Maturation of Human Pluripotent Stem Cell-Derived Cardiac Monolayer Structure and Electrophysiological Function. *Circ Arrhythm Electrophysiol* 9 (2016) e003638.
- [27] Kussauer, S.; David, R.; Lemcke, H., hiPSCs Derived Cardiac Cells for Drug and Toxicity Screening and Disease Modeling: What Micro- Electrode-Array Analyses Can Tell Us. *Cells* 8 (2019).
- [28] Van de Sande, D.; Kopljar, I.; Alaerts, M.; Teisman, A.; Gallacher, D.J.; Loeys, B.; Snyders, D.J.; Leybaert, L.; Lu, H.R.; Labro, A.J., The resting membrane potential of hSC-CM in a syncytium is more hyperpolarised than that of isolated cells. *Channels (Austin)* 15 (2021) 239-252.
- [29] Goodrow, Jr., R.J.; Desai, S.; Treat, J.A.; Panama, B.K.; Desai, M.; Nesterenko, V.V.; Cordeiro, J.M., Biophysical comparison of sodium currents in native cardiac myocytes and human induced pluripotent stem cell-derived cardiomyocytes. *J Pharmacol Toxicol Methods* 90 (2018) 19-30.
- [30] Paci, M.; Passini, E.; Klimas, A.; Severi, S.; Hyttinen, J.; Rodriguez, B.; Entcheva, E., All-Optical Electrophysiology Refines Populations of In Silico Human iPSC-CMs for Drug Evaluation. *Biophys J* 118 (2020) 2596-2611.
- [31] Shah, D.; Prajapati, C.; Penttinen, K.; Cherian, R.M.; Koivumaki, J.T.; Alexanova, A.; Hyttinen, J.; Aalto-Setälä, K., hiPSC-Derived Cardiomyocyte Model of LQT2 Syndrome Derived from Asymptomatic and Symptomatic Mutation Carriers Reproduces Clinical Differences in Aggregates but Not in Single Cells. *Cells* 9 (2020).
- [32] Shah, L.; Virtanen, D.; Prajapati, C.; Kiamehr, M.; Gullmets, J.; West, G.; Kreutzer, J.; Pekkanen-Mattila, M.; Helio, T.; Kallio, P.; Taimen, P.; et al., Modeling of LMNA-Related Dilated Cardiomyopathy Using Human Induced Pluripotent Stem Cells. *Cells* 8 (2019).

- [33] Higgins, E.M.; Bos, J.M.; Dotzler, S.M.; John Kim, C.S.; Ackerman, M.J., MRAS Variants Cause Cardiomyocyte Hypertrophy in Patient-Specific Induced Pluripotent Stem Cell-Derived Cardiomyocytes: Additional Evidence for MRAS as a Definitive Noonan Syndrome-Susceptibility Gene. *Circ Genom Precis Med* 12 (2019) e002648.
- [34] Ahola, A.; Polonen, R.P.; Aalto-Setälä, K.; Hyttinen, J., Simultaneous Measurement of Contraction and Calcium Transients in Stem Cell Derived Cardiomyocytes. *Ann Biomed Eng* 46 (2018) 148-158.
- [35] de la Roche, J.; Angutararux, P.; Kempf, H.; Janan, M.; Bolesani, E.; Thiemann, S.; Wojciechowski, D.; Coffee, M.; Franke, A.; Schwanke, K.; et al., Comparing human iPSC-cardiomyocytes versus HEK293T cells unveils disease-causing effects of Brugada mutation A735V of NaV1.5 sodium channels. *Sci Rep* 9 (2019) 11173.
- [36] Selga, E.; Sendfeld, F.; Martínez-Moreno, R.; Medine, C.N.; Tura-Ceide, O.; Wilmut, S.I.; Perez, G.J.; Scornik, F.S.; Brugada, R.; Mills, N.L., Sodium channel current loss of function in induced pluripotent stem cell-derived cardiomyocytes from a Brugada syndrome patient. *J Mol Cell Cardiol* 114 (2018) 10-19.
- [37] Davis, R.P.; Casini, S.; van den Berg, C.W.; Hoekstra, M.; Remme, C.A.; Dambrot, C.; Salvatori, D.; Oostwaard, D.W.; Wilde, A.A.; Bezzina, C.R.; et al., Cardiomyocytes derived from pluripotent stem cells recapitulate electrophysiological characteristics of an overlap syndrome of cardiac sodium channel disease. *Circulation* 125 (2012) 3079-91.
- [38] Veerman, C.C.; Mengarelli, I.; Guan, K.; Stauske, M.; Barc, J.; Tan, H.L.; Wilde, A.A.; Verkerk, A.O.; Bezzina, C.R., hiPSC-derived cardiomyocytes from Brugada Syndrome patients without identified mutations do not exhibit clear cellular electrophysiological abnormalities. *Sci Rep* 6 (2016) 30967.
- [39] Sakakibara, Y.; Furukawa, T.; Singer, D.H.; Jia, H.; Backer, C.L.; Arentzen, C.E.; Wasserstrom, J.A., Sodium current in isolated human ventricular myocytes. *Am J Physiol* 265 (1993) H1301-9.
- [40] Hoekstra, M.; Mummery, C.L.; Wilde, A.A.; Bezzina, C.R.; Verkerk, A.O., Induced pluripotent stem cell derived cardiomyocytes as models for cardiac arrhythmias. *Front Physiol* 3 (2012) 346.
- [41] Liang, P.; Sallam, K.; Wu, H.; Li, Y.; Itzhaki, I.; Garg, P.; Zhang, Y.; Vermglinchan, V.; Lan, F.; Gu, M. et al., Patient-Specific and Genome-Edited Induced Pluripotent Stem Cell-Derived Cardiomyocytes Elucidate Single-Cell Phenotype of Brugada Syndrome. *J Am Coll Cardiol* 68 (2016) 2086-2096.
- [42] Hong, K.; Guerchicoff, A.; Pollevick, G.D.; Oliva, A.; Dumaine, R.; de Zutter, M.; Burashnikov, E.; Wu, Y.S.; Brugada, J.; Brugada, P.; Brugada, R., Cryptic 5' splice site activation in *SCN5A* associated with Brugada syndrome. *J Mol Cell Cardiol* 38 (2005) 555-60.



Chapter 6. A Wild-goose Chase – in Search of Novel Brugada Syndrome Candidate Variants

Aleksandra Nijak¹, Eline Simons¹, Bert Vandendriessche¹, Dieter Van de Sande², Ewa Sieliwończyk², Peter Ponsaerts³, Dirk Snyders², Alain J Labro^{2,4}, Emeline Van Craenenbroeck⁵, Johan Saenen⁵, Dorien Schepers^{1,2}, Lut Van Laer¹, Bart Loeys^{1,6}, Maaïke Alaerts¹

¹Center of Medical Genetics, Faculty of Medicine and Health Sciences, University of Antwerp & Antwerp University Hospital, Antwerp, Belgium

²Laboratory of Molecular Biophysics, Cellular and Network Excitability, Department of Biomedical Sciences, University of Antwerp, Antwerp, Belgium

³Laboratory of Experimental Hematology, Vaccine & Infectious Disease Institute, Department of Biomedical Sciences, University of Antwerp, Antwerp, Belgium

⁴Department of Basic and Applied Medical Sciences, Faculty of Medicine and Health Sciences, Ghent University, Ghent, Belgium

⁵Department of Cardiology, Faculty of Medicine and Health Sciences, University of Antwerp and Antwerp University Hospital, Antwerp, Belgium

⁶Department of Human Genetics, Radboud University Medical Centre, Nijmegen, The Netherlands

6.1 Abstract

Rapid development in next generation sequencing methods over the past decade led to its' smooth implementation into clinical practice. In the Western World, where cardiac arrhythmias (including Brugada syndrome (BrS)) are an important health problem affecting mostly young adults, genetic testing with the use of whole exome sequencing or targeted gene panels became a standard procedure. Nevertheless, it is striking that although multiple genes have been linked with Brugada syndrome development, over 70% of cases remain genetically unresolved. Over the past ten years in the Cardiogenetic clinic at the Antwerp University Hospital we collected extensive phenotypic information on BrS families in which genetic screening with an in-house developed primary electrical disorders (PED) gene panel did not yield any result. Three of those families became the basis for this project, in which we used a combined linkage analysis and whole genome sequencing (WGS) approach to look for potential candidate variants involved in BrS pathophysiology.

We performed WGS on 10 selected BrS patients from the three families. For the linkage analysis, we recruited additional relatives and obtained several linked loci for each of the tested families. Combining the linkage and sequencing data, we identified one candidate variant of unknown significance affecting exon-intron boundary in *DCLRE1A* gene and four candidate deep intronic VUS (in genes *CTNNA3*, *GLI2*, *FOXP1* and *ROBO1*), which were predicted to alter normal splicing of the affected proteins. In order to evaluate a causal effect of these selected variants, we performed splicing analysis using RNA samples obtained from patient-derived induced pluripotent stem cell cardiomyocytes (iPSC-CMs). The splicing analysis of the identified 4 deep intronic candidate variants yielded negative results, leading to their removal from the potential candidate list. Due to the time constraints, analysis of the variant in *DCLRE1A* gene will be pursued in the follow-up studies after the completion of this PhD project.

As our combined WGS and linkage analysis approach was not successful in identification of a single strong shared candidate variant for each of the tested families, it can indicate a more complex inheritance of BrS in those families.

6.2 Introduction

Brugada syndrome (BrS) is characterized by incomplete penetrance and significant variability in the phenotypic expression. Some BrS patients present with spontaneously occurring ECG pattern with a characteristic coved-shape ST-segment elevation, while others are asymptomatic, presenting normal baseline ECG pattern, in which case in the presence of a specific trigger, such as fever or administration of a sodium channel blocker, the characteristic ST-elevation can be unmasked [1, 2]. A minority of patients experience ventricular arrhythmia, syncopes or sudden cardiac death (SCD), typically at rest or sleep [3, 4], which usually becomes a trigger for the family members to search for the diagnosis. As the first demonstrations of the disease phenotype occur most prevalently in the third or fourth decade of patients' lives, it is of great importance to look for preventive diagnostic screening methods. So far, only loss-of-function variants in the *SCN5A* gene have been confirmed to be diagnostically relevant in BrS. Nonetheless, those explain only about 20% of all of the cases. To date, over 20 other genes have been associated with BrS, however those can only explain about 5% of the remaining cases [3, 5].

With the development of next generation sequencing, genetic diagnosis and presymptomatic screening of individuals with a history of cardiac arrhythmias within the family became standard practice in the prevention and prognosis of primary electric disorders (PED), including Brugada syndrome. To date, whole exome sequencing (WES) has been proven to be useful in the identification of novel variants in cardiac arrhythmias, such as long-QT syndrome (LQTS) [6, 7], arrhythmogenic cardiomyopathy (ARVC) [8], as well as Brugada syndrome [9-11]. Over 150 genes have been successfully implemented in the clinical practice (NCBI genetic testing registry (GTR): 227 cardiac arrhythmia related gene panels from 38 laboratories, status from March 2021). Most of the existing gene panels or WES analyses, focus on analysis of copy number variation (CNV) or coding single nucleotide variants (SNVs) in the known arrhythmia-related genes. Nevertheless, some causal variants can lie within the non-coding parts of the genome, such as introns or regulatory regions of the disease-related genes. In that case, whole genome sequencing (WGS) comes as an aid.

The Cardiogenetic clinic at Antwerp University Hospital developed and implemented a PED-gene panel [12], which includes 60 arrhythmia-related genes, for diagnostic purposes in familial cases of cardiac arrhythmias. Over the years, we collected several familial Brugada syndrome patients in whom genetic variants within the PED-panel genes were excluded. For this study, we selected three well-characterized and highly informative BrS families. We used a combined approach with linkage analysis and WGS to identify the genetic variants underlying BrS in those families. This approach has been proven successful in identification of causal variants in cardiomyopathy with features of left ventricular noncompaction [13]. As this method can lead to the identification of multiple candidate variants of uncertain significance (VUS), we aimed to model in patient-derived iPSC-CMs the most interesting variants for which we were able to obtain the most convincing preliminary evidence for involvement in the arrhythmic or other cardiac disorders (e.g. cardiac-specific expression; involvement in pathways regulating cardiac development and electrical function; affecting genes or regions previously linked with cardiac disorders; deleterious/frameshift effect of the variant; impairment of normal splicing of the affected gene). For this purpose, we collected blood and fibroblast samples from selected probands for iPSC reprogramming, and differentiation to iPSC-CMs. iPSC-CMs have been proven to be useful in the research of Brugada syndrome [14] and provide a source of functional cardiomyocytes, which contain patients' genome, enabling investigation of the effect of the genetic variants in the tissue-specific environment (cardiac tissue specific transcription and translation). We performed splicing analysis of the most interesting variants using RNA samples from iPSC-CMs obtained from three selected individuals whose DNA samples were used in WGS, in comparison to one healthy unrelated control donor as well as (in case of one family) one unaffected family member. We investigated the effect of the selected VUS on splicing of the encoded proteins in iPSC-CMs cultured in normal conditions as well as in the presence of a nonsense mediated decay blocking agent – Puromycin. However, despite the obtained *in silico* prediction suggesting the effect of the variants to impair normal splicing of the affected proteins, we did not observe alternative splicing effects in patient iPSC-CMs in comparison to the controls.

6.3 Materials and methods

6.3.1 Genetic screening

6.3.1.1 Genotyping

DNA samples were extracted from whole blood samples using standard procedures. Diagnostic testing using in-house developed PED gene panel [12] was performed using standard procedures. SNP array Infinium HumanCore-24 Bead Chip (Illumina) was used to perform genotyping for linkage analysis. Genotyping was performed according to the supplier's protocol, using 30 ng of genomic DNA.

6.3.1.2 Whole genome sequencing

WGS was outsourced to BGI, China where 50 ng of genomic DNA was used for sequencing procedure. The raw sequencing reads underwent standard bioinformatic analysis including quality control and variant calling by BGI company. The obtained lists of variants were further analysed with in-house developed pipeline (**Figure 6-1**).

Variant filtering was performed using VariantDB [15]. Genomic data from each family was analysed separately. Four filtering approaches were used:

- (i) strategy A: variants shared by affected individuals from one family located within the coding regions of the whole genome (including arrhythmia-related genes),
- (ii) strategy B1: variants shared by affected individuals from one family located within non-coding regions of the 60 arrhythmia-related genes from our in-house developed diagnostic panel [12]
- (iii) strategy B2: non-coding variants located within the linkage peaks with the highest LOD scores, and
- (iv) strategy C: shared large copy number variations, throughout the whole genome, including the analysis of CNVs within the linked regions (**Figure 6-1**).

Filtering of the heterozygous shared variants from strategies A and B was performed with the following criteria:

- Minor allele frequency (MAF) ≤ 0.0001 in GnomAD (non TOPMED) database for the coding regions, and MAF ≤ 0.0001 in KAVIAR and GnomAD (non TOPMED) for the non-coding regions
- The allelic balance between 0.3-0.8
- For the variants within the coding regions we looked at CADD_phred score ≥ 10 (CADD_phred score ≥ 10 indicates that the analysed variant is predicted to be in the 10% most deleterious substitutions in human genome; ≥ 20 indicates the 1% most deleterious etc.) and for the variants within non-coding regions at CADD_phred scores =0 or ≥ 10 (for non-coding regions of the genome a CADD_phred score =0 does not necessarily suggest the non-deleterious nature of the variant, as a calculation power of the score for those regions is modest, and most of the time not possible. Thus the CADD_phred score of 0 may suggest that the scoring with this tool was not possible at the time of the analysis).

The additional quality check for each selected variant was performed using IGV programme to look at the variant coverage. Variants with coverage above 10x were considered for further prioritization. Prioritization of the coding variants was carried out using combined information from the following databases: Toppgene, The Human Protein Atlas, Gtex, Enhancer Atlas, ENCODE project, Regulation Spotter, Alamut, Decipher, Pubmed Fetcher and ROH Gene/Phenotype Listing.

Example prioritization criteria: focus on top 10 genes from Toppgene prioritization, which encoded proteins expressed in the heart (The human Protein Atlas, Gtex), for which the Mutation Taster or Regulation Spotter prediction was disease causing, and further splicing prediction in Alamut suggested affected splicing in minimum 3 out of 5 integrated scoring tools. For the CNV analysis or intergenic variants

from strategies B2 and C, additional information about potential enhancer effect of the affected loci in the left ventricle (Enhancer Atlas and/or ENCODE project) and previous link with arrhythmias or cardiac diseases (Decipher, Pubmed Fetcher, ROH Gene/Phenotype Listing) was considered. Recurrent deletions/duplications present in all of the tested families and controls were rejected from the candidate list, due to possible localization within a polymorphic region or a false positive readout in the affected locus.

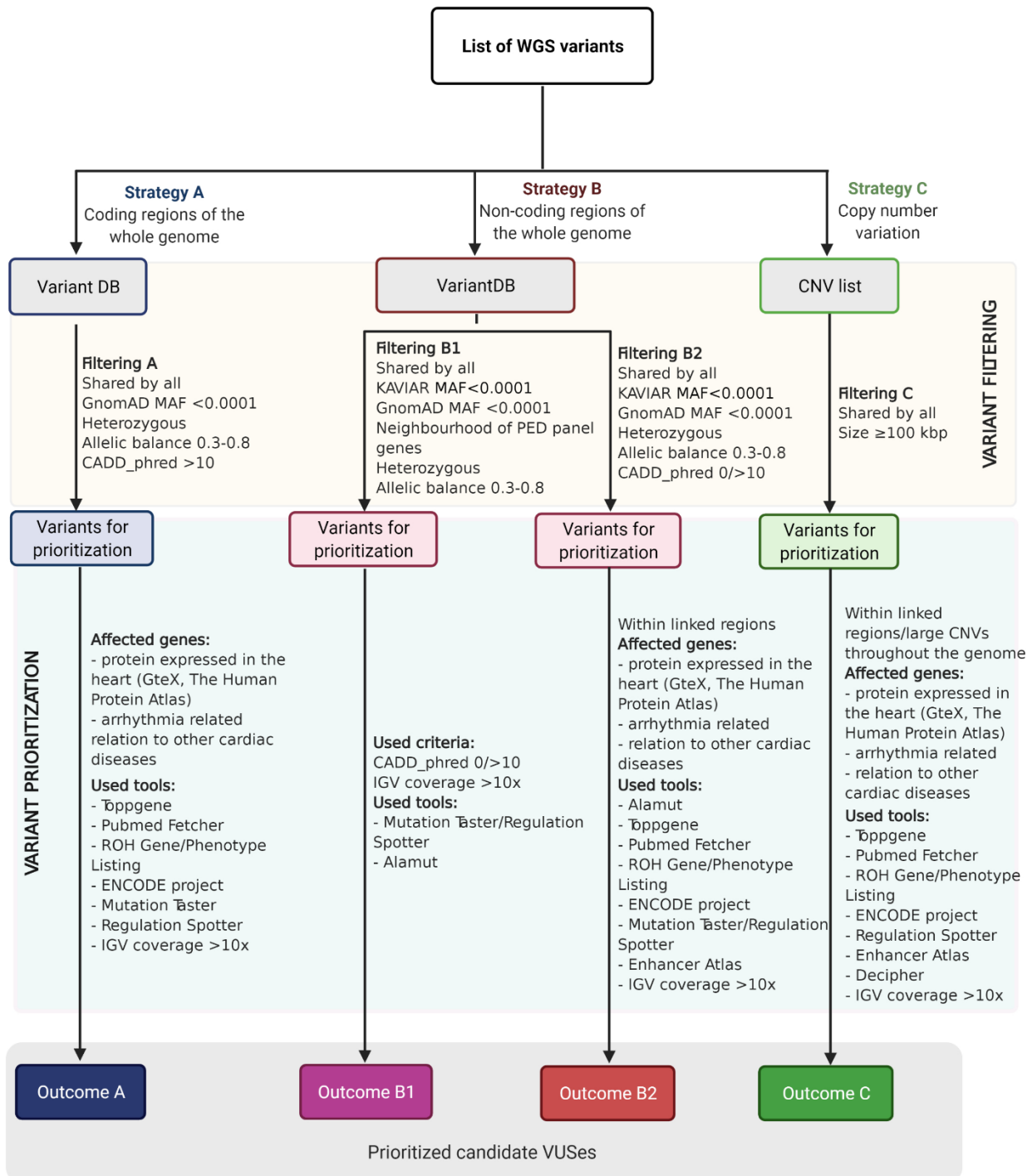


Figure 6-1 Whole genome sequencing analysis approach. The list of obtained variants was filtered using VariantDB [15]. Four analysis approaches were used: (i) analysis of shared coding variants within the whole genome (including arrhythmia-related genes) (A); (ii) analysis of shared variants in the non-coding regions of the 54 arrhythmia-related genes (B1); (iii) analysis of shared variants in non-coding regions of the whole genome, which were located within the linked regions (B2); (iv) analysis of shared CNVs (C). Tools and scores used for qualification and prioritization are indicated next to the arrows in the scheme. MAF – minor allele frequency; CADD score – combined annotation dependent depletion score; KAVIAR – known variants database; Gtex – genotype-tissue expression portal; ROH – regions of homozygosity; ENCODE – encyclopedia of DNA elements; IGV – integrated genomics viewer. Generated with biorender.com March, 2021

6.3.1.3 Linkage analysis

Genotyping using SNP chips was performed using iScan System (Illumina) and data collection was performed using Genome Studio Software (Illumina). LOD scores were calculated based on selection of roughly 13 000 SNPs from the array selected following the rules: SNPs heterozygous for at least one genotyped individual per family and one SNP every ~200 kbp physical distance throughout the whole genome. Selection was performed using an in-house developed R script, accounting for Mendelian inconsistencies. LOD score calculation was performed using Merlin for parametric linkage analysis with an autosomal dominant inheritance model, with reduced (0.95) penetrance and a phenocopy rate of 0.0001, on SNPs with disease allele frequency of 0.001. As in the analysed families obtaining a LOD score above three (LOD>3; statistically significant evidence for linkage) was not always feasible (highest possible LOD scores estimated based on the pedigree analysis and DNA samples availability: BrS family 1 – LOD 1.8 to 2.0; BrS family 2 – LOD 2.5 to 3.0; BrS family 3: LOD 1.5), we looked for the regions with the highest obtained LOD score per family (with LOD > 1.2).

6.3.2 Cell culture and derivation

6.3.2.1 Fibroblast/PBMC derivation and culture

Skin biopsies and fibroblast cultures were carried out as described in **Chapter 4**. Peripheral blood mononucleated cells (PBMCs) were obtained from whole blood samples as follows: 20 mL of whole blood sample was obtained from the patient and PBMC isolation was carried out within four hours after sample collection. Whole blood samples were diluted using 1 mM PBS-EDTA buffer (Life Technologies). Cell separation was performed with addition of 5 mL lymphocyte separation media (LSM) (VWR International) per 4 mL of diluted blood sample and spinning down for 25 minutes at room temperature (RT) without breaks. The top layer of the obtained gradient containing serum plasma was discarded and middle layer containing mononuclear cells (MNCs) was collected for further purification. Purification of MNCs was obtained by dilution in 1mM PBS-EDTA and centrifugation (repeated twice). The obtained pellet of MNCs was diluted in FBS + 10% DMSO (Sigma Aldrich) and frozen down at -80°C overnight before transfer to liquid nitrogen for long-time preservation. PBMCs were thawed for reprogramming and kept in StemSpan SFEM II media (Stem Cell Technologies) supplemented with 1% of StemSpan Erythroid expansion supplement (100x) (Stem Cell Technologies) for nine to 12 days before viral transduction. Media was changed gradually to E8 flex (Life Technologies) on day 7 of reprogramming (by addition of 50% StemSpan SFEM II media with StemSpan Erythroid supplement and 50% of E8 flex media to each reprogrammed well).

6.3.2.2 iPSC derivation, culture and iPSC-CM derivation

iPSC clones were derived and cultured for several passages according to previously published protocol (**Chapter 4**). Differentiation protocol was adapted from the previously published timeline. Briefly, iPSC-CMs on 80-90% of confluency were incubated on day 0 of differentiation with RPMI1640 media containing 6 µM CHIR99021 (Axon Medchem) and 1% of B27 supplement without insulin (Life Technologies) (DM1) for 48h, next (day 2) cells were incubated with RPMI1640 media (Life Technologies) containing 5 µM Wnt-C59 (SelleckChem) and 1% of B27 supplement without insulin (DM2) for 48h. On day 4 of differentiation cells were supplemented with RPMI1640 media with 1% B27 supplement without insulin (DM3) and media was changed every other day. Cells were kept in an incubator at 37°C, 80% humidity, 5% CO₂ and 5% O₂. From the day when the first contractions were visible, cells were supplemented with RPMI1640

media with 1% B27 supplement without insulin with addition of triiodothyronine (T3) (Sigma Aldrich) (20 ng/mL) (DM4) for the next 3 media changes and cells were transferred to an incubator with normoxic conditions (37°C, 80% humidity, 5% CO₂). After initial T3 treatment, a metabolic enrichment using RPMI1640 media without glucose (Life Technologies) supplemented with lactate (Sigma Aldrich), human serum albumin (500 µg/mL) (Sigma Aldrich) and L-ascorbic-acid (5 mM) (Sigma Aldrich) (DM5) was used for 6 days to homogenize the cell culture for further experiments. After the lactate treatment, cells were supplemented with differentiation media 4 (DM4), refreshed every other day until the end of experiments. RNA samples were collected on D35-40 of differentiation.

6.3.2.3 Splicing analysis

PCR validation of the splicing effect of the selected deep intronic VUS, predicted to affect normal splicing was performed on cDNA obtained from iPSC-CMs cultured under normal culture conditions as well as with 24h treatment with Puromycin (0.02%; Sigma Aldrich) before cells collection, to block nonsense mediated decay (NMD). cDNA was obtained from 1 µg of RNA using Super Script III First Strand Synthesis kit (Life Technologies) according to the manufacturer’s protocol using random hexamers method and RNase H treatment at the end of the reverse transcription procedure. Gel electrophoresis was performed to investigate differences in patient samples in comparison to controls.

6.4 Results

6.4.1 BrS family 1

Pedigree analysis revealed 11 (potential) BrS cases, and four obligate carriers without disease phenotype in this four-generation family (**Figure 6-2**). We selected three patients with a positive ajmaline test, ventricular fibrillation (III:3) or spontaneous BrS type-1 ECG pattern (III:10) or early onset disease (13-years old, IV:4) to perform WGS, and a total of 11 individuals for SNP chip for linkage analysis (six affected: II:9; III:3; III:4; III:10; III:11; IV:4; two obligate carriers: II:2; II:4; and three unaffected individuals: II:10; III:12; III:13). Overview of patient information, DNA sample availability and performed analysis are summarized in **Table 6-1**.

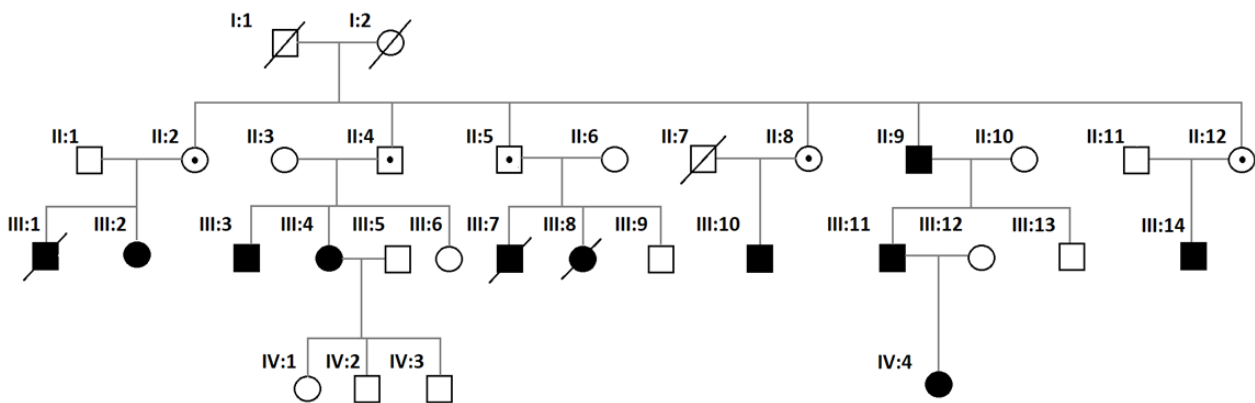


Figure 6-2 Pedigree of BrS family 1. Empty symbols indicate unaffected individuals, full symbols indicate affected individuals, dotted symbols indicate obligate carriers and crossed symbols indicate deceased individuals.

Table 6-1 BrS family 1 members information. SCD – sudden cardiac death; ICD – implantable cardioverter defibrillator; VF – ventricular fibrillation

Patient	Age	Gender	Disease status	Clinical phenotype	DNA sample	Linkage analysis	WGS
I:1	80	M	Unknown	-	No	No	No
I:2	86	F	Unknown	-	No	No	No
II:1	69	M	Unaffected	-	No	No	No
II:2	72	F	Obligate carrier	Prophylactic ICD implantation based on family history at age of 57	Yes	Yes	No
II:3	69	F	Unaffected	-	Yes	No	No
II:4	74	M	Obligate carrier	Asymptomatic	Yes	Yes	No
II:5	76	M	Obligate carrier	Asymptomatic	No	No	No
II:6	62	F	Unaffected	-	No	No	No
II:7	34	M	Unaffected	Deceased	No	No	No
II:8	59	F	Obligate carrier	Asymptomatic	No	No	No
II:9	71	M	Affected	Asymptomatic, ajmaline induced BrS type-1 ECG pattern	Yes	Yes	No
II:10	66	F	Unaffected	-	Yes	Yes	No
II:11	71	M	Unaffected	-	No	No	No
II:12	69	F	Unaffected	-	No	No	No
III:1	26	M	Affected	SCD at the age of 26	No	No	No
III:2	39	F	Affected	Unknown	No	No	No
III:3	43	M	Affected	Prophylactic ICD at the age of 38 based on the family history of SCD and electrophysiological examination, where VF was provoked	Yes	Yes	Yes
III:4	46	F	Affected	ICD implanted based on family history of SCD and abnormal electrophysiological examination	Yes	Yes	No
III:5	Unknown	M	Unaffected	-	No	No	No
III:6	44	F	Unaffected	-	No	No	No
III:7	20	M	Affected	SCD at the age of 20	No	No	No
III:8	19	M	Affected	SCD at the age of 19	No	No	No
III:9	Unknown	M	Unaffected	-	No	No	No
III:10	41	M	Affected	Spontaneous and ajmaline induced BrS type-1 ECG, no syncope and normal electrophysiological examination	Yes	Yes	Yes
III:11	40	M	Affected	Asymptomatic, ajmaline induced BrS type-1 ECG pattern	Yes	Yes	No
III:12	35	F	Unaffected	-	Yes	Yes	No
III:13	44	M	Unaffected	-	Yes	Yes	No
III:14	33	M	Affected	Asymptomatic, ajmaline induced BrS type-1 ECG pattern	No	No	No
IV:1	Unknown	F	Unaffected	Borderline negative ajmaline test	No	No	No
IV:2	16	M	Unaffected	Negative ajmaline test	No	No	No
IV:3	14	M	Unaffected	Negative ajmaline test	No	No	No
IV:4	13	F	Affected	Ajmaline induced BrS type 1 ECG, no syncope and normal electrophysiological examination	Yes	Yes	Yes

Linkage analysis led to identification of several loci with LOD scores between 1.020 to 1.460 (**Figure 6-3**). We identified four loci on chromosomes 1, 4, 10 and 20 (Chr1:87.753-94.753M LOD=1.277; Chr4:32.085-72.085M max LOD=1.407; Chr10:128.114-136.114M max LOD=1.460; Chr20:12.091-47.091M max LOD=1.295) (**Figure 6-3**).

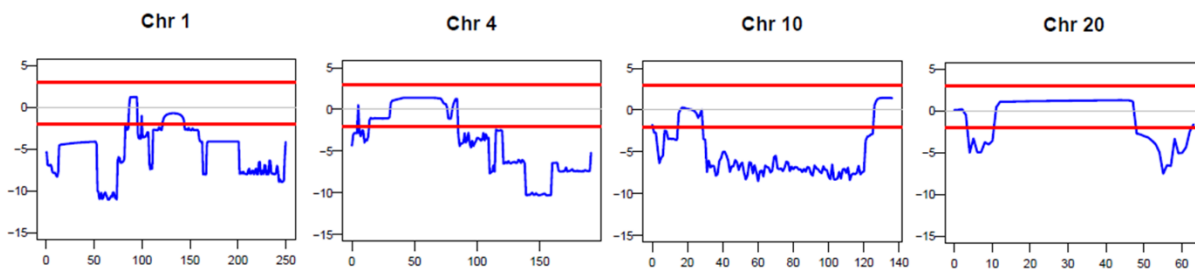


Figure 6-3 Linked regions and obtained LOD scores obtained from linkage analysis in BrS family 1.

We obtained a list of 4 218 647 variants shared by three family-members (III:3, III:10 and IV:4) who underwent WGS in BrS family 1. Out of those, six variants passed strategy A based on the allele frequency information and CADD_Phred score (**Figure 6-1**; **Table 6-2**). Two variants were predicted to be polymorphisms (in *ERFE* and *KRT4* genes). The affected genes encode respectively, proteins involved in erythropoiesis (OMIM 615099) or development of white sponge nevus 1 (OMIM 193900). The remaining four variants were predicted to be disease causing however, the affected genes were previously linked with glioblastoma or neurodegeneration, cancer development, hypercarotenemia and vitamin A deficiency or myoclonus epilepsy (respective genes: *RNF25* [16, 17], *CCNG1* [18], *BCO1* [19] and *MEAK7* [20]). As we could not identify a potential link to the Brugada phenotype, they were excluded from further consideration in this family.

Table 6-2 Results of the filtered and prioritized WGS data for BrS family 1 using strategy A. Ref. allele – reference allele; Alt. allele – alternative allele.

Genomic location	Ref. allele	Alt. allele	CADDv1 .4_phred	Variant effect/location	Mutation taster prediction	Amino acid change	Codon	Transcript ID	Gene
chr2:219529924	T	G	25.5	Nonsynonymous SNV	Disease causing	Y207S	1758	ENST00000295704	<i>RNF25</i>
chr2:239072994	C	T	26	Nonsynonymous SNV	Polymorphism	R294C	1240	ENST00000546354	<i>ERFE</i>
chr5:162868905	A	C	22.4	Nonsynonymous SNV	Disease causing	N178H	2297	ENST00000506186	<i>CCNG1</i>
chr12:53207583	C	CCACCA AAGCC ACCA GCCGA AACCA GCTCCG AAGCC GCCGG	13.28	Nonframeshift insertion	Polymorphism	S90_C91	481_482	ENST00000293774	<i>KRT4</i>
chr16:81298282	C	T	26.1	Nonsynonymous SNV	Disease causing	T101M	2134	ENST00000425577	<i>BCO1</i>
chr16:84516214	G	A	27	Nonsynonymous SNV	Disease causing	T22M	3396	ENST00000545792	<i>MEAK7</i>

Analysis using strategy B1 focused on 60 arrhythmia related genes and strategy B2, focused on linked non-coding regions did not yield any VUS that passed our filtering criteria (**Figure 6-1**). Next, we analysed a list of 1 100 CNVs shared by the WGS trio (III:3, III:10 and IV:4) (strategy C; **Figure 6-1**) and identified 33 shared CNVs larger than 100 kb, from which 8 deletions, all located in intergenic regions of the genome, were

unique for this family (identified only in the trio from BrS family 1). However, none of the identified deletions passed our prioritization criteria (**Table 6-3**).

Table 6-3 Large CNVs identified in BrS family 1. Empty cells in the table indicate no known genes were present in the neighbourhood (up to 1 Mb from the CNV boundaries) of the CNV.

Chromosome	Deletion start	Deletion end	Size of the overlapping deletion	Genes in the neighbourhood of the variant	Transcript ID
1	30093301	30243401	150 100		
1	148361301	148511400	150 100		
1	205922701	206072800	150 100	RHEX; SLC26A9	ENSG00000174502; ENSG00000263961
1	248908201	249058400	150 200		
2	5018801	5118800	100 000		
4	49660101	52660700	3000600	USP46-DT	ENSG00000248866
10	128664901	128814901	150 000		
17	623701	723801	100 100		

As our shared WGS analysis approach did not yield any candidate VUS for further validation, we investigated the WGS datasets from each of the sequenced patient individually. Interestingly, using filtering strategy A we identified a frameshift variant in *SCN5A* gene (c.2325delA; p.Tyr774Serfs; ENST00000449557) in individual III:10, which explains the development of BrS in this patient (**Figure 6-4**). Segregation analysis of the variant on available DNA samples revealed its presence in one of the obligate carriers (individual II:2) and one BrS patient (III:14), while other affected family members (n=5) did not carry this mutation (**Figure 6-4**) (despite repetitive efforts, we were unable to obtain DNA from individual III:2). Thus, we proceeded with further analysis of the WGS data from the other two individuals (III:3; IV:4).

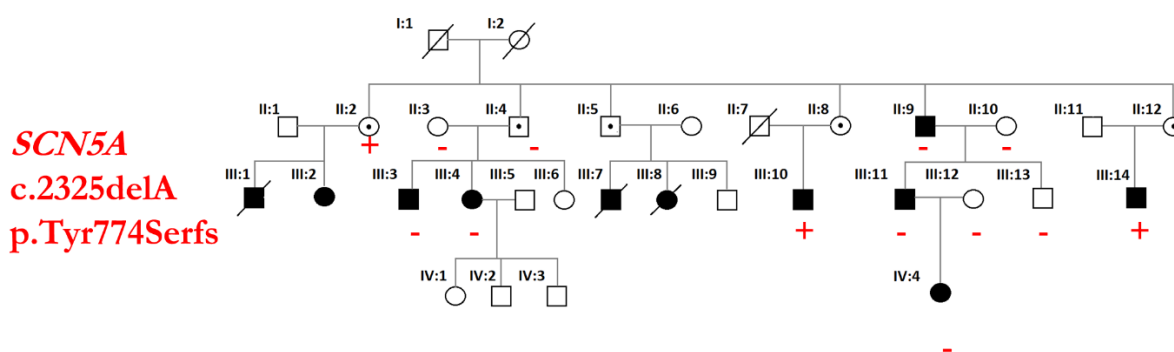


Figure 6-4 Segregation analysis of *SCN5A* c.2325delA (p.Tyr774Serfs) variant in available DNA samples from BrS family 1 members. + variant carriers; - variant absent.

Shared variant filtering using strategy A for the remaining duo (III:3 and IV:4) identified a single VUS in *TAS2R46* gene, which was predicted to be disease causing and showed a CADD_phred score of 33. The affected gene encodes the bitter taste receptor in humans [21], expressed at the surface of taste receptor cells, thus the possibility of the variant to have an effect on BrS phenotype in this family is low and this VUS was discarded from further analysis. Filtering strategy B1 did not yield any result (no variant passed our filtering criteria), while filtering strategy B2 led to identification of five variants on Chr4 and three variants on Chr20 shared by the duo. Further prioritization of those variants led to selection of one potential candidate on Chr4 in the 3'UTR region of *DCUN1D4* gene (predicted to be disease causing), (**Table 6-4**). CNV variants in *DCUN1D4* gene were previously reported in optic nerve meningioma (MalaCards) and expression of the affected protein shows low tissue specificity (protein present in multiple tissues in the human body). As the variant was not predicted to have an effect on splicing of the affected protein (no effect based on the five Alamut scoring tools), the variant was discarded from further consideration.

Table 6-4 Potential candidate variants identified during re-analysis of the results using strategy B2 in the BrS family 1 duo. Ref. allele – reference allele; Alt. allele – alternative allele.

Genomic location	Ref. allele	Alt. allele	CADDv1.4 _phred	Variant effect/location	Mutation taster/Regulation spotter prediction	Codon	Transcript ID	Gene
chr4:52781294	C	G	17.52	3'UTR	Disease causing	1026	ENST00000508257	DCUN1D4

6.4.2 BrS family 2

Pedigree analysis revealed five family members with a BrS phenotype in this four-generation family (**Figure 6-5**). We selected three affected individuals with positive ajmaline test (II:6, II:8 and III:2) (also ICD for II:6 and II:8) for WGS and a total number of 13 individuals (four affected: II:2; II:6; II:8; III:2; and 11 unaffected individuals: II:1; II:3; II:4; II:7; III:1; III:4; III:6; IV:1; IV:2) for SNP chip for linkage analysis. Patient information, DNA sample availability and performed tests are summarized in **Table 6-5**.

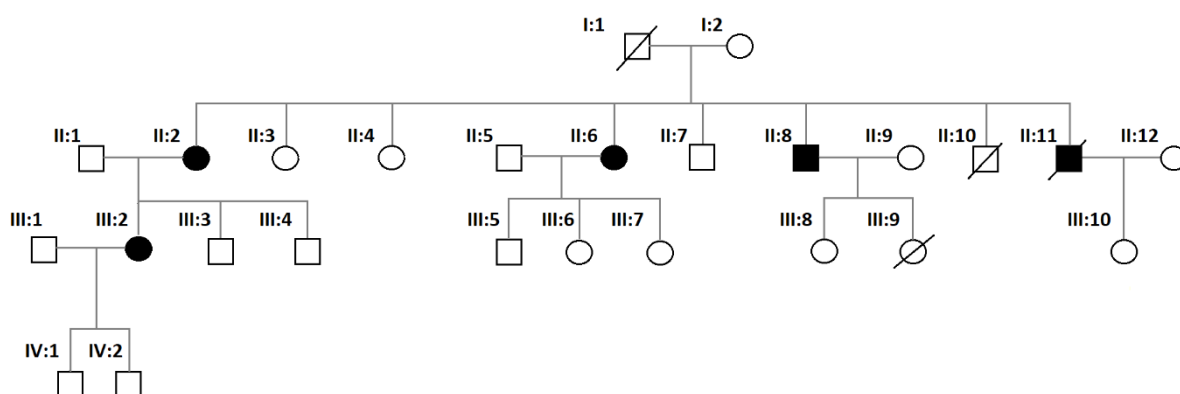


Figure 6-5 Pedigree of BrS family 2.

Table 6-5 BrS family 2 members information. SCD – sudden cardiac death; ICD – implantable cardioverter defibrillator.

Patient	Age	Gender	Disease status	Clinical phenotype	DNA sample	Linkage analysis	WGS
I:1	76	M	Unaffected	-	No	No	No
I:2	Unknown	F	Unaffected	-	No	No	No
II:1	77	M	Unaffected	-	Yes	Yes	No
II:2	72	F	Affected	Ajmaline induced BrS type-1 ECG pattern, abnormal electrophysiological examination, for which ICD was received	Yes	Yes	No
II:3	76	F	Unaffected	-	Yes	Yes	No
II:4	75	F	Unaffected	-	Yes	Yes	No
II:5	Unknown	M	Unaffected	-	No	No	No
II:6	70	F	Affected	History of syncope and ajmaline induced BrS type-1 ECG pattern. Patient received an ICD at the age of 65.	Yes	Yes	Yes
II:7	73	M	Unaffected	-	Yes	Yes	No
II:8	66	M	Affected	History of syncope from childhood, ajmaline induced	Yes	Yes	Yes

				BrS type-1 ECG, received ICD at the age of 62			
II:9	Unknown	F	Unaffected	-	No	No	No
II:10	Unknown	M	Unaffected	-	No	No	No
II:11	48	M	Affected	SCD during sleep	No	No	No
II:12	Unknown	F	Unaffected	-	Yes	Yes - initially not included in linkage analysis. Sample was added to linkage analysis in the second genotyping experiment.	No
III:1	50	M	Unaffected	-	Yes	Yes	No
III:2	50	F	Affected	Normal baseline ECG, exercise and ajmaline induced BrS type-1 ECG.	Yes	Yes	Yes
III:3	Unknown	M	Unaffected	Negative ajmaline test	No	No	No
III:4	43	M	Unaffected	-	Yes	Yes	No
III:5	Unknown	M	Unaffected	Negative ajmaline test	No	No	No
III:6	Unknown	F	Unaffected	Negative ajmaline test	Yes	Yes	No
III:7	Unknown	F	Unaffected	Negative ajmaline test	No	No	No
III:8	Unknown	F	Unaffected	Negative ajmaline test	No	No	No
III:9	Unknown	F	Unaffected	-	No	No	No
III:10	35	F	Initially considered unaffected, but later on became affected	Initially asymptomatic. Later palpitations and ajmaline induced BrS type-1 ECG. ANK2 polymorphism identified using diagnostic PED- gene panel	Yes (in second stage)	Yes (in repeated linkage)	No
IV:1	22	M	Unaffected	-	Yes	Yes	No
IV:2	19	M	Unaffected	-	Yes	Yes	No

Linkage analysis revealed four *loci* on chromosomes 2, 10 and 19 (Chr2:30.041M and 76.041-109.041M LOD=2.561; Chr2:110.041-129.041M LOD=1.260; Chr10:101.114-102.114M LOD=1.260; Chr19:15.261-28.261M LOD=1.260) (Figure 6), with the highest LOD score of 2.561 for two peaks on chromosome 2, which we focused on in our WGS data analysis with strategy B2.

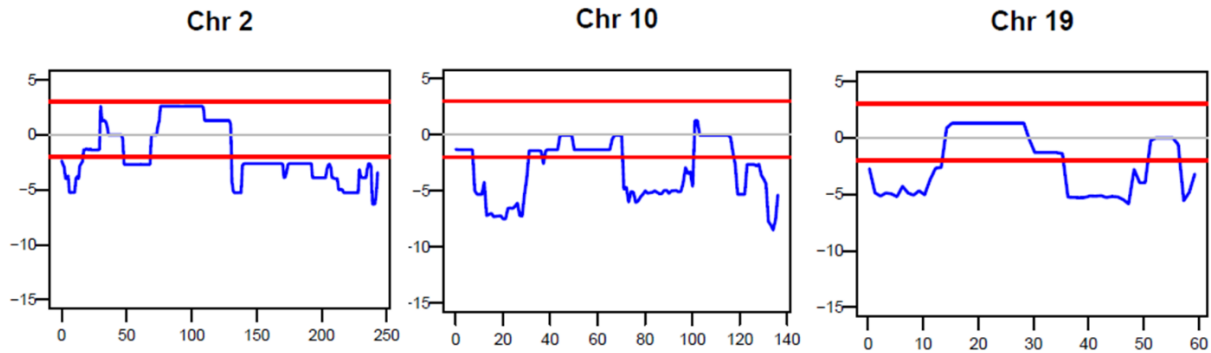


Figure 6-6 Linked regions and LOD scores obtained from linkage analysis in BrS family 2.

We obtained a list of 2 822 392 variants shared by the three affected individuals. Our filtering approach A (**Figure 6-1**) resulted in identification of 8 626 variants, and within those prioritization led to identification of an interesting VUS in *SNAP29*, which was predicted to be disease causing (c.280A>T; p.Met94Leu; start loss; CADD =34; Mutation taster prediction: disease causing). Moreover, the variant was located within the highest linkage peak on chromosome 2 (**Figure 6-6**). The gene was previously linked with 22q11.2 deletion syndrome [22-25], however the low tissue specificity of the encoded protein led to disclosing it from further consideration.

Strategy B1 focused on PED related genes led to identification of three intronic variants in one gene: *CTNNA3*, from which one single nucleotide variant was predicted to be disease causing and to affect splicing, and was selected for further validation (**Table 6-6** and **6-8**)

Table 6-6 PED-gene variants shared by the three individuals from BrS family 2. Ref. allele – reference allele; Alt. allele – alternative allele; * variants appointed for further validation.

Genomic location	Ref. allele	Alt. allele	CADD_phred	Variant location	Regulation spotter prediction	Transcript ID	Gene
*chr10:67793904	T	A	10.2	Intron	Disease causing	ENST00000373735	<i>CTNNA3</i>
chr10:67985148	AATAT	AATATAT	0	Intron	Polymorphism	ENST00000373744	<i>CTNNA3</i>
chr10:68492925	G	GA	0	Intron	Polymorphism	ENST00000373744	<i>CTNNA3</i>

Filtering B2 for shared variants in linked non-coding regions on chromosome 2 led to obtaining a list of nine rare variants. Out of those, after prioritization based on the CADD_Phred score, only five variants remained, where one VUS in *GLI2* predicted to be disease causing was selected for further validation (**Table 6-7**). The aforementioned VUS was selected for further validation based on the disease causing prediction and the involvement of *GLI2* in regulation of cardiogenesis [26].

Table 6-7 Variants identified from filtering strategy B2 for BrS family 2. Ref. allele – reference allele; Alt. allele – alternative allele; * selected candidate variant

Genomic location	Ref. allele	Alt. allele	CADD_phred	Variant location	Regulation spotter prediction	Transcript ID	Gene
chr2:100652811	A	T	15.5	Intron	Polymorphism	ENST00000444786	<i>AFF3</i>
chr2:109129906	AG	A	0	Downstream	Non-functional region	ENST00000480863	<i>GCC-AS1</i>
chr2:118578691	TA	T	0	Intron	Polymorphism	ENST00000474694	<i>DDX18</i>
chr2:121583674	AC	A	0	Intron	Polymorphism	ENST00000361492	<i>GLI2</i>
*chr2:121719971	TC	T	0	Intron	Disease causing	ENST00000361492	<i>GLI2</i>

Both selected candidate variants are located deep in the introns of the genes (*CTNNA3* and *GLI2*), and they were predicted to have an effect on splicing of the proteins (Alamut) encoded by the affected genes (**Table 6-8**). Effect of the VUS in *GLI2* is predicted to delete the existing donor site, while the VUS in *CTNNA3* is predicted to create a new acceptor site. First, we performed segregation analysis for the *CTNNA3* and *GLI2* variants using Sanger sequencing on the available DNA samples from family 2 (**Figure 6-7a**). Both of the variants segregate with the disease phenotype: they are present in all of the affected individuals (II:2; II:6; II:8; III:2). The *GLI2* variant was not present in any of the unaffected individuals, while the VUS in *CTNNA3* is also present in one of the tested unaffected individuals (II:4), which is still possible with the reduced penetrance characteristic of BrS. However, the tested splicing mRNA effect of both variants in patient iPSC-CMs (from individual II:8 (BrS2) and III:2 (BrS1)) did not differ from this observed in control iPSC-CMs (individual II:7 (Famctrl) and unrelated healthy donor (Ctrl)), which excluded those variants from the candidate list (**Figure 6-7b-c**).

Table 6-8 Alamut predictions for the analysed variants.

Genomic location	Gene	Ref. allele	Alt. allele	Acceptor site	Donor site	Prediction programs				
						SSF	MaxEnt	NN SPLICE	Gene Splicer	HSF
Chr10:67793904	<i>CTNNA3</i>	T	A	Intron 15 – c.2159+35176		–→73.37	4.55→5.81 (+27.6%)	–→0.47		=74.49
Chr2:121719971	<i>GLI2</i>	TC	T	Intron 4 – c.6544-5299		=80.62	2.81→1.01 (+64.0%)			=89.58
					Intron 4 – c.664-5321	75.52→–	3.16→0.88 (-72.3%)			86.83→71.75 (-17.4%)

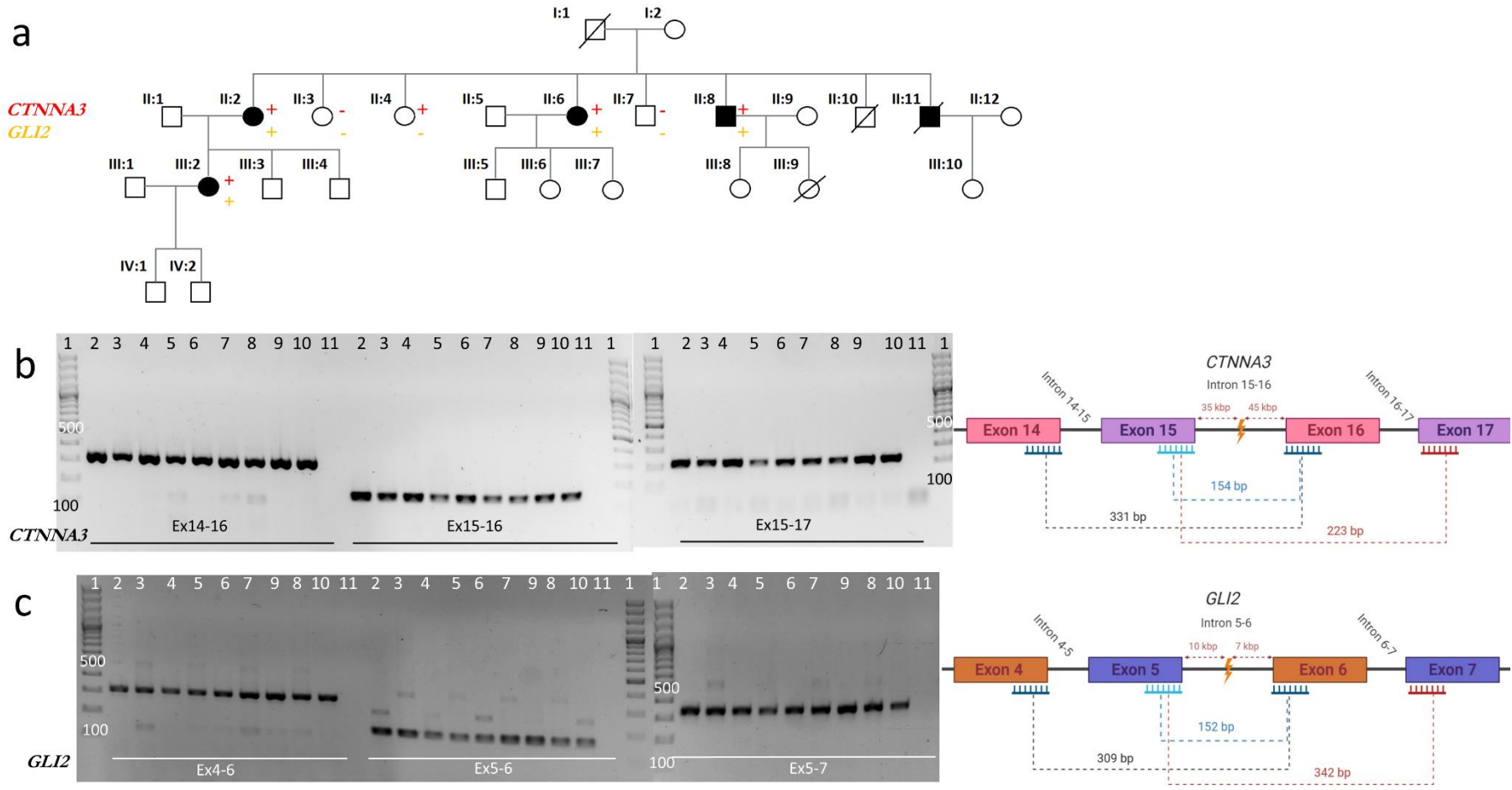


Figure 6-7 Segregation analysis (a) and gel electrophoresis results for *CTNNA3* (b) and *GLI2* (c) VUS. RNA samples obtained from iPSC-CMs derived in two independent differentiation batches, from untreated and Puromycin treated cells were isolated and different cDNA amplicons (surrounding the predicted splice VUS) were amplified. Legend: 1. 100 bp Plus Ladder (Life Technologies); 2. BrS1 batch 1; 3. BrS1 Batch 1 cultured with Puromycin; 4. BrS2 batch 1; 5. BrS2 batch 1 cultured with Puromycin; 6. Famctrl batch 1; 7. Famctrl batch 1 cultured with Puromycin; 8. Famctrl batch 2 cultured with Puromycin; 9. Famctrl batch 2; 10. Ctrl batch 1; 11. negative control. Analysed primer pairs are indicated underneath the obtained bands (with the number of exon with the forward – reverse primer).

Filtering C led to derivation of a list of 954 shared CNVs. Based on the size (cut off 100 kb) we reduced this list to 31 large deletions, from which three were family specific (**Table 6-9**). One of those CNVs was located in the intron of one of the PED-genes *DPP6*, however the check in the IGV database revealed this variant to be a false positive, excluding it from the candidate list. The remaining variants were excluded from further consideration, due to lack of data about the involvement of the affected loci in proper development and function of the heart or potential regulatory features of the affected regions.

Table 6-9 Shared large deletions (>100 kb) in BrS family 2 members. Empty cells in the table indicate no known genes were present in the neighbourhood (up to 1 Mb from the CNV boundaries) of the CNV. *Variant located within the linked region or nearby known PED-gene.

Chromosome	Deletion start	Deletion end	Size of the overlapping deletion	Genes in the neighbourhood of the variant	Transcript ID
1	29878101	30028100	150 000		
7	58054201	61054300	3 000 100		
*7	154270601	154370600	100 000	<i>DPP6</i>	ENSG00000130226; intron5-6 (6599 bp from exon-intron boundary (exon 5) and 5870 bp from intron-exon boundary (exon 6))

Recently, new information about disease status for individual II:10 (initially considered as unaffected) became available. Subsequent diagnostic genetic screening with a PED-panel for this patient led to identification of a polymorphism in *ANK2* gene (c.8659C>T; p.Pro2887Ser). This variant was absent from the WGS data obtained from the tested individuals, and as such no segregation analysis was performed on the available DNA samples from other family members. With this information, we performed additional SNP array on the DNA from patient III:10 (now revealed as an affected individual) and II:12 (unaffected parent) to repeat the linkage analysis in this family (with total number of 17 genotyped individuals: five affected and 12 unaffected) (**Table 6-5**). We noticed an increase in the LOD score obtained for the linkage peak on chromosome 2 (chr2: 76.041 – 109.041 LOD=3.162), while for the other two peaks obtained in the first linkage analysis, the LOD scores decreased below 0 (**Figure 6-8**).

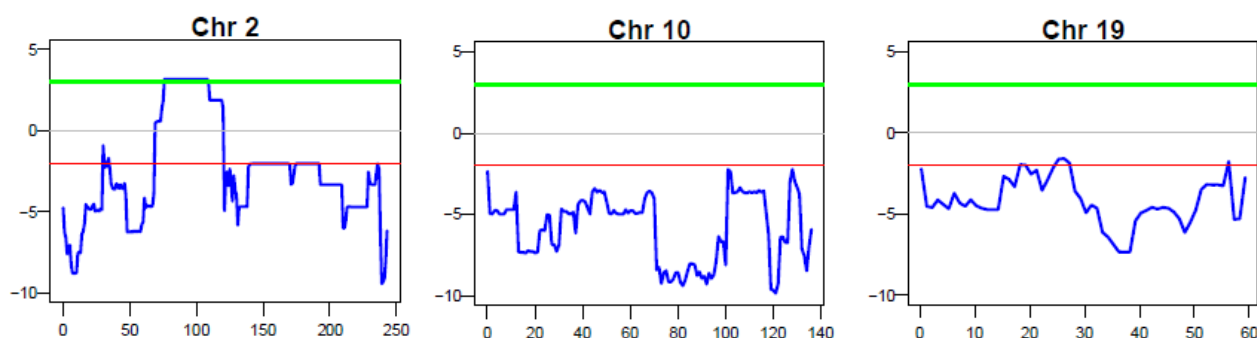


Figure 6-8 LOD scores obtained from linkage analysis in BrS family 2 with two additional individuals.

Due to a lack of candidate VUS after our WGS analysis approach and initial validation, we decided to perform re-filtering and analysis of the variants using strategies A and B1-2, using the adjusted LOD scores obtained in analysis of additional family members. We repeated filtering WGS strategy A (**Figure 6-1**) [27-30], with the assumption that with the updated versions of the GnomAD and CADD_Phred databases our outcome may lead to obtaining potential candidate variants that were missed in the previous filtering. This approach led to filtering of two disease causing variants in *DCLRE1A* (also known as *SNM1A* gene) and *CCER1* genes (**Table 6-10**), in addition to the previously identified VUS in *SNAP29*. Both new variants were predicted to affect the normal splicing of the affected proteins: *DCLRE1A* VUS is predicted to inactivate an existing acceptor site (**Table 6-11**) and VUS in *CCER1* gene is a frameshift insertion, which

results in a stop gain. Nevertheless, as *CCER1* protein is expressed exclusively in testis, the VUS in this gene was excluded from further consideration, as it would not explain the occurrence of BrS in individuals II:6 and III:2 (females) in the described family. As for the variant in *DCLRE1A* gene, the gene product is expressed in multiple tissues including heart and mutations in this gene have been previously reported in Fanconi anemia [31], where in some of the affected patents, congenital heart defects are identified [32]. The variant segregated with disease phenotype in the presented family (results of segregation analysis are shown in **Figure 6-9**), which supported the evidence for this variant to be a potential candidate in this family. Variant effect on splicing is currently under investigation.

Table 6-10 Shared variants obtained in repeated filtering strategy A in BrS family 2. Ref. allele – reference allele; Alt. allele – alternative allele; * candidate variant.

Genomic location	Ref. allele	Alt. allele	CADDv1.4 _phred	Variant effect/location	Mutation taster prediction	Transcript ID	Gene
chr10:115596964	T	G	26.5	Splicing, exon-intron boundary	Disease causing	ENST00000361384	<i>DCLRE1A</i>
chr12:91348022	C	CA	17.99	Exonic, frameshift insertion (stop gain)	Disease causing	ENST00000358859	<i>CCER1</i>

Table 6-11 Alamut predictions for the variants obtained in repeated filtering strategy A for BrS family 2. Ref. allele – reference allele; Alt. allele – alternative allele.

Genomic location	Gene	Ref. allele	Alt. allele	Acceptor site	Donor site	Prediction programs				
						SSF	MaxEnt	NN SPLICE	Gene Splicer	HSF
chr10:115596964	<i>DCLRE1A</i>	T	G	Exon 8 – c.2821		92.04→ ₋	7.81→ ₋	0.74→ ₋	5.24→ ₋	-

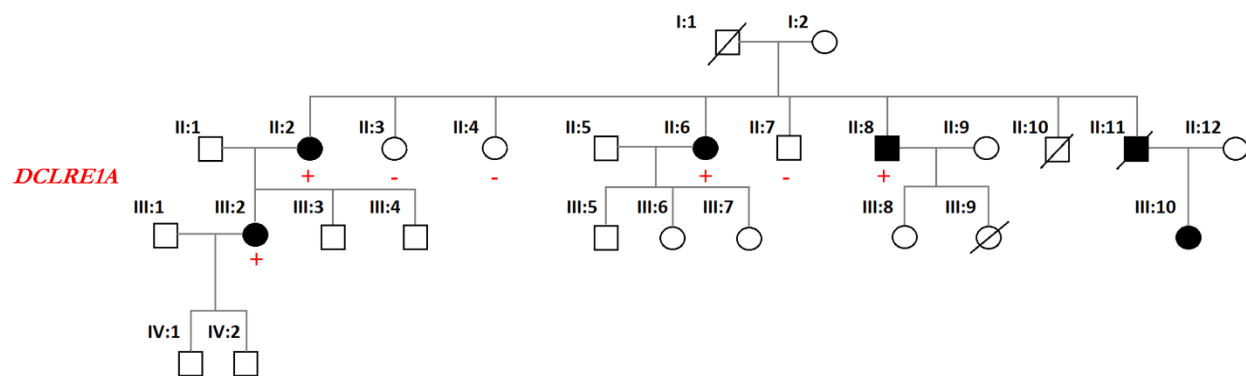


Figure 6-9 Segregation analysis of *DCLRE1A* VUS in BrS family 2.

We continued with the filtering strategy B1 and B2 focused on non-coding regions of PED genes and linked loci (**Figure 6-1**). While strategy B1 did not yield any result, we obtained two VUS in strategy B2 (**Table 6-12**). One of the variants was located in non-functional intergenic regions of the whole genome and their effect was predicted to not affect splicing of the genes located down- or upstream the affected loci. The variant in 3'UTR of *REEP1* gene was a rare polymorphism, the encoded protein is expressed preferentially in nervous system tissues and mutations in this gene were previously reported in neuropathy and spastic paraplegia (OMIM:609139). Thus, all of the filtered VUS were excluded as potential candidates.

Table 6-12 Shared variants obtained in repeated filtering strategy B2 in BrS family 2. Ref. allele – reference allele; Alt. allele – alternative allele.

Genomic location	Ref. allele	Alt. allele	CADDv1.4 _phred	Variant effect/location	Regulation spotter prediction	Transcript ID	Gene
chr2:83869653	C	G	13.36	Intergenic	Non-functional region	-	DHFRP3; FUNDC2P2
chr2:86442146	CT	C	13.73	3'UTR	Polymorphism	ENST00000337109	REEP1

6.4.3 BrS family 3

Pedigree analysis revealed six family members with BrS phenotype in this small, three generational family (Figure 8). We recruited four affected asymptomatic family members with a positive ajmaline test (II:6; III:1; III:2 and III:3) for WGS, and a total number of nine individuals for linkage analysis (five affected: II:2; II:6; III:1; III:2; III:3; and four unaffected individuals: II:3; II:5; II:7; III:4). Patient information, DNA availability and performed tests are listed in **Table 6-13**.

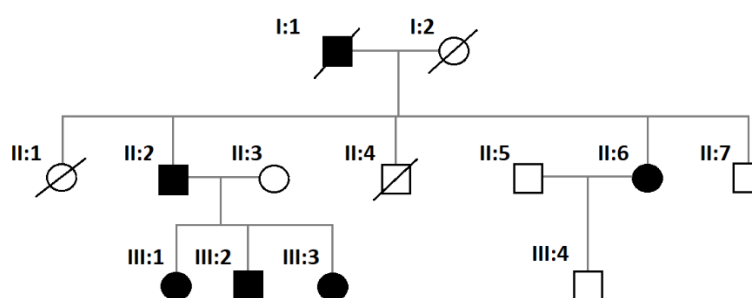


Figure 6-10 Pedigree of BrS family 3.

Table 6-13 BrS family 3 members information. SCD – sudden cardiac death; ICD – implantable cardioverter defibrillator.

Patient	Age	Gender	Disease status	Clinical phenotype	DNA sample	Linkage analysis	WGS
I:1	48	M	Affected	"Acute myocardial infarction", died at age 48	No	No	No
I:2	Unknown	F	Unaffected	-	No	No	No
II:1	71	F	Unaffected	-	No	No	No
II:2	69	M	Affected	Asymptomatic, spontaneous BrS type-1 ECG pattern	Yes	Yes	No
II:3	64	F	Unaffected	-	Yes	Yes	No
II:4	68	M	Unaffected	-	No	No	No
II:5	70	M	Unaffected	-	Yes	Yes	No
II:6	66	F	Affected	Ajmaline induced BrS type-1 ECG. Sudden syncope at the age of 65 after which ICD was implanted	Yes	Yes	Yes
II:7	59	M	Unaffected	Negative ajmaline test	Yes	Yes	No
III:1	42	F	Affected	Asymptomatic, normal baseline and ajmaline induced BrS type-1 ECG. Slight	Yes	Yes	Yes

				mitral valve thickening			
III:2	33	M	Affected	Asymptomatic, borderline positive ajmaline test. Slightly thickened mitral valve	Yes	Yes	Yes
III:3	31	F	Affected	Asymptomatic, normal baseline and ajmaline induced BrS type-1 ECG. Thickened mitral valve	Yes	Yes	Yes
III:4	37	M	Unaffected	Negative ajmaline test	Yes	Yes	No

Linkage analysis revealed seven loci on chromosomes 3, 4, 6, 7, 12, 13 and 22 (Chr3:66.067-95.067M; Chr4:22.085-34.085M; Chr6:44.234-63.234M; Chr7:9.045-20.045M; Chr12:21.192-22.192M; Chr13:25.264-37.264M; Chr22:24.856-34.856M), all with the same maximum LOD score of 1.462 (**Figure 6-9**).

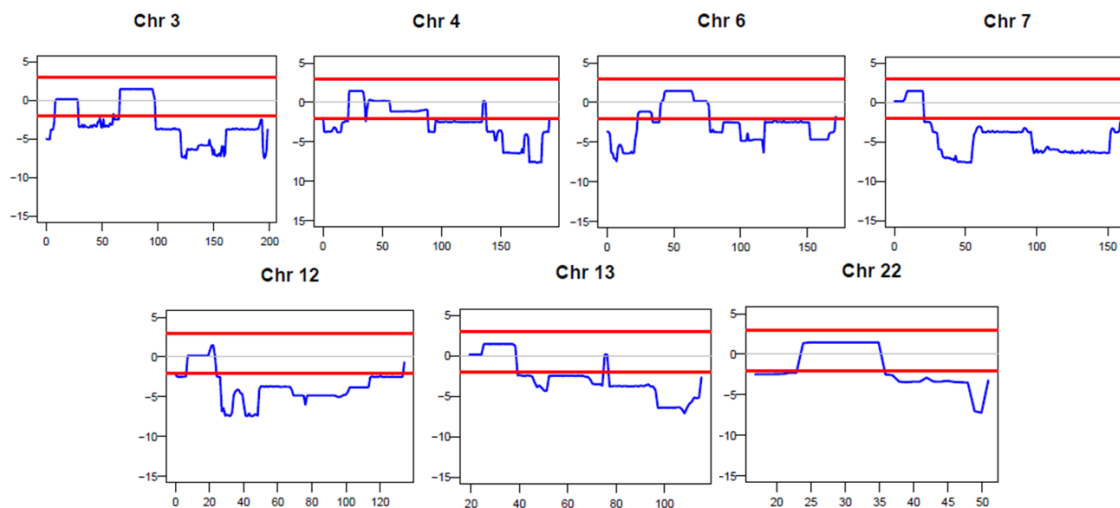


Figure 6-11 LOD scores obtained from linkage analysis of BrS family 3.

WGS variant filtering in all of the tested family members (II:6; III:1; III:2 and III:3) resulted in derivation of a list of 3 399 821 shared variants. However, our filtering strategy A did not yield any shared coding variants. Variant filtering B1 led to identification of two VUS (**Table 6-14**). Both of the variants are polymorphisms located within intronic sequences of the affected genes (*RYR2*, *SCN5A*), which do not affect the normal splicing of the encoded proteins and are located in the beginning of long repetitive stretches of adenine. Thus, both variants were excluded from further analysis.

Table 6-14 Shared prioritized variants obtained using filtering B1 in BrS family 3. Ref. allele – reference allele; Alt. allele – alternative allele; * variant located within the linked region/selected as a potential candidate.

Genomic location	Ref. allele	Alt. allele	CADD_phred	Variant location	Regulation spotter prediction	Transcript ID	Gene
chr1:237591082	CAAAAA	C	0	Intron	Polymorphism	ENST00000542537	RYR2
chr3:38668189	AC	A	0	Intron	Polymorphism	ENST00000476683	SCN5A

Variant filtering B2 resulted in derivation of a list of 526 variants. Variant prioritization led to selection of two deep intronic mutations on Chr3 (in *FOXP1* and *ROBO1*) (**Table 6-15**). Selected variants are predicted to create a new acceptor site (chromosome 13) or a donor site (chromosome 12); delete a donor site, resulting in a shift of the preferential existing donor site to the neighbouring one (chromosome 3 (both variants) and chromosome 6) (**Table 6-16**). Additional segregation analysis in this family was not useful as the only other available affected individual (II:2) is an obligate carrier of these variants (**Figure 6-8**).

Table 6-15 Results of filtering strategy B for the non-coding linked regions in BrS family 3.

Genomic location	Reference allele	Alternative allele	CADD_phred	Variant location	Mutation taster/Regulation spotter prediction	Transcript ID	Gene
*chr3:71045361	C	A	0.3	Intron	Polymorphism	ENST00000318779	<i>FOXP1</i>
*chr3:79561886	A	AG	0	Intron	Polymorphism	ENST00000492990	<i>ROBO1</i>

Table 6-16 Alamut predictions results for variants identified in BrS family 3.

Genomic location	Gene	Ref. allele	Alt. allele	Acceptor site	Donor site	Prediction programs				
						SSF	MaxEnt	NN SPLICE	Gene Splicer	HSF
chr3:71045361	<i>FOXP1</i>	C	A	Intron 13 – c.1062+4757		74.71>_	3.63>_			83.75>71.43 (-14.7%)
				Intron 13 – c.1062+4760		_>70.76	_>7,82	_>0.59	_>1.80	_>81.32
chr3:79561886	<i>ROBO1</i>	A	AG		Intron 2 – c.88+77088	78.47>_	7.52>_	0.93>_		84.38>_
					Intron 2 - c.88+77089	_>91.49	_>10.56	_>1.00	_>0.47	_>95.25
				Intron 2 – c.88+77094		76.05>73.07 (-2.7%)	2.22>2.51 (+13.3%)			80.19>76.23 (-4.9%)

We obtained fibroblasts from patient III:1 and performed differentiation of one reprogrammed iPSC clone (BrS3). For our splicing analysis, we used cDNA sample from untreated and Puromycin treated iPSC-CMs of BrS3, unrelated healthy donor (Ctrl) and unaffected control BrS family 2 member (Famctrl) (**Figure 6-10**). We saw alternative product for *FOXP1* in the BrS3 iPSC-CMs (obtained from individual III:1) treated with puromycin. But because this alternative splicing also occurred in control iPSC-CMs treated with puromycin (**Figure 6-10**), we concluded it concerns normal alternative and not pathogenic splicing. No difference in splicing for *ROBO1* was observed between the tested samples. This led to exclusion of the tested variants from further consideration as potential candidates.

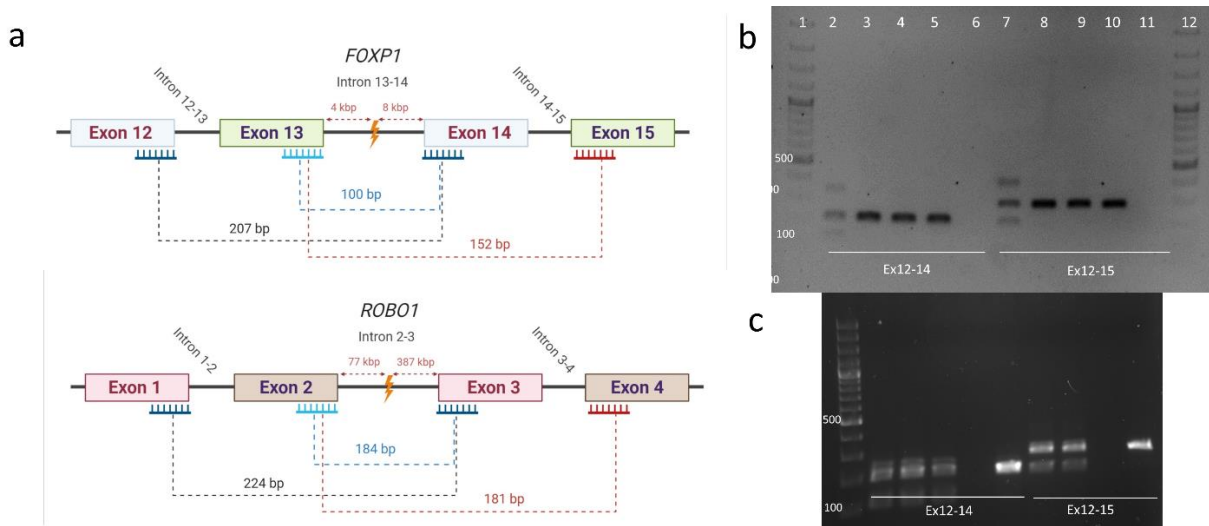


Figure 6-12 Splicing check of identified *FOXP1* VUS in BrS family 3. Legend: 1. 100 bp Plus Ladder (Life Technologies); 2. BrS3 batch 1 cultured with Puromycin; 3. BrS3 batch 1 sample 1.1; 4. BrS3 batch 1 sample 1.2; 5. Ctrl batch 1; 6. Negative control; 7. BrS3 batch 1 cultured with Puromycin; 8. BrS3 batch 1 sample 1.1; 9. BrS3 batch 1 sample 1.2; 10. Ctrl batch 1; 11. negative control; 12. & 13. 100bp Plus ladder; 14. Famctrl batch 1 cultured with Puromycin; 15. Famctrl batch 2 cultured with Puromycin; 16. Ctrl batch 1 cultured with Puromycin; 17. Negative control; 18. Ctrl batch 1; 19. Famctrl batch 1 cultured with Puromycin; 20. Famctrl batch 2 cultured with Puromycin; 21. Ctrl batch 1 cultured with Puromycin; 22. Negative control; 23. Ctrl batch 1. Analysed primer pairs are indicated underneath the obtained bands (with the number of exon with the forward – reverse primer).

From 732 shared CNVs, filtering and prioritization in strategy C led to identification of 29 large deletions, from which four were family specific (**Table 6-17**), however no association with cardiac arrhythmias or cardiovascular phenotype were found for the affected regions in available databases, thus excluding them from potential candidate list.

Table 6-17 Shared CNVs ≥ 100 kb identified in BrS family 3. Empty cells in the table indicate no known genes were present in the neighbourhood (up to 1 Mb from the CNV boundaries) of the CNV.

Chromosome	Deletion start	Deletion end	Size of the overlapping deletion	Genes in the neighbourhood of the variant	Transcript ID
1	205922701	206072800	150 100	-	-
10	128616101	128766100	150 000	-	-
17	43619601	44165200	545 600	-	-
20	26319501	29419700	3 100 200	-	-

Due to a lack of candidate VUS after our WGS analysis approach and initial validation, we decided to perform re-filtering and analysis of the variants using strategies A and B1-2. We assumed that with the updated versions of the population frequencies and prediction tools we might obtain different filtering results. None of the shared 3 399 821 VUS passed our analysis strategy A or B1 (**Figure 6-1**). Filtering B2 focused on linked non-coding regions led to identification of 11 VUS: two on chr3, two on chr4, four on chr6, and two on chr13. Within those, after prioritization one rare polymorphism 583 kb upstream of the *PPARGC1A* gene remained. The variant is located in the DNase I hypersensitive site in human heart tissue, which suggests that this locus is available for transcription factors. *PPARGC1A* gene encodes PGC-1 α protein, which was previously associated with hypertrophic cardiomyopathy and heart failure in PGC-1 α knock-out mice (**Table 6-18**) [33, 34]. *In silico* prediction of the variant effect on splicing showed no effect on splicing based on all integrated scoring tools in Alamut; thus this VUS was not further considered as a potential candidate.

Table 6-18 Re-filtering strategy B2 analysis results for BrS family 3.

Genomic location	Reference allele	Alternative allele	CADD_phred	Variant location	Regulation spotter prediction	Transcript ID	Gene
chr4:24474544	C	CGTGTGTGTGT	21.9	582 844 bp upstream	Polymorphism	ENST00000264867.2	PPARGC1A

6.5 Discussion

Although many genes have been reported to carry causal mutations in Brugada syndrome patients, pathophysiology of this disease is still unresolved in large fraction of the known cases. The key player in BrS development is undoubtedly the imbalanced function of Nav1.5. Nevertheless, mutations in the *SCN5A* gene encoding the cardiac sodium channel still explain only about 20% of the known BrS cases, while variation in the other known BrS-related genes resolves only 5% more. In this report we performed whole genome sequencing in combination with linkage analysis in three well characterized BrS families, in which genetic screening of arrhythmia-related genes using in-house developed PED gene panel previously did not yield any result. We performed WGS on a selection of ten BrS patients with a positive ajmaline challenge test. One patient presented spontaneous BrS type-1 ECG in BrS family 1 (III:10) (**Figure 6-2**); syncope were present in three sequenced individuals: two from BrS family 2 (II:6 and II:8) (**Figure 6-5**) and one from BrS family 3 (II:6) (**Figure 6-8**). We recruited additional family members for genotyping to perform linkage analysis in those families and obtained several loci for each of the families with potential interesting LOD-scores (**Figure 6-3, 6-6, 6-9**): four peaks in BrS family 1 with maximum LOD score of 1.460; three peaks in BrS family 2 with maximum LOD score of 2.561 and seven peaks in BrS family 3 with maximum LOD score of 1.42 (**Figure 6-3, 6-6, 6-9**). As in all the analysed families, the obtained LOD scores fell below the LOD=3 threshold, this raised the question if the obtained linkage peaks were true or false positives. We also did not observe a linked region that was shared between the three families (only a region on chr4 32 085 000-34 085 000 was shared between BrS family 1 and 3, however no shared rare candidate variants were identified in this region). Ideally, linkage analysis would be performed in a large, multigenerational family with good phenotype data and DNA samples available from many individuals. [35-37]. In case of this report, the number of available meioses was rather low, which had an impact on the possible result. The highest possible LOD scores that could have been obtained from the available samples for each of the tested families, estimated based on the pedigree were as follow: 1.8-2.0 for BrS family 1; 2.5-3.0 for BrS family 2 and 1.5 for BrS family 3. Although we did not reach these highest possible LOD scores in any of the families (except BrS family 2 in the repeated linkage analysis experiment), we still used the regions with the highest LOD scores as a filter criterium in our further analysis of WGS datasets. Alternatively, low LOD scores may also suggest more complex inheritance pattern of the disease, in which case the search for a single variant that may be involved in disease development will become difficult [36, 37].

We pursued genetic analysis of the shared variants in the WGS datasets in each family, focusing first on the shared variants located within the coding regions of the whole genome (filtering strategy A; **Figure 6-1**). In BrS family 1, this approach did not yield any result, thus we pursued analysis of the coding region of each individual WGS dataset separately. This approach led somewhat surprisingly to identification of an *SCN5A* frameshift variant (c.2325delA; p.Tyr774Serfs) in individual III:10, which was present also in two other family members: obligate carrier II:2 and affected individual III:14 (**Figure 6-4**), explaining (part of the) disease etiology in those cases. This family illustrates the fact that in a single family multiple genetic causes for BrS might be at play. This has also been reported in literature [38, 39]. Saber et al. performed genetic screening for *SCN5A* mutations in a large BrS family, which led to identification of a c.4516C>T (p.1506Ser/Asn) variant, that explained disease phenotype in two out of four affected individuals [38]. Two others showed presence of *KCNH2* variant c.73C>T (p.Arg25Trp/Asn) or both variants as compound heterozygous mutations. Similarly, Beziau et al. performed functional phenotyping in a BrS family where three mutations in *SCN5A* (c.5083C>T; p.Gln1695X), *ABCC9* (c.437A>T; p.Ile146Asn) and *CACNA1C*

(c.898A>G; p.Asn300Asp) were identified [39]. In this case, the variant in *ABCC9* led to development of BrS phenotype, *SCN5A* mutation led to cardiac conduction defect and the variant in *CACNA1C* led to development of BrS and/or prolonged QT in the mutation carriers, while presence of both *SCN5A* and *CACNA1C* variants led to development of overlapping symptoms. Further on, we pursued the analysis of the variants shared by the remaining affected individuals of family 1, however we did not identify any shared coding variants which could be linked with BrS phenotype. In BrS family 2, filtering strategy A led to identification of an interesting variant in *SNAP29* gene, which despite its link with 22q11.2 deletion syndrome [22, 24], was excluded from further consideration due to its low tissue expression specificity. More recently, we performed re-filtering of the data with the usage of the updated GnomAD and CADD_phred datasets, and identified two additional shared, disease-causing variants in *CCER1* and *DCLRE1A* genes, from which the latter gene was previously reported to be involved in Fanconi anemia with congenital heart defects [32]. Both variants segregated with disease phenotype in the family. Validation of the VUS effect on splicing is currently ongoing. In case of BrS family 3, our filtering approach A did not yield any result.

Initially, the non-coding parts of the genome were thought to be the junk DNA. Currently, this ‘dark matter’ of DNA is known to contain important sequences that undergo or regulate transcription, but are not translated into protein, such as non-coding RNAs, transcription enhancers or silencers [40], which are involved in regulation of gene expression. It has been previously shown, that deep intronic variants can be involved in the development of disorders like Stargardt disease [41], Becker muscular dystrophy [42] or hypertrophic cardiomyopathy [43]. Those variants can lead to alternative splicing events, which change the conformation of the protein. Splicing variants lead to changes in the usage of donor (the 5'-splice site at the exon-intron border) or acceptor (the 3'-splice site at the intron-exon border) sites, as well as branch points (located ~18-40 nucleotides upstream of the acceptor site) [44]. When an alternative splice site located within an intron becomes activated, it can give a signal for retention of a part of an intron or exon skipping, changing the length and conformation of the mRNA and the protein [45, 46]. Those events are relevant in multiple genetic disorders, like e.g. Timothy syndrome and BrS [45-47]. In this project, we screened the available WGS data for the candidate variants located in non-coding regions of the PED-related genes (filtering B1) as well as those located within the linked regions of the whole genome for each of the tested families (filtering B2) (**Figure 6-1**).

Filtering B1 did not yield any result in BrS family 1, while in BrS family 2 and 3 we identified three and two deep intronic VUS, respectively. While the variants in BrS family 3 were known polymorphisms, one of the variants identified in BrS family 2 in *CTNNA3* was predicted to be disease-causing and alter normal splicing of the affected mRNA (**Table 6-6, 6-8**). Nevertheless, our analysis of splicing effect of this variant in patient derived iPSC-CMs was negative, thus the variant was no longer considered to be the candidate we were searching for (**Figure 6-7b**). Finally, we proceeded with filtering strategy B2, which led to identification of potential candidates in BrS family 2 (in *GLI2*) and 3 (in *FOXP1*, *ROBO1*), which were predicted to affect normal splicing of the affected proteins (**Table 6-7, 6-8, 6-15, 6-16**). Each of the affected genes was involved in cardiac development. Activation of *GLI2* in Hedgehog signalling pathway indirectly regulates expression of myocyte specific enhancer factor Mef2c [26]; *FOXP1* null mice show defects in outflow tract septation, cardiomyocyte proliferation and maturation, together with ventricular septation defects [48, 49]; while loss of function of *ROBO1* results in ventricular septum defects and Tetralogy of Fallot [50, 51]. Our splicing analysis in available patient iPSC-CM samples revealed alternative products only for the VUS in *FOXP1*, however the same alternative product was present in our control iPSC-CMs (**Figure 6-10**). Thus, none of the selected candidates was further considered as a potential candidate. In 2014, van den Boogaard et al. proved an involvement of common intronic variant in *SCN10A* in the regulation of *SCN5A* expression in the cardiac tissue [52]. They investigated an SNP within an intronic enhancer of *SCN10A* (rs6801957) (identified in a GWAS study of Bezzina et al. in 2013 [53]), associated with QRS prolongation, which was in linkage disequilibrium with the variants predisposing to BrS. Due to a close physical distance of the enhancers and promoters in the *SCN10A-SCN5A* cluster, they hypothesized that the interactions of the enhancers can be influenced by common polymorphisms and indirectly influence expression pattern

of the Na_v1.5 channel. In their mouse experiments, they proved that the expression of a common polymorphism in the *SCN10A* locus affects cardiac physiology by disturbing *SCN5A* expression. Moreover, recently Man et al. reported based on their mouse studies that variants in linkage disequilibrium with the same SNV rs6801957 are associated with variability in *SCN10A* transcript expression in the heart, further supporting the role of the non-coding parts of the whole genome in modulation of proper function of cardiac conduction and disease development [54].

Copy number variation (CNV) is a well-known cause of inherited human disorders. CNVs include intragenic duplications or deletions, as well as aneuploidies [55]. Although those events are more prevalent in neurodevelopmental disorders (about 12% of the known cases) like e.g. autistic spectrum disorders [56, 57], their relevance was also shown in hypertrophic cardiomyopathy [58], LQTS [59, 60] and arrhythmogenic cardiomyopathy [61]. Traditionally, high resolution CNV analysis involved performance of comparative genomic hybridization array, which was focused on analysis of exonic sequences. With the implementation of WGS into clinical practice, not only exonic but also intronic and intergenic copy number variation analysis became possible, with proven good quality of the obtained data [57, 62]. We looked at the shared CNVs in the available WGS datasets (filtering strategy C; **Figure 6-1**). This approach led to identification of 33, 31 or 29 shared CNVs larger than 100 kbp for BrS family 1, 2 or 3, respectively. Out of those, only 8, 3 or 4 were family specific, in BrS family 1, 2 or 3, respectively (**Table 6-3, 6-9, 6-17**). We were not able to identify link with the BrS phenotype for CNVs in all tested BrS families. Truty et al. performed intragenic CNV analysis in a cohort of >143 000 unrelated individuals who were referred for diagnostic NGS gene panel to confirm suspected Mendelian disorder [62]. According to their analysis, gene panels for cardiovascular disorders fell within the group presenting with the lowest pathogenic CNV prevalence (4.7%), where interestingly Brugada syndrome was amongst the disorders with the highest frequencies of pathogenic CNVs. The analysis involved the published reports from the cardiology-related gene panels, where in total 108 genes were analysed for the presence of CNVs. 15 genes (*ACVRL1, BMPR2, COL3A1, COL5A1, DSC2, FBN1, FBN2, KCNQ1, LDLR, MYBPC3, PKP2, PLN, RYR2, SMAD3, TNNI*) showed high frequency of pathogenic CNVs. Three of the genes: *KCNQ1, PKP2* and *RYR2* were directly connected with arrhythmias, including Brugada syndrome. Looking at those genes, we identified one deletion of 1 200 bp-16 420 bp upstream *KCNQ1* gene in all members of BrS family 1 and 2 (chr11:2449801-2451000, no regulatory elements were identified in this location). This observation, together with results presented in this report support the necessity of analysis of this type of genetic variation in BrS cases.

Our combined linkage analysis and WGS approach was not successful in identification of a strong single shared candidate variant for each of the tested BrS families. Although in BrS family 2, where we obtained the highest LOD scores, we identified potential candidates (*CTNNA3, GLI2, DCLRE1A*), none of the appointed VUS was solely explaining the disease phenotype. Brugada syndrome is currently thought to be a disorder with a complex genetic background, where a polygenic inheritance is a highly possible explanation in the missing heritability of the disorder [4, 63-66]. Our results support that hypothesis, showing that it is highly possible that the development of the disease phenotype in the tested familial cases is an effect of an additive activity of multiple genetic variants. This fact may be true for BrS family 2, and BrS family 3, where we identified rare polymorphisms in two PED-related genes *SCN5A* and *RYR2*. Moreover, in one of our families – BrS family 1 – we have shown that more than one genetic cause can be the explanation for disease etiology within one family (*SCN5A* frameshift mutation in several affected family members, and multiple genetic inheritance or possible phenocopy in others). It has been previously reported, that common polymorphisms in the *SCN5A-SCN10A* cluster region can predispose to BrS development [53, 67]. In 2013, Bezzina et al. reported association with BrS for common single nucleotide variants (SNVs) in locus of *SCN10A* gene and neighbourhood of *HEY2* gene [53]. Recently, Pinsach-Abuin et al. performed fine-mapping of SNVs located within the *SCN5A-SCN10A* locus identified by Bezzina et al which led to identification of two haplotype blocks involved in BrS development (enhancer and promoter region) [67]. They have shown that the enhancer block is a heritable unit, where several common SNVs are associated with BrS. However, their individual association was not strong, thus they investigated the haplotype composition in their BrS samples and identified three haplotypes (Hap1-3) which showed

enrichment amongst BrS patients. Interestingly, Hap1/1 (rs6801957 + rs6799257 + rs9836859 + rs6790396 + rs9874633 + rs10428132; haplotype: TACCATT) presented a risk genotype, while Hap2/3 (Hap2: rs6799257 + rs9836859 + rs9874633; haplotype: CACGAGT; Hap 3: rs10428168; haplotype: CGGGGGC) was a protective haplotype (enriched in control samples). We looked for those alleles within the *SCN5A-SCN10A* block in our WGS datasets. We identified four patients with a protective haplotype (Hap2/3): individual III:10 from BrS family 1 (an *SCN5A* frameshift mutation carrier), individuals II:6 and II:8 from BrS family 2 and individual II:6 from BrS family 3. All of those individuals presented with positive ajmaline challenge, and/or spontaneous ECG type-1 or syncopes. In one of the tested individuals (III:3 from BrS family 2) we identified single allele rs9874633, while for the remaining individuals for which we performed WGS, we did not see any of the common alleles reported by Pinsach-Abuin. Recently, Barc et al. reported new GWAS study results identifying 10 novel loci associated with BrS, affecting *SCN5A-SCN10A* locus as well as loci affecting cardiac transcription factor genes [68]. Moreover, their functional tests performed in mice as well as iPSC-CM models for *MAPRE2* knockout confirm the mechanism of Na_v1.5 regulation through the microtubule network as an underlying mechanism in BrS development. They also report the first polygenic risk score analysis in BrS patients, which confirmed that the interplay between the rare *SCN5A* variants as well as common risk alleles and sodium channel loss-of-function contributes to variable expression of the disease phenotype.

In conclusion, failure of identification of a single genetic cause using combined approach with linkage analysis and WGS may indicate a more complex inheritance of BrS in the analysed families. Future research in the field of genetic studies of Brugada syndrome should focus on the analysis of the possible polygenic inheritance and stratification of the involvement of genetic modifiers, hence large-scale genome wide association studies are required to predict polygenic risk scores for BrS diagnostics.

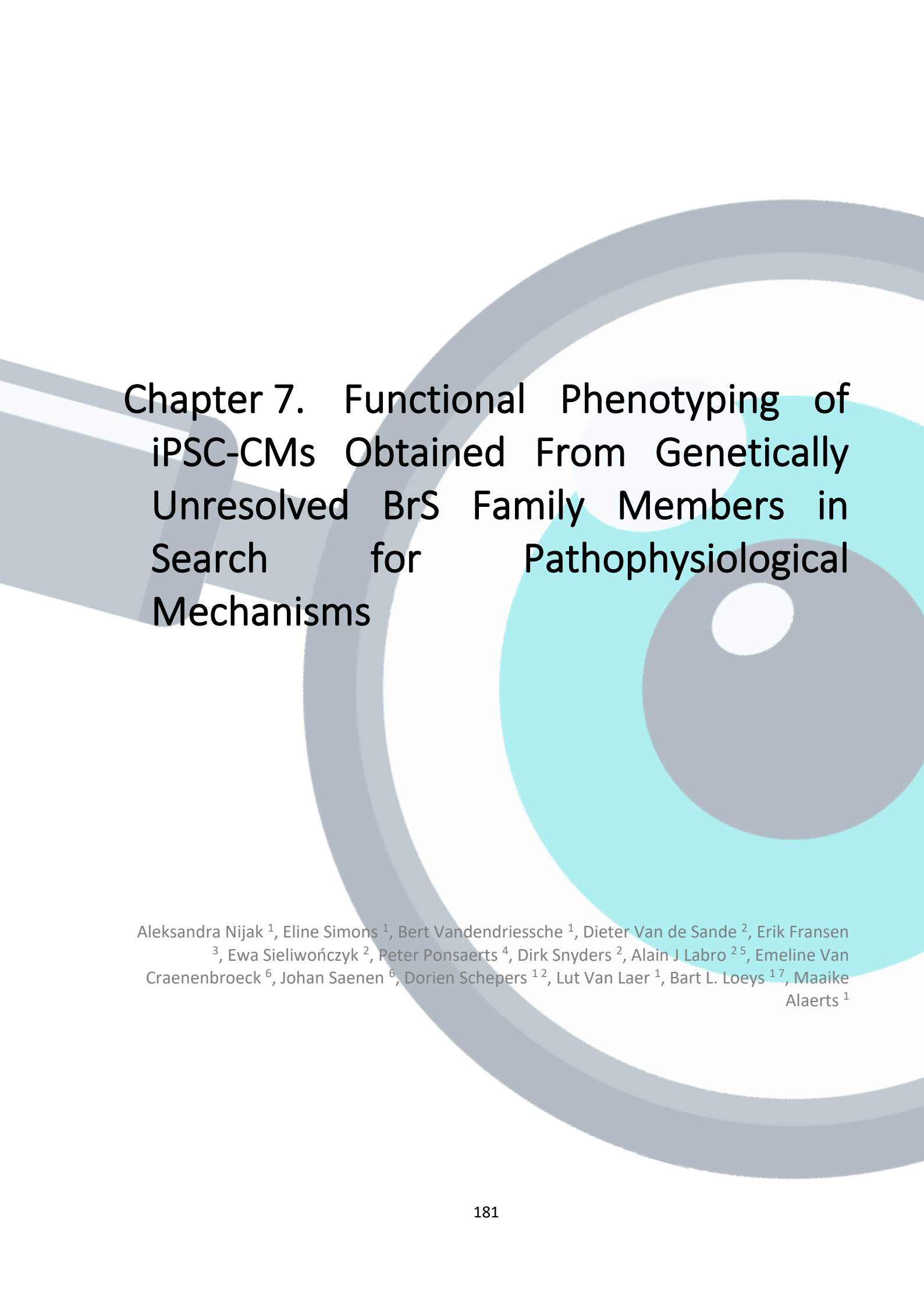
6.6 References

- [1] McMillan, M.R.; Day, T.G.; Bartsota, M.; Mead-Regan, S.; Bryant, R.; Mangat, J.; et al. Feasibility and outcomes of ajmaline provocation testing for Brugada syndrome in children in a specialist paediatric inherited cardiovascular diseases centre. *Open Heart*. 2014;1:e000023.
- [2] Hong, K.; Brugada, J.; Oliva, A.; Berruezo-Sanchez, A.; Potenza, D.; Pollevick, G.D.; et al. Value of electrocardiographic parameters and ajmaline test in the diagnosis of Brugada syndrome caused by *SCN5A* mutations. *Circulation*. 2004;110:3023-7.
- [3] Schwartz, P.J.; Ackerman, M.J.; Antzelevitch, C.; Bezzina, C.R.; Borggrefe, M.; Cuneo, B.F.; et al. Inherited cardiac arrhythmias. *Nat Rev Dis Primers*. 2020;6:58.
- [4] Pappone, C.; Santinelli, V. Brugada Syndrome: Progress in Diagnosis and Management. *Arrhythm Electrophysiol Rev*. 2019;8:13-8.
- [5] Bezzina, C.R.; Priori, S.G. Genetics of Sudden Cardiac Death. *Circulation Research*. 2015;116:1919-36.
- [6] Fan, L.L.; Chen, Y.Q.; Huang, H.; Yuan, Z.Z.; Jin, J.Y.; Hu, M.; et al. Exome sequencing identifies a novel nonsense mutation of Ring Finger Protein 207 in a Chinese family with Long QT syndrome and syncope. *J Hum Genet*. 2019;64:233-8.
- [7] Boczek, N.J.; Best, J.M.; Tester, D.J.; Giudicessi, J.R.; Middha, S.; Evans, J.M.; et al. Exome sequencing and systems biology converge to identify novel mutations in the L-type calcium channel, *CACNA1C*, linked to autosomal dominant long QT syndrome. *Circ Cardiovasc Genet*. 2013;6:279-89.
- [8] De Bortoli, M.; Postma, A.V.; Poloni, G.; Calore, M.; Minervini, G.; Mazzotti, E.; et al. Whole-Exome Sequencing Identifies Pathogenic Variants in *TJP1* Gene Associated With Arrhythmogenic Cardiomyopathy. *Circ Genom Precis Med*. 2018;11:e002123.
- [9] Huang, H.; Ding, D.B.; Fan, L.L.; Jin, J.Y.; Li, J.J.; Guo, S.; et al. Whole-exome sequencing identifies a Novel *SCN5A* mutation (C335R) in a Chinese family with arrhythmia. *Cardiol Young*. 2018;28:688-91.
- [10] Belbachir, N.; Portero, V.; Al Sayed, Z.R.; Gourraud, J.B.; Dilasser, F.; Jesel, L.; et al. *RRAD* mutation causes electrical and cytoskeletal defects in cardiomyocytes derived from a familial case of Brugada syndrome. *Eur Heart J*. 2019;40:3081-94.
- [11] Huang, H.; Chen, Y.Q.; Fan, L.L.; Guo, S.; Li, J.J.; Jin, J.Y.; et al. Whole-exome sequencing identifies a novel mutation of *GPD1L* (R189X) associated with familial conduction disease and sudden death. *J Cell Mol Med*. 2018;22:1350-4.
- [12] Proost, D.; Saenen, J.; Vandeweyer, G.; Rotthier, A.; Alaerts, M.; Van Craenenbroeck, E.M.; et al. Targeted Next-Generation Sequencing of 51 Genes Involved in Primary Electrical Disease. *J Mol Diagn*. 2017;19:445-59.
- [13] Hastings, R.; de Villiers, C.P.; Hooper, C.; Ormondroyd, L.; Pagnamenta, A.; Lise, S.; et al. Combination of Whole Genome Sequencing, Linkage, and Functional Studies Implicates a Missense Mutation in Titin as a Cause of Autosomal Dominant Cardiomyopathy With Features of Left Ventricular Noncompaction. *Circ Cardiovasc Genet*. 2016;9:426-35.
- [14] Nijak, A.; Saenen, J.; Labro, A.J.; Schepers, D.; Loeys, B.L.; Alaerts, M. iPSC-Cardiomyocyte Models of Brugada Syndrome - Achievements, Challenges and Future Perspectives. *International Journal of Molecular Sciences*. 2021;22:2825.
- [15] Vandeweyer, G.; Van Laer, L.; Loeys, B.; Van den Bulcke, T.; Kooy, R.F. VariantDB: a flexible annotation and filtering portal for next generation sequencing data. *Genome Med*. 2014;6:74.
- [16] Arisi, I.; D'Onofrio, M.; Brandi, R.; Felsani, A.; Capsoni, S.; Drovandi, G.; et al. Gene expression biomarkers in the brain of a mouse model for Alzheimer's disease: mining of microarray data by logic classification and feature selection. *J Alzheimers Dis*. 2011;24:721-38.
- [17] Du, Z.; Wu, B.; Xia, Q.; Zhao, Y.; Lin, L.; Cai, Z.; et al. LCN2-interacting proteins and their expression patterns in brain tumors. *Brain Res*. 2019;1720:146304.

- [18] Al-Shihabi, A.; Chawla, S.P.; Hall, F.L.; Gordon, E.M. Exploiting Oncogenic Drivers along the *CCNG1* Pathway for Cancer Therapy and Gene Therapy. *Mol Ther Oncolytics*. 2018;11:122-6.
- [19] Lindqvist, A.; Sharvill, J.; Sharvill, D.E.; Andersson, S. Loss-of-function mutation in carotenoid 15,15'-monooxygenase identified in a patient with hypercarotenemia and hypovitaminosis A. *J Nutr*. 2007;137:2346-50.
- [20] Malek, N.; Stewart, W.; Greene, J. The progressive myoclonic epilepsies. *Pract Neurol*. 2015;15:164-71.
- [21] Bufe, B.; Hofmann, T.; Krautwurst, D.; Raguse, J.D. Meyerhof W. The human TAS2R16 receptor mediates bitter taste in response to beta-glucoopyranosides. *Nat Genet*. 2002;32:397-401.
- [22] McDonald-McGinn, D.M.; Fahiminiya, S.; Revil, T.; Nowakowska, B.A.; Suhl, J.; Bailey, A.; et al. Hemizygous mutations in *SNAP29* unmask autosomal recessive conditions and contribute to atypical findings in patients with 22q11.2DS. *J Med Genet*. 2013;50:80-90.
- [23] Keser, V.; Lachance, J.B.; Alam, S.S.; Lim, Y.; Scarlata, E.; Kaur, A.; et al. Snap29 mutant mice recapitulate neurological and ophthalmological abnormalities associated with 22q11 and CEDNIK syndrome. *Commun Biol*. 2019;2:375.
- [24] Hou, H.T.; Chen, H.X.; Wang, X.L.; Yuan, C.; Yang, Q.; Liu, Z.G.; et al. Genetic characterisation of 22q11.2 variations and prevalence in patients with congenital heart disease. *Arch Dis Child*. 2020;105:367-74.
- [25] Sprecher, E.; Ishida-Yamamoto, A.; Mizrahi-Koren, M.; Rapaport, D.; Goldsher, D.; Indelman, M.; et al. A mutation in *SNAP29*, coding for a SNARE protein involved in intracellular trafficking, causes a novel neurocutaneous syndrome characterized by cerebral dysgenesis, neuropathy, ichthyosis, and palmoplantar keratoderma. *Am J Hum Genet*. 2005;77:242-51.
- [26] Fair, J.V.; Voronova, A.; Bosiljcic, N.; Rajgara, R.; Blais, A.; Skerjanc, I.S. BRG1 interacts with GLI2 and binds Mef2c gene in a hedgehog signalling dependent manner during *in vitro* cardiomyogenesis. *BMC Dev Biol*. 2016;16:27.
- [27] Madi, A.; Fisher, D.; Maughan, T.S.; Colley, J.P.; Meade, A.M.; Maynard, J.; et al. Pharmacogenetic analyses of 2183 patients with advanced colorectal cancer; potential role for common dihydropyrimidine dehydrogenase variants in toxicity to chemotherapy. *Eur J Cancer*. 2018;102:31-9.
- [28] Fachin, A.L.; Mello, S.S.; Sandrin-Garcia, P.; Junta, C.M.; Donadi, E.A.; Passos, G.A.; et al. Gene expression profiles in human lymphocytes irradiated *in vitro* with low doses of gamma rays. *Radiat Res*. 2007;168:650-65.
- [29] Shahi, R.B.; De Brakeleer, S.; Caljon, B.; Pauwels, I.; Bonduelle, M.; Joris, S.; et al. Identification of candidate cancer predisposing variants by performing whole-exome sequencing on index patients from *BRCA1* and *BRCA2*-negative breast cancer families. *BMC Cancer*. 2019;19:313.
- [30] Laporte, G.A.; Leguisamo, N.M.; Gloria, H.C.E.; Azambuja, D.B.; Kalil, A.N.; Saffi, J. The role of double-strand break repair, translesion synthesis, and interstrand crosslinks in colorectal cancer progression-clinopathological data and survival. *J Surg Oncol*. 2020;121:906-16.
- [31] Garner, E.; Smogorzewska, A. Ubiquitylation and the Fanconi anemia pathway. *FEBS Lett*. 2011;585:2853-60.
- [32] Lubinsky, M. Sonic Hedgehog, VACTERL, and Fanconi anemia: Pathogenetic connections and therapeutic implications. *Am J Med Genet A*. 2015;167A:2594-8.
- [33] Riehle, C.; Abel, E.D. PGC-1 proteins and heart failure. *Trends Cardiovasc Med*. 2012;22:98-105.
- [34] Karkkainen, O.; Tuomainen, T.; Mutikainen, M.; Lehtonen, M.; Ruas, J.L.; Hanhineva, K.; et al. Heart specific PGC-1alpha deletion identifies metabolome of cardiac restricted metabolic heart failure. *Cardiovasc Res*. 2019;115:107-18.
- [35] Pulst, S.M. Genetic linkage analysis. *Arch Neurol*. 1999;56:667-72.
- [36] Ott, J.; Wang, J.; Leal, S.M. Genetic linkage analysis in the age of whole-genome sequencing. *Nat Rev Genet*. 2015;16:275-84.
- [37] Cantor, R.M. Analysis of Genetic Linkage. In: Pyeritz REKBRGWW, editor. *Emery and Rimoin's Principles and Practice of Medical Genetics and Genomics (Seventh Edition)*: Elsevier Inc.; 2019. p. 277-36.

- [38] Saber, S.; Amarouch, M.Y.; Fazelifar, A.F.; Haghjoo, M.; Emkanjoo, Z.; Alizadeh, A.; et al. Complex genetic background in a large family with Brugada syndrome. *Physiol Rep*. 2015;3.
- [39] Beziau, D.M.; Barc, J.; O'Hara, T.; Le Gloan, L.; Amarouch, M.Y.; Solnon, A.; et al. Complex Brugada syndrome inheritance in a family harbouring compound *SCN5A* and *CACNA1C* mutations. *Basic Res Cardiol*. 2014;109:446.
- [40] Zhang, G.; Pradhan, S. Mammalian epigenetic mechanisms. *IUBMB Life*. 2014;66:240-56.
- [41] Sangermano, R.; Garanto, A.; Khan, M.; Runhart, E.H.; Bauwens, M.; Bax, N.M.; et al. Deep-intronic *ABCA4* variants explain missing heritability in Stargardt disease and allow correction of splice defects by antisense oligonucleotides. *Genet Med*. 2019;21:1751-60.
- [42] Trabelsi, M.; Beugnet, C.; Deburgrave, N.; Commere, V.; Orhant, L.; Leturcq, F.; et al. When a mid-intronic variation of *DMD* gene creates an ESE site. *Neuromuscul Disord*. 2014;24:1111-7.
- [43] Mendes de Almeida, R.; Tavares, J.; Martins, S.; Carvalho, T.; Enguita, F.J.; Brito, D.; et al. Whole gene sequencing identifies deep-intronic variants with potential functional impact in patients with hypertrophic cardiomyopathy. *PLoS One*. 2017;12:e0182946.
- [44] Wachutka, L.; Caizzi, L.; Gagneur, J.; Cramer, P. Global donor and acceptor splicing site kinetics in human cells. *Elife*. 2019;8.
- [45] Baralle, D.; Buratti, E. RNA splicing in human disease and in the clinic. *Clin Sci (Lond)*. 2017;131:355-68.
- [46] Jiang W, Chen L. Alternative splicing: Human disease and quantitative analysis from high-throughput sequencing. *Comput Struct Biotechnol J*. 2021;19:183-95.
- [47] Hong, K.; Guerchicoff, A.; Pollevick, G.D.; Oliva, A.; Dumaine, R.; de Zutter, M.; et al. Cryptic 5' splice site activation in *SCN5A* associated with Brugada syndrome. *J Mol Cell Cardiol*. 2005;38:555-60.
- [48] Zhang, Y.; Li, S.; Yuan, L.; Tian, Y.; Weidenfeld, J.; Yang, J.; et al. Foxp1 coordinates cardiomyocyte proliferation through both cell-autonomous and nonautonomous mechanisms. *Genes Dev*. 2010;24:1746-57.
- [49] Wang, B.; Weidenfeld, J.; Lu, M.M.; Maika, S.; Kuziel, W.A.; Morrissey, E.E.; et al. Foxp1 regulates cardiac outflow tract, endocardial cushion morphogenesis and myocyte proliferation and maturation. *Development*. 2004;131:4477-87.
- [50] Kruszka, P.; Tanpaiboon, P.; Neas, K.; Crosby, K.; Berger, S.I.; Martinez, A.F.; et al. Loss of function in *ROBO1* is associated with tetralogy of Fallot and septal defects. *J Med Genet*. 2017;54:825-9.
- [51] Zhao, J.; Mommersteeg, M.T.M. Slit-Robo signalling in heart development. *Cardiovasc Res*. 2018;114:794-804.
- [52] van den Boogaard, M.; Smemo, S.; Burnicka-Turek, O.; Arnolds, D.E.; van de Werken, H.J.; Klous, P.; et al. A common genetic variant within *SCN10A* modulates cardiac *SCN5A* expression. *J Clin Invest*. 2014;124:1844-52.
- [53] Bezzina, C.R.; Barc, J.; Mizusawa, Y.; Remme, C.A.; Gourraud, J.B.; Simonet, F.; et al. Common variants at *SCN5A-SCN10A* and *HEY2* are associated with Brugada syndrome, a rare disease with high risk of sudden cardiac death. *Nat Genet*. 2013;45:1044-9.
- [54] Man, J.C.K.; Bosada, F.M.; Scholman, K.T.; Offerhaus, J.A.; Walsh, R.; van Duijvenboden, K.; et al. Variant Intronic Enhancer Controls *SCN10A*-Short Expression and Heart Conduction. *Circulation*. 2021.
- [55] Macé, A.K. Z.; Valsesia, A. Copy Number Variation. In: Evangelou E, editor. *Genetic Epidemiology Methods in Molecular Biology*. New York: Humana Press; 2018. p. 231-58.
- [56] Levy, D.; Ronemus, M.; Yamrom, B.; Lee, Y.H.; Leotta, A.; Kendall, J.; et al. Rare *de novo* and transmitted copy-number variation in autistic spectrum disorders. *Neuron*. 2011;70:886-97.
- [57] Uddin, M.; Thiruvahindrapuram, B.; Walker, S.; Wang, Z.; Hu, P.; Lamoureux, S.; et al. A high-resolution copy-number variation resource for clinical and population genetics. *Genet Med*. 2015;17:747-52.

- [58] Mademont-Soler, I.; Mates, J.; Yotti, R.; Espinosa, M.A.; Perez-Serra, A.; Fernandez-Avila, A.I.; et al. Additional value of screening for minor genes and copy number variants in hypertrophic cardiomyopathy. *PLoS One*. 2017;12:e0181465.
- [59] Barc, J.; Briec, F.; Schmitt, S.; Kyndt, F.; Le Cunff, M.; Baron, E.; et al. Screening for copy number variation in genes associated with the long QT syndrome: clinical relevance. *J Am Coll Cardiol*. 2011;57:40-7.
- [60] Campuzano, O.; Sarquella-Brugada, G.; Mademont-Soler, I.; Allegue, C.; Cesar, S.; Ferrer-Costa, C.; et al. Identification of Genetic Alterations, as Causative Genetic Defects in Long QT Syndrome, Using Next Generation Sequencing Technology. *PLoS One*. 2014;9:e114894.
- [61] Mates, J.; Mademont-Soler, I.; Del Olmo, B.; Ferrer-Costa, C.; Coll, M.; Perez-Serra, A.; et al. Role of copy number variants in sudden cardiac death and related diseases: genetic analysis and translation into clinical practice. *Eur J Hum Genet*. 2018;26:1014-25.
- [62] Truty, R.; Paul, J.; Kennemer, M.; Lincoln, S.E.; Olivares, E.; Nussbaum, R.L.; et al. Prevalence and properties of intragenic copy-number variation in Mendelian disease genes. *Genet Med*. 2019;21:114-23.
- [63] Wijeyeratne, Y.D.; Tanck, M.W.; Mizusawa, Y.; Batchvarov, V.; Barc, J.; Crotti, L.; et al. *SCN5A* Mutation Type and a Genetic Risk Score Associate Variably With Brugada Syndrome Phenotype in *SCN5A* Families. *Circ Genom Precis Med*. 2020;13:e002911.
- [64] Cerrone, M.; Remme, C.A.; Tadros, R.; Bezzina, C.R.; Delmar, M. Beyond the One Gene-One Disease Paradigm: Complex Genetics and Pleiotropy in Inheritable Cardiac Disorders. *Circulation*. 2019;140:595-610.
- [65] Sieira, J.; Brugada, P. The definition of the Brugada syndrome. *Eur Heart J*. 2017;38:3029-34.
- [66] Walsh, R.; Tadros, R.; Bezzina, C.R. When genetic burden reaches threshold. *Eur Heart J*. 2020;41:3849-55.
- [67] Pinsach-Abuin, M.L.; Del Olmo, B.; Perez-Agustin, A.; Mates, J.; Allegue, C.; Iglesias, A.; et al. Analysis of Brugada syndrome loci reveals that fine-mapping clustered GWAS hits enhances the annotation of disease-relevant variants. *Cell Rep Med*. 2021;2:100250.
- [68] Barc, J.T.R.; Glinge, C.; Chiang, D.Y.; Jouni, M.; Simonet, F.; et al. Genome-wide association meta-analysis identifies novel Brugada syndrome susceptibility loci and highlights a new mechanism of sodium channel regulation in disease susceptibility. *Nature Genetics*. 2021.



Chapter 7. Functional Phenotyping of iPSC-CMs Obtained From Genetically Unresolved BrS Family Members in Search for Pathophysiological Mechanisms

Aleksandra Nijak¹, Eline Simons¹, Bert Vandendriessche¹, Dieter Van de Sande², Erik Fransen³, Ewa Sieliwończyk², Peter Ponsaerts⁴, Dirk Snyders², Alain J Labro^{2,5}, Emeline Van Craenenbroeck⁶, Johan Saenen⁶, Dorien Schepers^{1,2}, Lut Van Laer¹, Bart L. Loeys^{1,7}, Maaïke Alaerts¹

¹Center of Medical Genetics, Faculty of Medicine and Health Sciences, University of Antwerp & Antwerp University Hospital, Antwerp, Belgium

²Laboratory of Molecular Biophysics, Cellular and Network Excitability, Department of Biomedical Sciences, University of Antwerp, Antwerp, Belgium

³StatUa Center of Statistics, University of Antwerp, Antwerp, Belgium

⁴Laboratory of Experimental Hematology, Vaccine & Infectious Disease Institute, Department of Biomedical Sciences, University of Antwerp, Antwerp, Belgium

⁵Department of Basic and Applied Medical Sciences, Faculty of Medicine and Health Sciences, Ghent University, Ghent, Belgium

⁶Department of Cardiology, Faculty of Medicine and Health Sciences, University of Antwerp and Antwerp University Hospital, Antwerp, Belgium

⁷Department of Human Genetics, Radboud University Medical Centre, Nijmegen, The Netherlands

7.1 Abstract

The main characteristic of Brugada syndrome (BrS) is its variable phenotype severity and connection with loss-of-function mutations in the *SCN5A* gene, encoding $\text{Na}_v1.5$ protein, responsible for generation of sodium current (I_{Na}). However, mutations in *SCN5A* gene are diagnosed in about 25% of BrS cases, leaving the majority of patients genetically undiagnosed. iPSC-CM modeling of BrS has been successfully used to investigate disease phenotype at the cellular level.

In this report, we continue pursuing the correlation between the genetic and functional phenotype in a well characterized BrS family, where no known primary electrical disorder genes have been found to carry a pathogenic mutation. In previous chapter we performed genetic screening of this family using combined approach with whole genome sequencing and linkage analysis, which did not yield a single strong potential candidate variant, shared by the three sequenced affected individuals. Here we performed molecular and electrophysiological characterization of the phenotype in iPSC-CMs obtained from two affected and one unaffected family members, in comparison to iPSC-CMs of an unrelated healthy control as well as unrelated positive control *SCN5A* Belgian founder mutation carrier, to search for functional indications of the cardiac protein(s) that might be affected in this family.

One patient showed significantly reduced sodium current density, a positive shift in voltage dependence of sodium channel activation and reduced APA and dV/dT_{max} , consistent with previously reported sodium loss-of-function BrS phenotypes. The other patient showed changes in calcium transient duration and rise time, while in both patients arrhythmia-like events were observed in calcium recordings, suggesting abnormalities in calcium handling. The obtained results suggest different underlying disease mechanisms within one family, underscoring the complex nature of Brugada syndrome.

7.2 Introduction

Although to date over 20 genes have been associated with Brugada syndrome (BrS), only variants identified in the *SCN5A* gene, encoding the α subunit of the cardiac sodium channel $\text{Na}_v1.5$ [1], have been proven to demonstrate definitive evidence as a cause for this cardiac arrhythmia [2, 3]. Nevertheless, they explain only up to 30% of the known cases, leaving about 70% of patients with unknown genetic cause [4]. BrS is known to display reduced penetrance and variable expressivity, characterized by a wide range of phenotype severity from a life-time asymptomatic status to syncopes and SCD at a young age [5], which has an impact on patient risk stratification and management. Although initially thought to be a Mendelian disorder, currently BrS is recognized as a more complex disease, with the involvement of multiple common and rare genetic variants collectively contributing to its development [6-10]. Current application of next generation sequencing methods (e.g. gene panels, whole exome/genome sequencing) in (familial) patients will continue to identify variants potentially involved in BrS, although most of these remain “variants of uncertain significance” (VUS) and without functional studies, translation of potential genotype–phenotype correlation into clinical practice remains difficult.

Functional modeling of cardiac arrhythmias requires the use of a tissue specific material. As collection of a heart biopsy is extremely rare due to the high risk of consequences, the discovery of induced pluripotent stem cell (iPSC) reprogramming [11], and their subsequent differentiation to functional iPSC-derived cardiomyocytes (iPSC-CMs) provides a promising alternative to the field. It was previously shown that the major advantage of the iPSC-CMs over the conventional *in vitro* modeling approaches is their recapitulation of the whole genetic background of the donor, in addition to the expression of the whole repertoire of functional cardiac ion channels and accessory proteins, which undergo the natural tissue specific post-translational modifications [12]. Several reports, concerning iPSC-CMs modeling of BrS have been reported and their findings were discussed in detail in our recent review [13]. The general message there was that iPSC-CMs obtained from BrS donors with known genetic cause are suitable to investigate the electrophysiological phenotype of the disease, as they recapitulate patient phenotype. However, to date no success has been booked in reported models for phenotype-positive genotype-negative BrS donors [14, 15]. In these instances, when the genetic screening is not successful, comprehensive functional analysis of the electrophysiological properties of the obtained iPSC-CMs from the BrS patients may indicate which of the underlying ionic currents are impaired. In particular, detailed analysis of the action potential (AP) morphology can give insights on which current function is compromised and this, together with additional molecular screening (using techniques of transcriptomics and/or proteomics) can lead to a successful identification of the genetic players in the observed phenotype.

In the previous chapter (**Chapter 6**) we presented results from our combined genetic screening approach with linkage analysis and WGS in search for the genetic variants underlying BrS in three genetically unresolved Brugada syndrome families. For the family for which we obtained the highest LOD scores (BrS family 2; explained in detail in **Chapter 6**), we decided to generate iPSC-CM models for functional characterization. We collected peripheral blood mononucleated cells (PBMCs) from two affected relatives presenting with ajmaline induced BrS type-1 ECG pattern (III:2 (BrS1); II:8 (BrS2)) and one unaffected family member (II:7 Famctrl) (**Figure 7-1**) for iPSC reprogramming. In addition, already available iPSCs of an unrelated control donor (Ctrl) and one Belgian *SCN5A* founder mutation carrier (BrSfounder, presenting with ajmaline induced BrS type-1 ECG) [16] were used as controls. The iPSC clones were subsequently differentiated into iPSC-CMs and their molecular and structural phenotype, as well as

electrophysiological (EP) characteristics of the sodium current (I_{Na}), action potential (AP) and calcium transient (CT) were studied and compared.

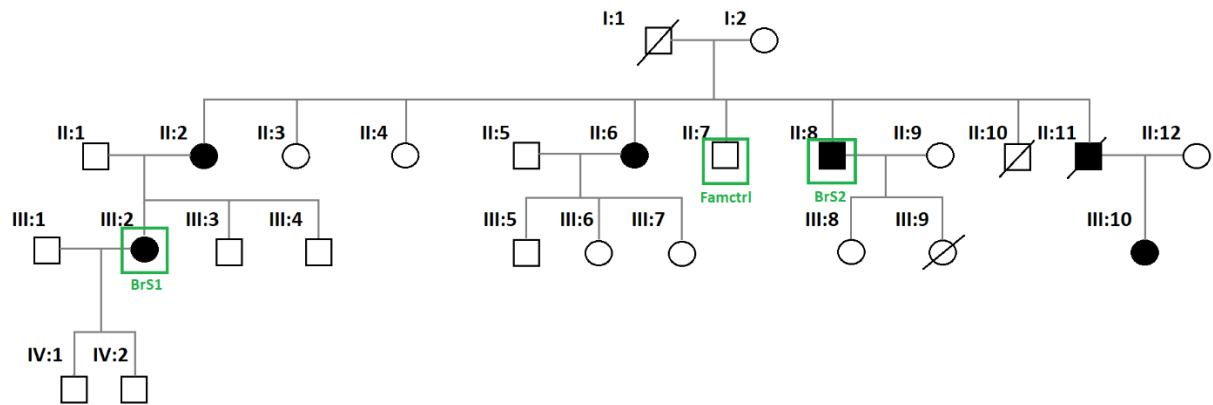


Figure 7-1 Pedigree of BrS family 2 selected for functional phenotyping. Indicated in green are the individuals from which PBMCs were obtained and used for reprogramming and differentiation for functional phenotyping.

7.3 Materials and methods

7.3.1 PBMC, iPSC and iPSC-CM derivation and culture

PBMCs were obtained from whole blood samples as described in materials and methods in **Chapter 6**. We obtained three blood samples from BrS family 2 members: two affected (III:2 (BrS1) and II:8 (BrS2)) and one unaffected individual (II:7 (Famctrl)) and performed reprogramming of the PBMCs and validation of single iPSC clone from each donor according to protocols reported in **Chapter 4**. Differentiation to iPSC-CMs was performed using the protocol described in the materials and methods section of **Chapter 6**. Briefly, on day 0 of differentiation the iPSCs were supplemented with RPMI1640 media containing 6 μ M CHIR99021 and 1% B27 supplement without insulin (differentiation medium DM1) for 48h. On day 2 of differentiation cells were incubated with RPMI1640 media containing 5 μ M Wnt-C59 and 1% B27 supplement without insulin (DM2) for 48h. On day 4 of differentiation cells were supplemented with RPMI1640 media with 1% B27 supplement without insulin (DM3) and media was changed every other day, cells were kept in an incubator at 37°C, 80% humidity, 5% CO₂ and 5% O₂. From the day of first visible contractions, cells were supplemented with DM3 media with addition of triiodothyronine (T3) (20 ng/mL) (DM4) and cells were transferred to an incubator with normoxic conditions the day after the start of T3 treatment (37°C, 80% humidity, 5% CO₂). A metabolic enrichment using RPMI1640 media without glucose (Life Technologies) supplemented with 5 mM lactate (Sigma Aldrich), human serum albumin (500 μ g/mL; Life Technologies) and L-ascorbic-acid (5 mM; Sigma Aldrich) (DM5) was used from day 11 to day 16 of differentiation to homogenize the cell culture for further experiments. Cells were supplemented with DM4 refreshed every other day, until the end of functional experiments (day 35-40). Results from iPSC-CMs of the family members were compared to iPSC-CMs of an unrelated healthy donor (Ctrl) as well as unrelated Belgian SCN5A BrS founder mutation carrier (BrSfounder) as a positive control. We performed simultaneous differentiations of those five cell lines, with a maximum five days difference in performed patch-clamping experiments. Each cell line was differentiated twice in 18 replicates (18 wells on 6-well culture dishes), to compare batch-to-batch effect of the observed phenotype.

7.3.2 Molecular characterization of obtained cell types

Characterization of the obtained iPSCs and iPSC-CMs was performed using methods previously described in **Chapter 5**. Immunocytochemistry (ICC) staining and qPCR analysis was performed to validate the expression of selected pluripotency as well as cardiac markers on protein and RNA levels. Genomic

integrity of iPSC lines was performed using HumanCytoSNP-12 array (Illumina). **Table 7-1** reports large deletions (>100 kb) identified in each of the tested iPSC lines.

Table 7-1 Genomic integrity test results for iPSC clones used for differentiation to iPSC-CMs. Deletions >100kb are reported in the table.

Cell line	Maximal region	Cytoband	Genes located within the region
BrS1	Chr1:873,558-1,404,809	1p36.33	ACAP3, CPTP, LOC148413, NOC2L, TAS1R3
	Chr1:2,418,625-2,733,587	1p36.32	FAM213B
	Chr1:3,109,151-3,243,017	1p36.32	PRDM16
	Chr1:3,359,687-3,592,436	1p36.32	ARHGEF16
	Chr1:86,488,232-86,684,713	1p22.3	COL24A1
	Chr1:194,348,173-194,650,899	1q31.3	-
	Chr3:90,111,765-93,632,198	3p11.1	PROS1
	Chr3:94,523,335-94,772,205	3q11.2	LINC00879
	Chr4:989,548-1,495,105	4p16.3	CTBP1, SPON2, CRIPAK
	Chr4:34,323,177-34,492,968	4p15.1	LINC02484
	Chr4:43,305,565-43,648,726	4p13	LINC02383
	Chr4:66,244,369-66,562,536	4q13.1	EPHA5, EPHA5-AS1
	Chr5:27,686,570-27,835,105	5p14.1	-
	Chr7:155,403,802-155,569,983	7q36.3	LOC100506302
	Chr8:83,629,042-83,734,562	8q21.13	-
	Chr8:144,695,499-144,905,947	8q24.3	BREA2, PUF60, TSTA3
	Chr8:145,081,248-145,504,343	8q24.3	CYC1, SHARPIN, BOP1, HGH1, MIR7112, SCX
	Chr9:139,958,645-140,158,650	9q34.3	ANAPC2, NDOR1, TMEM203
	Chr10:59,272,405-59,443,530	10q21.1	-
	Chr11:783,512-900,809	11p15.5	CD151, SNORA52, CEND1, LOC171391
	Chr11:1,054,625-1,250,488	11p15.5	LOC101927503, MUC5AC, MUC5B
	Chr11:2,070,570-2,201,163	11p15.5	IGF2, MIR4686, TH
	Chr11:90,933,499-91,034,922	11q14.3	-
	Chr12:132,703,218-133,176,925	12q24.33	FBRSL1, GALNT9, LOC100130238, LOC101928416
	Chr14:22,465,075-22,947,903	14q11.2	LOC105370401
	Chr14:105,231,879-105,407,208	14q32.33	AKT1, AHNAK2
	Chr17:22,026,080-22,142,172	17p11.2	-
	Chr17:79,670,386-80,031,680	17q25.3	ALYREF, LRRC45, PPP1R27, MRPL12
	Chr19:1,245,700-1,503,964	19p13.3	APC2, MUM1
	Chr22:30,438,447-30,590,026	22q12.2	HORMAD2, HORMAD2-AS1
ChrX:21,104,112-21,582,296	Xp22.12	CNKSR2	
ChrX:28,142,362-28,331,866	Xp21.3	-	
ChrX:80,372,083-80,490,620	Xq21.1	HMG5, SH3BGR1	
ChrX:106,739,860-107,073,048	Xq22.3	FRMPD3, MID2	
ChrX:107,530,520-107,642,857	Xq22.3	COL4A6	
BrS2	Chr14:20,213,937-20,305,431	14q11.2	OR4M1
	Chr17:44,163,925-44,369,335	17q21.31	KANSL1, ARL17B
	Chr19:21,256,249-21,399,204	19p12	ZNF431
	ChrX:317,940-1,210,687	Xp22.33	PP2R3B
	ChrX:1,257,358-1,451,162	Xp22.33	CRLF2
	ChrX:1,487,144-2,704,609	Xp22.33	AKAP17A, LINC00106
Famctrl	Chr2:242,917,734-243,029,573	2q37.3	LINC01237
	ChrX:161,341-287,573	Xp22.33	GTPBP6
BrSfounder	Chr5:105,465,733-105,866,862	5q21.3	-
	Chr7:56,727,843-57,208,666	7p11.2	LOC100130849, LOC401357, MIR4283-1, MIR4283-2, ZNF479
	Chr9:2,379,389-2,631,092	9p24.2	VLDLR
	Chr11:90,796,002-90,939,411	11q14.3	-
	Chr17:44,155,732-44,580,136	17q21.31	ARL17A, ARL17B, LRRC37A, NSFP1
Ctrl	ChrX:161,341-2,704,609	Xp22.33	AKAP17A, GTPBP6, PPP2R3B
	Chr2:242,517,966-243,029,573	2q37.3	LINC01237
	ChrX:954,768-1,322,594	Xp22.33	CRLF2

RNA samples and fixing of the cells for ICC staining for cardiomyocyte markers was performed on D30-35 according to previously reported protocols (**Chapter 4**). Quantitative RT-PCR of cardiac markers was performed using previously reported qPCR primers for the following genes: *ANK2*, *ANK3*, *CACNA1C*, *GJA1*, *HCN4*, *KCND3*, *KCNH2*, *KCNJ2*, *KCNJ8*, *KCNQ1*, *MLC2a*, *MLC2v*, *MYH6*, *MYH7*, *RYR2*, *SCN5A*, *TNNI3* and *TNNT2*. Expression on protein level was performed using primary antibodies for: cardiac α -actinin (cACT), cardiac troponin I (cTNNI), connexin 43 (Cnx43), myosin light chain 2 (MYL2), Nkx2.5 and Na_v1.5 (SCN5A) according to the protocols reported in **Chapter 4**. Fold changes in relative gene expression were determined using the comparative Ct method ($\Delta\Delta C_t$) with normalization to three reference genes: *GAPDH*, *ECHS1* and *RPL13A* and relative to the expression in iPSCs. Expression pattern of healthy donor left ventricle was used as a reference. Results were analysed as previously described in **Chapter 4**. Immunocytochemistry staining, fluorescent images acquisition and analysis, as well as acquisition and analysis of light-microscopy images was performed according to the protocols described in **Chapter 4**.

7.3.3 Imaging data analysis

The light microscopy images of contracting iPSC-CMs were acquired using cellSens software (Olympus LS) and converted to TIFF images for analysis using Fiji image analysis freeware [15], with manual indication of the areas of contracting cell monolayer. The calculated contracting area sizes were measured in mm² and divided by the area of the whole image of the culture surface (approximately 96 mm²). Differentiation efficiency was calculated based on an immunofluorescence staining for cACT, cTNNI, MYL2 and Na_v1.5. Fluorescence images were analysed using CellBlocks, a Fiji script for cell-based analysis [16] as described in **Chapter 4**.

7.3.4 Patch-clamping and calcium imaging

Electrophysiological experiments were performed 35-42 days after the start of differentiation. Perforated-patch action potential (AP) recordings and intracellular Ca²⁺ transients (CT) were carried out at 36±1°C on non-dissociated cells grown on glass cover slips, while ruptured-patch recordings were performed at room temperature (21±1°C), according to the protocol reported previously in **Chapter 4**. Pipettes were filled with an intracellular solution containing (in mM): 4 NaCl, 106 KCl, 5 K₂ATP, 2 MgCl₂, 5 K₄BAPTA and 10 HEPES adjusted to pH 7.2 with KOH and addition of 0.72 ng/mL amphotericin B (A9528, Sigma Aldrich). The cells were continuously superfused at 1mL/min rate with an extracellular solution (ECS) containing (in mM): 150 NaCl, 5.4 KCl, 1.8 CaCl₂, 1 MgCl₂, 15 HEPES, 15 glucose, 1 Na-pyruvate adjusted to pH 7.4 with NaOH. Junction potentials were compensated before sealing of the cell when the patch pipette made contact with the ECS.

AP data were analysed using in-house developed MATLAB script. For each cell recording, AP values are calculated as a mean of all subsequent recorded waveforms (5 to 15 per recording), and data are presented as a mean for each single cell of the 'n' cells analysed. The following parameters were analysed: AP amplitude (APA), resting membrane potential (RMP), upstroke velocity (dV/dT_{max}), APD30, APD50 and APD90. The beating frequency (BPM) was calculated from the time difference between two AP peaks and beat interval was presented as the mean ± SEM of the time difference between each subsequent AP waveform within single recording. APD was corrected to the beating rate using Fridericia formula: $cAPD = \frac{APD}{beat\ duration\ [ms]^{1/3}}$

CT data were analysed manually using pClamp10.6 software (Axon CNS Molecular Devices). For each cell recording, CT values are calculated as a mean of five subsequent recorded waveforms, and data are presented as mean ± SEM for each single cell of the 'n' cells analysed. The following parameters were analysed: calcium transient duration at 50% (CTD50) and 70% (CTD70) of depolarization, beating frequency (BPM), rise time and time constant of decay (RC).

AP recordings with RMP > -60 mV and BPM <20; and CT recordings with BPM <15 were excluded from the analysis, as the obtained phenotype could have been wrongly interpreted, due to very low beating rate, which could influence e.g. AP or calcium transient duration.

I_{Na} data were analysed using PClamp10.6 software. I_{Na} data are presented as a mean \pm SEM with 'n' as the number of cells analysed.

7.3.5 Statistical analysis

Comparison of the morphological as well as electrophysiological characteristics between the groups was performed with a two-way ANNOVA, while batch-to-batch differences were tested using Student's t-test (Systat Software Inc.). Comparison of the normalized Ct values between the groups was performed using a linear mixed model, with the normalized Ct value as dependent variable. The nonindependence between observations within the same cell line was accounted for using a random intercept for cell line, and a random slope for protocol. Pairwise comparisons between the protocols were carried out using a posthoc analysis with Tukey's correction for multiple hypothesis testing. Analyses were carried out in the software package R version 4.0.2, and the add on packages lme4 and multcomp. A P-value of ≤ 0.05 is considered statistically significant.

7.4 Results

7.4.1 Obtained iPSC-CMs show similar differentiation efficiency, transcript levels and protein organisation of the tested cardiac markers

We looked at the contracting area sizes within the differentiated replicates (18 wells per differentiation). We did not see significant differences in contracting area size or differentiation efficiency between two separate differentiation batches obtained from the tested cell lines (batch-to-batch differences; p-values >0.1 ; **Table 7-2**), thus we compared average values pooled from both differentiation batches for each tested characteristic between the lines (**Table 7-3**). Overall we could notice that iPSC-CMs generated from BrS1 showed the smallest contracting areas ($p=0.027$), while we did not see major differences in contracting areas for iPSC-CMs from BrS2 ($p=0.396$) in comparison to the controls. No significant differences in differentiation efficiency, as well as structural distribution of the analysed proteins was observed between the analysed cell lines and between differentiation batches ($p \geq 0.489$, $p \geq 0.195$, $p \geq 0.433$, $p \geq 0.417$ for the cardiac α -actinin (cACT), TNNI (cTNNI), MYL2, Nkx2.5 and $Na_v1.5$ between the tested lines, respectively) (**Figure 7-2**; **Table 7-3**). Also no difference in structural distribution of the analysed proteins was observed between the analysed cell lines (**Figure 7-2**).

Table 7-2 Calculated contracting areas and differentiation efficiencies. P values were calculated for using Student's t-test, a p value of ≤ 0.05 is considered statistically significant

Cell line	Batch	Contracting area [%]	P value	Differentiation efficiency (proportion of cells expressing marker) [%]							
				cACT	P value	cTNNI	P value	MYL2	P value	Na _v 1.5	P value
Ctrl	1	69±18	0.891	92±14	0.760	N/A	-	96	-	N/A	-
	2	64±30		85±17		93±4		N/A		92±7	
BrSfounder	1	63±0.5	0.472	N/A	-	67±44	0.616	N/A	-	84±10	0.353
	2	44±25		98±2		93±6		85±15		96±2	
Famctrl	1	81±14	0.108	93±6	0.581	90±8	0.368	91±4	0.181	N/A	-
	2	56±0.4		97±2		71±16		99±0.6		99±0.7	
BrS1	1	23±21	0.729	97±2	0.284	98±1	1.0	78±17	0.360	95±4	0.423
	2	15±9		99.9±0.1		98±2		98±0.8		99±0.4	
BrS2	1	65±21	0.554	94±6	0.581	97±0.6	0.673	98±2	0.554	100±0.7	0.557
	2	45±26		99±1		98±2		93±.7		93±10	

Table 7-3 Pooled average contracting areas and differentiation efficiencies for each of the tested iPSC-CM cell lines.

Cell line	Average contracting areas	Average differentiation efficiency (proportion of cells expressing the marker) [%]			
		cACT	cTNNI	MYL2	Na _v 1.5
Ctrl	67±24	89±16	93±4	96	92±7
BrSfounder	54±13	98±2	80±25	85±15	90±6
Famctrl	69±7	95±4	81±12	95±2.3	99±0.7
BrS1	19±15	99±1.1	98±1.5	88±8.9	97±2.2
BrS2	55±23	97±3.5	98±1.3	96±4.5	97±5.4

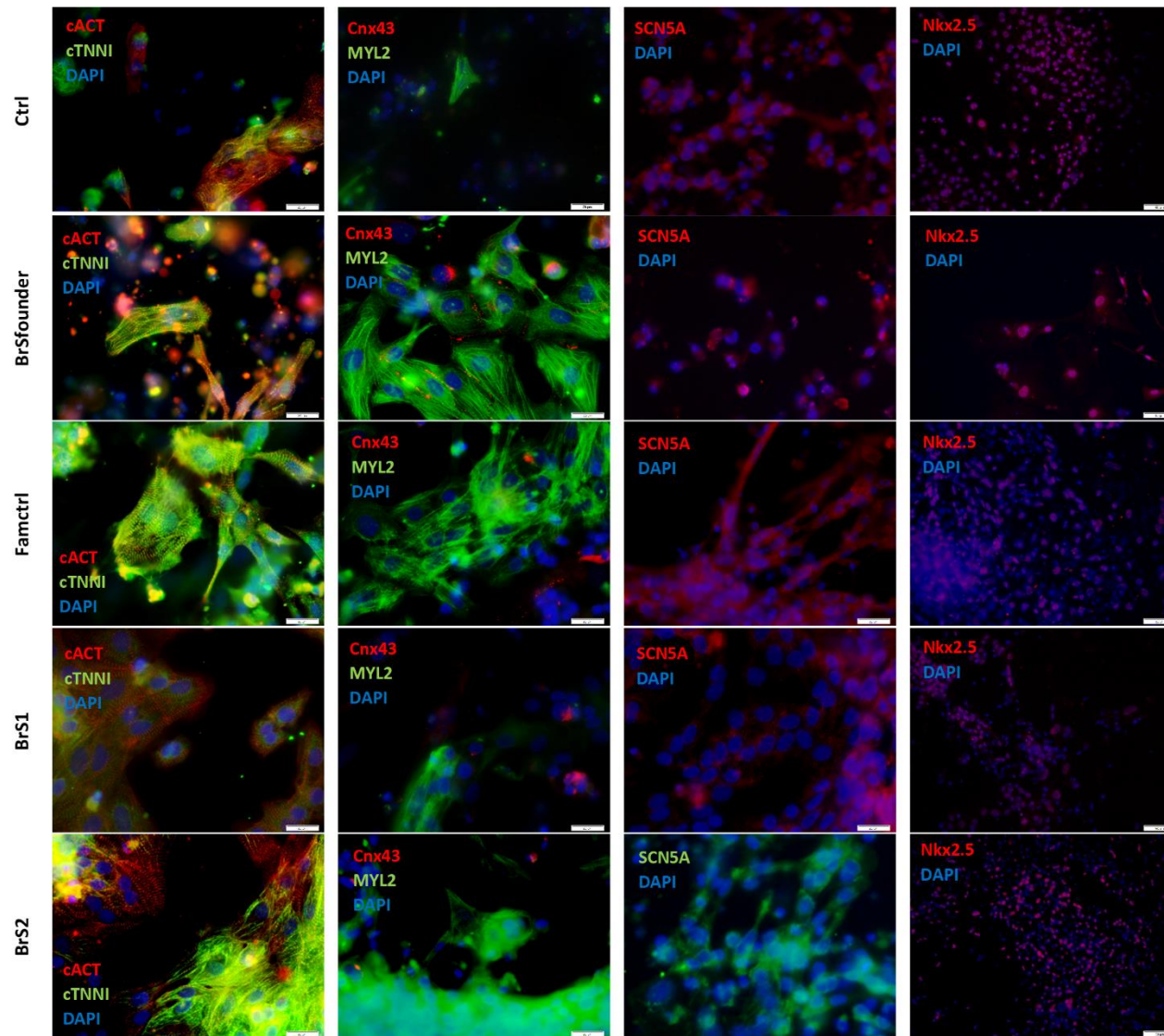


Figure 7-2 Immunofluorescent staining results, the images represent protein expression patterns of: ACT – cardiac α -actinin, TNNI – troponin I; Cnx43 – connexin 43; MYL2 – myosin light chain 2; SCN5A – $Na_v1.5$; Nkx2.5, with DAPI as a reference nuclei staining.

We analysed the transcript expression levels of the selected cardiac markers. The results showed expression of all of the tested cardiac markers in all generated iPSC-CMs (**Figure 7-3**). We looked at differences in transcript expression between patients and controls (calculated p values are summarized in **Table 7-4** and **7-5**; average $\Delta\Delta Ct$ values for each of the marker were calculated for each of the cell lines from the two performed differentiation batches, and batch-to-batch variability was addressed during the statistical analysis). For each tested marker (except of *SCN5A*) expression levels in the familial patients and control (BrS1, BrS2 and Famctrl) were comparable (all $p > 0.05$). Ctrl iPSC-CMs showed reduced *KCND3*, *MYH6* and *TNNI3* transcript levels in comparison to iPSC-CMs obtained from the tested family members (*KCND3* $p < 0.001$; *MYH6* $p \leq 0.001$; *TNNI3* $p \leq 0.002$). We observed reduced *SCN5A* transcript levels in Ctrl iPSC-CMs in comparison to the Famctrl ($p = 0.0164$), BrS2 and BrSfounder. We did not see differences in *SCN5A* expression in BrS2 iPSC-CMs, while transcript levels for this marker in BrS1 were statistically lower in comparison to Famctrl ($p < 0.001$). *SCN5A* transcript levels were statistically increased in BrS2 iPSC-CMs comparison to Ctrl ($p = 0.0016$). We observed increased expression of *GJA1* and *SCN5A* in BrSfounder iPSC-CMs in comparison to Ctrl ($p = 0.014$ and $p = 0.007$, respectively), while the difference in expression of those markers compared to Famctrl was not statistically significant ($p = 0.108$ and $p = 0.526$, for *GJA1* and *SCN5A* respectively).

Table 7-4 Calculated p values for the transcript expression analysis. To test for differences in normalized $\Delta\Delta Ct$ between the groups, a linear mixed models were fitted for each gene, accounting for the nonindependence of observations within the same cell line by entering cell line as a random intercept. Significance of the fixed effect of group is shown in the column "Overall p-values", testing the null hypothesis that the normalized $\Delta\Delta Ct$ is (on average) the same across all groups.

Tested cardiac marker	Overall p value
<i>ANK2</i>	0.892
<i>ANK3</i>	0.801
<i>CACNA1C</i>	0.251
<i>HCN4</i>	0.465
<i>KCNH2</i>	0.068
<i>KCNJ2</i>	0.276
<i>KCNJ8</i>	0.5
<i>KCNQ1</i>	0.416
<i>MLC2a</i>	0.79
<i>MLC2v</i>	0.872
<i>MYH7</i>	0.1
<i>RYR2</i>	0.102
<i>TNNT2</i>	0.102
<i>GJA1</i>	0.0007*
<i>KCND3</i>	0.007*
<i>MYH6</i>	0.008*
<i>SCN5A</i>	0.008*
<i>TNNI3</i>	0.0009*

Table 7-5 Comparison of the transcript expression levels between the groups for the markers for which the fixed effect of group was significant, a posthoc analysis with Tukey correction was carried out for pairwise comparison of $\Delta\Delta Ct$ values.

Gene expression between patients and controls	Tested cardiac marker				
	<i>GJA1</i>	<i>KCND3</i>	<i>MYH6</i>	<i>SCN5A</i>	<i>TNNI3</i>
Ctrl vs. Famctrl	0.865	<0.001*	<0.001*	0.016*	0.002*
Ctrl vs. BrS1	0.109	<0.001*	0.001*	0.077	<0.001*
Ctrl vs. BrS2	0.109	<0.001*	0.001*	0.002*	<0.001*
Ctrl vs. BrSfounder	0.014*	<0.001*	0.161	0.007*	0.979
Famctrl vs. BrS1	0.524	0.512	0.608	<0.001*	0.1
Famctrl vs. BrS2	0.524	0.512	0.608	0.721	0.1
Famctrl vs. BrSfounder	0.108	0.473	0.134	0.526	<0.001*

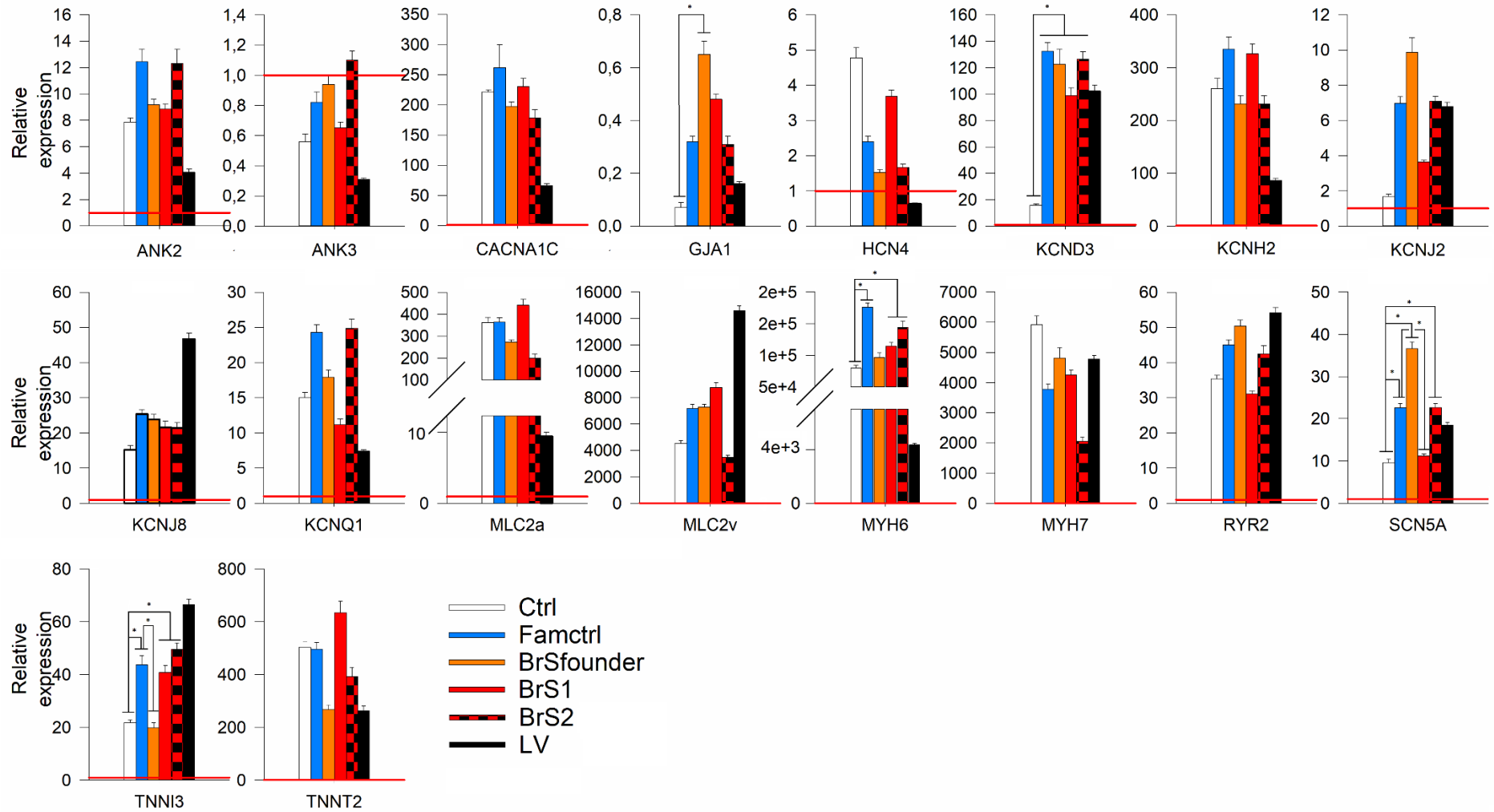


Figure 7-3 Relative expression of the tested cardiac markers. The graphs represent average relative expression of the tested cardiac markers in iPSC-CMs from two differentiation batches of: Ctrl (in white), BrSfounder (in orange), Famctrl (in blue), BrS1 (in red), BrS2 (in checked red), in comparison to iPSCs. Relative expression from healthy human heart left ventricle (LV) tissue (in black) is plotted as a reference. The red horizontal line on each plot indicates the relative expression level in iPSCs (relative expression=1).

7.4.2 Sodium current analysis revealed differences in channel function between the tested affected family members

We tested differences between the generated batches of the tested cell lines (**Table 7-6**). We saw that for both negative controls: Ctrl and Famctrl, the only parameter that differed significantly between the obtained batches was the slope factor of inactivation curve, while other tested parameters did not differ significantly. In case of patient lines, all of the tested I_{Na} parameters differed significantly between the batches. Thus, for the comparison with the patient lines we pooled data from both generated batches for each control line and compared the obtained average values with each of the tested batches from the tested patient lines separately.

We did not see significant differences in peak I_{Na} density of BrS2 iPSC-CMs in comparison with Famctrl (**Table 7-6; Figure 7-4b,e**), while for BrS1 iPSC-CMs we observed a drastic >85% reduction in peak I_{Na} in both differentiation batches in comparison to Famctrl ($p=0.011$ for batch I and $p=0.01$ for batch II of BrS1) (-29 ± 5 or -8 ± 2 pA/pF for BrS1; -243 ± 54 pA/pF for Famctrl at -10 mV) (**Figure 7-4a,b; Table 7-6, 7-7**). We did not see differences in peak I_{Na} density in BrS2 iPSC-CMs, while BrS1 showed significant peak I_{Na} reduction in both of the performed differentiation batches in comparison to Ctrl (-343 ± 90 pA/pF for Ctrl; 92% reduction in batch I and 98% reduction in batch II; p values are listed in **Table 7-6**). The measured peak density of BrS1 iPSC-CMs was even lower than that of our positive control BrSfounder in both tested differentiation batches. There were no significant I_{Na} differences between BrSfounder and BrS2 iPSC-CMs. However, no peak I_{Na} reduction was noted for BrSfounder iPSC-CMs in comparison to both Ctrl and Famctrl (**Table 7-6, 7-7**).

We did not observe significant differences in kinetics of channel activation for BrS1 and BrS2 in comparison to Famctrl in both differentiation batches (**Figure 7-4c,f; Table 7-6**). We observed a significant 33 or 31 mV positive shift in $V_{1/2}$ of activation for BrS1, while BrS2 showed a 2 mV negative shift only in one of the differentiation batches in comparison to Famctrl (**Table 7-6, 7-7**). There were no significant differences in activation kinetics of BrS1 and BrS2 or $V_{1/2}$ of activation of BrS2 in comparison to Ctrl (**Figure 7-4d,g**). Looking at $V_{1/2}$ of activation of BrS1, there was a 31 and 29 mV positive shift in batch I and batch II, respectively in comparison to Ctrl iPSC-CMs. Looking at the channel activation in BrSfounder, we observed accelerated activation kinetics in comparison to Ctrl in batch I, while BrSfounder obtained in batch II showed a 14 or 16 mV positive shift in $V_{1/2}$ of activation in comparison to both Ctrl and Famctrl, respectively.

We did not observe differences in inactivation kinetics and voltage dependence, as well as recovery from inactivation in tested BrS lines (BrS1, BrS2 and BrSfounder) in comparison to Famctrl as well as Ctrl iPSC-CMs (**Figure 7-5c-d,f-g; Table 7-6, 7-7**).

Table 7-6 Sodium current properties measured in the obtained iPSC-CMs. P values were calculated using Student's t-test. A p value ≤ 0.05 is considered statistically significant. Recovery from inactivation recordings were collected from a single batch of differentiation from each of the tested iPSC lines.

CELL LINE	PEAK I _{NA}		P VALUE	ACTIVATION					INACTIVATION					RECOVERY					
	pA/pF	n		τ [ms]	P value	V _{1/2} [mV]	P value	κ	P value	n	τ [ms]	P value	V _{1/2} [mV]	P value	κ	P value	n	τ [ms]	n
Ctrl	-358±	28	0.189	0.35±	0.232	-34±	1.0	4.9±	0.745	11	1.9±	0.166	-88±	0.612	7.13±	0.002*	22	53±	18
Batch 1	77			0.1		0.5		0.9		11	0.1		3		0.67		16	9.4	
Ctrl	-331±	13	0.035*	0.48±	0.041*	-34±	<0.001*	5.6±	0.251	10	1.7±	0.587	-86±	<0.001*	10.05±	0.216	10	77±	14
Batch 2	87			0.08		0.5		1.9		10	0.1		2.5		0.56		9	13.9	
BrSfounder	-262±	9	0.077	0.17±	0.916	-35±	1.0	4.6±	0.305	5	1.5±	0.130	-95±	0.161	9.81±	<0.001*	16	15±	14
Batch 1	47			0.04		0.5		0.6		5	0.3		2.3		0.4		17	2.1	
BrSfounder	-110±	13	0.001*	0.35±	0.807	-20±	0.013*	3.2	0.025*	12	1.7±	0.584	-70±	0.224	8.64±	0.004*	10	15±	6
Batch 2	48			0.07		0.5		0.9		12	0.2		1.3		0.80		3	7.2	
Famctrl	-319±	15	0.047*	0.47±	0.614	-36±	<0.001*	4.4±	0.004*	13	1.3±	0.042*	-87±	0.453	11.07±	0.367	23	29±	32
Batch 1	74			0.31		0.5		0.5		13	0.1		2.4		0.53		17	3.7	
Famctrl	-167±	16	0.001*	0.52±	0.807	-36±	0.013*	3.4±	0.025*	10	1.6±	0.130	-92±	0.161	7.38±	<0.001*	17	2.1	14
Batch 2	34			0.35		0.5		0.8		10	0.2		1.7		0.38		17	2.1	
BrS1	-29±	14	0.001*	0.20±	0.807	-3±	0.013*	1.6±	0.025*	7	2.5±	0.584	-69±	0.224	5.24±	0.004*	10	15±	6
Batch 1	5			0.18		0.5		0.4		7	0.6		1.7		0.55		10	7.2	
BrS1	-8±	12	0.047*	0.14±	0.614	-5±	<0.001*	0.4±	0.004*	10	1.8±	0.042*	-72±	0.453	11.42±	0.367	3	7.2	6
Batch 2	2			0.16		0.5		0.2		10	1		1.5		0.86		3	7.2	
BrS2	-375±	16	0.047*	0.33±	0.614	-34±	<0.001*	2.9±	0.004*	16	1.5±	0.042*	-95±	0.453	11.1±	0.367	23	29±	32
Batch 1	47			0.06		0.5		0.7		16	0.1		9.1		0.53		14	3.7	
BrS2	-211±	9	0.047*	0.39±	0.614	-37±	<0.001*	6.1±	0.004*	10	1.8±	0.042*	-88±	0.453	7.7±	0.367	14	3.7	32
Batch 2	61			0.10		0.5		0.7		10	0.1		1.5		0.35		14	3.7	

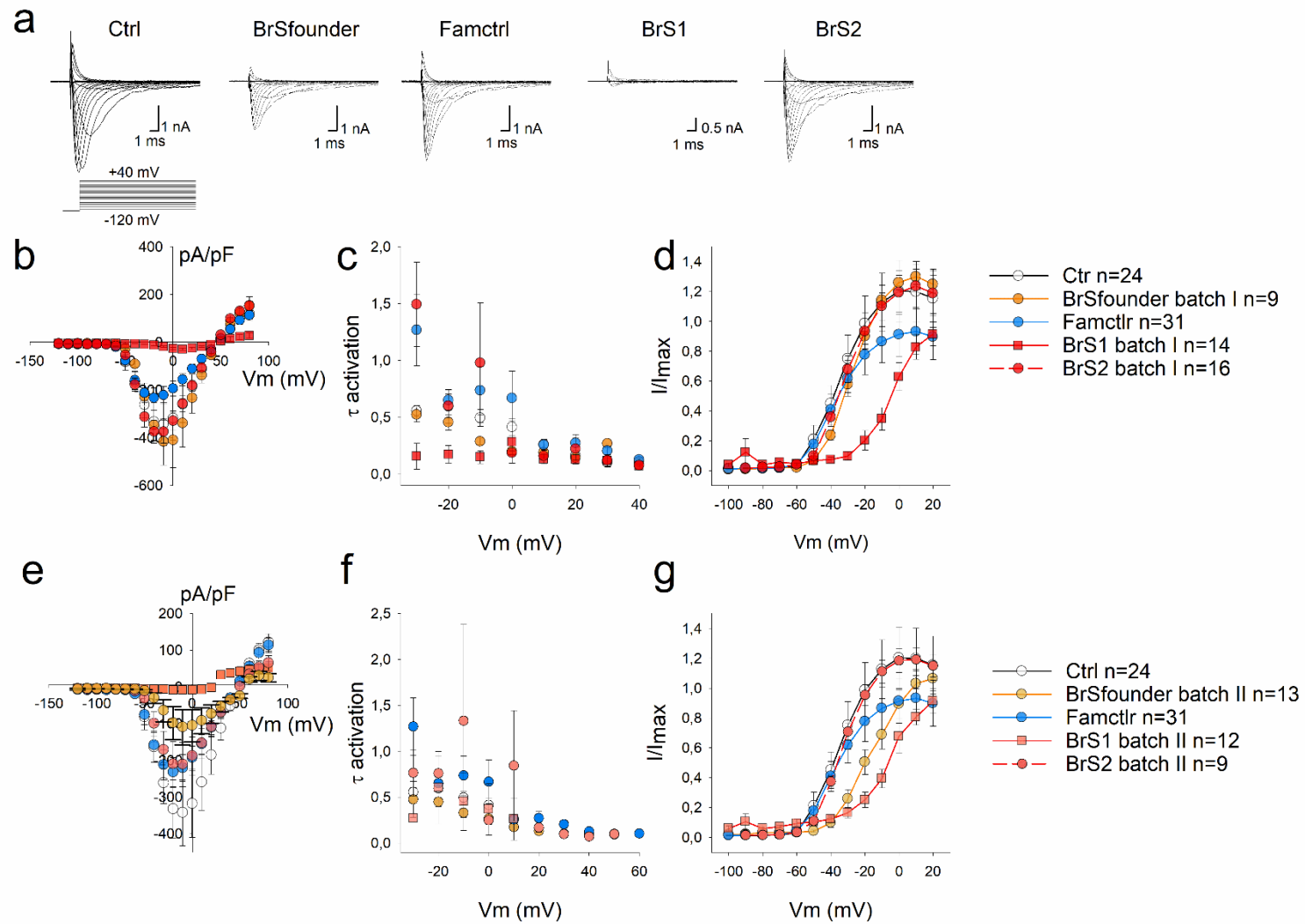


Figure 7-4 Sodium current density and activation properties. (a) The graph represents from left to right representative traces of I_{Na} for Ctrl, BrSfounder, Famctrl, BrS1 and BrS2. The used protocol is represented below the traces. Middle panel represents current-voltage relation (I - V) plot (b), activation kinetics (c) and normalized activation (G - V) curve (d) for batch I of the tested patient iPSC-CMs, with white dots for Ctrl, orange dots for BrSfounder, blue dots for Famctrl, red squares for BrS1 and red dots for BrS2. Data are represented as average \pm SEM. Lower panel represents current-voltage relation (I - V) plot (e), activation kinetics (f) and normalized activation (G - V) curve (g), for batch II of the tested patient iPSC-CMs, with white dots for Ctrl, light orange dots for BrSfounder, blue dots for Famctrl, light red squares for BrS1 and light red dots for BrS2.

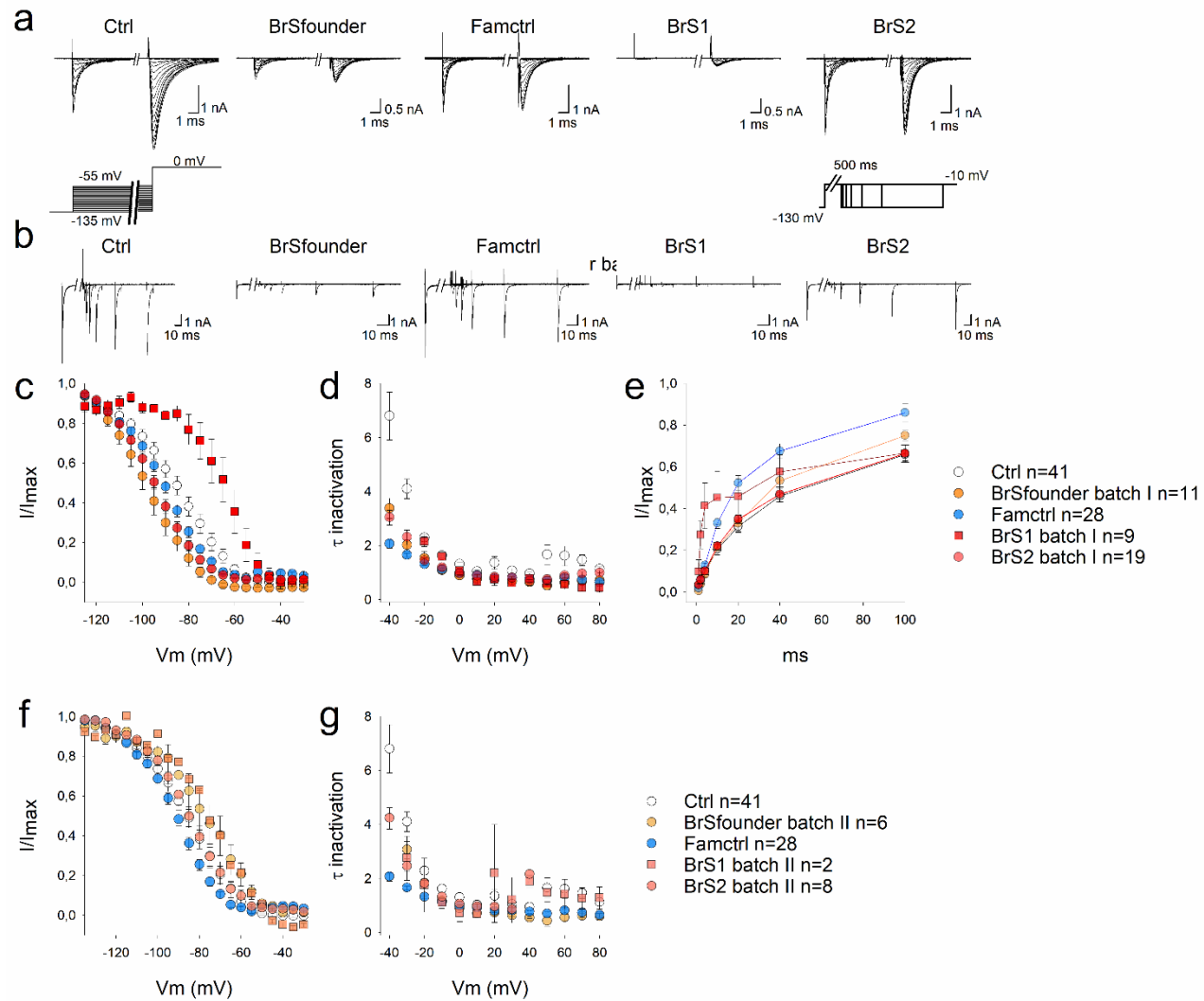


Figure 7-5 Sodium channel inactivation properties. From left to right displayed are representative traces of I_{Na} inactivation (a) and recovery (b) for Ctrl, BrSfounder, Famctrl, BrS1 and BrS2. The used protocol is represented below the traces. Middle panel represents voltage dependence of inactivation curve (c), inactivation kinetics (d) and recovery from inactivation (e) for the first batch of differentiation of patient iPSC-CMs, with white dots for Ctrl, orange dots for BrSfounder, blue dots for Famctrl, red squares for BrS1 and red dots for BrS2. Data are represented as average \pm SEM. Bottom panel represents voltage dependence of inactivation curve (f) and inactivation kinetics (g) for the second batch of differentiation of the patient iPSC-CMs, with white dots for Ctrl, light orange dots for BrSfounder, blue dots for Famctrl, light red squares for BrS1 and light red dots for BrS2.

Table 7-7 Calculated *p* values for the comparison of *I_{Na}* parameters between the tested cell lines

Tested <i>I_{Na}</i> characteristic	Ctrl versus							Famctrl versus						
	Famctrl	BrSfounder batch I	BrSfounder batch II	BrS1 batch I	BrS1 batch II	BrS2 batch I	BrS2 batch II	BrSfounder batch I	BrSfounder batch II	BrS1 batch I	BrS1 batch II	BrS2 batch I	BrS2 batch II	
Peak <i>I_{Na}</i> density	0.863	0.966	0.158	0.007*	0.006*	0.993	0.854	0.833	0.789	0.011*	0.01*	0.756	0.979	
τ activation	0.817	0.02*	0.573	0.313	0.155	0.438	0.854	0.339	0.671	0.493	0.341	0.627	0.763	
<i>V</i> _{1/2} of activation	0.008*	0.526	<0.001*	<0.001*	<0.001*	1.0	0.584	0.666	<0.001*	<0.001*	<0.001*	0.021*	0.584	
τ inactivation	0.665	0.994	1	0.557	1	0.93	1	1	1	0.21	1	1	0.987	
<i>V</i> _{1/2} of inactivation	0.999	0.982	0.465	0.319	0.97	0.928	1	0.994	0.291	0.177	0.938	0.984	1	
Recovery from inactivation	0.150	0.182		0.205		0.798		0.751		0.892		0.195		

7.4.3 iPSC-CMs of one of the affected donors reveal dV/dT_{max} and APA reduction, while ajmaline testing in the obtained iPSC-CMs yielded inconclusive results

Next, we looked at action potential properties. We did not see significant differences in AP parameters between the generated batches for iPSC-CMs of Ctrl and Famctr. For BrS1 we observed difference in APD, dV/dT_{max} , BPM and beat interval between the obtained batches, and for BrS2 we observed significant differences in BPM and beat interval (**Table 7-8**). Thus, we pooled the data of both batches from Ctrl and Famctr and compared those average values for tested parameters with each batch of the tested patient iPSC-CMs separately (including a single differentiation batch of BrSfounder).

We did not see significant differences in RMP ($p > 0.1$) between the tested cell lines (**Figure 7-6a**). We observed reduced APA in BrS1 iPSC-CMs in comparison to Famctr ($p < 0.001$ and $p = 0.003$ in batch I and batch II, respectively) and Ctrl ($p = 0.004$ or $p = 0.011$ in batch I and batch II, respectively), BrSfounder ($p < 0.008$ in both batches) and BrS2 ($p < 0.003$ in both batches) (**Figure 7-6a**; p values for the comparison between the groups are listed in **Table 7-9**). There was a significant reduction in dV/dT_{max} in BrS1 compared to both tested negative controls ($p = 0.007$ and 0.005 for batch I and batch II in comparison to Famctr; $p = 0.024$ and $p = 0.012$ for batch I and batch II in comparison to Ctrl), as well as in comparison to BrS2 ($p < 0.004$ for both batches) and BrSfounder ($p < 0.007$ for both batches) (**Figure 7-6a**). As we observed differences in beat rate and beat intervals between the groups, we compared APD between the obtained iPSC-CM lines after normalization of the APD to the beating rate. There were no significant differences in cAPD for batch I of BrS1 and both batches of BrS2 in comparison to controls, while in BrS1 iPSC-CMs from batch II of differentiation we observed cAPD90 prolongation in comparison to Famctr. There were no significant differences in cAPD for BrSfounder in comparison to tested control iPSC-CMs (**Figure 7-6a**). We could also observe loss of the characteristic notch in BrS1 and BrSfounder AP waveforms, while BrS2 AP shapes were similar to those recorded from both negative controls (**Figure 7-6b**).

As Brugada syndrome phenotype can be unmasked during sodium channel blocker challenge, we performed AP recordings in presence of ajmaline at different concentrations: from 0.3 to 10 μM , as well as 40 μM quinidine as a positive control (complete $\text{Na}_v1.5$ channels block) (**Figure 7-7**; details in **Table 7-10**). We looked at RMP, APA, APD30, APD50, APD90, dV/dT_{max} , BPM and beating interval characteristics in obtained iPSC-CMs. There were no statistically significant differences in tested AP parameters in Ctrl and Famctr iPSC-CMs at all tested channel blockers concentrations (even with the positive control 40 μM quinidine), thus we concluded that the performed experiment was most likely unsuccessful in our control lines, making the results obtained in our patient-derived iPSC-CMs inconclusive.

Table 7-8 Calculated p-values for batch-to-batch differences for the AP properties. No batch to batch differences were calculated for BrSfounder due to the low number of recordings in one of the tested batches (n=1). Batch-to-batch differences were calculated using Student's t-test. cAPD – corrected APD

Cell line		RMP	p-value	APA	p-value	APD30	p-value	cAPD30	P value	APD50	p-value	cAPD50	n
Ctrl	Batch 1	-59±	0.583	81±	0.121	112±	0.096	103±	0.292	156±	0.079	143±	2
		6.7		3.6		19.6		18.8		39.6		37.9	
	Batch 2	-64±		98±		163±		136±		239±		199±	9
		3.1		9.6		20.9		19.1		16		14.6	
BrSfounder	Batch 1	-69±	-	120±	-	277±	-	204±	-	358±	-	264±	19
		1.9	4.8	25.6	21.9	23.1	19.8						
Famctrl	Batch 1	-58±	0.769	82±	0.064	176±	0.165	149±	0.297	210±	0.671	183±	6
		4.7		10.3		18.6		17.1		22.3		22.1	
	Batch 2	-59±		107±		137±		122±		196±		176±	15
		2.3		5.4		19.3		18.3		23.7		22.4	
BrS1	Batch 1	-59±	0.704	88±	0.582	175±	<0.001*	153±	0.011*	237±	<0.001*	208±	26
		1.3		2		9		8.4		10.5		9.9	
	Batch 2	-58±		86±		285±		208±		379±		276±	12
		2.1		2.7		20.1		17.2		20.9		17.9	
BrS2	Batch 1	-64±	0.118	103±	0.311	148±	0.126	143±	0.36	212±	0.136	206±	19
		2.5		6.4		16.4		16.2		18.2		17.9	
	Batch 2	-55±		91±		235±		188±		334±		268±	8
		4.5		9.7		48.9		43.7		71.3		63.8	

Cell line		P value	APD90	p-value	cAPD90	P value	dV/dT _{max}	p-value	BPM	p-value	Beat interval	SD	p-value	n
Ctrl	Batch 1	0.357	289	0.187	266±	0.498	6±	0.072	52±	0.482	1288±	607	0.392	2
			87.6		84		0.4		17.5		429.5			
	Batch 2		449±		349±		26±		39±		1718±	670.6		9
			24.1		22		9.9		4.3		223.5			
BrSfounder	Batch 1	-	471±	-	346±	-	44±	-	24±	-	2510±	865.1	-	19
			20.8		17.8		6.5		1.3		198.5			
Famctrl	Batch 1	0.827	331	0.902	281±	0.682	16±	0.059	45±	0.433	1508±	1002.3	0.805	6
			34.5		31.6		7.2		7.2		411.6			
	Batch 2		337±		301±		37±		53±		1392±	733.1		15
			27.4		26		7.3		5.5		189.3			
BrS1	Batch 1	0.004*	355±	<0.001*	311±	0.004*	12±	0.002*	66±	<0.001*	1475±	325.9	<0.001*	26
			14.3		13.4		1.8		1.5		63.9			
	Batch 2		551±		402±		5±		25±		2578±	675.5		12
			28.4		24.3		1.1		1.9		195			
BrS2	Batch 1	0.376	347±	0.094	337±	0.353	36±	0.06	60±	<0.001*	1094±	385.4	0.007*	19
			17.5		17.3		5.9		4.2		88.4			
	Batch 2		522±		418±		17±		34±		1947±	656.2		8
			89.4		80		7.6		3.7		232			

Table 7-9 Calculated p values for the differences between patients and controls in the obtained AP characteristics. p values were obtained using pairwise one way ANOVA comparison.

AP characteristic	Ctrl versus						Famctrl versus				
	Famctrl	BrSfounder	BrS1 batch I	BrS1 batch II	BrS2 batch I	BrS2 batch II	BrSfounder	BrS1 batch I	BrS1 batch II	BrS2 batch I	BrS2 batch II
RMP	0.138	0.138	0.138	0.138	0.1238	0.138	0.138	0.138	0.138	0.138	0.138
APA	0.999	1	0.004*	0.011*	0.593	0.126	0.99	<0.001*	0.003*	0.492	0.08
cAPD30	0.985	0.075	0.915	0.103	0.986	0.504	0.093	0.98	0.149	0.939	0.702
cAPD50	0.998	0.115	0.925	0.100	0.918	0.284	0.068	0.925	0.065	0.924	0.269
cAPD90	0.443	0.504	0.950	0.127	0.606	0.271	0.160	0.587	0.012*	0.235	0.176
dV/dT _{max}	0.822	0.994	0.024*	0.012*	0.987	0.393	0.996	0.007*	0.005*	0.957	0.385
BPM	0.086	0.204	<0.001*	0.101	<0.001*	<0.001*	<0.001*	0.006*	<0.001*	0.312	0.015*
Beat interval	0.236	0.011*	0.613	<0.001*	0.056	0.548	<0.001*	0.461	<0.001*	0.723	0.012*

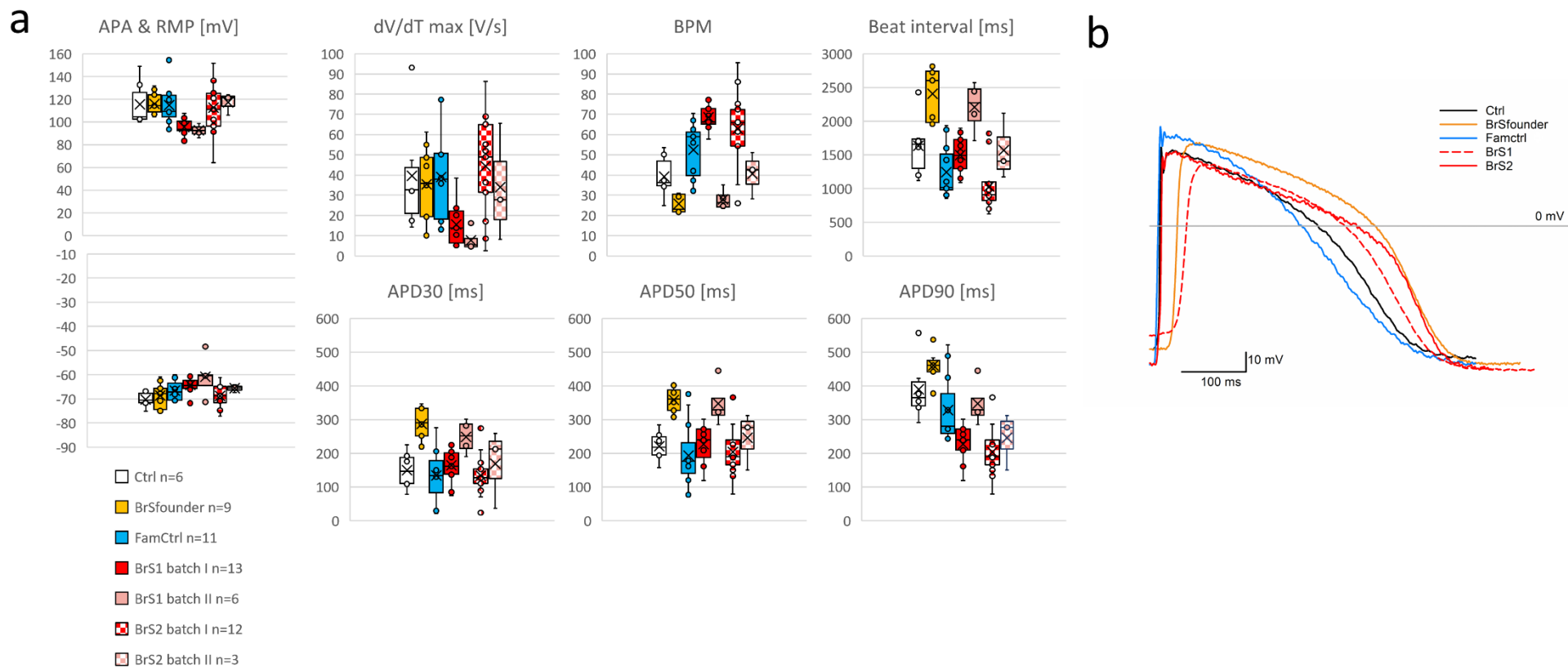


Figure 7-6 Action potential properties at baseline. (a) From left to right displayed are box plots for calculated average \pm SEM for each 'n' cell analysed for: Ctrl (in white; n=6), BrSfounder (in orange; n=9), Famctrl (in blue; n=11), BrS1 batch I (in red; n=13), BrS1 batch II (in light red; n=6), BrS2 batch I (red checked; n=12) and BrS2 batch II (light red checked; n=3). (b) Example AP waveform morphology for each of the tested cell lines.

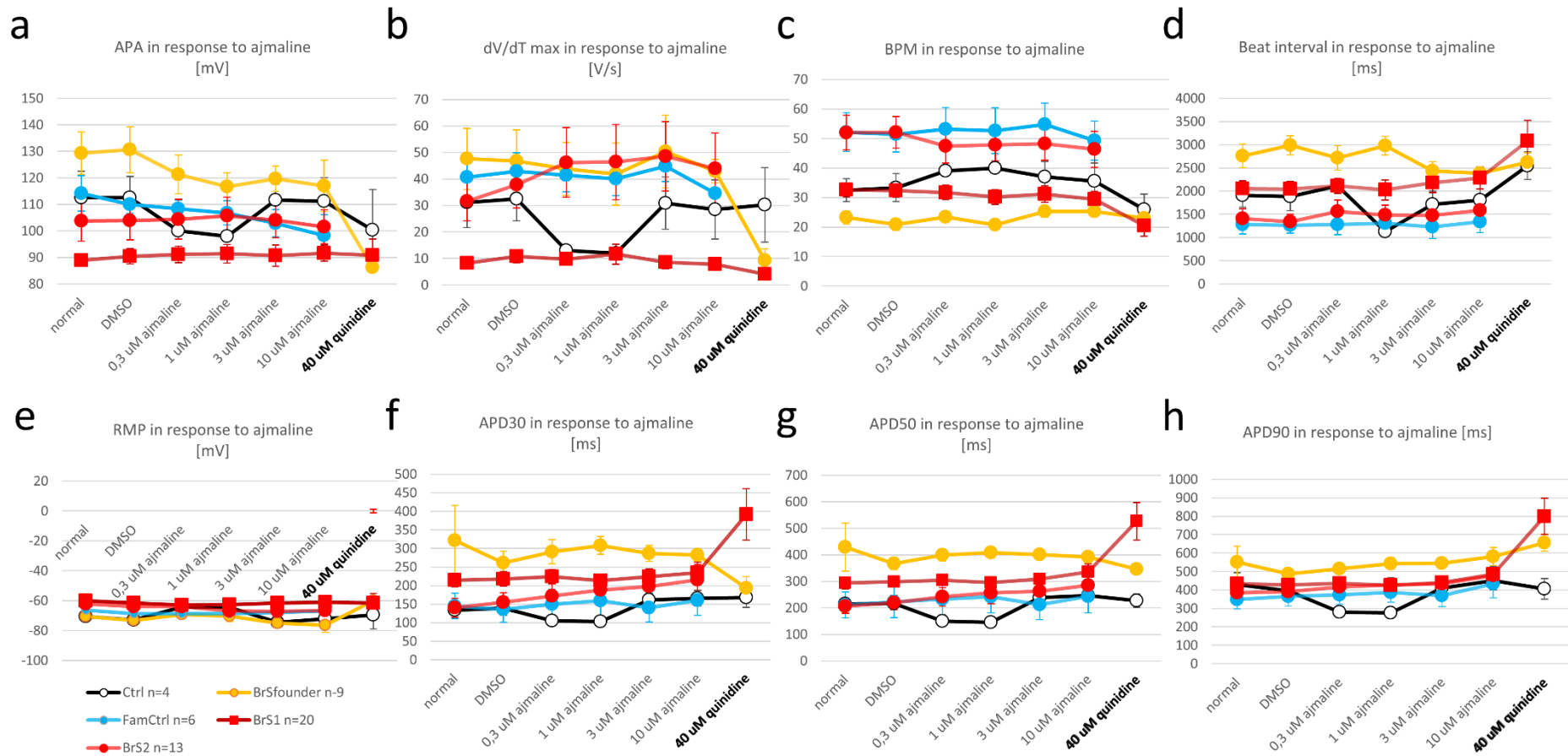


Figure 7-7 Action potential properties in response to ajmaline. Measured APA (a), dV/dT_{max} (b), BPM (c), beat interval (d), RMP (e), APD30 (f), APD50 (g) and APD90 (h) response in presence of different concentrations of ajmaline, with 40 μ M quinidine used as a positive control. Presented symbols represent average \pm SEM for 'n' cells analysed for: Ctrl (white symbols with black lines; n=4), BrSfounder (in orange; n=9); Famctrl (in blue; n=6); BrS1 (red squares with dark red lines; n=20) and BrS2 (in red; n=13).

Table 7-10 AP properties.

Cell line	Baseline					0.3 μ M ajmaline					1 μ M ajmaline					3 μ M ajmaline				
	Ctrl	BrS	Famctrl	BrS1	BrS2	Ctrl	BrS	Famctrl	BrS1	BrS2	Ctrl	BrS	Famctrl	BrS1	BrS2	Ctrl	BrS	Famctrl	BrS1	BrS2
	founder					founder					founder					founder				
RMP [mV]	-70.3 \pm 1.3	-68.7 \pm 1.8	-66.7 \pm 1.3	-64.3 \pm 0.8	-68.5 \pm 1.1	-64.3	-69.3 \pm 2.8	-68.7 \pm 1.4	-62.9 \pm 1.7	-63.9 \pm 2.5	-64.5	-70.2 \pm 3.7	-68.8 \pm 1.7	-62.6 \pm 2	-66.8 \pm 1.6	-74.5 \pm 2.4	-75.1 \pm 2.7	-67.8 \pm 1	-61.5 \pm 2.1	-67.2 \pm 1.6
APA [mV]	116 \pm 8	116 \pm 3	115 \pm 5	95 \pm 2	118 \pm 4	100	121 \pm 7	108 \pm 3	91 \pm 3	104 \pm 8	98	117 \pm 5	107 \pm 5	91 \pm 4	106 \pm 7	112 \pm 6	120 \pm 5	103 \pm 5	91 \pm 4	104 \pm 7
APD30 [ms]	150 \pm 23	287 \pm 20	134 \pm 24	187 \pm 14	146 \pm 18	105	291 \pm 32	150 \pm 40	224 \pm 19	172 \pm 32	103	308 \pm 24	159 \pm 42	214 \pm 16	188 \pm 37	162 \pm 16	287 \pm 21	140 \pm 39	225 \pm 21	198 \pm 43
APD50 [ms]	221 \pm 19	358 \pm 13	193 \pm 30	259 \pm 18	220 \pm 18	150	400 \pm 22	234 \pm 60	305 \pm 19	242 \pm 35	145	408 \pm 19	242 \pm 60	296 \pm 15	257 \pm 42	238 \pm 16	400 \pm 13	213 \pm 56	309 \pm 13	263 \pm 47
APD90 [ms]	390 \pm 38	461 \pm 14	328 \pm 31	402 \pm 28	344 \pm 16	280	515 \pm 21	374 \pm 51	437 \pm 22	417 \pm 35	275	543 \pm 31	387 \pm 59	426 \pm 16	427 \pm 40	410 \pm 40	546 \pm 18	370 \pm 59	440 \pm 21	433 \pm 42
dV/dT_{max} [V/s]	40 \pm 12	33 \pm 6	38 \pm 7	13 \pm 2	45 \pm 6	13	44 \pm 10	41 \pm 6	10 \pm 2	46 \pm 13	12	42 \pm 12	40 \pm 6	12 \pm 4	46 \pm 14	31 \pm 10	50 \pm 14	45 \pm 6	9 \pm 2	49 \pm 13
BPM	39 \pm 4	26 \pm 2	52 \pm 4	57 \pm 5	61 \pm 4	39	24 \pm 2	53 \pm 7	32 \pm 3	48 \pm 6	40	21 \pm 1	53 \pm 8	30 \pm 3	48 \pm 5	37 \pm 5	25 \pm 2	55 \pm 7	31 \pm 3	48 \pm 6
Beat interval [ms]	1634 \pm 191	2405 \pm 136	1243 \pm 119	1741 \pm 126	1072 \pm 97	2112	2716 \pm 264	1281 \pm 220	2113 \pm 161	1564 \pm 248	1129	2983 \pm 204	1311 \pm 236	2026 \pm 217	1483 \pm 218	1516 \pm 288	2441 \pm 188	1228 \pm 251	2179 \pm 211	1590 \pm 209
n	6	9	11	18	16	1	9	6	20	13	1	9	6	20	13	4	9	6	20	13

Cell line	10 μ M ajmaline					40 μ M quinidine		
	Ctrl	BrS founder	Famctrl	Brs1	BrS2	Ctrl	BrS	BrS1
RMP [mV]	-72 \pm 6.6	-76.3 \pm 4.8	-67 \pm 3	-60.9 \pm 2.4	-66.5 \pm 2	-69.5 \pm 15.5	-60.1 4.8	-61.5 \pm 4.8
APA [mV]	111 \pm 9	117 \pm 10	98 \pm 8	92 \pm 3	102 \pm 6	100 \pm 23	86 4	91 \pm 4
APD30 [ms]	166 \pm 20	282 \pm 18	161 \pm 40	234 \pm 29	215 \pm 42	168 \pm 17	194	392 \pm 77
APD50 [ms]	247 \pm 21	392 \pm 21	244 \pm 63	336 \pm 29	285 \pm 48	228 \pm 3	346	527 \pm 82
APD90 [ms]	450 \pm 50	582 \pm 49	433 \pm 75	485 \pm 32	478 \pm 49	406 \pm 0.4	657	799 \pm 119
dV/dT_{max} [V/s]	29 \pm 11	43 \pm 4	35 \pm 6	8 \pm 2	44 \pm 13	30 \pm 21	9	4 \pm 1
BPM	36 \pm 6	25 \pm 2	49 \pm 7	29 \pm 3	46 \pm 6	26 \pm 8	23	21 \pm 3
Beat interval [ms]	1808 \pm 355	2390 \pm 84	1340 \pm 235	2287 \pm 238	1590 \pm 258	2544 \pm 758	2626	3082 \pm 394
n	4	9	6	20	13	4	9	20

7.4.4 CT analysis revealed arrhythmia-like events in both BrS patient iPSC-CMs

As calcium influx plays an important role in cardiac rhythmicity, and it may be affected in BrS patients, we looked at calcium transients in the iPSC-CMs. As there were significant differences in tested CT parameters in all of the tested cell lines between the differentiation batches, we performed analysis of the results in each of the tested batches separately (**Table 7-11**). We observed significant CTD and rise time prolongation and reduced beating rate in BrSfounder iPSC-CMs, while for BrS1 batch I we did not note significant differences in those parameters in comparison to both controls (**Figure 7-8a**). We observed CTD and RC prolongation in BrS1 batch II in comparison with Ctrl batch I. Both batches obtained from BrS2 iPSC-CMs showed significant CTD changes (shortening for batch I and prolongation for batch II) in comparison to Famctrl and Ctrl (p values for case-control comparison are listed in **Table 7-12**).

In the raw CT recordings we observed abnormal patterns in BrS2 iPSC-CMs (**Figure 7-8b**). We looked at the presence of arrhythmia-like events in recorded CT traces. We calculated the number of recordings which presented with arrhythmia-like CT patterns in relation to all recordings recorded for each of the cell lines. In 5% of all traces from BrS1 and 33% of all traces from BrS2 we observed EAD/DAD, while in both negative and one positive control those events were not detected. It is worth noting that we observed irregular beating patterns in CT recordings from three out of five characterized cell lines (BrS1 55%, BrS2 100%, Ctrl 85% of recorded cells; observed in irregular beating pattern observed as regularly occurring premature starting calcium transients in collected CT recordings (e.g. **Figure 7-8b** BrS2)). As our CT recordings revealed presence of arrhythmia-like events, we also looked at recorded AP traces in search for abnormal patterns. Although we did not observe arrhythmia-like events in AP recordings from any of the tested cell lines, interestingly we observed inconsistent beating patterns (based on beating interval variability within single-cell AP recording, interval variability >100ms) in all patched cell lines. However, those were more prevalent in BrS2 and BrSfounder in comparison to other cell lines (47.5%; 91%; 65%; 59%; 19% for BrS1, BrS2, BrSfounder, Famctrl and Ctrl, respectively) (percent of cells with interval variability >100 ms in total number of taken recordings for each of the tested cell lines) (**Table 7-8**). In conclusion, we observed CTD, rise time and beating rate changes in BrS2 iPSC-CMs, and observed increased prevalence of arrhythmia-like events in both BrS1 and BrS2 iPSC-CMs.

Table 7-11 Calcium transient properties from the obtained iPSC-CMs.

Cell line		CTD50 [ms]	P value	CTD70 [ms]	P value	BPM	P value	Rise time [ms]	P value	RC [ms]	P value	n	Beat interval [ms]	SD
Ctrl	Batch I	378±9.72	<0.001*	569±18.2	<0.001*	33±2.5	0.912	215±11.1	0.547	325±16	<0.001*	10	1917±120.4	380.9
	Batch II	479±11.3		710±18.6		33±1.4		227±16		443±11.8		10	1862±80.1	269
Famctrl	Batch I	536±62.7	-	795±104.9	-	29±5.3	-	266±53.3	-	526±75.9	-	5	3760±254.6	804.9
Brsfounder	Batch I	705±36.6	-	1112±57.9	-	17±0.9	-	484±28.8	-	630±33.7	-	10	1173±433.2	1369.7
BrS1	Batch I	486±13.4	0.003*	722±22.7	0.005*	33±1.4	0.08	244±22	0.013*	453±14.6	0.013*	10	1878±85.1	269.2
	Batch II	577±22.2		857±34		27±2.5		324±18.7		528±22.5		10	2484±352.3	1114.2
BrS2	Batch I	273±6.5	<0.001*	391±9.2	<0.001*	77±2	<0.001*	182±5.9	<0.001*	203±7.5	<0.001*	10	782±23.3	73.6
	Batch II	700±45.6		1031±71.8		18±2.5		447±36.4		585±41.2		11	3949±548.7	1735.3

Table 7-12 Calculated p values for the comparison of the CT characteristics between patient and control iPSC-CMs.

	Cell line	CTD50	CTD70	BPM	Rise time	RC
Ctrl batch I versus	Famctrl	0.014*	0.043*	0.918	0.882	0.003*
	Brsfounder	<0.001*	<0.001*	<0.001*	<0.001*	<0.001*
	BrS1 batch I	0.204	0.350	0.999	0.922	0.159
	BrS1 batch II	<0.001*	0.004*	0.774	0.117	0.002*
	BrS2 batch I	0.221	0.191	<0.001*	0.928	0.208
	BrS2 batch II	<0.001*	<0.001*	0.002*	<0.001*	<0.001*
Ctrl batch II versus	Famctrl	0.725	0.784	0.944	0.945	0.575
	Brsfounder	<0.001*	<0.001*	<0.001*	<0.001*	0.006*
	BrS1 batch I	0.986	0.884	0.996	0.893	0.972
	BrS1 batch II	0.244	0.373	0.786	0.227	0.58
	BrS2 batch I	<0.001*	0.001*	<0.001*	0.912	<0.001*
	BrS2 batch II	<0.001*	<0.001*	0.002*	<0.001*	0.072
Famctrl versus	Brsfounder	0.007*	0.001*	0.018*	<0.001*	0.367
	BrS1 batch I	0.746	0.701	0.946	0.932	0.627
	BrS1 batch II	0.762	0.663	0.993	0.805	0.961
	BrS2 batch I	<0.001*	<0.001*	<0.001*	0.411	<0.001*
	BrS2 batch II	0.007*	0.027*	0.047*	<0.001*	0.723

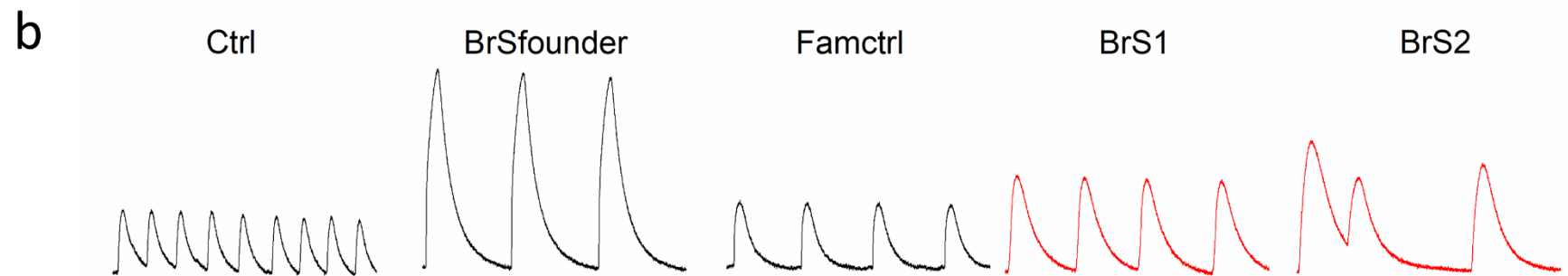
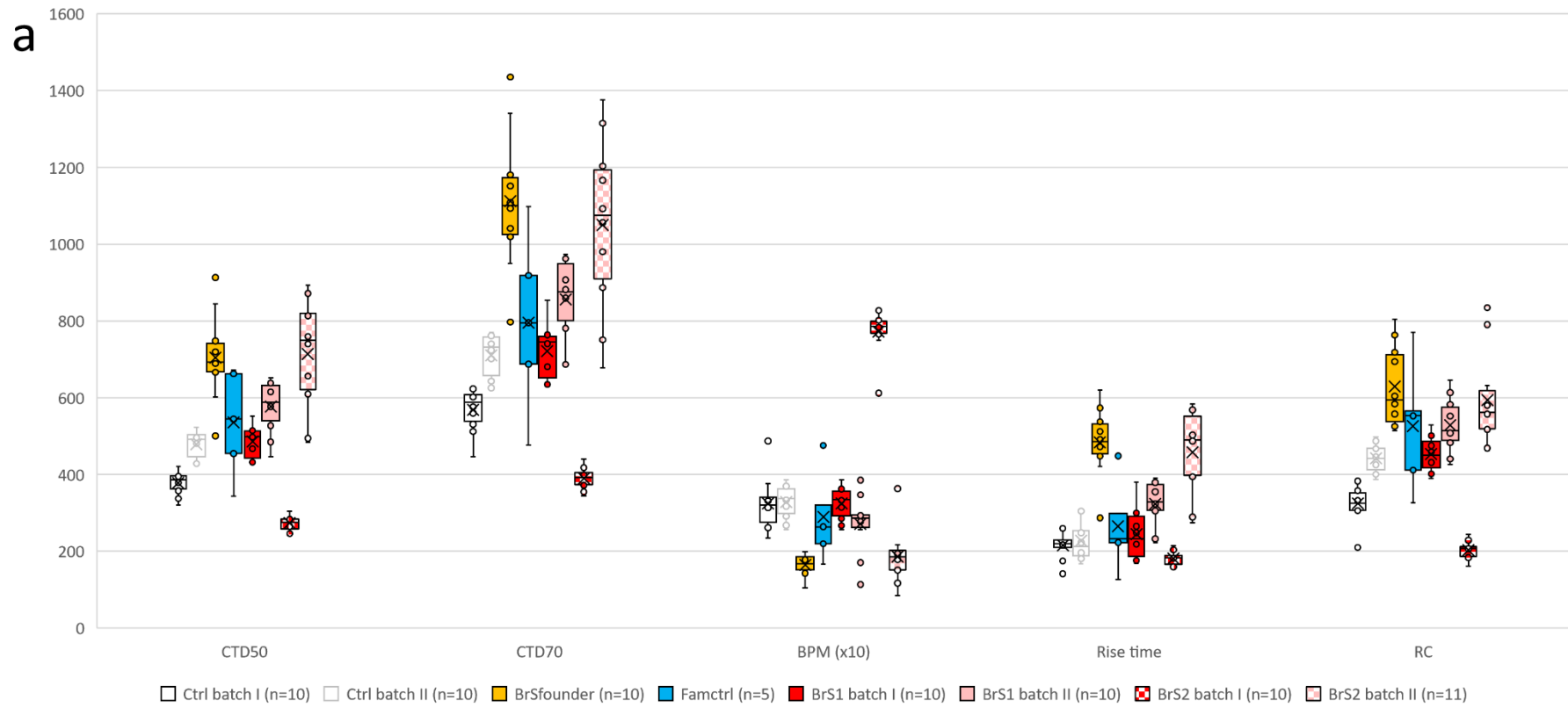


Figure 7-8 Calcium transient properties (a) and example CT transients for analysed cell lines (b).

7.5 Discussion

Although many genes have been associated with Brugada syndrome, the genetic cause of this disease is still unknown in a large fraction of the patients. In **Chapter 6** we introduced three genetically unresolved BrS families, for which we performed combined whole genome sequencing and linkage analysis in search for candidate variants. As the initial genetic screening for one of the tested families (BrS family 2) yielded highest LOD score (3.162) (**Chapter 6**) and the potential candidate variants were disqualified from further analysis due to a negative result of the splicing effect tests for the affected proteins in patient iPSC-CMs in comparison to controls, we decided to investigate the molecular and electrophysiological phenotype of the obtained iPSC-CMs to look for clues for genetic contributors. For this purpose, we selected three family members: two affected individuals presenting with syncope and/or ajmaline-induced BrS type-1 ECG pattern (II:6 and II:8; **Figure 7-1**) as well as one unaffected family member (II:7) for functional characterization in comparison with a negative control unrelated healthy donor and a positive control – obtained from a Belgian SCN5A founder mutation carrier [14].

Obtained iPSC-CMs expressed all of the tested cardiac markers on both protein as well as RNA level. We did not observe significant differences between patient and control iPSC-CMs in the proportion of cells expressing (**Table 7-3**) or the localization of the tested cardiac protein markers (**Figure 7-2**). Our iPSC-CMs showed differences in transcript expression of several cardiac markers in relation to native left ventricular tissue. We observed increased transcript levels of *ANK2*, *CACNA1C*, *HCN4*, *KCNH2*, *KCNQ1*, *MLC2a* and *MYH6*, as well as reduced levels of *KCNJ8*. Those observations suggest incomplete maturation of the obtained iPSC-CMs. *MYH6* and *MLC2a* are expressed at high levels in early stage cardiomyocytes (CMs), whereas in adult CMs *MYH7* and *MLC2v* are preferred isoforms (their expression increases with the duration of the differentiation procedure) [12, 17, 18]. Although ventricular CMs express both isoforms *MLC2a* and *MLC2v*, *MLC2v* is considered to be a ventricular-specific marker due to its absence in atrial-like CMs [19]. Similarly, *MYH7* is considered a ventricular- while *MYH6* atrial-specific marker. While the observed increased transcript levels of *MYL2a* and *MYH6* could suggest higher prevalence of atrial-like iPSC-CMs in our cell cultures, the expression of *GJA1* (Cnx43) - a ventricular-specific marker - as well as detectable presence of *MLC2v* suggest presence of ventricular-like iPSC-CMs in the obtained cell cultures (**Figure 7-3**) [17, 19, 20]. We also looked at differences in expression of the cardiac markers between patients and controls. We observed significantly increased transcript levels of *KCND3*, *MYH6* and *TNNI3* in BrS1 and BrS2 in comparison to the unrelated control, while there were no significant differences in transcript expression of the tested markers between iPSC-CMs from affected and an unaffected family member (**Figure 7-3**). *KCND3* and *GJA1* were significantly increased in BrSfounder in comparison to Ctrl, but not Famctrl. Interestingly, *KCND3* and *TNNI3* levels in patient and familial control iPSC-CMs were similar to those observed in reference LV tissue, while in Ctrl those genes were significantly downregulated in comparison to the reference tissue. *KCND3* encodes K_v4.3 channel, responsible for generation of I_{to} current, which is involved in the generation of the notch in phase 1 of the AP [13]. We observed the loss of the notch in AP waveforms obtained from BrSfounder and BrS1 iPSC-CMs, while in the Ctrl where the measured *KCND3* transcript levels were the lowest from the obtained iPSC-CMs we observed a proper AP waveform morphology. This shows that the measured transcript levels are not corresponding with the observed EP characteristics. *TNNI3* and *MYH6* encode sarcomeric proteins, which form the myofilaments involved in the excitation-contraction coupling of the cardiomyocytes [12, 19-21]. *TNNI3* was shown to be expressed on higher levels in mature CMs, while as mentioned earlier, *MYH6* is expressed on high levels in early stages of differentiation. The observed differences in transcript levels of those markers could suggest the immaturity of the obtained iPSC-CMs, thus it would be interesting to investigate their expression of the protein level to assess the accuracy of the transcript level measurements.

While there were no significant differences in differentiation efficiency between two differentiation batches of each of the tested cell lines, we observed significant differences in EP characteristics between the tested batches of differentiation for all of the tested patient cell lines (no batch-to-batch differences

were observed in I_{Na} and AP characteristics for both control cell lines, while CT characteristics were significantly different in Ctrl iPSC-CMs between batches). Thus, in this discussion we treated the changes that were consistently observed in both obtained differentiation batches for each patient iPSC-CMs as a true phenotype characteristic (e.g. I_{Na} reduction observed in both differentiation batches in the patient cell line when compared to control). BrS1 iPSC-CMs showed a loss-of-function effect observed in reduced I_{Na} in comparison to all other tested cell lines, which corresponded with low *SCN5A* transcript expression in this cell line (**Figure 7-3, 7-4**). However, low *SCN5A* transcript levels were also measured in our unrelated control iPSC-CM line, which presented with high peak I_{Na} density, suggesting that there is no correlation with the transcript expression levels and I_{Na} density in our iPSC-CMs. We also observed a positive shift in voltage-dependence of activation in BrS1 iPSC-CMs in comparison to other cell lines. Both tested affected family members showed accelerated recovery from inactivation in comparison to Ctrl, however no changes in I_{Na} density or voltage dependence of activation/inactivation were observed in BrS2 iPSC-CMs. I_{Na} properties can be affected by multiple factors, like the expression of accessory beta subunit proteins [22], posttranslational modifications of the channel subunits and/or cytoskeletal changes in the investigated cells. Thus, it is possible that the observed changes in I_{Na} characteristics in BrS1 iPSC-CMs may be related to a combination of lower *SCN5A* transcript expression and other factors. In most of the published iPSC-CM models of Brugada syndrome, reduction in peak I_{Na} sometimes together with a positive shift in $V_{1/2}$ of activation and/or negative shift in $V_{1/2}$ of inactivation has been reported in iPSC-CMs obtained from *SCN5A* or *SCN1B* mutation carriers, while no changes in I_{Na} properties in iPSC-CMs of genotype-negative carrier were observed [13]. Here we report a loss-of-function of I_{Na} in a female genotype-negative BrS patient, while in iPSC-CMs from her male relative donor we did not observe BrS phenotype based on the I_{Na} properties. Interestingly, observations from BrSfounder iPSC-CMs showed no difference in peak sodium current or kinetics and voltage dependence of inactivation (**Figures 7-4, 7-5**). Moreover, *SCN5A* transcript levels in BrSfounder iPSC-CMs were increased, in comparison with the other tested iPSC-CMs (**Figure 7-3**). Those observations may point out occurrence of a compensatory mechanism in the tested BrSfounder iPSC-CMs, in which case the *SCN5A* is overexpressed to balance the effect of the founder mutation on the I_{Na} properties, making the tested BrSfounder not the most straightforward positive control for the BrS specific I_{Na} characteristics. However, this hypothesis requires further explanation and a closer look on the other cell characteristics, e.g. $Na_v1.5$ protein levels, composition of WT/mutant $Na_v1.5$, protein localization, as well as cytoskeleton structure in the obtained iPSC-CMs to assess the localization of the translated channel proteins.

Next we investigated the AP properties of the iPSC-CMs (**Figure 7-6**). Here, we noted reduced APA and dV/dT_{max} in BrS1 iPSC-CMs in comparison to other tested cell lines, which corresponds with our observations from relative transcript expression and I_{Na} experiments (**Figure 7-6a**). Furthermore, we observed loss of the characteristic notch in BrS1 and BrSfounder AP waveforms, while BrS2 AP shapes were similar to those recorded from both negative controls (**Figure 7-6b**). This observation points out possible abnormal I_{to} function in the tested BrS1 and BrSfounder lines [13]. We did not observe differences in APD for iPSC-CMs from affected BrS family 2 members as well as BrSfounder in comparison to negative controls (**Figure 7-6a**). Previous attempts of iPSC-CM modeling of genotype-negative BrS donors reported by Veerman *et al.* were not successful to recapitulate the BrS phenotype *in vitro* [21]. They did not observe BrS characteristic changes in their I_{Na} and APD properties in three iPSC-CM lines from genotype-negative BrS donors. Meanwhile in our observations we report genotype-negative BrS donor iPSC-CMs, which recapitulated peak I_{Na} reduction, APA and dV/dT_{max} reduction, while in the other affected family member we did not observe characteristic BrS electrophysiological features. Interestingly, in our iPSC-CMs generated from an *SCN5A* Belgian founder mutation carrier we were also not able to pick up the BrS-specific EP characteristics.

As we did not observe a BrS phenotype in BrS2 or BrSfounder iPSC-CMs in basic conditions, based on the clinical phenotype of the patients we decided to try ajmaline addition at different concentrations in order to induce Brugada syndrome-specific changes through its sodium channel blocking activity. However, our ajmaline challenge tests were unsuccessful in control lines, thus we were not able to determine the effect

of the channel blocker in the tested patient iPSC-CMs (**Figure 7-7**). Similarly, Miller *et al.* performed ajmaline challenge on genotype-negative BrS iPSC-CMs, however they did not observe significant changes in their experiments in comparison to their control iPSC-CMs [22]. It might thus not be possible to recapitulate the effect of sodium channel blocker in the patients, during ajmaline testing on the iPSC-CMs generated with the current differentiation methods. This may be caused by the general immaturity of the generated iPSC-CMs, observed in differences in transcript expression pattern of the cardiac ionic currents (e.g. I_{K1}) or by the use of an isolated cell type, while heart tissue is rather a composite of cardiomyocytes as well as e.g. cardiac fibroblasts or vascular cells or cardiac neurons [23]. Thus, an *in silico* injection of I_{K1} , pacing of the cells or a stimulation of the iPSC-CMs with e.g. isoprenaline (simulating beta adrenergic stimulation) to lower their RMP and increase their beating rate, as well as a co-culture with cardiac fibroblasts and/or vascular cells and/or cardiac neurons to more closely recapitulate physiological tissue conditions could be beneficial for ajmaline testing in iPSC-CMs [24-27].

In addition, we performed CT characterization in obtained iPSC-CMs using immunofluorescent dyes. We did not observe CTD differences in BrS1 iPSC-CMs, in comparison to both controls (**Figure 7-8**), while BrS2 and BrSfounder iPSC-CMs showed CTD and rise time changes in comparison to Famctrl and one of the tested Ctrl differentiation batches. We observed clear abnormal patterns in the raw CT recordings from BrS2 iPSC-CMs (**Figure 7-8b**). We noted arrhythmia-like events in 5% of all traces from BrS1 and 33% of all traces from BrS2, while those events were absent in recordings from both negative controls and BrSfounder (**Figure 7-8b**). Interestingly, we did not observe arrhythmic events in AP recordings from any of the tested cell lines. However, we noted inconsistent beating patterns in obtained AP recordings (based on beating interval variability within a single cell AP recording) in all patched cell lines. Nevertheless, those were more prevalent in BrS2 and BrSfounder in comparison to other tested cell lines (47.5%; 91%; 65%; 59%; 29% for BrS1, BrS2, BrSfounder, Famctrl and Ctrl, respectively) (**Table 7-8**). Our observations suggest a spontaneous Ca^{2+} release in BrS2 iPSC-CMs, meaning elevated basal Ca^{2+} level that might trigger arrhythmia in those cells. Our observations go in line with the previous reports from iPSC-CM models of BrS, where spontaneous arrhythmia-like events were observed in calcium transient recordings, with or without prolongation of CTD, reduction of rise rate or transient decay [13].

BrS is currently considered a disease with a complex inheritance, where more than one genetic variant may be involved in disease etiology [10, 28, 29]. This contributes to different presentation of disease phenotype in BrS patients within the same family. In this case, patient specific iPSC-CMs can be used as an *in vitro* model to study the cellular phenotype of the disease for potential clues about which channel or structural proteins can be contributing to the disease phenotype in the patient, which could help pointing out in which direction to look while analysing the genomic data. In case of this study, one of the tested affected individuals (BrS2) presented with history of syncope in childhood and ajmaline induced BrS type-1 ECG pattern, while the other patient (BrS1) presented with normal baseline ECG, for whom exercise and ajmaline challenge induced a BrS type-1 ECG pattern. Those differences were also visible in our EP recordings from the obtained iPSC-CMs. We noticed BrS phenotype in BrS1 in basic conditions in I_{Na} and AP recordings, while BrS2 presented normal I_{Na} as well as AP properties. Furthermore, we observed CTD, rise time and transient decay rate differences in BrS2 iPSC-CMs, as well as spontaneously occurring arrhythmia-like events in obtained CT recordings in both iPSC-CM patient lines, with higher prevalence in BrS2, pointing out the disturbance of calcium handling in this patient cell line.

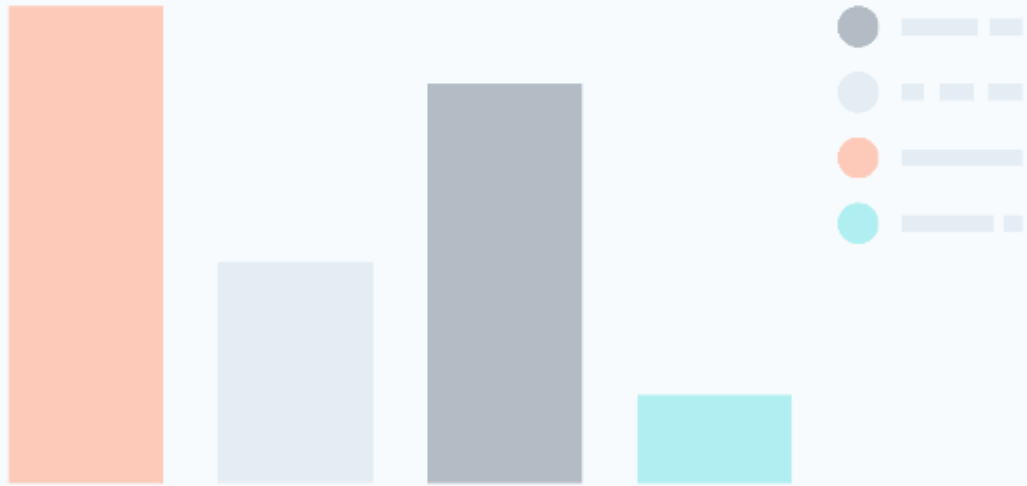
Although our functional characterization of BrS phenotype in selected patient iPSC-CMs showed affected sodium channel function and/or calcium flux abnormalities, the identified potential candidate variant in *DCLRE1A* in this family was not solely sufficient to explain the genetic inheritance of the observed phenotypes. The described functional experiments were performed in a single clone of iPSCs obtained from the donors, thus we cannot exclude the possible clone-specific phenotype observations for the obtained results. Hence, further experiments in additional iPSC clone for each of the tested patient lines will be pursued to determine the true phenotype of the donors. Based on the obtained EP characteristics and transcript expression profiles, the functional phenotyping of those cell lines will be expanded by the characterisation of potassium and calcium currents as well as more detailed characterization of their

cytoskeleton to look for potential explanation of the obtained EP phenotypes. Moreover, investigation of the full transcriptome of the obtained iPSC-CM models using RNA sequencing will be pursued to identify differentially expressed genes and affected signalling pathways to understand the molecular mechanisms at play in this family.

7.6 References

- [1] Brugada, J.; Campuzano, O.; Arbelo, E.; Sarquella-Brugada, G.; Brugada, R. Present Status of Brugada Syndrome: JACC State-of-the-Art Review. *J Am Coll Cardiol.* 2018;72:1046-59.
- [2] Le Scouarnec, S.; Karakachoff, M.; Gourraud, J.B.; Lindenbaum, P.; Bonnaud, S.; Portero, V.; et al. Testing the burden of rare variation in arrhythmia-susceptibility genes provides new insights into molecular diagnosis for Brugada syndrome. *Hum Mol Genet.* 2015;24:2757-63.
- [3] Hosseini, S.M.; Kim, R.; Udupa, S.; Costain, G.; Jobling, R.; Liston, E.; et al. Reappraisal of Reported Genes for Sudden Arrhythmic Death: Evidence-Based Evaluation of Gene Validity for Brugada Syndrome. *Circulation.* 2018;138:1195-205.
- [4] Kapplinger, J.D.; Tester, D.J.; Alders, M.; Benito, B.; Berthet, M.; Brugada, J.; et al. An international compendium of mutations in the *SCN5A*-encoded cardiac sodium channel in patients referred for Brugada syndrome genetic testing. *Heart Rhythm.* 2010;7:33-46.
- [5] Antzelevitch, C. Brugada syndrome. *Pacing Clin Electrophysiol.* 2006;29:1130-59.
- [6] Sotoodehnia, N.; Isaacs, A.; de Bakker, P.I.; Dorr, M.; Newton-Cheh, C.; Nolte, I.M.; et al. Common variants in 22 loci are associated with QRS duration and cardiac ventricular conduction. *Nat Genet.* 2010;42:1068-76.
- [7] Bezzina, C.R.; Barc, J.; Mizusawa, Y.; Remme, C.A.; Gourraud, J.B.; Simonet, F.; et al. Common variants at *SCN5A-SCN10A* and *HEY2* are associated with Brugada syndrome, a rare disease with high risk of sudden cardiac death. *Nat Genet.* 2013;45:1044-9.
- [8] Wilde, A.A.; Bezzina, C.R. Genetics of cardiac arrhythmias. *Heart.* 2005;91:1352-8.
- [9] Polovina, M.M.; Vukicevic, M.; Banko, B.; Lip, G.Y.H.; Potpara, T.S. Brugada syndrome: A general cardiologist's perspective. *Eur J Intern Med.* 2017;44:19-27.
- [10] Schwartz, P.J.; Ackerman, M.J.; Antzelevitch, C.; Bezzina, C.R.; Borggrefe, M.; Cuneo, B.F.; et al. Inherited cardiac arrhythmias. *Nat Rev Dis Primers.* 2020;6:58.
- [11] Takahashi, K.; Yamanaka, S. Induction of pluripotent stem cells from mouse embryonic and adult fibroblast cultures by defined factors. *Cell.* 2006;126:663-76.
- [12] Karakikes, I.; Ameen, M.; Termglinchan, V.; Wu, J.C. Human induced pluripotent stem cell-derived cardiomyocytes: insights into molecular, cellular, and functional phenotypes. *Circ Res.* 2015;117:80-8.
- [13] Nijak, A.; Saenen, J.; Labro, A.J.; Schepers, D.; Loeyls, B.L.; Alaerts, M. iPSC-Cardiomyocyte Models of Brugada Syndrome - Achievements, Challenges and Future Perspectives. *International Journal of Molecular Sciences.* 2021;22:2825.
- [14] Sieliwarczyk, E.; Alaerts, M.; Robyns, T.; Schepers, D.; Claes, C.; Corveleyn, A.; et al. Clinical characterization of the first Belgian *SCN5A* founder mutation cohort. *Europace.* 2020.
- [15] Schindelin, J.; Arganda-Carreras, I.; Frise, E.; Kaynig, V.; Longair, M.; Pietzsch, T.; et al. Fiji: an open-source platform for biological-image analysis. *Nat Methods.* 2012;9:676-82.
- [16] De Vos, W.H.; Van Neste, L.; Dieriks, B.; Joss, G.H.; Van Oostveldt, P. High content image cytometry in the context of subnuclear organization. *Cytometry A.* 2010;77:64-75.
- [17] Guo, Y.; Pu, W.T. Cardiomyocyte Maturation: New Phase in Development. *Circ Res.* 2020;126:1086-106.
- [18] Lewandowski, J.; Rozwadowska, N.; Kolanowski, T.J.; Malcher, A.; Zimna, A.; Rugowska, A.; et al. The impact of *in vitro* cell culture duration on the maturation of human cardiomyocytes derived from induced pluripotent stem cells of myogenic origin. *Cell Transplant.* 2018;27:1047-67.
- [19] Kane, C.; Terracciano, C.M.N. Concise Review: Criteria for Chamber-Specific Categorization of Human Cardiac Myocytes Derived from Pluripotent Stem Cells. *Stem Cells.* 2017;35:1881-97.

- [20] Cyganek, L.; Tiburcy, M.; Sekeres, K.; Gerstenberg, K.; Bohnenberger, H.; Lenz, C.; et al. Deep phenotyping of human induced pluripotent stem cell-derived atrial and ventricular cardiomyocytes. *JCI Insight*. 2018;3.
- [21] Veerman, C.C.; Mengarelli, I.; Guan, K.; Stauske, M.; Barc, J.; Tan, H.L.; et al. hiPSC-derived cardiomyocytes from Brugada Syndrome patients without identified mutations do not exhibit clear cellular electrophysiological abnormalities. *Sci Rep*. 2016;6:30967.
- [22] Miller, D.C.; Harmer, S.C.; Poliandri, A.; Nobles, M.; Edwards, E.C.; Ware, J.S.; et al. Ajmaline blocks I_{Na} and I_{Kr} without eliciting differences between Brugada syndrome patient and control human pluripotent stem cell-derived cardiac clusters. *Stem Cell Res*. 2017;25:233-44.
- [23] Litvinukova, M.; Talavera-Lopez, C.; Maatz, H.; Reichart, D.; Worth, C.L.; Lindberg, E.L.; et al. Cells of the adult human heart. *Nature*. 2020;588:466-72.
- [24] Verkerk, A.O.; Veerman, C.C.; Zegers, J.G.; Mengarelli, I.; Bezzina, C.R.; Wilders, R. Patch-Clamp Recording from Human Induced Pluripotent Stem Cell-Derived Cardiomyocytes: Improving Action Potential Characteristics through Dynamic Clamp. *Int J Mol Sci*. 2017;18.
- [25] Dhamoon, A.S.; Jalife, J. The inward rectifier current (I_{K1}) controls cardiac excitability and is involved in arrhythmogenesis. *Heart Rhythm*. 2005;2:316-24.
- [26] Madamanchi, A. Beta-adrenergic receptor signaling in cardiac function and heart failure. *McGill J Med*. 2007;10:99-104.
- [27] Sampson, K.J.; Kass, R.S. Molecular mechanisms of adrenergic stimulation in the heart. *Heart Rhythm*. 2010;7:1151-3.
- [28] Bezzina, C.R.; Lahrouchi, N.; Priori, S.G. Genetics of sudden cardiac death. *Circ Res*. 2015;116:1919-36.
- [29] Cerrone, M.; Remme, C.A.; Tadros, R.; Bezzina, C.R.; Delmar, M. Beyond the One Gene-One Disease Paradigm: Complex Genetics and Pleiotropy in Inheritable Cardiac Disorders. *Circulation*. 2019;140:595-610.



Chapter 8. General discussion

[Placeholder for text content]

The worldwide prevalence of Brugada syndrome (BrS) is estimated to be approximately 0.05% [1], which accounts for about 3 950 000 cases. In roughly 20-30% of those patients, a pathogenic mutation in the so far known genes related with the disease pathomechanism can be detected, which means more genes are to be identified that are involved in the disease development [2]. BrS affects young adults (40±15 years old) as well as children, becoming a significant clinical burden worldwide. The disease is characterized by variable phenotypical severity and reduced penetrance, which additionally makes the diagnosis more complicated. For many years BrS was assumed to be a monogenic Mendelian disorder, which is explained by variations in the *SCN5A* gene, encoding cardiac voltage-gated sodium channel protein Na_v1.5. Today, after almost three decades of research, the disease is considered to have a more complex inheritance, where genetic modifiers as well as an oligogenic nature may be involved. *In silico* analysis of the genetic variants of unknown significance (VUS) and their implications in disease etiology are not always straightforward, thus BrS research requires additional functional characterization and validation of the genetic findings with the use of cell models relevant for the electrophysiological phenotyping.

8.1 Brugada syndrome development – the status of current knowledge

Typically, the first phenotypical representation of the disease is a syncope or resuscitated SCD event as a consequence of ventricular tachycardia (VT) or fibrillation (VF). In most cases, the symptoms occur at rest or during sleep, however episodes during exercise have also been reported. More often, asymptomatic BrS cases are identified in a course of family screening. To date the only diagnostic criterium to define a Brugada syndrome is presence of a specific cove-shaped ECG pattern (ST-segment elevation, J-wave elevation) in the right precordial leads, which occurs spontaneously or in the presence of specific triggers such as febrile temperature or administration of sodium channel blockers [2; 3; 4; 5]. This ST-elevation can be followed up by a QT-interval prolongation, a prolongation of P-wave, PR or QRS intervals, especially in patients carrying *SCN5A* mutations. The mechanism underlying the observed ECG phenotype is attributed to imbalance of ionic currents which causes abnormalities in AP duration, as well as in the transmural voltage gradient generated by the transient outward potassium current (*I_{to}*), which is responsible for a characteristic notch in the AP waveform of ventricular epicardium [6]. Two hypotheses for the cellular and ionic mechanisms underlying BrS development are commonly discussed: (i) the repolarization and (ii) the depolarization hypothesis. (i) Repolarization hypothesis suggests that the reduced depolarizing force attributable to genetic mutations in ionic channel genes, imbalances currents at the end of phase 1 of the right ventricular epicardial AP, which results in the heterogenous loss of the AP dome. This leads to the transmural dispersion of repolarization, which can contribute to the development of re-entry during phase 2 of the AP, generating closely coupled premature beats which can trigger polymorphic VT or VF. (ii) Depolarization theory declares that fibrosis and reduced expression of gap junction $\alpha 1$ protein (connexin 43) and sodium channels in the right ventricular outflow track (RVOT) lead to delayed conduction that is responsible for the development of the premature beats which trigger re-entrant arrhythmias, where the ECG manifestations of BrS may originate at the perimeter of early and late depolarizations [2; 3; 6].

While *SCN5A* mutations are considered the only relevant genetic diagnostic finding, mutations in more than 20 other genes have been reported in BrS cases [7]. This observation contributed to shifting of the idea that this disease is a monogenic Mendelian disorder, where a rare mutation has a large effect, to one that can be explained by a more complex inheritance model. The incomplete penetrance of the disease, occurrence of phenotype-positive genotype-negative individuals as well as a sporadic presentation of the disorder are the main supporting arguments for this theory [2; 5; 8; 9]. The main genes involved in cardiac arrhythmia like *SCN5A*, are characterized by high pleiotropy, where the functional effect of the mutation (loss- or gain-of-function) is the only determinant in the phenotypic expression of the disorder (e.g. *SCN5A* loss-of-function mutations underlie BrS and gain-of-function mutations underlie LQTS) [8; 10]. In addition, multiple cases of overlapping symptoms, such as SSS/BrS, LQTS/BrS or BrS/arrhythmogenic or dilated cardiomyopathy have been reported [4; 5; 8]. These overlapping syndromes suggest that Brugada

syndrome phenotype might be implicated in a spectrum disease with other cardiac disorders. Recently, more focus is put on research of the genome-wide association studies with identification of common variants in the BrS cases. Several reports support the role of the common SNVs in the *SCN5A-SCN10A* cluster located on chromosome 3 in the disease development [11; 12; 13].

8.2 Looking for a candidate in a haystack of genetic information

The main goal of this thesis was to pursue the genetic explanation of the BrS etiology in clinically well characterized BrS families without pathogenic genetic variation in the currently known genes. We opted for performing a combined WGS and linkage analysis. While WGS is a powerful tool in analysis of the genome, it provides a long list of variants within a single family. Identification of a causal variant from this large amount of data is very difficult and time consuming, thus linkage analysis can serve to narrow this search to the linked genetic *loci*, which can carry the potential genetic candidate [14]. We performed whole genome sequencing of 10 individuals from three BrS families, and performed genotyping of on average 13±4 individuals from each of the tested families. We identified 12 linked *loci* (four in BrS family 1; one in BrS family 2; seven in BrS family 3), from which *locus* on chromosome 2 in BrS family 2 reached a LOD score of 3.162, supporting the evidence for genetic linkage. The analysis of the shared rare variants, which were located within the linked regions of the whole genome or within the non-coding regions of the PED-related genes and were predicted to affect normal splicing of the affected proteins, led to identification of two deep intronic VUS in both BrS family 2 (in *CTNNA3* and *GLI2*) and 3 (in *FOXP1* and *ROBO1*). Analysis of the effect of those variants on the normal splicing in patient and control iPSC-CMs did not yield result that could suggest occurrence of alternative splicing in patient cells, thus the selected VUS were not further pursued as candidates. While in case of BrS family 1 the shared rare variants analysis did not yield any result, through the analysis of each WGS dataset separately we surprisingly identified one patient with an *SCN5A* frameshift variant (c.2325delA; p.Tyr774Serfs), which explained disease phenotype in this individual. Interestingly, although this patient additionally carried the protective haplotype Hap2/3 in the *SCN5A-SCN10A* cluster, recently reported by Pinsach-Aubin et al. [13], the protective effect of the haplotype was not observed in patients' phenotype (spontaneous and ajmaline induced BrS type-1 ECG pattern). Although in re-filtering of the WGS data in BrS family 2 we identified one potential candidate VUS (in *DCLRE1A* gene), it was not solely explaining disease etiology in the presented cases. Thus we hypothesize that the effect of a sum of identified candidate variants and common polymorphisms may contribute to development of symptoms in those patients, correlating with the recent theory about the complex nature of inheritance of BrS.

8.3 iPSC-CMs in Brugada syndrome modeling – a challenge of maturity

In the era of next generation sequencing (NGS), where multiple VUS are identified, the functional testing of novel genetic variants is the key to prove their functional implications in disease development. In multiple cases, *in silico* predictions of the VUS are not straightforward, thus nowadays *in vitro* phenotyping became a standard validation procedure of novel genetic variants. In **Chapter 3** of this thesis we performed functional characterization of an *SCN5A* c.4711T>C (p.Phe1571Leu) variant in a severe Brugada syndrome case [15]. For this purpose we applied a gold standard approach with the use of transient transfection of the mutant protein co-expressed with the wild type accessory β subunit of the affected ionic channel. This method is an efficient way to functionally validate VUS of interest as well as test potential pharmacotherapies. We provided evidence for a loss-of-function of the mutant p.Phe1571Leu Na_v1.5 channel, which was caused by the change in voltage-dependence of inactivation. Moreover, we proposed a therapeutic approach to recover the function of the mutant channel with a sodium current activator toxin nemertide 1- α , which in our hands rescued the channel function. Nevertheless, heterologous expression models are not the most ideal setting to study complex cardiac arrhythmias, as the expression of a single ion channel does not recapitulate the physiological response of the cell. The necessity of a proper tissue- and even better patient-specific cell types which mimic the physiological conditions of the cellular setup are necessary to study complex disorders as Brugada

syndrome. Thus, the iPSC reprogramming and differentiation technology provided a potential remedy to this problem.

Obtaining a blood or fibroblast sample for somatic cell reprogramming is much easier than performing a tissue biopsy on a patient heart. Multiple approaches to obtain iPSC-cardiomyocytes (iPSC-CMs) have been employed, starting from reprogramming methods with either integrating or non-integrating vectors, through different differentiation approaches based on either 3-dimensional or monolayer cell culture conditions. In **Chapter 4** we performed a comparison of two previously published, commonly used monolayer-based differentiation approaches for the purposes of molecular as well as electrophysiological characterization of disease phenotype. We selected one of those two protocols, which produced iPSC-CMs that more closely resemble the protein expression pattern of the reference tissue – left ventricle of a healthy adult human heart, and presenting biologically relevant characteristics of the tested electrophysiological parameters. iPSC-CMs are known for their immaturity. This was shown to have an impact not only on the structural morphology, but also on the molecular as well as electrophysiological presentation of iPSC-CMs, which in general is more close to that of fetal cardiomyocytes [16; 17]. Nevertheless, the current methods for obtaining iPSC-CMs has been shown to produce iPSC-CMs which despite their imperfect maturation status, enable investigation of disease phenotypes of patients with the known causal genetic abnormalities (as reviewed in **Chapter 1** [18]), as well as perform drug response modeling [19; 20]. In **Chapter 5**, we examined the morpho-functional iPSC-CM characteristics obtained with the selected basic differentiation protocol, as well as the protocol complemented with additional T3 and lactate treatment. T3 treatment during *in vitro* differentiation of iPSC-CMs was shown to improve expression of structural cardiac markers, and the contractile function of the obtained cells [21; 22; 23]. Lactate treatment, which aims to enrich the cell culture in more mature iPSC-CMs, which are able to metabolize an energy source different than glucose (similarly to the mature cardiac muscle cells), was shown to further improve contractility and excitation-contraction coupling of the cells [24; 25; 26]. In our hands T3 treatment improved all of the tested parameters: more organized expression of the structural cardiac proteins, increased transcript levels of the tested cardiac genes, increased I_{Na} density, measurement of more negative RMP and higher APA. In contrast, additional lactate treatment did not influence tested parameters significantly. We observed high variability in the obtained I_{Na} characteristics between the clonal cell lines obtained from the same donor, regardless of the used differentiation protocol (with or without additional maturation treatment (T3)). Interestingly, the differences between several differentiation batches of each of the tested cell lines were insignificant, suggesting high reproducibility of the used differentiation procedure. Small patches of monolayers of the iPSC-CMs represent more physiological condition for EP experiments, which enables recordings of AP waveforms with parameters similar to those obtained in native ventricular CMs [27], as well as performance of more high throughput experiments like calcium imaging or field potential recordings with the application of multi-electrode arrays [18; 28]. Thus, in our AP and CT experiments we opted for recording traces from cells growing in this cell growth mode.

In **Chapters 5** and **7** we pursued functional characterization of the iPSC-CMs obtained from carriers of a known loss-of-function *SCN5A* Belgian founder mutation, as well as phenotype-positive genotype-negative donors from BrS family 2 (for which we performed linkage analysis with WGS and obtained the highest LOD score).

In **Chapter 5** we compared the electrophysiological phenotype of iPSC-CMs obtained from several Belgian BrS *SCN5A* founder mutation carriers, who presented with a different phenotype severity, ranging from asymptomatic to sudden cardiac death. The investigated *SCN5A* founder mutation was previously modelled in the transient expression system, which demonstrated a loss-of-function of the I_{Na} , due to activation of an alternative splice site in exon 27 of *SCN5A*, which results in a deletion of 32 amino acids in the protein. As such, parts of the segment 2 and 3 of domain IV of $Na_v1.5$ are spliced out, which leads to a translation of a non-functional channel [29; 30; 31]. In cells generated using basic differentiation protocol we observed a loss-of-function effect on I_{Na} (reduced peak I_{Na} density) in all tested individuals, and acceleration of the recovery from inactivation in only one of the tested BrS iPSC-CM lines. In addition,

in T3 treated cells we noticed shifts in $V_{1/2}$ of inactivation in all tested patient cell lines. Interestingly, no effect on recovery from inactivation was detected in T3 treated cells. It is worth noting that the subtle differences in the applied differentiation protocol have a pronounced impact on the obtained electrophysiological phenotype of the tested patient iPSC-CMs. This differential effect depending on the used treatment can be explained by the changes in the transcript levels of the tested cardiac markers between the tested treatments, as well as visible changes in cytoskeleton organization [16; 17; 32; 33]. Similar effect was observed by de la Roche et al., where their results obtained from iPSC-CMs from a genetically manipulated iPSC-CMs carrying an *SCN5A* mutation (g.2204C > T; p.A735V) unveiled additional changes in sodium current gating (a positive shift of voltage dependence of activation and reduced I_{Na} protein expression), which were not visible in the results obtained from HEK293 cells [34] (extensively discussed in **Chapter 1**). Moreover, in our hands the effect of the founder *SCN5A* mutation on APD and CTD was reduced in cells obtained with T3 treatment. Our observations confirm, that with the expression of tissue-specific forms of the ion channels and the whole repertoire of their auxiliary proteins, the phenotype of the variants modelled previously in heterologous expression systems might differ and be more or less pronounced [34].

In **Chapter 7** we attempted modeling of phenotype-positive, genotype-negative BrS donors from a family in which we performed WGS. While we did not see differences in the measured expression of the cardiac markers in patient iPSC-CMs (on the contrary to the observed increased *SCN5A* transcript levels in positive control - BrS founder iPSC-CMs), we noticed a positive shift in $V_{1/2}$ of activation, together with peak I_{Na} , APA and upstroke velocity reduction in one of the patients (BrS1), compared to unrelated and family controls (no differences in I_{Na} or AP properties were observed for BrS founder iPSC-CMs). Although iPSC-CMs from the second affected donor (BrS2) did not show I_{Na} abnormalities, we noticed abnormal calcium transient patterns in the obtained recordings, which suggested spontaneous Ca^{2+} release in BrS2 iPSC-CMs due to elevated basal Ca^{2+} level that might trigger arrhythmic events in those cells. Similarly, the BrS founder iPSC-CMs showed CTD and rise time change in comparison to tested control lines, however no arrhythmic events were visible in this iPSC-CMs line, supporting involvement of abnormal calcium handling in the development of BrS phenotype. We performed AP characterization in presence of ajmaline, however, no effect of the channel blocker was registered in our control iPSC-CMs, suggesting a failure of the channel blocker experiment. As reported in **Chapter 1**, Miller et al. and Veerman et al. also performed iPSC-CM modeling of genotype-negative donors. In their experiments, they were not able to recapitulate disease phenotype in control conditions as well as sodium blocker challenge experiments [35; 36]. On the other hand, attempts of modeling *SCN5A* frameshift mutation carriers with ajmaline-induced BrS type-1 ECG showed the expected I_{Na} and dV/dT_{max} reduction [37].

The question arises – why were we not able to pick up the typical BrS phenotype in most of our BrS iPSC-CMs? Although we were able to improve the maturation status of the obtained iPSC-CMs, the phenotype features characteristic for BrS (in particular dV/dT_{max} reduction) was not visible in our model for the Belgian *SCN5A* founder mutation. Several reasons may explain this issue. First, we observed a higher ratio of the atrial-like cardiomyocytes in the obtained iPSC-CM cultures (elevated expression of *MLC2a*), while the BrS is predominantly a ventricular disease. Second, we obtained iPSC-CMs with more positive RMP levels than those observed in physiological conditions. This may contribute to lower availability of the sodium channels, which may mask the effect of the mutant on the sodium function in the AP waveforms. A more positive RMP also contributes to a more pronounced spontaneous activity of the iPSC-CMs, which can be overinterpreted as the presence of arrhythmia-like events. One may wonder why in this case we did not opt to use the *in silico* I_{K1} injection to lower our RMP threshold. While the I_{K1} injection resolves the RMP threshold issue, virtually increasing the availability of the sodium channels [38; 39], it is not solving the issue of the general immaturity of the ion channel proteins in the tested iPSC-CMs. Thus, it may be possible, that in case of the *in silico* injection of the I_{K1} current, one is measuring the effect of the immaturity of the sum of the obtained channel proteins, instead of the true effect of the sodium channel mutation. Action potential waveforms are in fact the products of the cascade action of the ion channels present in the active cardiomyocytes (as discussed in **Chapter 1**). It would be ideal if by the virtual injection

of a single current one would be able to compensate the immaturity of all of the currents involved in the AP development. While the existing technology for *in sillico* I_{K1} injection is promising and found application in many laboratories, it may not be the ideal solution for the current issues with the generation of functional, mature iPSC-CMs. Even though I_{K1} injection can virtually help changing the AP waveform by lowering the measured RMP values, it will not have an influence on the total sodium current recorded in the voltage-clamp experiments, which are important in determination of the loss-of-function effect of the $Na_v1.5$ channel. The potential immaturity of the currents in the iPSC-CMs is also apparent in the data collected in this PhD thesis for the Belgian *SCN5A* founder mutation. Here, the expected reduction in peak I_{Na} was less pronounced in iPSC-CMs, compared to the reported effect of this founder mutation in the heterologous expression models (**Chapter 5 & 7**). Furthermore, possible immaturity of the calcium handling in the obtained iPSC-CMs, visible in spontaneous contractions of the obtained monolayers can contribute to mask the effect on the observed phenotype. Electrical stimulation and combined T3 and Akt or β -adrenergic signalling stimulation of the cells may be solving problems with the spontaneous activity of the iPSC-CMs. Both approaches were shown to improve the maturity of the SR, which has an influence on the calcium modulation of the contractile work of the iPSC-CMs [17; 33; 40]. With more mature SR, contractions of the cells become more simultaneous, which improves signal propagation between the cells and increases contraction force, via enlarged SR Ca^{2+} storage capacity. Application of either of the combined maturation approaches generates a model that enables investigation of signal propagation which represents more mature electrophysiological properties, similar to those observed in mature cardiomyocytes [40; 41]. Combination of those techniques could overcome the drawbacks of sole application of the *in sillico* I_{K1} injection.

8.4 It's always the small pieces that make the big picture

With the advancement of the next generation sequencing techniques, BrS research went from the hypothesis based genetic screening to exploratory research for the genetic players in disease etiology. Current view on the Brugada syndrome to be a more complex disorder, where more than a single genetic cause are at play in predisposition to disease development, gives opportunities for future explorations. First of all, due to the high variability in the phenotypic presentation of the disease in familial cases with a single causal variant (e.g. Belgian *SCN5A* founder mutation) it is highly likely that genetic modifiers play a role in the development of the symptoms. Genetic modifiers can be variants or genes which influence the transcription/translation of the other causal gene/protein. This assumption led to a discovery of genetic associations, where specific haplotypes of common SNVs in the enhancer region of *SCN5A-SCN10A* cluster were correlated with a protective and worsening effect in disease presentation [13]. However, as shown in **Chapter 6**, some of the BrS patients may not carry the specific SNVs or present the protective haplotype, and still present symptoms. To improve the genetic diagnostics in those complex cases, a concept of polygenic risk score (PRS) has been proposed, which weights the sum of the number of risk alleles in the individual to predict the disease status [42; 43; 44]. While currently many controversy still surrounds the PRS, especially because it is thought to be limited in its predictions due to the incomplete lists of variants associated with the disorder [44; 45], it serves as an alternative genetic explanation for those patients, for which the symptoms of the disease are present, while the clear genetic explanation is missing. Recently, Barc et al. reported first attempt in application of a PRS model on a series of 2 469 Brugada syndrome patients [46]. The results shown that BrS related PRS predicts an increased risk for atrioventricular conduction disorders, as well as appearance of atrial fibrillation/flutter, increased P-wave, PQ interval and QRS duration, and a negative correlation with QT interval duration. As those results show promising potential, further genome-wide association studies including greater populations from different ethnic backgrounds are necessary to provide more information for proper assessment of the PRS in Brugada syndrome and their implementation to the diagnostics of the disease. While it is tempting to rely solely on the genetics, one should also consider the possibility that genetics are not the sufficient explanation for BrS origins. Environmental factors are known modulators of the disease phenotype of other cardiovascular disorders [47; 48]. For example, investigation of the methylation patterns and transcript analysis of the affected individuals can point out the changes in gene and pathway

regulations that are underlying the disease [49]. While this type of studies has been so far successfully applied in the field of arrhythmic disorders for atrial fibrillation research [50; 51; 52; 53; 54; 55], it might be also interesting to look more deep into the environmental regulation of genetic architecture of BrS patients.

Rapid progress in the genetic screening technologies triggered the necessity of functional validation of the theoretical findings. Although discovery of iPSC reprogramming and further differentiation to CMs is unequivocally a great achievement, the methodology still needs further improvements to be accepted as an undisputed source of functional evidence for genetic aberrations. High sensitivity of the model to subtle changes in the experimental setup, which affect the obtained readout is an important drawback of the approach. This becomes a great issue for investigation of the patients who are phenotype-positive but genotype-negative. If the experimental setup can influence the readout so much, how will we be able to distinguish the changes that are contributed to the genetic variance and not to the faulty of the setup? Future research should be focused on improvement of the differentiation protocols and their standardization across the research centres, which would contribute to improvement of reproducibility of the functional test results and their reliability. Potential remedy to the problem could be culture of cardiomyocytes in co-culture with other cell types which are present in the heart tissue (e.g. cardiac fibroblasts or neurons) [17; 56; 57]. Focus on an isolated cell type in the *in vitro* iPSC-CM cultures may partially explain the immaturity of the electrophysiological properties of the obtained cells. In the human heart, interplay between the different cell types as well as different organs and their metabolites and excreted modulators (e.g. hormones) contributes to the development of the functional mature heart tissue. Furthermore, heart is a complex organ in which the intercellular connections develop in a 3D system. Development of 3D scaffolds for 3D cardiomyocyte culture, or cardiac organoids can serve as a system to recapitulate this complex architecture of the human heart *in vitro* [58; 59; 60; 61; 62] and improve the electrophysiology of the tested tissues.

In conclusion, a combined approach of the genetic and functional analysis of the disease phenotype of BrS is the way to go for the future research. However, maybe more focus should be paid to the environmental modulation of the genome in the BrS patients and a more extensive efforts to improve the electrophysiological and structural iPSC-CM maturity should be provided before attempting the analysis of the cellular phenotypes of the patients with undefined genetic background.

8.5 References

- [1] Vutthikraivit, W.; Rattanawong, P.; Putthapiban, P.; Sukhumthammarat, W.; Vathesatogkit, P.; Ngarmukos, T.; Thakkinstian, A. Worldwide Prevalence of Brugada Syndrome: A Systematic Review and Meta-Analysis. *Acta Cardiol Sin* 34 (2018) 267-277.
- [2] Schwartz, P.J.; Ackerman, M.J.; Antzelevitch, C.; Bezzina, C.R.; Borggrefe, M.; Cuneo, B.F.; Wilde, A.A.M. Inherited cardiac arrhythmias. *Nat Rev Dis Primers* 6 (2020) 58.
- [3] Antzelevitch, C.; Brugada, P.; Brugada, J.; Brugada, R. Brugada syndrome: from cell to bedside. *Curr Probl Cardiol* 30 (2005) 9-54.
- [4] Sieira, J.; Brugada, P. The definition of the Brugada syndrome. *Eur Heart J* 38 (2017) 3029-3034.
- [5] Pappone, C.; Santinelli, V. Brugada Syndrome: Progress in Diagnosis and Management. *Arrhythm Electrophysiol Rev* 8 (2019) 13-18.
- [6] Meregalli, P.G.; Wilde, A.A.; Tan, H.L. Pathophysiological mechanisms of Brugada syndrome: depolarization disorder, repolarization disorder, or more? *Cardiovasc Res* 67 (2005) 367-78.
- [7] Campuzano, O.; Sarquella-Brugada, G.; Fernandez-Falgueras, A.; Cesar, S.; Coll, M.; Mates, J.; Arbelo, E.; Perez-Serra, A.; Del Olmo, B.; Jorda, P.; et al. Genetic interpretation and clinical translation of minor genes related to Brugada syndrome. *Hum Mutat* 40 (2019) 749-764.
- [8] Cerrone, M.; Remme, C.A.; Tadros, R.; Bezzina, C.R.; Delmar, M. Beyond the One Gene-One Disease Paradigm: Complex Genetics and Pleiotropy in Inheritable Cardiac Disorders. *Circulation* 140 (2019) 595-610.
- [9]. Bezzina, C.R.; Lahrouchi, N.; Priori, S.G. Genetics of sudden cardiac death. *Circ Res* 116 (2015) 1919-36.
- [10] Cerrone, M.; Napolitano, C.; Priori, S.G. Genetics of ion-channel disorders. *Curr Opin Cardiol* 27 (2012) 242-52.
- [11] Bezzina, C.R.; Barc, J.; Mizusawa, Y.; Remme, C.A.; Gourraud, J.B.; Simonet, F.; Verkerk, A.O.; Schwartz, P.J.; Crotti, L.; Dagradi, F.; et al. Common variants at *SCN5A-SCN10A* and *HEY2* are associated with Brugada syndrome, a rare disease with high risk of sudden cardiac death. *Nat Genet* 45 (2013) 1044-9.
- [12] Walsh, R.; Tadros, R.; Bezzina, C.R. When genetic burden reaches threshold. *Eur Heart J* 41 (2020) 3849-3855.
- [13] Pinsach-Abuin, M.L.; Del Olmo, B.; Perez-Agustin, A.; Mates, J.; Allegue, C.; Iglesias, A.; Ma, Q.; Merkurjev, D.; Konovalov, S.; et al. Analysis of Brugada syndrome loci reveals that fine-mapping clustered GWAS hits enhances the annotation of disease-relevant variants. *Cell Rep Med* 2 (2021) 100250.
- [14] Cantor, R.M.; Analysis of Genetic Linkage. in: R.E.K.B.R.G.W.W. Pyeritz, (Ed.), *Emery and Rimoin's Principles and Practice of Medical Genetics and Genomics* (Seventh Edition), Elsevier Inc., 2019, pp. 277-236.
- [15] Nijak, A.; Labro, A.J.; De Wilde, H.; Dewals, W.; Peigneur, S.; Tytgat, J.; Snyders, D.; Sieliwonczyk, E.; Simons, E.; Van Craenenbroeck, E.; et al. Compound Heterozygous *SCN5A* Mutations in Severe Sodium Channelopathy With Brugada Syndrome: A Case Report. *Front Cardiovasc Med* 7 (2020) 117.
- [16] Karakikes, I.; Ameen, M.; Termglinchan, V.; Wu, J.C. Human induced pluripotent stem cell-derived cardiomyocytes: insights into molecular, cellular, and functional phenotypes. *Circ Res* 117 (2015) 80-8.
- [17] Kolanowski, T.J.; Antos, C.L.; Guan, K. Making human cardiomyocytes up to date: Derivation, maturation state and perspectives. *Int J Cardiol* 241 (2017) 379-386.
- [18] Nijak, A.; Saenen, J.; Labro, A.J.; Schepers, D.; Loeyls, B.L.; Alaerts, M., iPSC-Cardiomyocyte Models of Brugada Syndrome - Achievements, Challenges and Future Perspectives. *International Journal of Molecular Sciences* 22 (2021) 2825.
- [19] Liang, P.; Lan, F.; Lee, A.S.; Gong, T.; Sanchez-Freire, V.; Wang, Y.; Diecke, S.; Sallam, K.; Knowles, J.W.; Wang, P.J.; et al. Drug screening using a library of human induced pluripotent stem cell-derived cardiomyocytes reveals disease-specific patterns of cardiotoxicity. *Circulation* 127 (2013) 1677-91.

- [20] Yamamoto, W.; Asakura, K.; Ando, H.; Taniguchi, T.; Ojima, A.; Uda, T.; Osada, T.; Hayashi, S.; Kasai, C.; Miyamoto, N.; et al. Electrophysiological Characteristics of Human iPSC-Derived Cardiomyocytes for the Assessment of Drug-Induced Proarrhythmic Potential. *PLoS One* 11 (2016) e0167348.
- [21] Parikh, S.S.; Blackwell, D.J.; Gomez-Hurtado, N.; Frisk, M.; Wang, L.; Kim, K.; Dahl, C.P.; Fiane, A.; Tonnessen, T.; Kryshnal, D.O.; et al. Thyroid and Glucocorticoid Hormones Promote Functional T-Tubule Development in Human-Induced Pluripotent Stem Cell-Derived Cardiomyocytes. *Circ Res* 121 (2017) 1323-1330.
- [22] Yang, X.; Rodriguez, M.; Pabon, L.; Fischer, K.A.; Reinecke, H.; Regnier, M.; Sniadecki, N.J.; Ruohola-Baker, H.; Murry, C.E. Tri-iodo-L-thyronine promotes the maturation of human cardiomyocytes-derived from induced pluripotent stem cells. *J Mol Cell Cardiol* 72 (2014) 296-304.
- [23] Li, M.; Iismaa, S.E.; Naqvi, N.; Nicks, A.; Husain, A.; Graham, R.M. Thyroid hormone action in postnatal heart development. *Stem Cell Res* 13 (2014) 582-91.
- [24] Tohyama, S.; Hattori, F.; Sano, M.; Hishiki, T.; Nagahata, Y.; Matsuura, T.; Hashimoto, H.; Suzuki, T.; Yamashita, H.; Satoh, Y.; et al. Distinct metabolic flow enables large-scale purification of mouse and human pluripotent stem cell-derived cardiomyocytes. *Cell Stem Cell* 12 (2013) 127-37.
- [25] Fuerstenau-Sharp, M.; Zimmermann, M.E.; Stark, K.; Jentsch, N.; Klingenstein, M.; Drzymalski, M.; Wagner, S.; Maier, L.S.; Hehr, U.; Baessler, A.; et al. Generation of highly purified human cardiomyocytes from peripheral blood mononuclear cell-derived induced pluripotent stem cells. *PLoS One* 10 (2015) e0126596.
- [26] Nose, N.; Werner, R.A.; Ueda, Y.; Gunther, K.; Lapa, C.; Javadi, M.S.; Fukushima, K.; Edenhofer, F.; Higuchi, T. Metabolic substrate shift in human induced pluripotent stem cells during cardiac differentiation: Functional assessment using *in vitro* radionuclide uptake assay. *Int J Cardiol* 269 (2018) 229-234.
- [27] Van de Sande, D.V.; Kopljar, I.; Alaerts, M.; Teisman, A.; Gallacher, D.J.; Loeys, B.; Snyders, D.J.; Leybaert, L.; et al. The resting membrane potential of hSC-CM in a syncytium is more hyperpolarised than that of isolated cells. *Channels (Austin)* 15 (2021) 239-252.
- [28] Garg, P.; Garg, V.; Shrestha, R.; Sanguinetti, M.C.; M.C. Kamp, M.C.; Wu, J.C. Human Induced Pluripotent Stem Cell-Derived Cardiomyocytes as Models for Cardiac Channelopathies: A Primer for Non-Electrophysiologists. *Circ Res* 123 (2018) 224-243.
- [29] Hong, K.; Guerchicoff, A.; Pollevick, G.D.; Oliva, A.; Dumaine, R.; de Zutter, M.; Burashnikov, E.; Wu, Y.S.; Brugada, J.; Brugada, P.; et al. Cryptic 5' splice site activation in *SCN5A* associated with Brugada syndrome. *J Mol Cell Cardiol* 38 (2005) 555-60.
- [30] Rossenbacker, T.; Schollen, E.; Kuiperi, C.; de Ravel, T.J.; Devriendt, K.; Matthijs, G.; Collen, D.; Heidbuchel, H.; Carmeliet, P. Unconventional intronic splice site mutation in *SCN5A* associates with cardiac sodium channelopathy. *J Med Genet* 42 (2005) e29.
- [31] Sieliwarczyk, E.; Alaerts, M.; Robyns, T.; Schepers, D.; Claes, C.; Corveleyn, A.; Willems, R.; Van Craenenbroeck, E.M.; Simons, E.; Nijak, A.; et al. Clinical characterization of the first Belgian *SCN5A* founder mutation cohort. *Europace* (2020).
- [32] Guo, Y.; Pu, W.T. Cardiomyocyte Maturation: New Phase in Development. *Circ Res* 126 (2020) 1086-1106.
- [33] Lewandowski, J.; Rozwadowska, N.; Kolanowski, T.J.; Malcher, A.; Zimna, A.; Rugowska, A.; Fiedorowicz, K.; Labedz, W.; Kubaszewski, L.; Chojnacka, K.; et al. The impact of *in vitro* cell culture duration on the maturation of human cardiomyocytes derived from induced pluripotent stem cells of myogenic origin. *Cell Transplant* 27 (2018) 1047-1067.
- [34] de la Roche, J.; Angsutararux, P.; Kempf, H.; Janan, M.; Bolesani, E.; Thiemann, S.; Wojciechowski, D.; Coffee, M.; Franke, A.; Schwanke, K.; et al. Comparing human iPSC-cardiomyocytes versus HEK293T cells unveils disease-causing effects of Brugada mutation A735V of NaV1.5 sodium channels. *Sci Rep* 9 (2019) 11173.
- [35] Veerman, C.C.; Mengarelli, I.; Guan, K.; Stauske, M.; Barc, J.; Tan, H.L.; Wilde, A.A.; Verkerk, A.O.; Bezzina, C.R. hiPSC-derived cardiomyocytes from Brugada Syndrome patients without identified mutations do not exhibit clear cellular electrophysiological abnormalities. *Sci Rep* 6 (2016) 30967.

- [36] Miller, D.C.; Harmer, S.C.; Poliandri, A.; Nobles, M.; Edwards, E.C.; Ware, J.S.; Sharp, T.V.; McKay, T.R.; Dunkel, L.; Lambiase, P.D.; et al. Ajmaline blocks I_{Na} and I_{Kr} without eliciting differences between Brugada syndrome patient and control human pluripotent stem cell-derived cardiac clusters. *Stem Cell Res* 25 (2017) 233-244.
- [37] Liang, P.; Sallam, K.; Wu, H.; Li, Y.; Itzhaki, I.; Garg, P.; Zhang, Y.; Vermglinchan, V.; Lan, F.; Gu, M.; et al. Patient-Specific and Genome-Edited Induced Pluripotent Stem Cell-Derived Cardiomyocytes Elucidate Single-Cell Phenotype of Brugada Syndrome. *J Am Coll Cardiol* 68 (2016) 2086-2096.
- [38] Meijer van Putten, R.M.; Mengarelli, I.; Guan, K.; Zegers, J.G.; van Ginneken, A.C.; Verkerk, A.O.; Wilders, R. Ion channelopathies in human induced pluripotent stem cell derived cardiomyocytes: a dynamic clamp study with virtual IK1. *Front Physiol* 6 (2015) 7.
- [39] Verkerk, A.O.; Veerman, C.C.; Zegers, J.G.; Mengarelli, I.; Bezzina, C.R.; Wilders, R. Patch-Clamp Recording from Human Induced Pluripotent Stem Cell-Derived Cardiomyocytes: Improving Action Potential Characteristics through Dynamic Clamp. *Int J Mol Sci* 18 (2017).
- [40] Nunes, S.S.; Miklas, J.; Liu, R.; Aschar-Sobbi, Y.; Xiao, B.; Zhang, J.; Jiang, S.; Masse, M.; Gagliardi, A.; Hsieh, N.; et al. Biowire: a platform for maturation of human pluripotent stem cell-derived cardiomyocytes. *Nat Methods* 10 (2013) 781-7.
- [41] Veerman, C.C.; Kosmidis, G.; Mummery, C.L.; Casini, S.; Verkerk, A.O.; Bellin, M. Immaturity of human stem-cell-derived cardiomyocytes in culture: fatal flaw or soluble problem? *Stem Cells Dev* 24 (2015) 1035-52.
- [42] Lewis, C.M.; Vassos, E. Polygenic risk scores: from research tools to clinical instruments. *Genome Med* 12 (2020) 44.
- [43] Torkamani, A.; Wineinger, N.E.; Topol, E.J. The personal and clinical utility of polygenic risk scores. *Nat Rev Genet* 19 (2018) 581-590.
- [44] Lambert, S.A.; Abraham, G.; Inouye, M. Towards clinical utility of polygenic risk scores. *Hum Mol Genet* 28 (2019) R133-R142.
- [45] Janssens, A. Validity of polygenic risk scores: are we measuring what we think we are? *Hum Mol Genet* 28 (2019) R143-R150.
- [46] Barc, R.; Glinge, C.; Chiang, D.Y.; Jouni, M.; Simonet, F.; Jurgens, S.J.; Baudic, M.; Nicastro, M.; Potet, F.; Offenhaus, J.A.; et al. Genome-wide association meta-analysis identifies novel Brugada syndrome susceptibility loci and highlights a new mechanism of sodium channel regulation in disease susceptibility. *Nature Genetics* (2021).
- [47] Parsa, N. Environmental factors inducing human cancers. *Iran J Public Health* 41 (2012) 1-9.
- [48] Cosselman, K.E.; Navas-Acien, A.; Kaufman, J.D. Environmental factors in cardiovascular disease. *Nat Rev Cardiol* 12 (2015) 627-42.
- [49] Zhang, G.; Pradhan, S. Mammalian epigenetic mechanisms. *IUBMB Life* 66 (2014) 240-56.
- [50] Lin, H.; Yin, X.; Xie, Z.; Lunetta, K.L.; Lubitz, S.A.; Larson, M.G.; Ko, D.; Magnani, J.W.; Mendelson, M.M.; Liu, C.; et al. Methylome-wide Association Study of Atrial Fibrillation in Framingham Heart Study. *Sci Rep* 7 (2017) 40377.
- [51] Steenman, M. Insight into atrial fibrillation through analysis of the coding transcriptome in humans. *Biophys Rev* 12 (2020) 817-826.
- [52] Sun, H.; Shao, Y. Transcriptome analysis reveals key pathways that vary in patients with paroxysmal and persistent atrial fibrillation. *Exp Ther Med* 21 (2021) 571.
- [53] Yue, H.; Liang, W.; Gu, J.; Zhao, X.; Zhang, T.; Qin, X.; Zhu, G.; Wu, Z. Comparative transcriptome analysis to elucidate the therapeutic mechanism of colchicine against atrial fibrillation. *Biomed Pharmacother* 119 (2019) 109422.
- [54] Zhao, G.; Zhou, J.; Gao, J.; Liu, Y.; Gu, S.; Zhang, X.; Su, P. Genome-wide DNA methylation analysis in permanent atrial fibrillation. *Mol Med Rep* 16 (2017) 5505-5514.

- [55] Wu, D.M.; Zhou, Z.K.; Fan, S.H.; Zheng, Z.H.; Wen, X.; Han, X.R.; Wang, S.; Wang, Y.J.; Zhang, Z.F.; Shan, Q.; et al. Comprehensive RNA-Seq Data Analysis Identifies Key mRNAs and lncRNAs in Atrial Fibrillation. *Front Genet* 10 (2019) 908.
- [56] Kaur, K.; Zarzoso, M.; Ponce-Balbuena, D.; Guerrero-Serna, G.; Hou, L.; Musa, H.; Jalife, J. TGF-beta1, released by myofibroblasts, differentially regulates transcription and function of sodium and potassium channels in adult rat ventricular myocytes. *PLoS One* 8 (2013) e55391.
- [57] Iseoka, H.; Miyagawa, S.; Fukushima, S.; Saito, A.; Masuda, S.; Yajima, S.; Ito, E.; Sougawa, N.; Takeda, M.; Harada, A.; et al. Pivotal Role of Non-cardiomyocytes in Electromechanical and Therapeutic Potential of Induced Pluripotent Stem Cell-Derived Engineered Cardiac Tissue. *Tissue Eng Part A* 24 (2018) 287-300.
- [58] Sacchetto, C.; Vitiello, L.; de Windt, L.J.; Rampazzo, A.; Calore, M. Modeling Cardiovascular Diseases with hiPSC-Derived Cardiomyocytes in 2D and 3D Cultures. *Int J Mol Sci* 21 (2020).
- [59] Beauchamp, P.; Jackson, C.B.; Ozhatil, L.C.; Agarkova, I.; Galindo, C.L.; Sawyer, D.B.; Suter, T.M.; Zuppinger, C. 3D Co-culture of hiPSC-Derived Cardiomyocytes With Cardiac Fibroblasts Improves Tissue-Like Features of Cardiac Spheroids. *Front Mol Biosci* 7 (2020) 14.
- [60] Zuppinger, C. 3D Cardiac Cell Culture: A Critical Review of Current Technologies and Applications. *Front Cardiovasc Med* 6 (2019) 87.
- [61] Drakhlis, L.; Biswanath, S.; Farr, C.M.; Lupanow, V.; Teske, J.; Ritzenhoff, K.; Franke, A.; Manstein, F.; Bolesani, E.; Kempf, H.; et al. Human heart-forming organoids recapitulate early heart and foregut development. *Nat Biotechnol* 39 (2021) 737-746.
- [62] Richards, D.J.; Li, Y.; Kerr, C.M.; Yao, J.; Beeson, G.C.; Coyle, R.C.; Chen, X.; Jia, J.; Damon, B.; Wilson, R.; et al. Human cardiac organoids for the modelling of myocardial infarction and drug cardiotoxicity. *Nat Biomed Eng* 4 (2020) 446-462.

Curriculum Vitae

Aleksandra Nijak-Paeske

e-mail	contact@aleksandranijak.com
DOB	26.06.1991
Nationality	Polish

EDUCATION

2016–2022

PHD / SPECIALIZATION: BIOMEDICINE, MEDICAL GENETICS (CARDIOGENETICS)

University of Antwerp, Antwerp, Belgium

Thesis: “Genomics and innovative induced pluripotent stem cell (iPSC) modeling to improve understanding of pathomechanisms underlying Brugada syndrome (BrS)”

2014–2015

MASTER’S IN BIOTECHNOLOGY / SPECIALIZATION: MEDICAL DIAGNOSTICS

Poznań University of Life Sciences, Poznań, Poland

Thesis: “The analysis of the effect of *LATS1* knockdown on melanoma growth in a pre-clinical model”

2010–2014

ENGINEER IN BIOTECHNOLOGY / GENERAL BIOTECHNOLOGY

Poznań University of Life Sciences, Poznań, Poland

Thesis: “Evaluation of the prognostic value of serum miRNAs in melanoma patients treated with a genetic melanoma vaccine”

2010–2014

ENGINEER IN FOOD TECHNOLOGY / SPECIALIZATION: FERMENTATION

Poznań University of Life Sciences, Poznań, Poland

Thesis: “Comparison of ethanol derivation from starch and sucrose raw materials”

2007–2010

SECONDARY EDUCATION / PROFILE: BIOLOGY AND CHEMISTRY

III LO im. Królowej Jadwigi, Inowrocław, Poland

RESEARCH ACTIVITIES

FEBRUARY 2016 - PRESENT

PHD STUDENT / CENTRE OF MEDICAL GENETICS, CARDIOGENETICS RESEARCH GROUP, UNIVERSITY OF ANTWERP, ANTWERP, BELGIUM

Promotors: Prof. Dr. Bart Loeys, Prof. Dr. Maaike Alaerts, Dr. Alain Labro

Used techniques: DNA/RNA extraction from cell cultures, Sanger sequencing, WGS samples preparation, immunocytochemistry staining of human iPSCs/iPSC-CMs/HEK293 cells/fibroblasts, lipofections, patch-clamping in voltage- and current-clamp modes, electrophysiological/imaging/sequencing data analysis, primer design, fibroblast and PBMC derivation from skin biopsies and blood samples, fibroblast/PBMC reprogramming to iPSCs using Sendai virus transduction, clonal selection and validation of the obtained

iPSC lines, iPSC-CM differentiation using small molecules, pluripotency assessment through embryoid body formation assay, molecular cloning, RT-PCR, PCR.

AUGUST 2012 – DECEMBER 2015

VOLUNTEER AS LABORATORY ASSISTANT / GREATER POLAND CANCER CENTRE, DIAGNOSTICS AND CANCER IMMUNOLOGY DEPARTMENT

Performed research for Engineer's and Master's degree in Biotechnology

Promotors: Dr. Anna Przybyła (Engineer's) and Dr. Urszula Kazimierczak (Master's)

Used techniques: DNA/RNA/protein extraction from blood, tumour tissue or bacterial suspension culture; Western blot, PCR, qRT-PCR, cell culture of: HEK293T, mouse fibroblasts, MHC7 α and iPSC cells in suspension and monolayer; immunocytochemistry staining, viral transduction using lentiviral vectors, plasmid transfections, cytotoxicity assays, proliferation assay (soft agar), restriction analysis, molecular cloning, injections, scarification and dissections of laboratory animals.

OTHER ACADEMIC ACTIVITIES AND DIPLOMAS

JUNE 2020

INTRODUCTION TO PROGRAMMING WITH MATLAB / VANDERBILT UNIVERSITY

Online certification course, coursera.org

APRIL 2016

EMBRYONIC AND INDUCED PLURIPOTENT STEM CELL TRAINING PROGRAM / STEM CELL INSTITUTE KU LEUVEN, BELGIUM

Reprogramming and Introduction to Differentiation

PEER-REVIEWED ARTICLES

FEBRUARY 2022

VAN BREEDAM E., NIJAK A., BUYLE-HUYBRECHT T., DI STEFANO J., BOEREN M., GOVAERTS J., QUARTA A., SWARTENBROEKX T., JACOBS E.Z., MENTEN B., GIHSBERS R., DELPUTTE P., ALAERTS M., HASSANNIA B., LOEYS B., BERNEMAN Z., TIMMERMANS J-P., JORENS P.G, VANDEN BERGHE T., FRANSEN E., WOUTERS A., DE VOS W.H., PONSARTS P.

Luminescent human iPSC-derived neurospheroids enable modelling of neurotoxicity after oxygen-glucose deprivation

Neurotherapeutics. 2022, Ma 14. Doi:10.1007/s13311-022-01212-z

FEBRUARY 2022

SIMONS E., NIJAK A., LOEYS B.L., ALAERTS M.

Generation of two induced pluripotent stem cell (iPSC) lines (BRANTWi006-A, BRANTWi007-A) from Brugada syndrome patients carrying an *SCN5A* mutation

Stem Cell Res. 2022, 60: 102719. doi: 10.1016/j.scr.2022.102719

FEBRUARY 2022

NIJAK A., SIMONS E., VANDENDRIESSCHE B., VAN DE SANDE D., FRANSEN E., SIELIWONCZYK E., VAN GUCHT I., VAN CRAENENBROECK E., SAENEN J., HEIDBUCHEL H., PONSARTS P., LABRO A.J., SNYDERS D, DE VOS W., SCHPERS D., ALAERTS A., LOEYS B.L.

Morpho-functional comparison of differentiation protocols to create iPSC-derived cardiomyocytes

Biol Open. 2022, 11 (2): bio059016. doi: 10.1042/bio.059016

AUGUST 2021

SIMONS E., LABRO A.J., SAENEN J., NIJAK A., SIELIWONCZYK E., VANDENDRIESSCHE B., DABROWSKA M., VAN CRAENENBROECK E., SCHEPERS D., VAN LAER L., LOEYS B.L., ALAERTS M.

Molecular autopsy and subsequent functional analysis reveal de novo *DSG2* mutation as cause of sudden death

Eur. J. Med. Genet. 2021, 23;64(11):104322. doi: 10.1016/j.ejmg.2021.104322.

MARCH 2021

NIJAK A., SAENEN J., LABRO A.J., SCHEPERS D., LOEYS B.L., ALAERTS M.

iPSC cardiomyocyte models of Brugada syndrome – achievements, challenges and future perspectives
Int. J. Mol. Sci. 2021, 22(6), 2825; doi:10.3390/ijms22062825

NOVEMBER 2020

SIELIWOŃCZYK E.; ALAERTS M., ROBYNS T., SCHEPERS D., CORVELEYN A., WILLEMS R., VAN CRAENENBROECK E.M., SIMONS E., NIJAK A., VANDENDRIESSCHE B., MORTIER G., VRINTS C., KOOPMAN P., HEIDBUCHEL H., VAN LAER L., SAENEN J., LOEYS B.L.

Clinical characterization of the first Belgian *SCN5A* founder mutation

Europace. 2020, Nov 22:euaa305. doi: 10.1093/europace/euaa305.

JULY 2020

NIJAK A., LABRO A.J., DE WILDE H., DEWALS W., PEIGNEUR S., TYTGAT J., SNYDERS D., SIELIWOŃCZYK E., SIMONS E., VAN CRAENENBROECK E., SCHEPERS D., VAN LAER L., SAENEN J., LOEYS B.L., ALAERTS M.

Compound heterozygous *SCN5A* mutations in severe sodium channelopathy with Brugada syndrome: A case report

Front. Cardiovasc. Med., 7:117. doi: 10.3389/fcvm.2020.00117

JANUARY 2018

NIJAK A., ALAERTS M., KUIPERI C., CORVELEYN A., SUYS B., PAELINCK B., VAN CRAENENBROECK E., VAN LAER L., LOEYS B., VERSTRAETEN A.

Left ventricular non-compaction with Ebstein anomaly attributed to a *TPM1* mutation

Eur. J. Med. Genet. 2018; 61(1):8-10. doi: 10.1016/j.ejmg.2017.10.003.

NOVEMBER 2016

GŁADYCH M., NIJAK A., LOTA P., OLEKSIEWICZ U.

Epigenetics: the guardian of pluripotency and differentiation

Turk. J. Biol. 2016; 40:1018-1032 doi:10.3906/biy-1509-30.

JUNE 2015

GLAPA A., NIJAK A.

TAZ oncogene as a prognostic factor in breast cancer

JMS 2015; 84(2) doi:10.20883/medical.e25.

SCIENTIFIC CONFERENCES AND PRESENTATIONS

MARCH 2020

20TH ANNUAL BESHG MEETING: GENOME FOR ALL? / BRUSSELS, BELGIUM

Poster presentation: „Compound heterozygous *SCN5A* mutations in a severe Brugada syndrome case”

NOVEMBER 2019

SECOND ANNUAL MEETING OF BELGIAN WORKING GROUP BASIC RESEARCH IN CARDIOLOGY (BWGBRC) / ANTWERP, BELGIUM

Poster presentation: „Compound heterozygous *SCN5A* mutations in a severe Brugada syndrome case”

APRIL 2019
FOURTH EUROPEAN SOCIETY OF HUMAN GENETICS TRAINING COURSE ON CARIOGENETICS /
EUROPEAN SOCIETY OF HUMAN GENETICS, ANTWERP, BELGIUM

MARCH 2019
19TH ANNUAL MEETING OF THE BESHG / LIEGE, BELGIUM

Poster presentation: „Comparison of three differentiation protocols to create iPSC-derived cardiomyocytes”

NOVEMBER 2018
FIRST ANNUAL MEETING OF BELGIAN WORKING GROUP BASIC RESEARCH IN CARDIOLOGY (BWGBRC)
/ LOUVAIN-LA-NEUVE, BELGIUM

Oral presentation: „Comparison of three differentiation protocols to create iPSC-derived cardiomyocytes”

OCTOBER 2018
5TH ANNUAL MEETING OF BELGIAN SOCIETY OF STEM CELL RESEARCH / LEUVEN, BELGIUM
Poster presentation: „Comparison of three differentiation protocols to create iPSC-derived cardiomyocytes”

JUNE 2018
42ND EWGCCE MEETING / EUROPEAN WORKING GROUP OF CARDIAC CELLULAR
ELECTROPHYSIOLOGY, ESSEN, GERMANY
Poster presentation: „Compound heterozygous *SCN5A* mutations in a severe Brugada syndrome case”

APRIL 2018
F-TALES WORKSHOP: GENOMIC MEDICINE / FLANDERS TRAINING NETWORK LIFE SCIENCES, LEUVEN,
BELGIUM

APRIL 2018
FRONTIERS IN CARDIOVASCULAR BIOLOGY / EUROPEAN SOCIETY OF CARDIOLOGY, VIENNA, AUSTRIA
Poster presentation: „Combined genetic and electrophysiological studies resolve an unexplained SCD case”

APRIL 2018
THIRD CARIOGENETICS TRAINING COURSE / EUROPEAN SOCIETY OF HUMAN GENETICS,
MANCHESTER, UK

FEBRUARY 2018
18TH ANNUAL MEETING OF THE BELGIAN SOCIETY OF HUMAN GENETICS: “THE EPIGENOME IN
DEVELOPMENT AND DISEASE” / GHENT, BELGIUM

APRIL 2017
SECOND EUROPEAN SOCIETY OF HUMAN GENETICS TRAINING COURSE ON CARIOGENETICS /
EUROPEAN SOCIETY OF HUMAN GENETICS, ANTWERP, BELGIUM

FEBRUARY 2017
17TH ANNUAL MEETING OF THE BELGIAN SOCIETY OF HUMAN GENETICS / LOUVAIN-LA-NEUVE,
BELGIUM
Poster presentation: Left ventricular non-compaction with Ebstein anomaly attributed to a *TPM1* mutation

NOVEMBER 2016

ADVANCES IN CELL ENGINEERING, IMAGING AND SCREENING: VIB TOOLS & TECHNOLOGIES / VIB, LEUVEN, BELGIUM

MAY 2016

29TH COURSE IN MEDICAL GENETICS / EUROPEAN SOCIETY OF HUMAN GENETICS, BERTINORO, ITALY

GRANTS AND AWARDS

JUNE 2018

TRAVEL GRANT AWARD / 42ND EUROPEAN WORKING GROUP OF CARDIAC CELLULAR ELECTROPHYSIOLOGY, ESSEN, GERMANY

JANUARY 2017

SB PHD FELLOWSHIP / RESEARCH FOUNDATION FLANDERS (FWO), BELGIUM

AUGUST 2014

LABORATORY TRAINEE FELLOWSHIP INNOMED / NATIONAL CENTRE FOR RESEARCH & DEVELOPMENT (NCBR), POLAND

AUGUST 2014

WELCOME FELLOWSHIP FOR MASTER STUDENT / FOUNDATION FOR POLISH SCIENCE (FNP), POLAND

EDUCATIONAL ACTIVITIES

2017-2018

CO-SUPERVISOR / MASTER THESIS ILSE VAN GUCHT

„Optimization of the methods to generate an advanced cellular model for a Belgian *SCN5A* founder mutation and search for novel genes for the Brugada syndrome”

2016-2017

CO-SUPERVISOR / MASTER THESIS ELINE SIMONS

„Onderzoek naar de genetics van primaire elektrische hartaandoeningen en ontwikkeling van een celmodel voor Brugada syndroom”

Acknowledgements

It has been a journey with some ups and downs to get to this moment however, the end product (this thesis) is a cherry on top of it all. Now I can say: I made it! As Hellen Keller once said: “Alone we can do so little, together we can do so much”. And if there would be only one thing I would keep from this experience, it is the blessing which was meeting amazing people on the way here, without whom this thesis would not be possible.

First and foremost, I would like to thank my promotor prof. Bart Loeys for giving me a chance, and trusting me those 7 years ago. It has been a leap of faith for both sides, that an ambitious student from Poland can take the challenge of introducing the lab procedures for iPSC culture, derivation, and differentiation at your facility. I hope you also think it was a decision that paid off 😊. It has been an honour to study and grow as a geneticist with your guidance and to be a part of your team. Thank you for the affirmative and critical feedback throughout the past years, as well as the patience it took to get here.

It would be impossible to write this thesis without the guidance of my other promotor – prof. Maaïke Alaerts. The hours spent on the technical manuscripts, common growth in the topic of iPSC modeling, cardiomyocyte differentiation, and electrophysiology... thank you for your support and being a partner in brainstorming about those topics.

As a young, and maybe a bit naïve student, during the course of this PhD I wanted to become an electrophysiologist. I still remember the first time prof. Alain Labro heard that. Your honesty has put me down on earth that day 😊. Thank you for all the patience with the explanation of the basics of electrophysiology, and for showing me your support when the hours spent on patch-clamping were not always bringing expected results. It was a great experience to have you as a mentor in this process.

I would like to thank my doctoral committee members for their time spent on reading this thesis and the provided feedback. I would also like to thank all the members of the GOA consortium: prof. Peter Ponsaerts, prof. Dirk Snyders, prof. Johan Saenen, prof. Lut Van Laer, prof. Emeline Van Craenenbroeck and prof. Hein Heidbuchel for their support, immense knowledge, and plentiful experience which have been invaluable helpful in performing and writing this thesis.

My gratitude extends to prof. Erik Fransen, dr. Geert Vandeweyer, prof. Winnok de Wos and Philip Holmgren, for granting their technical support and expertise in processing of the data generated throughout this project.

I would like to thank all the members of the Centre of Medical Genetics and the Administrative staff of the Department of Medical Genetics at the University of Antwerp, that made it possible for me to focus on my studies and make them proceed smoothly.

Moving to Belgium was a huge step for me, as I left my friends and family in Poland. However, the help I received at the beginning of my studies from members of the Cardiogenetics team – Maaïke and Aline, with the search for accommodation and the official paperwork showed me, that it will be a great adventure, where I would not be left alone. Aorta group... I think I have been very lucky to be a part of such a great mix of people! Aline and Dorine, thank you for being my ‘interim promoters’. It is not an easy situation for a fresh student to have no leader for a few months right at the start of the PhD project. I appreciate your help and guidance in this process, I would be totally lost without it! 😊 The success of a PhD student is in the support obtained from the laboratory technicians. Celine, Maaïke B., Jarl, Gerarda, Laura from the Cardiogenetics group, as well as Abbi and Evy from the Electrophysiology group. I would not manage to make it here without your help. Thank you! Ilse L. and Jeannette, thank you for integrating me with the team and for our all-you-can-eat afternoon meetups. When speaking of the Cardiogenetics group, I cannot forget other fellow PhD students: Joe, Lotte, Jotte, Hanne, Pauline. It was such a great experience to meet you and together be a part of a team. During my PhD studies, I was a part of not only the Cardiogenetics group. Here I would like to also mention Electrophysiology and Experimental

Hematology teams. Kenny, Laura, Rohit, Debbie, Alessandra, Elise, Tamariche, Marlies, and Julia, thank you for letting me feel like a part of your teams and for your support in the lab. Iedereen hartelijk bedankt!

As Matthew Woodring Stover said: “If you take out the team out of teamwork, it’s just work. And who wants that?” Here, I would like to mention a few people who made long hours with cell work and patch-clamping true fun. Eline – thank you for the exchanged holiday and weekend schedules with cells, for all the patching help, and for sharing all the frustrations as well as successes with the functional cell work 😊. Ilse VG, Melanie, and Ewa – I am so grateful that (together with Eline and Jolien) we formed a team for laughter and venting out. It’s been great fun to share an office with you! Bert and Dieter – thank you for sharing experiences with calcium imaging and patch-clamping. The dark humour when something was going wrong and teaching me patience in those moments when all you want to do is give up and trash some things out 😊 – those are the things that kept me going.

Vielen Dank an mein neues Team in München: Die Array-Abteilung bei SYNLAB MVZ Humane Genetik. Vielen Dank für euer Verständnis, eure Unterstützung und euren Zuspruch in der letzten Phase der Erstellung meiner Doktorarbeit.

I would like to thank my friends – those I made in Belgium and those I already had in Poland. I think all of you heard me talking about my research and I think you have never said I should shut up even if you did not understand what I am talking about 😊. Thanks for being my support system!

I would not be here without the help of my family. To my husband – thank you for being so understanding, especially in the past two years, when the writing of this thesis became my priority. I think by now this thesis is as much yours as it is mine 😊 (we made it!).

Last but not least – chciałam podziękować moim wspaniałym rodzicom. Dziękuję za wasze wsparcie, to finansowe i przede wszystkim to psychiczne. Dziękuję, że mimo waszego zmartwienia, że będę tak daleko, wspieraliście mnie na każdym kroku i okazywaliście swoje zrozumienie. Oraz za wasze odwiedziny w Belgii i wszystkie przesyłki z Polski 😊. Dziękuję!